

Politecnico di Milano  
Department of Physics



**POLITECNICO**  
MILANO 1863

DIPARTIMENTO DI FISICA

*Doctoral Programme in Physics*

# Phase Transitions, Dynamics, and Avalanches in Disordered Ising Models

SUPERVISOR:  
Prof. Paolo Biscari

PHD CANDIDATE:  
Federico Etori

CO-SUPERVISOR:  
Prof. Timothy J. Sluckin

TUTOR:  
Prof. Maurizio Zani

XXXVII cycle  
2021–2024



# Contents

<b>1</b>	<b>Introduction</b>	<b>1</b>
<b>2</b>	<b>Simulation of magnetic systems</b>	<b>5</b>
2.1	Thermodynamic phases . . . . .	6
2.2	The Ising model . . . . .	7
2.2.1	Few words on the one-dimensional Ising model . . . . .	8
2.2.2	Two-dimensional Ising model . . . . .	9
2.3	Random Ising models . . . . .	12
2.3.1	RBIM and the SG phase . . . . .	13
2.3.2	RFIM and the Imry-Ma argument . . . . .	16
2.3.3	The model with defects . . . . .	18
2.4	Monte Carlo simulations for the Ising model . . . . .	21
2.4.1	Markov chains . . . . .	22
2.5	Monte Carlo algorithms and techniques . . . . .	24
2.5.1	Metropolis algorithm . . . . .	24
2.5.2	Multi-spin coding algorithm . . . . .	25
2.5.3	N-Fold way algorithm . . . . .	26
2.5.4	Parallel tempering technique . . . . .	27
2.5.5	Glauber dynamics for out-of-equilibrium simulations . . . . .	29
<b>3</b>	<b>Thermodynamic Properties</b>	<b>31</b>
3.1	Equilibrium configuration . . . . .	32
3.2	Quasi-phases investigation . . . . .	34
3.2.1	Analysis of overlap distribution . . . . .	36
3.3	Phase transition characterisation . . . . .	39
<b>4</b>	<b>Dynamic Properties</b>	<b>47</b>
4.1	Reversal process in homogeneous systems . . . . .	48
4.1.1	Mechanisms of reversal . . . . .	50
4.1.2	Classical nucleation theory . . . . .	51
4.1.3	Validation of CNT with Ising model . . . . .	54
4.1.4	Johnson-Mehl-Avrami-Kolmogorov theory . . . . .	61
4.1.5	Metastable lifetime and spinodal line . . . . .	64

4.2	Reversal process in heterogeneous systems . . . . .	67
4.2.1	CNT in the model with defects . . . . .	68
4.2.2	Validation of CNT in the model with defects . . . . .	70
4.2.3	JMAK theory in heterogeneous systems . . . . .	77
4.2.4	Metastable lifetime and spinodal line modification . . . . .	79
<b>5</b>	<b>Dynamic phase transition</b>	<b>89</b>
5.1	DPT in homogeneous systems . . . . .	90
5.1.1	Dynamic order parameter . . . . .	91
5.1.2	Hysteresis loop area . . . . .	94
5.1.3	Experimental observations . . . . .	95
5.2	DPT in random systems . . . . .	95
5.2.1	Random bond and random field Ising models . . . . .	96
5.2.2	The model with defects . . . . .	98
5.2.3	Dynamic local properties of the model with defects . . . . .	102
5.2.4	Tuning the DPT with randomness . . . . .	104
<b>6</b>	<b>Avalanches in random magnetic systems</b>	<b>111</b>
6.1	Avalanches and crackling noise . . . . .	111
6.1.1	Power law analysis . . . . .	113
6.2	Barkhausen noise statistics . . . . .	116
6.2.1	Temperature behaviour of the Barkhausen noise statistic . . . . .	118
6.3	IET statistics in complex systems . . . . .	123
6.3.1	Poissonian IET statistics in homogeneous systems . . . . .	125
6.3.2	Two-states Markov process for homogeneous systems . . . . .	125
6.3.3	Fat-tailed IET statistics in disordered systems . . . . .	130
6.3.4	Four-states Markov process for heterogeneous systems . . . . .	133
<b>7</b>	<b>Conclusion</b>	<b>143</b>
<b>A</b>	<b>Investigation of the defect-potential</b>	<b>147</b>
<b>B</b>	<b>Avrami's law derivation</b>	<b>149</b>
<b>C</b>	<b>Optimal defect unbalance</b>	<b>151</b>

# Chapter 1

## Introduction

The study of *complex systems* represents one of the most dynamic and challenging areas in modern science, encompassing disciplines as diverse as Physics, Biology, Economics, and Social Sciences. Complex systems are characterized by interactions among many components, giving rise to emergent phenomena that cannot be predicted solely from the properties of individual components. The significance of this field was reaffirmed in 2020 when Giorgio Parisi was awarded the Nobel Prize in Physics for his groundbreaking contributions to understanding disordered and complex systems. This recognition highlighted the importance of the field, confirming its pivotal role in addressing fundamental questions about the behaviour of real-world systems. Statistical mechanics can unravel the intricate dynamics of complex phenomena, bridging the gap between theoretical frameworks and empirical observations.

Within this vast landscape, the *Ising model* has emerged as a paradigmatic framework for exploring complex systems. Originally introduced by Wilhelm Lenz and Ernst Ising in the early 20th century to describe magnetic phase transitions, the Ising model has since transcended its origins. Its simplicity (binary spins interacting on a lattice) belies its profound ability to capture the essence of critical phenomena and collective behaviour. Modelling magnetic systems, the Ising model has illuminated patterns of avalanches in systems driven by external fields, such as *Barkhausen noise*, where clusters of spins flip in a correlated manner. Similarly, it has provided insight into opinion dynamics in social networks and neural activation in the brain, where local interactions give rise to global patterns. By abstracting the core mechanisms of such systems, the Ising model bridges theoretical constructs and empirical observations, offering a universal framework to understand phenomena as diverse as phase transitions and emergent dynamics.

Expanding on the classical Ising model, *random Ising models* incorporate disorder and heterogeneity, reflecting the complexities of real-world systems. These models, such as the *Random Bond Ising Model* (RBIM) and the *Random Field Ising Model* (RFIM), introduce randomness into interactions or external fields, respectively. This randomness mimics the effects of impurities, defects, or environmental variability, making these models particularly relevant for studying disordered magnetic systems, spin glasses, and other heterogeneous materials.

**Focus of the thesis** Real systems often operate far from equilibrium, influenced by time-dependent external drives. The study of *out-of-equilibrium* behaviour is crucial for understanding processes such as relaxation, hysteresis, and dynamic phase transitions, which are pivotal in magnetic materials and glassy systems. Despite the extensive work on the equilibrium properties of Ising models, much remains to be understood about their out-of-equilibrium dynamics. This thesis aims to explore the dynamic behaviour of random Ising models. By focusing on the interplay between disorder, dynamic stimuli, and response, this work seeks to shed light on universal behaviour, advancing our understanding of nonequilibrium processes in complex random systems.

At the heart of this thesis lies a novel variant of the random Ising model, incorporating *defects* as a form of quenched randomness. This model builds on the insights from the RFIM and RBIM but introduces a simpler and more computationally efficient framework. Defects are implemented as fixed spins, introducing localized heterogeneity that mimics impurities or frozen dynamics. Notably, the model with defects shows strong evidence of belonging to the same universality class as the RFIM. Furthermore, highly efficient algorithms, including the  $N$ -Fold way and Multi-Spin coding methods are easy to implement for the model with defects. These techniques enhance the efficiency of Monte Carlo simulations, particularly at low temperatures, where traditional methods often struggle.

This thesis uncovers compelling evidence of metastable states in the model with defects, which significantly complicate the system's time evolution. These metastable states mirror the behaviour of real systems, such as Barkhausen noise in ferromagnets, where the system exhibits sudden, avalanche-like changes due to the presence of pinning sites and metastable states. The presence of these metastable states not only delays relaxation but also introduces memory effects, reflecting the inherent complexity of disordered systems.

**Real-world applications** The Ising model with defects extends its relevance beyond magnetism to a wide range of systems characterized by competing interactions and disorder. In biological systems, could offer insights into processes such as protein folding, where the disorder in the energy landscape leads to metastable configurations [1], and neural networks, where the balance between excitatory and inhibitory connections amidst static noise resembles spin clustering [2]. Similarly, in socio-economic contexts, the model can describe collective decision-making dynamics, with fixed agents (analogous to defects) resisting external influences, forming localized subpopulations with stable opposing opinions [3].

Beyond these domains, the Ising model with defects serves as a versatile framework for understanding various real-world phenomena:

- Solute precipitation in heterogeneous media: the model captures the influence of heterogeneity as a catalyst in precipitation processes, providing insights into material formation in contexts like Materials Science and Geochemistry.
- Bistable systems and magnetic switching devices: it describes the presence of im-

purities in magnetic devices that could be used for storage technologies. This reveals critical for designing devices with reliable and deterministic transitions.

- Crackling noise in magnetic materials: by modelling avalanche-like behaviour driven by external fields, the Ising model with defects helps analyse the impact of impurity and defect concentrations in magnetic systems, helping to understand phenomena like Barkhausen noise and its link to material microstructure.
- Queueing systems and information exchange: the model's ability to reproduce power-law and exponential inter-event time distributions makes it applicable to systems such as communication networks, where temporal patterns predictability is essential for efficiency and robustness.

**Overview of the thesis** This thesis is structured as follows. Chapter 2 introduces the theoretical and computational methodologies employed, detailing the Ising model, its random variants, and the Monte Carlo algorithms central to this work. Chapter 3 examines equilibrium configurations, quasi-phases, and the characterization of phase transitions in the model with defects. Chapter 4 explores the reversal processes in homogeneous and heterogeneous systems, focusing on nucleation theories and metastability. Chapter 5 investigates dynamic phase transitions, contrasting behaviour in homogeneous and heterogeneous systems, and analysing local dynamic properties. Finally, Chapter 6 analyses avalanche phenomena and crackling noise, emphasizing the statistical characteristics of inter-event times in reversal processes. A final concluding chapter summarises the main findings of the work and the implications in the analysis of complex phenomena across disciplines.



## Chapter 2

# Simulation of magnetic systems

The Ising model stands as a cornerstone of *Statistical Mechanics*, offering a fundamental framework to study phase transitions and order-disorder phenomena. Originally conceived to describe ferromagnetic materials, the model has found applications in diverse fields, from lattice gases to neural networks and social dynamics. At its core, the Ising model encapsulates the interaction between discrete spins, which can assume one of two states, arranged on a lattice. These simplified assumptions yield remarkable insights into critical behaviour and emergent phenomena, making the model a paradigmatic example of simplicity yielding deep universality. Variants of the Ising model have further expanded its relevance, adapting to the complexities of real-world systems.

Incorporating randomness into the Ising model allows for the representation of disordered systems, such as diluted magnets, spin glasses, and other materials exhibiting non-uniform behaviour. These extensions, including the RFIM and the RBIM, address site- or bond-specific disorder, capturing the effects of impurities, defects, or irregular interactions. Modelling such randomness is essential to understanding the interplay between local heterogeneity and macroscopic phenomena, particularly in systems far from equilibrium. Through these modifications, the Ising framework becomes a versatile tool for studying systems where disorder and fluctuations dominate, yielding insights into glassy dynamics and other complex behaviour.

*Monte Carlo simulations* are indispensable for exploring the Ising model, particularly in disordered or high-dimensional scenarios. As the model scales to more complex systems, the number of possible configurations explodes, rendering analytical solutions infeasible. Monte Carlo methods bridge this gap by employing statistical sampling to explore the system's configuration space, enabling the study of equilibrium and dynamic processes. These algorithms reveal critical properties, dynamic transitions, and the effects of quenched randomness in systems where analytical techniques fall short.

This chapter outlines the methodological foundation of the thesis. We begin by introducing the Ising model, emphasizing its applicability to homogeneous and heterogeneous systems and discussing its extensions to capture disorder. Subsequently, we delve into the principles of Monte Carlo simulations, focusing on the algorithms employed to investigate both equilibrium and out-of-equilibrium properties, including the Metropolis and

$N$ -Fold way algorithms, as well as computational optimizations like multi-spin coding and parallel tempering. Finally, we describe *Glauber dynamics*, the primary framework used to model dynamic processes, and discuss its relevance to out-of-equilibrium systems. These tools and approaches form the basis for the investigations presented in subsequent chapters.

## 2.1 Thermodynamic phases

*Phase transitions* and the influence of disorder on them are central themes explored throughout this thesis. Before delving into the specifics, we briefly remind how their transitions are defined and studied.

In magnetic materials, phase transitions mark a fundamental shift in the system's behaviour, typically driven by temperature. For instance, ferromagnetic materials exhibit a magnetically ordered phase at low temperatures, where atomic spins align to produce a net magnetisation. As the temperature rises, thermal fluctuations disrupt this alignment. At the critical Curie temperature, the system transitions to a paramagnetic phase, where spins are randomly oriented, and net magnetisation vanishes. This change reflects the profound influence of external conditions, such as temperature, on the macroscopic properties of magnetic systems.

More generally, phase transitions describe changes in a system's state characterized by the emergence or loss of order, often quantified by an order parameter. In the case of magnetic systems, the order parameter measures the degree of spin alignment, remaining non-zero in the ordered ferromagnetic phase and dropping to zero in the disordered paramagnetic phase. This behaviour encapsulates a broader phenomenon where phase transitions signify a symmetry change, as the system evolves from a state with defined order to one where no specific structure or orientation dominates.

Building on the concept of phase transitions in magnetic systems, the *free energy* of the system serves as a fundamental tool to describe the transition between ordered and disordered phases. In thermodynamics, the free energy is expressed as:

$$F = U - TS \tag{2.1}$$

where  $U$  represents the system's internal energy and  $S$  its entropy. If volume and temperature are held constant from the outside, the phase of the system is determined by the configuration that minimizes the free energy.

At low temperatures, the entropic term  $TS$  becomes negligible, making the internal energy  $U$  the dominant factor. Since ordered configurations typically have lower internal energy, these states are favoured in the low-temperature regime. Conversely, at high temperatures, the entropic term becomes significant, favouring disordered configurations with higher entropy. At the critical temperature, the free energy landscape undergoes a qualitative change, leading to a shift in stability from the ordered to the disordered phase.

In addition to changes in free energy, the system's magnetic susceptibility, which quantifies the response of magnetisation to an external magnetic field, diverges at the

critical point. This divergence reflects the emergence of strong correlations between spins over long distances, a hallmark of the cooperative behaviour that defines the phase transition.

**Classification scheme of phase transitions** In 1933, Paul Ehrenfest introduced a classification scheme for phase transitions based on the lowest-order derivative of the free energy that exhibits a discontinuity. According to this framework [4], [5], phase transitions can be broadly divided into two main types.

*First-order* phase transitions are characterized by a discontinuity in the first derivative of the free energy at the transition point. These transitions typically involve abrupt changes in the order parameter and are often accompanied by hysteresis, indicating a lagged response of the system to external stimuli.

*Second-order* phase transitions, on the other hand, exhibit continuity in the first derivative of the free energy but a discontinuity in the second derivative. Unlike first-order transitions, the order parameter changes continuously across the transition, and other extensive thermodynamic quantities also vary smoothly.

While Ehrenfest’s classification theoretically allows for third- and higher-order phase transitions, such transitions are rarely observed in practice.

Ehrenfest classification reached its final version in 1960, where it was hybridized with other schemes surpassing the limitations of the original classification (presence of continuous divergence of the latent heat or the susceptibility and lack of universal exponents and universality).

1. First-order phase transitions present a latent heat. The system absorbs or releases a specific amount of energy per unit volume while keeping the temperature fixed allowing the conversion of all the material in the new phase [6]. This is typical of many physical processes, such as the transition from solid-liquid-gas.
2. Second-order phase transitions, also called “continuous phase transitions”, are characterised by the divergence of the susceptibility (second derivative of the free energy) and of the correlation length (typical length within which the material shows the same phase). Typical second-order phase transitions are the ferromagnetic-paramagnetic phase transition for a ferromagnetic material and the superconducting phase transition.

## 2.2 The Ising model

The Ising model was initially proposed by Wilhelm Lenz in 1920 and studied by Ernst Ising to model the behaviour and properties of magnetic materials [7]. In its simplest form, the Ising model is composed of an ensemble of spin variables which can assume only quantised values  $\pm 1$ . They are located on a set  $\Lambda$  of lattice sites composing a graph. To each spin configuration  $\sigma = \{\sigma_i\}_{i \in \Lambda}$  is associated an energy through the Hamiltonian:

$$\mathcal{H}(\sigma) = -J \sum_{\langle i,j \rangle} \sigma_i \sigma_j - h \sum_i \sigma_i \quad (2.2)$$

where  $\langle i, j \rangle$  indicates that the sum considered only neighbouring sites  $i$  and  $j$  given the geometry of  $\Lambda$ .  $J$  is the exchange interaction between neighbouring spins and  $h$  is the local external field. Throughout this thesis  $h$  is expressed in units of  $J$ . The analogy with the magnetic materials rises strongly. In particular,  $\sigma$  indicated in the Ising Hamiltonian represents the magnetic dipole moment of an atom or particle. This dipole moment originates from the intrinsic angular momentum, or “spin”, of electrons within the atom. Nuclear spins attain discrete values because of Quantum Mechanics. The Ising model further simplifies the picture by assuming only two states. This simplification captures the essential interaction between magnetic moments, especially in cases where alignment due to quantum effects or interactions with neighbouring atoms leads to overall magnetisation and collective magnetic behaviour in materials.

The Ising model provides a powerful framework for exploring the equilibrium behaviour of magnetic systems through the principles of Statistical Mechanics. A primary goal is to determine the system’s free energy, which serves as a cornerstone for deriving other thermodynamic quantities that characterize equilibrium states. Depending on the temperature of the system  $T$ , each configuration has a probability  $P_\beta(\sigma)$  to be sampled at equilibrium. Considering the Boltzmann distribution for the canonical ensemble (i.e. a system that can exchange energy with a heat bath), we write

$$P_\beta(\sigma) = \frac{e^{-\beta\mathcal{H}(\sigma)}}{Z_\beta} \quad (2.3)$$

where  $\beta = 1/k_B T$ ,  $k_B$  is the Boltzmann constant and  $Z_\beta$  is a normalization constant called partition function. Throughout this thesis we set  $k_B = 1$ .  $T$  is therefore measured in energy units. The partition function is written as:

$$Z_\beta(\sigma) = \sum_{\sigma} e^{-\beta\mathcal{H}(\sigma)} \quad (2.4)$$

The free energy of the system is computed as the mean free energy of all the configurations weighted by their probability given by the Boltzmann distribution:

$$\langle F \rangle_\beta = -\frac{1}{\beta} \log(Z_\beta) \quad (2.5)$$

An analytical expression of the free energy can be reasonably derived for the one-dimensional Ising model. In two dimensions, it took over twenty years of dedicated effort by the scientific community. In three dimensions, it remains an unsolved problem even after a century of active research on the topic. Moreover, a direct computation of the free energy becomes computationally unfeasible even for moderate values of the total number of spins  $N$ . For this reason, numerical simulations (especially Monte Carlo simulations) that produce approximate expressions of the free energy have been developed.

### 2.2.1 Few words on the one-dimensional Ising model

In his studies, Ising demonstrated, through an exact computation of the free energy, that the one-dimensional Ising model does not exhibit a thermodynamic phase transition at

any finite  $T$  [7]. This result stems from the inability of the one-dimensional system to sustain long-range order, as thermal fluctuations dominate and prevent the alignment of spins across the system.

To illustrate Ising's findings, we now present an analytical derivation of this result. Consider the Hamiltonian for the homogeneous one-dimensional Ising model with periodic boundary conditions and in the absence of an external field ( $h = 0$ ):

$$\mathcal{H}_{1D}(\sigma) = -J \sum_i s_i s_{i+1} \quad (2.6)$$

Periodic boundary conditions are used to simplify the analysis of systems with translational symmetry and to mitigate boundary effects that can arise in finite systems. In this case, periodic boundary conditions imply that the lattice sites are arranged in a closed loop, such that the first site is connected to the last site. Mathematically, this is expressed as:

$$s_{N+1} = s_1, \quad (2.7)$$

where  $N$  is the total number of spins in the system.

We can write the partition function as follows

$$Z_\beta = \lambda_+^N + \lambda_-^N \quad (2.8)$$

where  $\lambda_\pm = (e^{J\beta} \pm e^{-J\beta})$ . This expression can be derived by explicitly expanding the binomial terms and rewriting the partition function as a series of terms of the form  $e^{J\beta(N-4k)}$  with  $k \in \mathbb{N} : k < N/2$ . Each term is equivalent to the Boltzmann factor of a configuration with exactly  $2k$  neighbouring sites having opposite spins and  $N - 2k$  neighbouring sites with aligned spins. This factor is multiplied by the number of permutations for such configurations and a symmetry factor of two, accounting for the invariance under  $\sigma \rightarrow -\sigma$ . Then, considering Eq. (2.5), the free energy per site becomes

$$f(\beta) = -\frac{1}{N\beta} \log(Z_\beta) = -\frac{1}{N\beta} \log(\lambda_+^N + \lambda_-^N) \approx -\frac{1}{\beta} \log(\lambda_+) \quad (2.9)$$

where in the last passage  $N \rightarrow \infty$  was considered. Finally, we can write

$$f(\beta) = -\frac{1}{\beta} \log(2 \cosh(\beta J)) \quad (2.10)$$

Since  $f$  remains analytic for all temperatures, no cusp or discontinuity can be observed in the free energy. This result shows that in one dimension, the Ising model at the thermodynamic limit does not exhibit a phase transition at any finite temperature.

### 2.2.2 Two-dimensional Ising model

After completing his PhD thesis, Ernst Ising stepped away from the field of research. Based on the arguments he developed for the one-dimensional Ising model, Ising hypothesized that no phase transition would occur in higher-dimensional versions of the

model. However, subsequent studies and decades of significant effort within the statistical physics community revealed that a phase transition does indeed exist in two or more dimensions.

The first rigorous demonstration was provided by Peierls in 1936 [8]. The argument can be summarized as follows. Consider a square lattice where all spins are aligned coherently (e.g., all spins are positive). We calculate the free energy difference  $\Delta F$  associated with the formation of a domain of negative spins with perimeter  $L$ . We consider again Eq. (2.1) and we write the free energy difference as  $\Delta F = \Delta U - T\Delta S$ . The internal energy related to domain formation accounts only for the presence of a boundary which separates positive from negative spins. Since the energetic cost for each unity of boundary is  $+2J$ , we write  $\Delta E = +2JL$ . For the entropic part, we consider the Boltzmann formula  $\Delta S = k_B \log \Omega$ . Here  $\Omega$  refers to the number of ways the system can be arranged given a specific macrostate (for example, the one with a cluster with perimeter  $L$ ). It turns out that  $\Omega \sim \mu^L$  for a suitable value of  $\mu < 3$ . Combining these terms, the total free energy variation becomes:

$$\Delta F = 2JL - k_B T L \log \mu \quad (2.11)$$

We can identify a critical temperature  $T_c$  defined as the point where  $\Delta F = 0$ .

$$T_c = \frac{2J}{k_B} \log \mu \quad (2.12)$$

Then, for  $T > T_c$  the formation of domains is actually favoured by the system, resulting in a disordered configuration with null magnetisation (disordered phase). On the contrary, for  $T < T_c$  the formation of domains is energetically unfavoured and the system prefers to orient spins toward the same direction. In this ordered phase, the magnetisation is non-zero, marking the onset of long-range order.

In 1944, Lars Onsager derived the exact expression for the free energy of the two-dimensional Ising model [9]. The free energy per site is given by:

$$-\beta f = \log 2 + \frac{1}{8\pi^2} \int_0^{2\pi} d\theta_1 \int_0^{2\pi} d\theta_2 \log [\cosh^2(2\beta J) - \sinh(2\beta J)(\cos \theta_1 + \cos \theta_2)], \quad (2.13)$$

Onsager also demonstrated that at the critical temperature:

$$T_c = \frac{2J}{k_B \log(1 + \sqrt{2})}, \quad (2.14)$$

the system undergoes a phase transition. At  $T = T_c$ , the total magnetisation defined through:

$$m = \frac{1}{N} \sum_i \sigma_i \quad (2.15)$$

changes continuously from 0 (paramagnetic phase) to  $\approx \pm 1$  (ferromagnetic phase) as the temperature decreases below  $T_c$ . This result conclusively establishes the existence of a second-order phase transition in the two-dimensional Ising model.

The two-dimensional Ising model serves as a paradigmatic case study for understanding systems undergoing phase transitions. From Eq. (2.13), all thermodynamic quantities can be derived.

One of the most fundamental quantities is the magnetisation  $m(T)$ , which characterizes the system's degree of order. In the thermodynamic limit ( $L \rightarrow \infty$ ), the magnetisation is given by:

$$m(T) = \begin{cases} \left[1 - \sinh^{-4} \left( \frac{2J}{k_B T} \right) \right]^{1/8} & \text{for } T < T_c, \\ 0 & \text{for } T \geq T_c. \end{cases} \quad (2.16)$$

Another critical quantity is the magnetic susceptibility  $\chi_M$ , which measures the response of the magnetisation to an external field:

$$\chi_m = \frac{\partial M}{\partial H}. \quad (2.17)$$

Near the critical temperature  $T_c$ , the magnetic susceptibility exhibits a power-law divergence:

$$\chi_m \sim |T - T_c|^{-\gamma}, \quad (2.18)$$

where the critical exponent is  $\gamma = 7/4$ .

The specific heat  $C(T)$ , derived from the second derivative of the free energy, also displays critical behaviour. It shows a logarithmic divergence near  $T_c$ :

$$C(T) \sim -\log |T - T_c|, \quad (2.19)$$

further confirming that the phase transition is of second order.

An essential aspect of the Ising model's behaviour is captured by the correlation between spins at different lattice sites. This is quantified using the two-point connected correlation function:

$$G_c(i, j) = \langle \sigma_i \sigma_j \rangle - \langle \sigma_i \rangle \langle \sigma_j \rangle, \quad (2.20)$$

where  $\langle \dots \rangle$  denotes a thermal average. The correlation function  $G_c(i, j)$  measures the statistical dependence between spins at sites  $i$  and  $j$ . When the temperature  $T \gg T_c$ , spins fluctuate independently, and  $G_c(i, j)$  approaches zero for large separations. As  $T$  approaches  $T_c$ , correlations extend over larger distances, reflecting the system's growing coherence. Below  $T_c$ , long-range order emerges, and  $G_c(i, j)$  approaches unity for nearby spins.

Near  $T_c$ , the spatial decay of the correlation function can be described as:

$$G_c(r) \sim e^{-r/\xi}, \quad (2.21)$$

where  $\xi$  is the correlation length. Remarkably, the correlation length follows a power law near the critical temperature and diverges as  $T \rightarrow T_c$ :

$$\xi(T) \sim |T - T_c|^{-\nu}, \quad (2.22)$$

with a critical exponent  $\nu = 1$ .

The 2D Ising model is also a cornerstone of the theory of universality. Universality implies that critical exponents like  $\gamma$  and  $\nu$  depend only on broad features of the system, such as dimensionality and symmetry, rather than microscopic details like lattice geometry or interaction strength. This insight makes the Ising model a representative example of a wide class of systems exhibiting phase transitions, enabling predictions far beyond magnetic systems. Universality bridges diverse physical phenomena, from liquid-vapour transitions to social dynamics and opinion spreading, underscoring the profound reach of the Ising model in modern physics.

### 2.3 Random Ising models

Random Ising models are a variation of the classical Ising model in statistical physics, designed to study systems with disorder or quenched randomness representing the effects of impurities, defects, or random environments. The capability to adapt to more realistic conditions makes the random Ising model an essential tool for understanding disordered magnetic systems [10], alloys [11], and even complex phenomena in areas like neural networks [12] and spin glasses [13].

The random Ising model in its general form is described by the Hamiltonian:

$$\mathcal{H}(\sigma) = - \sum_{\langle i,j \rangle} J_{i,j} \sigma_i \sigma_j - \sum_i h_i \sigma_i, \quad (2.23)$$

where both  $J_{i,j}$  and  $h_i$  are spatially dependent parameters. The pure Ising model is recovered when  $J_{i,j} = J$  and  $h_i = h$ , with  $J$  and  $h$  constants. In the random Ising model, randomness is introduced by allowing these parameters to vary as  $J_{i,j} = J + \delta J_{i,j}$  and  $h_i = h + \delta h_i$ , where  $\delta J_{i,j}$  and  $\delta h_i$  represent spatially random fluctuations. These fluctuations are quenched, meaning they are fixed upon initialization and do not evolve with time. This quenching captures the effect of static disorder in the system, distinguishing it from dynamic randomness, which would fluctuate over time.

The effect of randomness on the critical behaviour of the system is governed by the Harris criterion [14]. According to this criterion, weak randomness alters the critical behaviour near a second-order phase transition only if  $\nu d < 2$ , where  $\nu$  is the correlation length exponent and  $d$  is the spatial dimension. When  $\nu d > 2$ , upon coarse-graining, weak disorder decreases and becomes negligible on large length scales. For the three-dimensional Ising model, the condition  $\nu d < 2$  holds, and weak randomness can affect the critical behaviour. By contrast, for the two-dimensional Ising model,  $d\nu = 2$ , and the random counterparts must be treated with greater care.

In the context of random Ising models, we now present two widely studied models that incorporate randomness in distinct ways:

- The Random Field Ising Model (RFIM), where  $\delta J_{i,j} = 0$  and randomness is introduced primarily through spatial variations in the local field  $h_i$ .

- The Random Bond Ising Model (RBIM), where  $\delta h_i = 0$  and randomness arises from fluctuations in the interaction strengths  $J_{i,j}$ .

Lastly, we will present a novel model to embed randomness in the Ising model, which reveals interesting properties in equilibrium and out-of-equilibrium conditions. The model implements randomness by fixing the orientation of a given fraction of spins. This thesis focuses on the characterisation of the static and dynamic properties of the system while giving ideas for potential applications of the developed model.

### 2.3.1 RBIM and the SG phase

For  $\delta J_{i,j} \ll J$ , the influence of randomness is limited, resulting in small deviations from the pure Ising model. In particular, the critical temperature of the magnetic phase transition can be modified by varying the strength of the bond perturbation [14] and the first-order phase transition induced by variation of the external field is transformed into a second-order transition [15]. However, for stronger perturbations where  $\delta J_{i,j} \gtrsim J$ , the system's behaviour changes radically.

In the absence of an external field, the system is commonly referred to as the Edwards-Anderson (EA) model, first introduced in 1975 by S. Edwards and P. W. Anderson [16], [17]. The Hamiltonian of the EA model is typically expressed as:

$$\mathcal{H}(\sigma) = - \sum_{\langle i,j \rangle} J_{i,j} \sigma_i \sigma_j, \quad (2.24)$$

where  $J_{i,j}$  is a Gaussian random variable with mean  $J_0$  and variance  $J^2$ . Because the bond distribution is continuous, antiferromagnetic bonds ( $J_{i,j} < 0$ ) can occur, introducing *frustration* into the system.

Frustration refers to a situation in which not all pairwise interactions within a system can be simultaneously satisfied, leading to conflicting constraints. In the context of the EA model, frustration arises due to the random nature of the interaction strengths  $J_{i,j}$ , which can include both ferromagnetic ( $J_{i,j} > 0$ ) and antiferromagnetic ( $J_{i,j} < 0$ ) bonds. For instance, in a triangular loop with one bond being antiferromagnetic and the others ferromagnetic, it is impossible to arrange the spins such that all interactions are energetically minimized.

The presence of frustration significantly impacts the system's behaviour, as it prevents the spins from settling into a simple ordered state. Instead, the system exhibits a rugged energy landscape characterized by numerous local minima, where the system could be trapped as the temperature decreases. This leads to a highly non-trivial behaviour, including glassy dynamics and a lack of long-range magnetic order, which are hallmarks of spin glass systems.

Two key order parameters are considered in this context. The first is the magnetisation, as already defined in Eq. (2.15) and the second is the Edwards-Anderson (EA) order parameter:

$$q_{\text{EA}} = \frac{1}{N} \sum_i \langle \sigma_i \rangle^2, \quad (2.25)$$

where  $\langle \dots \rangle$  denotes the thermal average. At high temperatures, the system behaves like a normal magnetic material in the paramagnetic phase, characterized by  $m = 0$  and  $q_{\text{EA}} = 0$ . As the temperature decreases, ordering emerges, but its nature is markedly different from that of the ferromagnetic phase. The system freezes into a non-ordered configuration, dependent on the specific realization of  $\{J_{i,j}\}$ , with  $m = 0$  but  $q_{\text{EA}} \neq 0$ . This phase, known as the *spin glass* (SG) phase, is of great interest.

In the SG phase, the system dynamics becomes extremely slow, exhibiting long relaxation times for thermodynamic variables. In this regime, the system “remembers” past magnetic states. For instance, after being cooled in the presence of an external field, the system retains a partial magnetisation even after the field is removed. Furthermore, this residual magnetisation and the system’s configuration depend on the intensity of the external field, a phenomenon termed *memory*. These characteristics are observed in real magnetic materials that exhibit the SG phase, such as metallic alloys like CuMn, AuFe, and AgMn [18]–[20].

The behaviour of the EA model varies with the system’s dimensionality. In one dimension, the system does not exhibit an SG or ordered phase. In two dimensions, the SG phase appears only in the limit  $T \rightarrow 0$ , as confirmed numerically [21]. In three dimensions, the EA model is believed to undergo a finite-temperature spin glass transition, supported by extensive numerical simulations [22].

**The SK model** A mean-field version of the EA model, known as the Sherrington-Kirkpatrick (SK) model, was proposed by D. Sherrington and S. Kirkpatrick in 1975 [23], [24]. Its Hamiltonian is given by:

$$\mathcal{H}(\sigma) = - \sum_{i < j} J_{i,j} \sigma_i \sigma_j, \quad (2.26)$$

where the summation extends over all lattice sites with  $i < j$ , rather than being restricted to nearest neighbours. Sherrington and Kirkpatrick assumed that the SK model accurately describes the EA model in the case of infinite-range interactions. This assumption can be contentious, as the mean-field theory for spin glasses assumes that the interaction distributions  $J_{i,j}$  are independent of the distance between spins. Nevertheless, similar to the mean-field theory for the homogeneous Ising model, the SK model serves as a valuable paradigm that captures the essential behaviour of real spin glasses.

Handling the randomness in interactions  $J_{i,j}$  is a central challenge for models with quenched randomness. Indeed, the system free energy should take into account the average over the different realisation of the set  $\{J_{i,j}\}$ :

$$f_{\text{SK}} = \bar{f} = - \frac{1}{N\beta} \overline{\log(Z)} \quad (2.27)$$

where  $f$  and  $Z$  refer to a single realisation of  $\{J_{i,j}\}$  and  $\overline{\dots}$  indicates the average over different randomness realisation, i.e. systems prepared with a different set of bounds  $\{J_{i,j}\}$ . This presents an intrinsic difficulty because the single partition function  $Z$  is not translationally invariant and contains infinitely many parameters ( $N \rightarrow \infty$ ). To derive

the free energy, the replica trick was developed which derives  $\overline{\log(Z)}$  indirectly. To do so, one computes the disorder-averaged partition function  $\overline{Z^n}$  for integer  $n$  representing the number of considered replicas and then extends this to the limit  $n \rightarrow 0$ . Indeed, from a mathematical point of view, one can write

$$\overline{\log(Z)} = \lim_{n \rightarrow 0} \frac{1}{n} (\overline{Z^n} - 1) \quad (2.28)$$

Even though computing the limit  $n \rightarrow 0$  has no physical meaning, the replica trick greatly simplifies the evaluation of the partition function and was proven to give the correct results.

After some mathematical manipulation (for a derivation, see [13]) and considering the replica trick, one arrives at the following expression

$$-\beta f_{\text{SK}} = \lim_{n \rightarrow 0} \left[ \frac{(\beta J)^2}{4} \left( 1 - \frac{1}{n} \sum_{\alpha, \beta} q_{\alpha\beta}^2 \right) + \frac{\beta J_0}{2} \frac{1}{n} \sum_{\alpha} m_{\alpha}^2 + \frac{1}{n} \log \text{Tr} \exp(L) \right] \quad (2.29)$$

where  $q_{\alpha\beta}$  and  $m_{\alpha}$  are given by

$$q_{\alpha\beta} = \langle \sigma_i^{\alpha} \sigma_i^{\beta} \rangle \quad \text{and} \quad m_{\alpha} = \langle \sigma_i^{\alpha} \rangle \quad (2.30)$$

and represents the overlap between different replicas  $\alpha$  and  $\beta$  (with the same set of  $\{J_{i,j}\}$ ) and the average magnetisation of replica  $\alpha$ , respectively.  $L$  is given by

$$L[q_{\alpha\beta}] = (\beta J)^2 \sum_{\alpha < \beta} q_{\alpha\beta} \sigma^{\alpha} \sigma^{\beta} + \beta \sum_{\alpha} (J_0 m_{\alpha} + H) \sigma^{\alpha} \quad (2.31)$$

Sherrington and Kirkpatrick considered the replica symmetric solution  $q_{\alpha,\beta} = q$  and  $m_{\alpha} = m$ , independent from the considered replicas  $\alpha$  and  $\beta$ . With this, they computed the free energy and described the phase space in terms of  $J_0$  and  $J^2$  for the infinite range SK model. The problem with this solution was the prediction of a negative value of the entropy for  $T \rightarrow 0$ , which is clearly unfeasible for a system with a countable number of states.

The correct solution of the SK model was proposed by Parisi in 1980 [25], later confirmed rigorously by Francesco Guerra [26], [27] and Michel Talagrand [28]. The groundbreaking idea lies in considering a distribution for  $q_{\alpha,\beta}$ , the overlap between replicas  $\alpha$  and  $\beta$ , rather than a single value. This distribution reflects a hierarchical organization of states, where configurations are nested within each other in a tree-like structure. Such a hierarchy corresponds to an ultrametric energy landscape, with valleys within valleys, representing metastable states of varying stability. Giorgio Parisi's groundbreaking work on RSB provides a deeper theoretical understanding of this phase, revealing a non-trivial structure to the spin glass phase that cannot be described by standard replica symmetry alone. This approach has since become essential in describing the thermodynamics of spin glasses and complex systems more broadly.

### 2.3.2 RFIM and the Imry-Ma argument

The element of randomness arises from a local field  $h_i$  that independently affects each site. This model is commonly referred to as the Random Field Ising Model. For comprehensive reviews, we refer the reader to [29], [30]. The RFIM serves as a theoretical framework for describing a variety of physical systems. Notable examples include diluted antiferromagnets in a homogeneous external field [31], [32], binary liquids confined in porous media [33], and hydrogen absorption in metals [34], among others.

The Hamiltonian can be rewritten as

$$\mathcal{H}(\sigma) = -J \sum_{i,j} \sigma_i \sigma_j - \sum_i h_i \sigma_i \quad (2.32)$$

where, in the absence of an external field,  $h_i$  has zero mean and  $\overline{h_i h_j} = h^2 \delta_{i,j}$ . Here  $\delta_{i,j}$  is the Dirac delta function. The case  $h_i \gg J$  can be treated exactly, and it has been shown that the system does not exhibit long-range order in the low-temperature regime [35]. Conversely, the case  $h_i \ll J$  is more complex and has intrigued scientists for decades. Under this condition, the equilibrium properties of the system can be analysed and understood using the *Imry-Ma argument* [36], which was pivotal in popularizing the RFIM. The argument states that no long-range order can exist for dimensions  $d < 2$ . The dimension  $d = 3$  is known as the *lower critical dimension*, representing the lowest dimension at which the system may display long-range order.

The Imry-Ma argument considers the energetic balance associated with the formation of a droplet. Suppose a region of the system in the ferromagnetic phase flips, forming a droplet. The energy cost for the surface separating regions with oppositely oriented spins is proportional to the droplet's surface area:  $E_{\text{ex}} \sim JR^{d-1}$ . Conversely, the droplet can gain energy by aligning a region of the lattice with the local random field's average direction. For a magnetized system, the interaction energy with the local random field has a variance  $E_{\text{RF}}^2 \sim h^2 R^d$ . By selecting regions where  $E_{\text{RF}} > 0$  and reversing their orientation, the energy gain becomes  $-2E_{\text{RF}}$ . Thus, the energetic balance for a droplet of radius  $R$  in a favourable region reads:

$$\Delta E = E_{\text{ex}} - 2E_{\text{RF}} \approx JR^{d-1} - 2hR^{d/2}. \quad (2.33)$$

For  $d \geq 2$ ,  $\Delta E > 0$ , indicating that breaking the ordered structure yields no energetic gain. For  $d < 2$ , however,  $\Delta E < 0$ , meaning that no long-range order survives. Binder [37] demonstrated that even for  $d = 2$ , the system spontaneously forms domains. While the energy of droplet formation becomes negative in the thermodynamic limit, this can only be observed for systems with  $L > L_0 \propto \exp(C(J/h)^2)$ , where  $C$  is a suitable constant [37].

**Absence of SG phase in the RFIM** Interestingly, the RFIM does not exhibit a spin-glass phase for any dimension  $d$ . Chatterjee [38] proved the absence of replica symmetry breaking in the RFIM. This result was later corroborated using a different approach by Krzkalá *et al.* [39], [40]. For  $d \leq 2$ , their findings align with Aizenman and

Wehr's earlier result [15], which states that only one ground state exists for an RFIM in  $d \geq 2$ . Krzkalá's argument revolves around the spin-glass susceptibility,

$$\chi_{\text{SG}} = \frac{1}{N} \sum_{i,j} (\langle \sigma_i \sigma_j \rangle - \langle \sigma_i \rangle \langle \sigma_j \rangle)^2, \quad (2.34)$$

which characterizes the transition to the spin-glass phase. It can be demonstrated that this susceptibility is bounded above by the ferromagnetic susceptibility,

$$\chi_{\text{F}} = \frac{1}{N} \sum_{i,j} (\langle \sigma_i \sigma_j \rangle - \langle \sigma_i \rangle \langle \sigma_j \rangle), \quad (2.35)$$

for any lattice structure and any  $h$ , provided no frustration arises. Since  $\chi_{\text{F}}$  does not diverge in either the paramagnetic or ferromagnetic phases, no spin-glass transition occurs.

**Universality and self-averaging property** The universality class of the RFIM has remained a topic of debate for decades. Using Perturbative Renormalization Group (PRG) theory, it can be shown that the critical exponents obey the relation [41]–[43]:

$$\lambda_{\text{RF}}(d) = \lambda_0(d - 2). \quad (2.36)$$

This suggests that the  $d$ -dimensional RFIM shares the same universality class as the  $(d - 2)$ -dimensional ferromagnetic Ising model. Consequently, the three-dimensional RFIM should not exhibit long-range order in the low-temperature limit. However, extensive Monte Carlo simulations [44], [45] have shown otherwise. Similarly, the four-dimensional RFIM yielded different critical exponents than those predicted by PRG [46], [47]. Consistency with PRG predictions emerges only in five dimensions [48], though no theoretical proof exists yet.

Another intriguing property of the RFIM is the lack of *self-averaging*. Consider a physical quantity  $P$  and its thermal average for a specific realization of randomness  $\{J_{i,j}\}$ , denoted as  $\langle P_{\mathbf{J}} \rangle$ . The ensemble average,  $\overline{\langle P_{\mathbf{J}} \rangle}$ , is used to infer the system's general behaviour. The variance  $V_{\text{P}} = (\langle P_{\mathbf{J}} \rangle - \overline{\langle P_{\mathbf{J}} \rangle})^2$  and its ratio to the squared ensemble average,  $V_{\text{P}} / \overline{\langle P_{\mathbf{J}} \rangle}^2$ , reveal the extent of sample-to-sample fluctuations. When  $V_{\text{P}} / \overline{\langle P_{\mathbf{J}} \rangle}^2 \rightarrow 0$  as  $L \rightarrow \infty$ , the quantity  $P$  shows self-averaging property.

Away from critical conditions, where  $L \gg \xi$ , systems generally exhibit the self-averaging property for extensive quantities. This behaviour can be explained using the Brout argument [49], which also applies to random systems. However, the behaviour of intensive quantities, particularly near critical conditions, differs significantly.

Physical quantities can be categorized into three classes based on the scaling behaviour of the ratio  $V_{\text{P}} / \overline{\langle P_{\mathbf{J}} \rangle}^2$  with system size  $L$  [50]:

1. Strongly self-averaging: if the ratio scales as  $V_{\text{P}} / \overline{\langle P_{\mathbf{J}} \rangle}^2 \sim L^{-d}$ , the physical quantity is said to be strongly self-averaging. This occurs for the energy and magnetisation of homogeneous systems in non-critical conditions.

2. Weakly self-averaging: if the ratio scales as  $V_P/\overline{\langle P_J \rangle}^2 \sim L^{-x_1}$ , with  $0 < x_1 < d$ , the quantity is weakly self-averaging. Examples include the magnetic susceptibility and specific heat of homogeneous systems in non-critical conditions, as well as the energy in critical conditions.
3. Non-self-averaging: if the ratio does not converge to zero as  $L \rightarrow \infty$ , the quantity is non-self-averaging. For instance, in the three-dimensional RFIM, the susceptibility is non-self-averaging [45].

The lack of self-averaging can pose significant challenges when analysing the behaviour of physical quantities. Discussions of universality classes and critical exponents are meaningful only in the thermodynamic limit. Achieving this limit requires proper finite-size scaling analysis of physical variables, often performed using Monte Carlo simulations, especially for models lacking a comprehensive theoretical approach. The absence of self-averaging properties implies that numerous realizations of quenched randomness must be considered, particularly as the system size increases. This necessity can make reliable Monte Carlo measurements computationally expensive, potentially becoming a bottleneck in the analysis of such systems.

### 2.3.3 The model with defects

We now introduce an alternative approach for incorporating quenched randomness into the system, designed to simulate the presence of magnetic impurities and defects that disrupt the system's homogeneity [51]. Below, we summarize the key features of this model, which has been developed in previous works [51]–[54].

The model assumes a fraction  $f$  of spins with frozen dynamics, meaning these spins are unable to change their orientation. To preserve the overall neutrality of the lattice, the frozen spins are equally distributed between positive ( $q = +1$ ) and negative ( $q = -1$ ) orientations. A graphical representation of the model is provided in the top panel of Fig. 2.1, where red dots indicate positive defects ( $q = +1$ ) and black dots indicate negative defects ( $q = -1$ ).

**The model with defects as a RFIM** The presence of defects can be interpreted as the effect of a particular type of random-field distribution, given by

$$h_{\text{RF},i} = \begin{cases} +h_{\text{RF}} & \text{if } i \in D^+, \\ -h_{\text{RF}} & \text{if } i \in D^-, \\ 0 & \text{otherwise.} \end{cases} \quad (2.37)$$

where  $D^+$  (resp.  $D^-$ ) denote the set of defects with fixed positive (negative) orientation. In the regime  $h_{\text{RF}} \gg J$ , any reversal of the specified spins is prevented at any finite temperature, causing these spins to effectively act as defects. The appropriate magnitude of  $h_{\text{RF}}$  depends on the selected temperature.

The RFIM does not exhibit a spin-glass phase in thermal equilibrium and at the thermodynamic limit [39], [40]. Additionally, in two dimensions, no long-range ordered

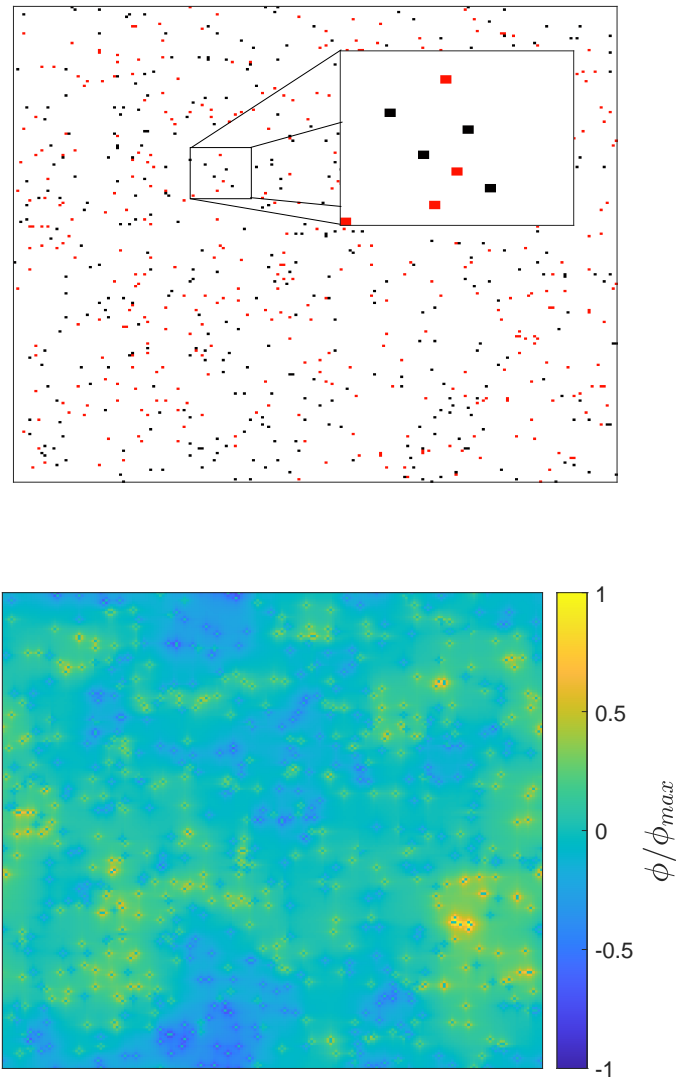


Figure 2.1: Top panel: representation of the distribution of defects for a system with  $L = 200$  and a fraction of defects  $f = 0.02$ . Red dots represent positive defects  $q = +1$  and black dots represent negative defects  $q = -1$ . The sum of the value of the defects is neutral to maintain the symmetry negative-positive magnetisation. The inset shows a zoom-in of a portion of the lattice. Bottom panel: potential associated with the defects' distribution as defined in Eq. (2.38). The colour bar shows the intensity of the defect potential, rescaled by its maximum over the lattice  $\phi_{max}$ .

phase persists in the RFIM due to the Imry-Ma argument [36]. Consequently, neither ferromagnetic nor spin-glass phases are expected in the thermodynamic limit. However, in finite systems, pseudo-phases can emerge [55], where finite-size effects and domain clustering result in pseudo-ferromagnetic or pseudo-glassy states, contingent on temperature and defect density. In three or more dimensions, ferromagnetic order can be restored, and phase transitions may occur in the model with defects. The detailed analysis of this system's static properties and its connection to the RFIM will be discussed in Chapter 3.

**Defect potential definition** The presence of fixed defects at specific positions directly affects their nearest neighbours. Over time, the influence of a single defect propagates throughout the system, though it diminishes with increasing distance from the defect. Following the approach outlined in [53], a defect-potential, analogous to an electric potential, is introduced. The key assumption is that the effect of a defect at position  $i$  on a free spin at position  $j$  is inversely proportional to their lattice distance  $d(i, j)$ . Considering multiple defects, the total defect-potential acting on a free spin at position  $j$  is given by:

$$\phi(j) = \sum_{i \in D^+} \frac{1}{d(i, j)} - \sum_{i \in D^-} \frac{1}{d(i, j)}, \quad (2.38)$$

where  $d(i, j)$  represents the shortest path length between the defect at position  $i$  and the free spin at position  $j$ , taking into account the lattice geometry and applying periodic boundary conditions. The total potential  $\phi(j)$  is computed by summing contributions from the two defect sets,  $D^+$  and  $D^-$ . Appendix A shows an investigation of the spatial distribution of the defect-potential. At the thermodynamic limit, it can be assumed to follow a Gaussian distribution with variance determined by the defect fraction.

Clusters of defects with the same charge create regions with high (absolute) potential, significantly influencing the behaviour of nearby spins. Conversely, regions containing mixed defects exhibit lower potential values due to partial cancellation between opposing signs. This effect is visually evident in the bottom panel of Fig. 2.1, where regions of intense yellow and blue indicate areas of strong positive and negative potential, respectively, while green regions represent areas with weaker potential.

To quantitatively characterize the defect configuration, we define the total potential  $\phi_{\text{tot}}$  as the Euclidean norm of  $\phi$ :

$$\phi_{\text{tot}} = \left( \sum_{j \notin D^+ \cup D^-} \phi(j)^2 \right)^{1/2}. \quad (2.39)$$

Additionally, we introduce the potential index  $\phi_{\text{def}}$ , which normalizes  $\phi_{\text{tot}}$  by its maximum possible value  $\phi_{\text{max}}^{\text{tot}}$ :

$$\phi_{\text{def}} = \frac{\phi_{\text{tot}}}{\phi_{\text{max}}^{\text{tot}}}, \quad \phi_{\text{def}} \in [0, 1]. \quad (2.40)$$

Appendix A presents a brief analysis on the dependency of  $\phi_{\text{def}}$  from the system size  $L$  and the defect fraction  $f$ .

Due to the complexity of the interactions and the high dimensionality of the parameter space, numerical simulations become essential. Monte Carlo methods provide a powerful framework to explore the equilibrium properties and dynamic responses of the system under various conditions. In the next section, we will review the fundamental aspects of Monte Carlo simulations, emphasizing their application to the study of systems with quenched randomness.

## 2.4 Monte Carlo simulations for the Ising model

As discussed in previous sections, the primary goal of Statistical Mechanics is to understand the macroscopic behaviour of complex systems, which can be viewed as an ensemble of particles interacting with each other and their environment. This framework applies to the Ising model and its variants, which we have considered so far. The Hamiltonian serves as a fundamental tool, encapsulating all relevant information about the interactions between particles.

Key questions arise concerning the existence or absence of a phase transition, the system's thermodynamic properties (including the relationship between microscopic quantities and macroscopic behaviour), and the prediction of the probability distribution of microstates at equilibrium or in a steady state. Statistical Mechanics addresses these questions using probabilistic techniques to reveal the macroscopic behaviour of complex systems.

Consider a canonical ensemble of particles (or spins) in thermal contact with a heat bath at temperature  $T$ . The heat bath maintains the system's temperature by exchanging thermal energy. The system's Hamiltonian  $\mathcal{H}$  defines the energy  $E_\nu$  of each microstate  $\nu$ . The transition probability per unit time for the system to move from state  $\nu$  to state  $\mu$  is given by the transition rate  $R(\nu \rightarrow \mu)$ . For simplicity, we assume  $R$  is independent of time; this assumption will be relaxed in subsequent sections when we examine out-of-equilibrium processes.

The system's behaviour can be described by the master equation:

$$\frac{dw_\mu}{dt} = \sum_\nu [w_\nu R(\nu \rightarrow \mu) - w_\mu R(\mu \rightarrow \nu)], \quad (2.41)$$

where  $w_\mu$  represents the probability of the system being in state  $\mu$  at time  $t$ . The first term in the summation represents the flow coming in state  $\mu$ , whereas the second term represents the flow exiting from state  $\mu$ . This equation forms a set of coupled equations, one for each possible state of the system. Once the probabilities  $w_\mu$  are known, the expectation value of any macroscopic quantity  $Q$  can be computed as a weighted mean:

$$\langle Q \rangle = \sum_\mu w_\mu Q_\mu, \quad (2.42)$$

where  $Q_\mu$  is the value of the macroscopic quantity  $Q$  in state  $\mu$ .

Under equilibrium conditions, where the expectation values of macroscopic quantities do not change with time (though fluctuations are allowed), the probabilities  $w_\nu$  become constant and are given by the Boltzmann distribution:

$$w_\mu = P_\mu = \frac{e^{-\beta E_\mu}}{Z}, \quad (2.43)$$

where  $Z$  is the partition function, defined as  $Z = \sum_\mu e^{-\beta E_\mu}$ . Consequently, the expectation value of  $Q$  is:

$$\langle Q \rangle = \frac{\sum_\mu Q_\mu e^{-\beta E_\mu}}{Z}. \quad (2.44)$$

However, computing this expression is non-trivial. Analytical derivations, while desirable, are often infeasible for even simple models like the Ising model in higher dimensions (e.g., three dimensions). In such cases, an alternative approach is required to approximate  $\langle Q \rangle$ .

A potential approach involves considering a subset of states  $\{\mu_1, \dots, \mu_M\}$ , drawn with probabilities  $\{p_1, \dots, p_M\}$ . The estimator of  $\langle Q \rangle$  can then be written as:

$$Q_M = \frac{\sum_{i=1}^M Q_{\mu_i} p_{\mu_i}^{-1} e^{-\beta E_{\mu_i}}}{\sum_{i=1}^M p_{\mu_i}^{-1} e^{-\beta E_{\mu_i}}}. \quad (2.45)$$

In the simplest case, where all states have equal probability  $p_1 = \dots = p_M = 1/M$ ,  $Q_M$  becomes the weighted average of the physical quantity under investigation measured in microstates  $\mu$ . As  $M \rightarrow \infty$ ,  $Q_M \rightarrow \langle Q \rangle$ , making the estimator well-defined.

The primary challenge with this approach lies in the sheer number of states that must be sampled to obtain a reliable estimation. The phase space grows exponentially with the degrees of freedom, necessitating the inclusion of increasingly more states as the system size increases. A solution to this problem is provided by importance sampling technique. This technique selects only the most influential states in the summation of Eq. (2.45). By fine-tuning the probabilities  $p_\mu$ , states contributing significantly to Eq. (2.45) are sampled more frequently, while less influential states are sampled less often.

The core idea of importance sampling is to set  $p_\mu$  proportional to the Boltzmann distribution,  $p_\mu = Z^{-1} \exp(-\beta E_\mu)$ . With this choice, Eq. (2.45) simplifies to:

$$Q_M = \frac{1}{M} \sum_{i=1}^M Q_{\mu_i}. \quad (2.46)$$

To generate states proportional to the Boltzmann probability distribution, we employ a Markov chain of states with appropriate transition probabilities.

### 2.4.1 Markov chains

A *Markov chain* is a mathematical model that describes a sequence of states or events, where the transition from one state to another depends solely on the current state and

not on the sequence of preceding states. This “memoryless” property is a defining characteristic of Markov processes. In the context of Monte Carlo simulations, each microstate (e.g., a spin configuration) is connected to others through a transition probability  $P(\nu \rightarrow \mu)$ . The significance of the Markov process lies in its ability to control the equilibrium probability of observing a system in a specific microstate. By manipulating the transition rates between microstates, one can establish a specific equilibrium distribution, such as the Boltzmann distribution, to sample microstates at equilibrium.

A Markov process should satisfy two essential properties:

- *Ergodicity*: This property ensures that the system can access all possible states over time. If the state space is divided into disjoint subsets of microstates, the system may converge to different steady-state conditions depending on the subset it starts from. Ergodicity guarantees that the system explores the entire state space, enabling it to reach a unique steady-state distribution.
- *Detailed Balance*: This condition ensures that the stationary distribution of the Markov chain matches the desired equilibrium distribution, such as the Boltzmann distribution. Mathematically, the detailed balance condition is expressed as:

$$\frac{P(\mu \rightarrow \nu)}{P(\nu \rightarrow \mu)} = \frac{p_\nu}{p_\mu}, \quad (2.47)$$

where  $p_\nu$  represents the desired probability distribution at equilibrium. For the Boltzmann distribution:

$$\frac{P(\mu \rightarrow \nu)}{P(\nu \rightarrow \mu)} = \exp \{ -\beta(E_\nu - E_\mu) \}, \quad (2.48)$$

where  $E_\mu$  and  $E_\nu$  are the energies of states  $\mu$  and  $\nu$ , respectively.

The transition probability  $P(\nu \rightarrow \mu)$  is commonly factorized into two components:

$$P(\nu \rightarrow \mu) = g(\nu \rightarrow \mu)A(\nu \rightarrow \mu), \quad (2.49)$$

where  $g(\nu \rightarrow \mu)$  is the selection probability, representing the probability of generating the microstate  $\mu$  starting from  $\nu$ .  $A(\nu \rightarrow \mu)$  is the acceptance probability, representing the probability of accepting  $\mu$  as the next state in the Markov chain. This factorization allows flexibility in designing algorithms for Monte Carlo simulations. Different algorithms use distinct approaches to balance these probabilities while satisfying the detailed balance condition.

The Metropolis algorithm assumes constant selection probabilities  $g(\nu \rightarrow \mu)$ , provided that the proposed states differ by only one spin. The acceptance probability  $A(\nu \rightarrow \mu)$  is then adjusted to satisfy the detailed balance condition. This approach is computationally efficient but may reject some proposed states, resulting in time loss. The  $N$ -Fold way algorithm uses non-uniform selection probabilities  $g(\nu \rightarrow \mu)$  while setting  $A(\nu \rightarrow \mu) = 1$ . This approach eliminates rejections, ensuring that every proposed state

is accepted. However, it requires more computational resources to generate the next state in the chain. The choice of algorithm depends on the specific requirements of the simulation, with trade-offs between computational efficiency and rejection minimization. We now review these two algorithms, highlighting the main differences.

## 2.5 Monte Carlo algorithms and techniques

We now present the main algorithms used to conduct Monte Carlo simulations. For extensive reviews we refer to references [56], [57]. We give a general understanding of the algorithms and specify the modifications to account for the model with defects.

### 2.5.1 Metropolis algorithm

The Metropolis algorithm [58] is one of the most widely used methods for implementing Monte Carlo simulations. It operates by defining a Markov chain where each new state is selected with a uniform probability  $g(\nu \rightarrow \mu) = 1/N$  where  $N$  is the total number of spins in the lattice (equivalent to the total number of available states that differ from the flipping of a single spin). The newly proposed random state is then accepted with a probability  $A(\nu \rightarrow \mu)$ , ensuring the detailed balance condition is satisfied. Specifically, the detailed balance condition reads

$$\frac{A(\mu \rightarrow \nu)}{A(\nu \rightarrow \mu)} = e^{-\beta(E_\nu - E_\mu)} \quad (2.50)$$

As this equation involves only the ratio of reciprocal moves, there is some freedom in choosing the acceptance probability. The standard approach is to maximize the acceptance of proposed states to accelerate convergence to equilibrium. The acceptance probability is typically chosen as:

$$A(\mu \rightarrow \nu) = \begin{cases} e^{-\beta(E_\nu - E_\mu)} & \text{if } E_\nu - E_\mu > 0 \\ 1 & \text{otherwise} \end{cases} \quad (2.51)$$

This leads to the following steps in the Metropolis algorithm:

1. Select a spin with uniform probability
2. Derive the energy variation  $\Delta E$  associated with flipping the spin.
3. Accept the new state with probability given by the Metropolis acceptance criteria in Eq. (2.51).
4. If the move is accepted, update the system's state and compute any macroscopic quantities of interest, such as magnetisation or energy.

The time progression of the algorithm is measured by the number of attempted spin flips, including both accepted and rejected moves. Typically, one Monte Carlo time unit,

referred to as Monte Carlo Steps per Spin (MCSS), corresponds to  $N$  spin-flip attempts, where  $N$  is the number of spins in the lattice. On average, this results in one spin-flip per site, making the time unit independent of the system size.

In systems with quenched randomness, the algorithm requires minimal modification. In these cases, the randomness affects only the energy differences calculated in step 2. For systems with defects, the algorithm should exclude selecting a defect in step 1. To maintain consistency with the defect-free model, an MCSS in this case corresponds to  $N(1 - f)$  attempted spin flips, where  $f$  is the defect fraction.

The Metropolis algorithm is highly efficient in standard conditions and remains one of the easiest Monte Carlo methods to implement. However, especially for systems with significant energy barriers or slow dynamics which can hinder convergence to equilibrium, it shows important limitations. Over time, alternative techniques, such as cluster algorithms and rejection-free methods, have been developed to address these challenges and enhance the efficiency of Monte Carlo simulations.

One such alternative is the Multi-Spin Coding (MSC) algorithm, which leverages the structure of modern computer architectures to optimize computational efficiency. By encoding multiple configurations into individual machine words, MSC enables simultaneous simulation of multiple systems, dramatically increasing performance. The next section introduces the MSC technique for the Ising model.

### 2.5.2 Multi-spin coding algorithm

The MSC technique was designed to fully exploit the capabilities of modern computer architectures, particularly the efficient use of machine words. The key observation behind MSC is that a single spin can occupy the smallest unit of information available in modern computers: a single bit. In the Ising model, each spin is a two-valued variable, which can be mapped into a bit as  $b = 0$  (spin down) or  $b = 1$  (spin up). Given that modern CPUs typically allocate 64 bits per machine word, storing each spin as an independent variable would waste 63 out of every 64 bits.

The essence of MSC is to pack 64 independent lattice configurations of  $N$  spins into  $N$  machine words, where each bit in a word represents a spin in one of the 64 configurations. This allows bit-wise operations to be performed simultaneously across all 64 configurations. Through operations such as AND, OR, and XOR, it is possible to apply the Metropolis acceptance criterion concurrently to all 64 replicas. As a result, MSC enables the simulation of 64 independent systems at the same computational cost as simulating a single system, though it comes at the expense of increased algorithmic complexity.

An MSC version of most Monte Carlo algorithms can be implemented, but the enhanced complexity arises from the need to manipulate individual bits using logical operations rather than conventional arithmetic. Standard functions provided by programming languages are often insufficient for MSC, requiring intricate “translation” of code. In this work, the MSC technique is applied to the standard Metropolis algorithm for the two-dimensional Ising model without an external field. For a detailed explanation of MSC, we refer to [56], while only the main concepts are summarized here for completeness.

Suppose we select the  $i$ -th spin in the lattice during step 1 of the Metropolis procedure. The probability of flipping this spin depends on its neighbouring spins. Specifically:

- If two or more neighbours point in the opposite direction, the spin reversal is certain.
- If exactly one neighbour points in the opposite direction, the spin flips with probability  $\exp(-4\beta J)$ .
- If no neighbours point in the opposite direction, the spin flips with probability  $\exp(-8\beta J)$ .

This logic can be compactly expressed using a bitwise implementation as:

$$\sigma'_i = \sigma_i \oplus [R_{\geq 2} \vee (R_1 \wedge r_1) \vee (R_0 \wedge r_0)], \quad (2.52)$$

where  $\oplus$  represents the exclusive logical “or” (XOR),  $\wedge$  the logical “and,” and  $\vee$  the logical “or.” Here:

- $R_{\geq 2}$ ,  $R_1$ , and  $R_0$  are logical expressions that evaluate to 1 if there are  $\geq 2$ , exactly 1, or 0 neighbouring spins pointing in the opposite direction, respectively.
- $r_0$  and  $r_1$  are random variables that are 1 with probabilities  $\exp(-8\beta J)$  and  $\exp(-4\beta J)$ , respectively.

The expression in Eq. (2.52) can be implemented in a programming language of choice using bitwise operations. These operations enable simultaneous computation across the 64 replicas packed within a machine word, significantly increasing computational efficiency.

For further optimization, a more machine-friendly version of Eq. (2.52) can be developed, simplifying the logic and reducing computational overhead. Such refinements can further accelerate simulations, demonstrating the flexibility and power of the MSC approach in leveraging modern computer architectures.

### 2.5.3 N-Fold way algorithm

At low temperatures, the Metropolis algorithm becomes inefficient due to the sharply reduced acceptance probability for spin flips that increase the system’s energy. This inefficiency arises because the acceptance criterion, based on the Boltzmann factor  $\exp(-\Delta E/k_B T)$ , overwhelmingly rejects moves with large positive  $\Delta E$ , especially when  $\Delta E \gg k_B T$ . Consequently, the algorithm spends substantial time proposing and rejecting moves, leading to sluggish dynamics and difficulty exploring the configuration space, particularly in systems with large energy barriers.

The  $N$ -Fold way algorithm [59] addresses this inefficiency by directly selecting and executing the next accepted spin flip, skipping over all intermediate rejections. Instead of testing individual spin flips sequentially, the algorithm categorizes all spins into classes

based on their energy change  $\Delta E$  and associated transition rates. It then probabilistically selects a spin flip based on these rates, advancing the simulation directly to the next accepted event. This approach significantly reduces wasted computational effort, making the  $N$ -Fold way algorithm up to an order of magnitude more efficient than the standard Metropolis algorithm at low temperatures [59].

The implementation of the  $N$ -Fold way algorithm involves the following steps:

1. Initialization: Compute  $\Delta E$  values for all spins and group them into classes corresponding to distinct energy changes (e.g.,  $\Delta E = -8J, -4J, 0, +4J, +8J$  in a 2D Ising model). For example, all spins with  $\Delta E = -4J$  are grouped together, as are those with  $\Delta E = 0$ , and so on. Each class is assigned a transition rate  $w(\Delta E)$ , which can be taken equal to the metropolis rule or the Glauber transition rates.
2. Class selection: Select a class with probability proportional to its total rate  $N_c w(\Delta E_c)$ , where  $N_c$  is the number of spins in the class. This ensures that classes with higher transition rate or that are highly populated are more likely to be chosen.
3. Spin selection and flip: Randomly select a spin from the chosen class and flip it. The spin flip alters the local energy configuration, potentially changing the  $\Delta E$  values for the flipped spin and its neighbours.
4. Update: Adjust the class populations to reflect the new  $\Delta E$  values. Spins are moved between classes as their local environments change.

Efficient data structures, such as linked lists or arrays, are used to manage spins within each class and allow rapid updates after each spin flip. By focusing on relevant spins and avoiding lattice-wide scans, the  $N$ -Fold way algorithm minimizes computational overhead and achieves significant speed-ups compared to the Metropolis algorithm.

#### 2.5.4 Parallel tempering technique

Exploring the configuration space of systems with rugged energy landscapes, such as spin systems or protein folding models, is a significant challenge in Monte Carlo simulations. Traditional approaches like simple Metropolis algorithm can struggle to escape local energy minima, especially at low temperatures, where thermal fluctuations are insufficient to overcome energy barriers. To address this, temperature annealing was introduced as a basic strategy to improve sampling efficiency [60]. This technique involves starting the simulation at a high temperature, where the system can easily overcome barriers and explore a wide range of configurations, and then gradually lowering the temperature according to a predefined schedule.

While temperature annealing can help identify low-energy states, it has limitations. The success of the method depends critically on the annealing schedule. If the temperature is reduced too quickly, the system may become trapped in metastable states, failing to reach equilibrium. Conversely, a very slow annealing process can be computationally prohibitive, especially for large systems or those with complex energy landscapes. Additionally, annealing often struggles in systems with multiple deep energy minima

separated by high barriers, as the system's ability to equilibrate at intermediate temperatures is limited.

These shortcomings lead to the conceptual foundation of parallel tempering [61]–[63], which improves upon temperature annealing by introducing simultaneous simulations of the system at multiple temperatures. By enabling exchanges between configurations at different temperatures, parallel tempering allows replicas at higher temperatures to assist those at lower temperatures in escaping local minima, effectively overcoming the primary challenges of temperature annealing.

In the Ising model, parallel tempering is used to address the challenges posed by critical slowing down near the critical temperature and the ruggedness of the energy landscape in disordered systems, such as those with quenched randomness or defects. By simulating replicas across a range of temperatures, the algorithm ensures efficient sampling of spin configurations and allows the system to equilibrate even in the presence of deep energy wells. In the case of the two-dimensional Ising model with defects, parallel tempering is particularly valuable for characterizing low-temperature equilibrium states and exploring the influence of defects on critical behaviour.

To satisfy the detailed balance condition in parallel tempering, the acceptance probability for swapping configurations between two replicas  $i$  and  $j$  at temperatures  $T_i$  and  $T_j$  is given by

$$P_{\text{swap}} = \min(1, \exp[(\beta_j - \beta_i)(E_i - E_j)]), \quad (2.53)$$

where  $\beta_i = 1/T_i$  is the inverse temperature, and  $E_i$  and  $E_j$  are the energies of the configurations in replicas  $i$  and  $j$ , respectively. This swapping rule ensures that the overall simulation satisfies the Boltzmann distribution at each temperature, preserving the equilibrium condition.

The choice of temperature spacing is critical for the efficiency of the algorithm. Temperatures must be spaced closely enough to ensure sufficient overlap in the energy distributions of neighbouring replicas, thereby maintaining high acceptance probabilities for swaps. However, if the temperature spacing is too small, the computational cost increases due to the need to simulate a larger number of replicas. In practice, the temperature spacing is often optimized empirically or through methods such as analysing the acceptance rates and energy histograms of replicas.

To implement parallel tempering effectively, one must also carefully balance the frequency of swap attempts and the duration of equilibration steps at each temperature. Frequent swap attempts help facilitate exchanges across the temperature ladder, while sufficient sampling at each temperature ensures an accurate representation of equilibrium properties. Together, these considerations enable efficient exploration of the configuration space.

The ability to seamlessly traverse temperature scales enables to study both high- and low-temperature regimes in a single simulation, making parallel tempering a powerful tool for investigating critical phenomena, glassy dynamics, and ground state properties. By integrating parallel tempering with techniques like MSC, simulations can further benefit from enhanced efficiency and scalability, enabling the study of large systems with high statistical reliability.

### 2.5.5 Glauber dynamics for out-of-equilibrium simulations

Glauber dynamics [64], [65] is a stochastic process introduced to study the time evolution of spin systems, such as the Ising model, in both equilibrium and out-of-equilibrium regimes. Unlike equilibrium-focused methods like the Metropolis algorithm, which uses the acceptance rule given by Eq. (2.51), Glauber dynamics explicitly incorporates time dependence into the transition probabilities, enabling the modelling of transient phenomena. This approach is widely used to investigate relaxation processes, dynamic phase transitions, and the response of magnetic systems to time-dependent external fields.

The central concept underlying Glauber dynamics is the time-dependent master equation:

$$\begin{aligned} \frac{d}{dt}p(\sigma_1, \dots, \sigma_N, t) = & - \sum_{j=1}^N \omega_j(\sigma_j)p(\sigma_1, \dots, \sigma_j, \dots, \sigma_N, t) \\ & + \sum_{j=1}^N \omega_j(-\sigma_j)p(\sigma_1, \dots, -\sigma_j, \dots, \sigma_N, t), \end{aligned} \quad (2.54)$$

where  $p(\sigma_1, \dots, \sigma_N, t)$  denotes the probability of being in a specific configuration  $\{\sigma\} = \{\sigma_1, \dots, \sigma_N\}$  at time  $t$ , and  $\omega_j(\sigma_j, t)$  is the transition probability per unit time for flipping the  $j$ -th spin  $\sigma_j \rightarrow -\sigma_j$ . By imposing that, at steady state ( $dp/dt = 0$ ),  $p$  follows the Boltzmann distribution, we obtain:

$$\frac{\omega_j(\sigma_j)}{\omega_j(-\sigma_j)} = \frac{1 - \sigma_j \tanh(\beta E_j)}{1 + \sigma_j \tanh(\beta E_j)}, \quad (2.55)$$

where

$$E_j = h_j + \sum_{k=1}^N J_{j,k} \sigma_k. \quad (2.56)$$

Following Suzuki and Kubo [66], the transition rates for Glauber dynamics can be finally written as:

$$\omega_j(\sigma_j) = \frac{1}{2\alpha} (1 - \sigma_j \tanh(\beta E_j)), \quad (2.57)$$

where  $\alpha$  represents the time scale of the dynamic process. For simplicity, we often set  $\alpha = 1$ ; however,  $\alpha$  can be tuned to accelerate or slow down the dynamics. This tunable parameter becomes particularly important when different types of moves are present. For instance, in a model where defects move according to Kawasaki-type dynamics while normal spin flips occur, distinct  $\alpha$  values for the two processes allow exploration of various dynamical regimes. Such analysis has been performed for neutral impurities [67].

The time-dependent behaviour of the system is naturally recovered by incorporating the time dependency of  $E_j(t)$  or  $\beta(t)$  and adjusting the transition rates accordingly at each time step.

In simulations, Glauber dynamics provides key insights into how systems evolve toward equilibrium, how they respond to external perturbations, and how transient

phenomena manifest. For this reason, the Glauber transition rates will be used for all out-of-equilibrium simulations discussed in subsequent chapters.

## Chapter 3

# Thermodynamic Properties

The Ising model with defects provides a foundational framework for investigating the interplay between quenched disorder and the equilibrium properties of magnetic systems. As discussed in Chapter 2, this model incorporates defects represented by frozen spins, which remain fixed during the system's evolution. These static defects introduce frustration, creating a highly intricate energy landscape that gives rise to numerous metastable states. As a result, the model is classified as a disordered spin system.

In Section 2.3.3, we saw that the Ising model with defects can be viewed as a specific case of the RFIM. At low temperatures, the 2D version of this model is expected to exhibit a clustered stable state, characterized by spin droplets aligned in opposite directions, a hallmark feature of the two-dimensional RFIM. These domains emerge from the competition between thermal fluctuations and the constraints imposed by the defects, resulting in complex configurations that differ significantly from the ferromagnetic or paramagnetic phases typically observed in the homogeneous Ising model.

The two-dimensional Ising model with defects offers a powerful framework for understanding the equilibrium behaviour of complex disordered systems encountered in nature and technology. One notable application is in the study of magnetically disordered materials, such as diluted ferromagnets or amorphous magnetic alloys, where defects and impurities create local frustration, leading to behaviour akin to those predicted by the model [68]. Similarly, the model could be used to analyse and explain the behaviour of glassy systems, where the presence of quenched disorder mirrors the role of frozen spins in forming metastable, heterogeneous configurations [53].

This chapter examines the equilibrium properties of the 2D Ising model with defects, emphasizing the formation and stability of clustered configurations at low temperatures. Using numerical Monte Carlo simulations, it investigates how defect-induced disorder influences critical behaviour, phase transitions, and domain formation. The main original findings include the identification and characterization of the clustered phase, the analysis of the role of the system size in determining the phase behaviour, and the analysis of the phase transition between the clustered and the paramagnetic phases through a novel order parameter. These results offer qualitative and quantitative insights into disordered magnetic systems, serving as a foundation for studying their dynamic properties

in subsequent chapters and informing broader implications for analogous models.

### 3.1 Equilibrium configuration

As seen in section 2.3.3, the two-dimensional Ising model with defects shares significant theoretical parallels with the RFIM, a system known to exhibit peculiar equilibrium properties in low dimensions. In particular, the RFIM in two dimensions is characterized by the emergence of clustered configurations, where the interplay between quenched disorder and thermal fluctuations leads to stable domains of spins with varying orientations [15], [69]. These unusual features underscore the need for careful treatment of the 2D case in the model with defects. With the presented analysis, we aim to elucidate how these analogies manifest in equilibrium configurations and investigate the effects of defects on the system's low-temperature behaviour.

As a first step, we aim to characterize the system's equilibrium configurations and approximate ground state. To this end, we employ Monte Carlo simulations enhanced by MSC techniques for the model with defects and various defect fractions. Specifically, 64 replicas of a lattice with size  $L = 200$  are simulated simultaneously using the Metropolis algorithm. All 64 replicas are prepared with defects in the same position but with defect orientations which change from replica to replica. We induce defect neutrality for each one by fixing half of them as positive and the others as negative. To improve statistical reliability, the simulations are repeated three times, each with a different realization of defect positions.

To accelerate equilibration, we used the parallel tempering technique, detailed in Section 2.5.4. The temperature range spans from  $T_{\text{low}} = 1$  to  $T_{\text{high}} = 2.5$ , divided into 80 evenly spaced intervals. To ensure effective sampling, we verify that configurations at  $T = T_{\text{low}}$  have a non-zero probability of reaching  $T = T_{\text{high}}$  within the equilibration process. During the simulation, temperature swaps between adjacent replicas at different temperatures are proposed every 10 Monte Carlo Steps per Spin (MCSS).

The equilibration phase consists of 5000 MCSS, during which the system achieves thermal stability across the temperature range. This is followed by a data acquisition phase of an additional 5000 MCSS, where configurations are recorded every 10 MCSS for averaging, with no further temperature swaps. The reaching of equilibration was verified by monitoring all replica spin configurations to ensure no significant changes occurred between the beginning and the end of the data acquisition phase.

The equilibrium configurations for a specific realization of defects are shown in Fig. 3.1. The panels illustrate the system's state at  $T = 1.6$ ,  $T = 2.26$  and  $T = 2.5$  (top right, bottom left, and bottom right, respectively). The top-left panel represents the local defect-potential distribution, highlighting the effects of defect-induced disorder.

As expected, the system breaks into domains at low temperatures. Moreover, we observe a strong correlation between the local defect-potential of Eq. (2.38) and the equilibrium configurations, particularly near the critical temperature of the homogeneous system. Regions with positive (negative) local potential tend to align their spins in the

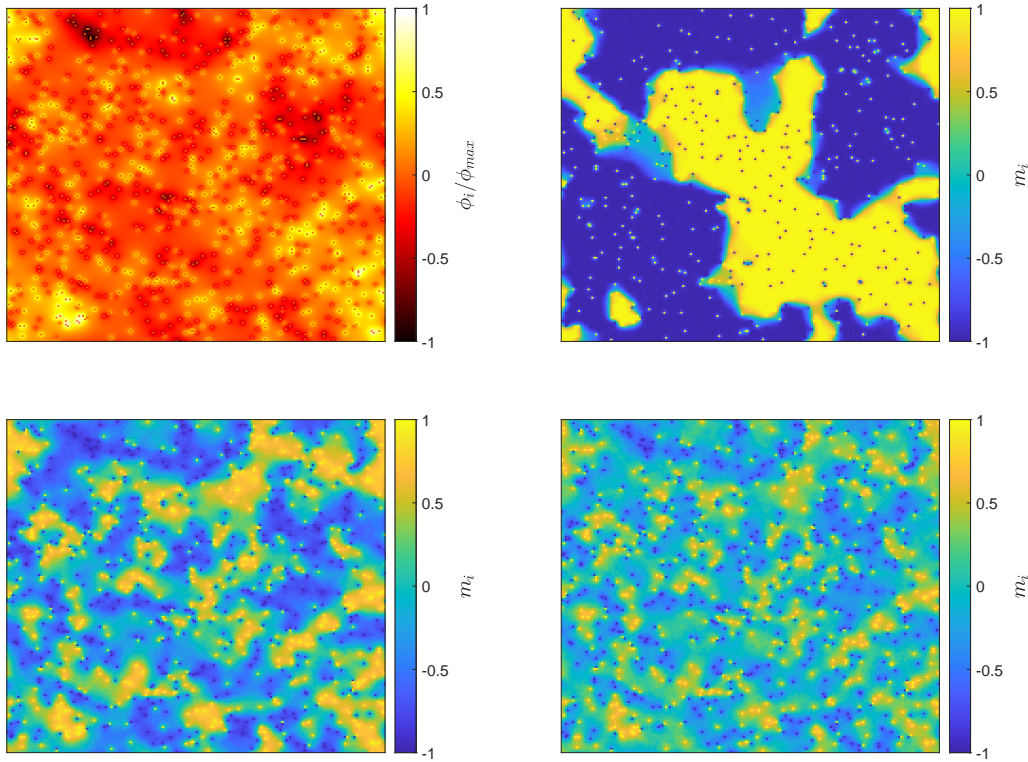


Figure 3.1: Equilibrium configurations of the two-dimensional Ising model with defects for a specific realization of disorder. The panels show spin configurations at  $T = 1.6$  (top right),  $T = 2.26$  (bottom left), and  $T = 2.5$  (bottom right), illustrating the clustering and domain formation induced by frozen defects. The top-left panel represents the local defect-potential distribution, highlighting the influence of defects on the energy landscape. These configurations are obtained after equilibration through parallel tempering, with defect positions fixed and spin orientations averaged over 5000 MCSS. Simulation parameters:  $L = 200$ ,  $f = 0.02$ .

positive (negative) direction, indicating that defects influence free spins through a local effective field which biases the average spin orientation.

We examine the connection between the local defect-potential,  $\phi_i$ , and the local magnetization,  $m_i = \langle \sigma_i \rangle$ . This analysis is performed by creating a scatterplot that includes all spins across the lattice for the 64 replicas and the three independent defect realizations. The function  $m(\phi)$  is derived by grouping the spins into 100 bins based on the value of  $\phi_i$ , with the potential range divided into 100 equally spaced intervals. For each bin, the median of  $m_i$  is calculated, producing the solid lines in Fig. 3.2, while the dashed lines represent the first and third quartiles within each bin.

The narrow spread between the quartiles and the median in all cases suggests that the defect-potential definition effectively captures the local behaviour of the system. At high temperatures, the shape of  $m(\phi)$  resembles the magnetization curve  $m(h)$  of a homogeneous system, further supporting the analogy between the defect-potential and a local effective field. At low temperatures,  $m(\phi)$  approaches a Heaviside function centred at zero, reflecting a strong alignment of spins with the local potential. This finding has practical implications for initializing the model with defects. To expedite the equilibration process, the system can be prepared by orienting each spin  $\sigma_i$  in the same direction as its corresponding defect-potential  $\phi_i$ . This initialization ensures a configuration closer to equilibrium, reducing the required equilibration time.

Finally, we note that the correlation between the two quantities is assessed by deriving the Spearman correlation coefficient, which is larger than 0.7 for all the analysed temperatures.

This preliminary analysis of equilibrium configurations shows that the two-dimensional Ising model with defects produces clustered states similar to those seen in the two-dimensional RFIM. Moreover, the introduced local potential captures well the local properties of the model with defects. We will come back to the correlation with the defect-potential for other local dynamical properties.

## 3.2 Quasi-phases investigation

In the previous section, we discussed how the presence of defects in the model leads to the formation of unique configurations. These configurations consist of regions with aligned spins, driven by the symmetry-breaking effects of the defects. Let us now examine the role of system size in shaping the system's properties.

The system size  $L$  plays a crucial role in the emergence of clustered configurations. Intuitively, reducing  $L$  also reduces the number of defects present in the system. In the limit where only a few defects exist, the clustered configuration is unlikely to be energetically favoured over the coherent (fully magnetized) configuration. To better understand the interplay between system size and defect fraction, we analyse the concept of *quasi-phases*. While a pure thermodynamic phase is meaningful only in the thermodynamic limit (where system properties become size-independent), our focus here is on the emergence and modification of quasi-phases at finite system sizes.

Typically, phases are distinguished by analysing an order parameter that exhibits

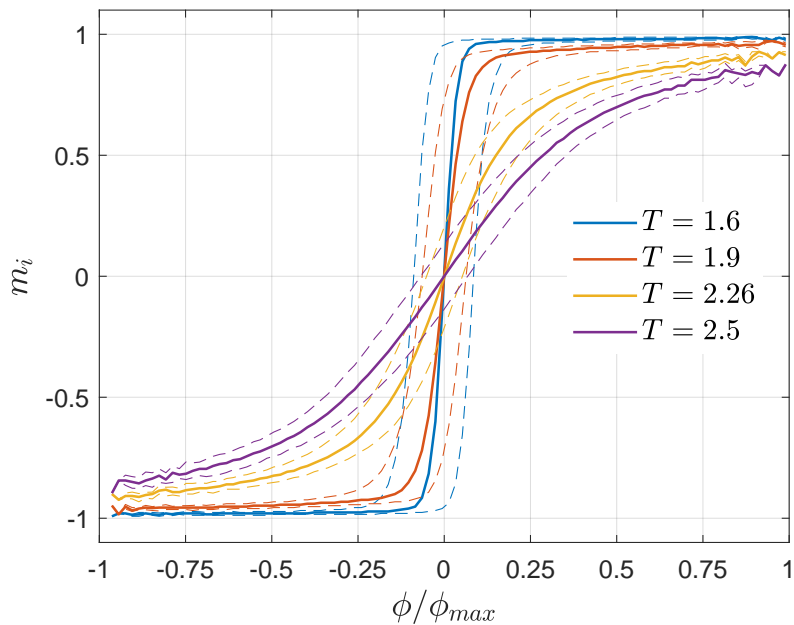


Figure 3.2: Relationship between the local defect-potential  $\phi_i$  and the local magnetization  $m_i = \langle \sigma_i \rangle$  for the two-dimensional Ising model with defects. The solid lines represent the median values of  $m_i$  within each of 100 equally spaced bins of  $\phi_i$  while the dashed lines correspond to the first and third quartiles. The narrow spread between the quartiles and the median indicates the robustness of the defect-potential as a measure of the local field. Simulation parameters:  $L = 200$ ,  $f = 0.02$ .

distinct behaviour in different phases. In this study, we identify up to four quasi-phases which could be observed in a system with quenched randomness. Alongside the paramagnetic and ferromagnetic phases, we must account for the clustered phase and the spin-glass phase. The latter arises due to the frustration and randomness introduced by defects, characterized by multiple stable energetic minima and complex relaxation behaviour. Identifying these quasi-phases requires at least two order parameters to fully distinguish their features. However, we adopt a different approach.

### 3.2.1 Analysis of overlap distribution

A preliminary analysis is conducted using the overlap distribution  $P(q)$ , introduced in Section 2.3.1. The function  $P(q)$  represents the probability distribution of the “scalar product” between two replicas (systems with identical defect configurations) that evolve independently. Mathematically, the scalar product between two replicas  $\alpha$  and  $\beta$  is defined as

$$q = \sum_i \sigma_i^\alpha \sigma_i^\beta \quad (3.1)$$

The overlap distribution  $P(q)$  is crucial for identifying phases, as it provides insight into the system’s structure and phase transitions. Moreover,  $P(q)$  exhibits a self-averaging property, meaning that its behaviour becomes increasingly representative of the whole system as the system size grows [70]. The characteristics of  $P(q)$  vary depending on the quasi-phase:

- Paramagnetic phase: In this phase, replicas evolve independently, with spins predominantly influenced by thermal fluctuations. Consequently, the overlap  $q$  is close to zero, and  $P(q)$  approximates a Gaussian distribution centred at zero with a size-dependent standard deviation. The hallmark of the paramagnetic phase is a single peak at  $q = 0$ , with  $P(q = 0) \neq 0$ .
- Ferromagnetic phase: Here, replicas are magnetized, with symmetry requiring both positive and negative magnetizations. Overlaps  $q \approx 1$  (for equally magnetized replicas) and  $q \approx -1$  (for oppositely magnetized replicas) dominate. As a result,  $P(q)$  exhibits two peaks, centred at  $q \approx \pm 1$ , with  $P(q = 0) = 0$ .
- Clustered phase: In this phase, no spontaneous magnetization forms and replicas evolve into identical configurations. The overlap  $q$  assumes a single non-zero value. Due to finite-size effects and temperature fluctuations  $P(q)$  maintains a bell-shaped form while peaking at a positive value. Therefore, a distinctive feature of this phase is a single peak in  $P(q)$  with  $P(q = 0) \neq 0$ .
- Spin-glass phase: This phase is characterized by multiple energetic minima, leading replicas to evolve into distinct configurations. According to Parisi’s description,  $P(q)$  becomes non-trivial, spanning a broad range of values symmetrically around  $q = 0$ . Indicators of this phase include  $P(q = 0) \neq 0$  and symmetric peaks for positive and negative  $q_{EA}$ .

$L$	60	100	140	180	220
$N_T$	40	60	80	100	120
$n_{\text{eq}}$	32000	16000	8000	4000	2000

Table 3.1: Simulation parameters for the parallel tempering algorithm used to determine the overlap distribution  $P(q)$  for different system sizes.

These characteristics serve as fingerprints for identifying quasi-phases and tracking their evolution as the system size changes. While this analysis provides valuable insights, it is not exhaustive and should be intended as a foundation for more detailed investigations.

To derive  $P(q)$  distributions, we employ a multi-spin coding algorithm with parallel tempering. The minimum and maximum of the temperature were fixed at  $T_{\text{min}} = 0.8$  and  $T_{\text{max}} = 2.6$  respectively, evenly divided in  $N_T$  intermediate temperatures.  $N_T$  depends on the system size, ensuring at least a probability of 25% of swapping between configurations simulated at neighbouring temperatures. The values of  $N_T$  are reported in Table 3.1. For each simulated temperature  $T_i$ , we prepare 64 replicas with identical defect configurations and evolve them independently for 10 MCSS. Then, configuration swaps between replicas at adjacent temperatures are proposed according to the parallel tempering rule. Each simulation block (comprising the multi-spin simulation and parallel tempering swaps) is repeated  $n_{\text{eq}}$  times for equilibration, where  $n_{\text{eq}}$  depends on the system size. For the largest system ( $L = 220$ ),  $n_{\text{eq}} = 2000$ . Other values are reported in Table 3.1.

After equilibration, another  $n_{\text{eq}}$  simulation blocks are run for data collection. Following each block, configurations are stored, and overlaps are computed for all replica pairs, producing  $P(q, t)$  for the  $t$ -th block. The final  $P(q)$  is obtained by averaging  $P(q, t)$  over time. A total of 2016 overlaps are considered, ensuring reliable characterization of the quasi-phases.

Fig. 3.3 shows the probability distribution  $P(q)$  for a system with size  $L = 140$  and defect fraction  $f = 0.01$  as a function of temperature. The top-left panel shows the superposition of  $P(q)$ , where the colour transitions from red ( $T_{\text{max}} = 2.6$ ) to blue ( $T_{\text{min}} = 0.8$ ) as the temperature is reduced. At high temperatures,  $P(q)$  is a Gaussian distribution centred at the origin, indicating the presence of a paramagnetic quasi-phase.

As the temperature decreases,  $P(q)$  deviates from the Gaussian shape and shifts toward higher  $q$  values, signalling a transition to the clustered phase. In this phase, replicas become increasingly similar as clusters with uniform spin orientations emerge across replicas. At even lower temperatures,  $P(q)$  develops a second peak near  $q \approx -1$ . Visual inspection of the configurations reveals that all replicas reach complete magnetization, either positive or negative. Interestingly, the two peaks are slightly asymmetric, with  $P_{\text{max}}(q > 0) > P_{\text{max}}(q < 0)$ . This asymmetry reflects that the evolution paths of different replicas are correlated, making one of the two magnetized states (positive or negative) more probable.

The top-right panel of Fig. 3.3 shows the temperature dependence of the overlap

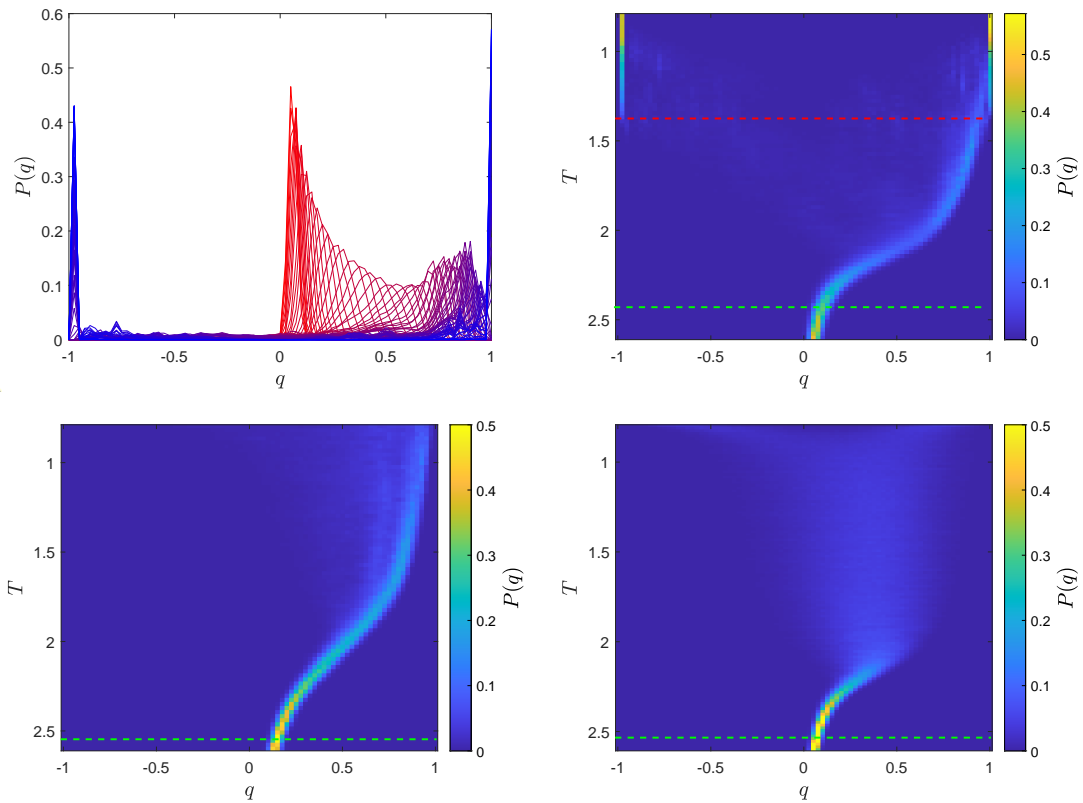


Figure 3.3: Probability distribution  $P(q)$  for different system sizes and defect fractions. (Top-left)  $P(q)$  for  $L = 140$ ,  $f = 0.01$ , with temperature decreasing from  $T_{\max} = 2.6$  (red) to  $T_{\min} = 0.8$  (blue). (Top-right) Temperature dependence of  $P(q)$  for the same system. (Bottom-left)  $P(q)$  for  $L = 140$ ,  $f = 0.03$ . (Bottom-right)  $P(q)$  for  $L = 220$ ,  $f = 0.01$ .

distribution. Horizontal lines indicate the transitions between different quasi-phases, as defined by the criteria discussed earlier. Specifically, the progression of quasi-phases (in decreasing temperature order) is paramagnetic, clustered, and ferromagnetic. Interestingly, no spin-glass quasi-phase is recognised, as for all other choices of system sizes and defect fractions.

We extend the analysis to a higher defect fraction ( $f = 0.03$ ) and a larger system size ( $L = 220$ ), as shown in the bottom-left and bottom-right panels of Fig. 3.3, respectively. For these cases, we observe the disappearance of the cluster-to-ferromagnetic quasi-phase transition. This result indicates that both  $L$  and  $f$  contribute to the suppression of the ferromagnetic quasi-phase, similar to findings in the RFIM [37].

Fig. 3.4 presents the quasi-phase diagram as a function of system size  $L$  and temperature  $T$  for various defect fractions:  $f = 0.01$  (blue),  $f = 0.015$  (orange),  $f = 0.02$  (yellow),  $f = 0.025$  (purple), and  $f = 0.03$  (green). Once again, the fingerprints listed above were used to determine the quasi-phase shown by the system at different temperatures. The diagram labels the distinct quasi-phases exhibited by the system: paramagnetic (P), clustered (CL), and ferromagnetic (F). Solid lines are included to guide the eye, marking the quasi-phase transitions. Upward triangles denote the transitions from the paramagnetic to the clustered phase, while downward triangles indicate the transitions from the clustered to the ferromagnetic phase.

From Fig. 3.4, it is evident that the clustered phase becomes increasingly prominent as both  $L$  and  $f$  grow. This expansion underscores the significant role of these parameters in stabilizing the clustered quasi-phase. Furthermore, the transition temperatures from the paramagnetic to the clustered quasi-phase appear to stabilise as the system size  $L$  increases, suggesting a limiting behaviour. By contrast, the transition from the clustered to the ferromagnetic quasi-phase decreases without showing asymptotic behaviour, indicating that the ferromagnetic quasi-phase is progressively suppressed at higher defect fractions and larger system sizes.

This visualization highlights the intricate interplay between system size, temperature, and defect fraction, offering a comprehensive understanding of how these factors influence the stability and transitions between quasi-phases. Anyway, we remark the purely informative role played by the considered methodology. The transitions are not obtained from order parameters, but from objective criteria that are not universal.

We can anyway conclude that the system shows peculiar properties related to the RFIM behaviour. Specifically, no spin glass phase is observed for different choices of the system size and defect fractions. Moreover, the observation of the ferromagnetic phase is possible only at finite sizes. In the thermodynamic limit, only the paramagnetic and the clustered phase can be observed.

### 3.3 Phase transition characterisation

Our investigation reveals that even the smallest fraction of defects introduce frustration in the system, breaking spatial symmetry in sufficiently large systems. The system's properties diverge significantly between the low-temperature clustered phase and the

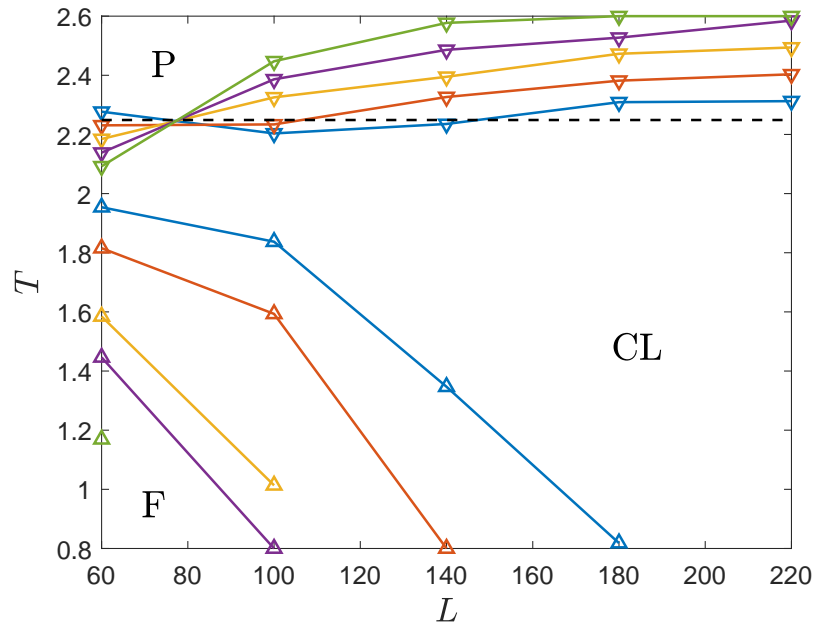


Figure 3.4: Quasi-phase diagram as a function of system size  $L$  and temperature  $T$  for different defect fractions  $f = 0.01$  (blue),  $f = 0.015$  (orange),  $f = 0.02$  (yellow),  $f = 0.025$  (purple), and  $f = 0.03$  (green). The quasi-phases are marked as F (ferromagnetic), CL (clustered), and P (paramagnetic). Solid lines guide the eye, marking the transitions between quasi-phases. Upward triangles indicate transitions from the paramagnetic to the clustered phase, while downward triangles represent transitions from the clustered to the ferromagnetic phase. The black dashed line represents the homogeneous thermodynamic critical temperature in Eq. (2.14).

high-temperature paramagnetic phase. Notably, the system's response to an external field changes across these phases, and long-range correlations, absent in the paramagnetic phase, emerge in the clustered phase. We now try to characterise this phase transition by properly defining an order parameter and looking at the modification of the system's energy.

The conventional order parameter for magnetic phase transitions, the total magnetization  $m = N^{-1} \sum_i \sigma_i$  is unsuitable in this case. This is because no spontaneous magnetization is observed as the temperature decreases;  $m$  remains zero even in the clustered phase due to the overall neutrality of clustered configurations. Instead, to distinguish the clustered state, where spins are constrained by surrounding defects, from the paramagnetic phase, where spins freely reorient, we propose a novel order parameter.

First, we compute the average direction of each spin,  $\langle \sigma_i \rangle$ , and then perform a spatial average of its absolute value:

$$\hat{m} = \frac{1}{N} \sum_i |\langle \sigma_i \rangle|, \quad (3.2)$$

This new order parameter effectively captures the key differences between the two phases. In the paramagnetic phase, where  $\langle \sigma_i \rangle \approx 0$  for all spins, we find  $\hat{m} \approx 0$ . Conversely, in the clustered phase, where spins align in a specific direction due to local constraints imposed by defects,  $\langle \sigma_i \rangle \neq 0$  on average, leading to  $\hat{m} > 0$ .

To further investigate the phase transition, we define a generalized magnetic susceptibility based on the fluctuations of the new order parameter:

$$\hat{\chi}_m = \frac{\langle \hat{m}^2 \rangle - \langle \hat{m} \rangle^2}{k_B T}. \quad (3.3)$$

Although the conjugate field associated with  $\hat{m}$  is unknown,  $\hat{\chi}_m$  serves as a proxy for the system's susceptibility to fluctuations in the clustered phase.

In addition to  $\hat{m}$  and  $\hat{\chi}_m$ , we also consider the standard system energy per spin,  $E$ , and the specific heat,  $\chi_E$ , defined as:

$$E = -\frac{J}{2N} \sum_{\langle i, j \rangle} \sigma_i \sigma_j, \quad \chi_E = \frac{\beta^2}{N} (\langle E^2 \rangle - \langle E \rangle^2), \quad (3.4)$$

where  $\beta = 1/(k_B T)$ ,  $J$  is the interaction strength, and the summation  $\langle i, j \rangle$  is taken over all nearest-neighbour spin pairs.

The proposed metrics, including  $\hat{m}$ ,  $\hat{\chi}_m$ ,  $E$ , and  $\chi_E$ , are systematically analysed to explore the nature of the phase transition and its dependence on the presence of defects. Figure 3.5 presents their behaviour as functions of temperature for various system sizes  $L$  and defect fractions  $f$ . The simulations were performed using a parallel tempering algorithm, with temperatures ranging from  $T_{\min} = 2.0$  to  $T_{\max} = 2.6$ . This range ensures the system reaches the paramagnetic phase therefore avoiding the possibility to remain trapped into a metastable state. The plotted curves are averaged over ten distinct realizations of defect configurations.

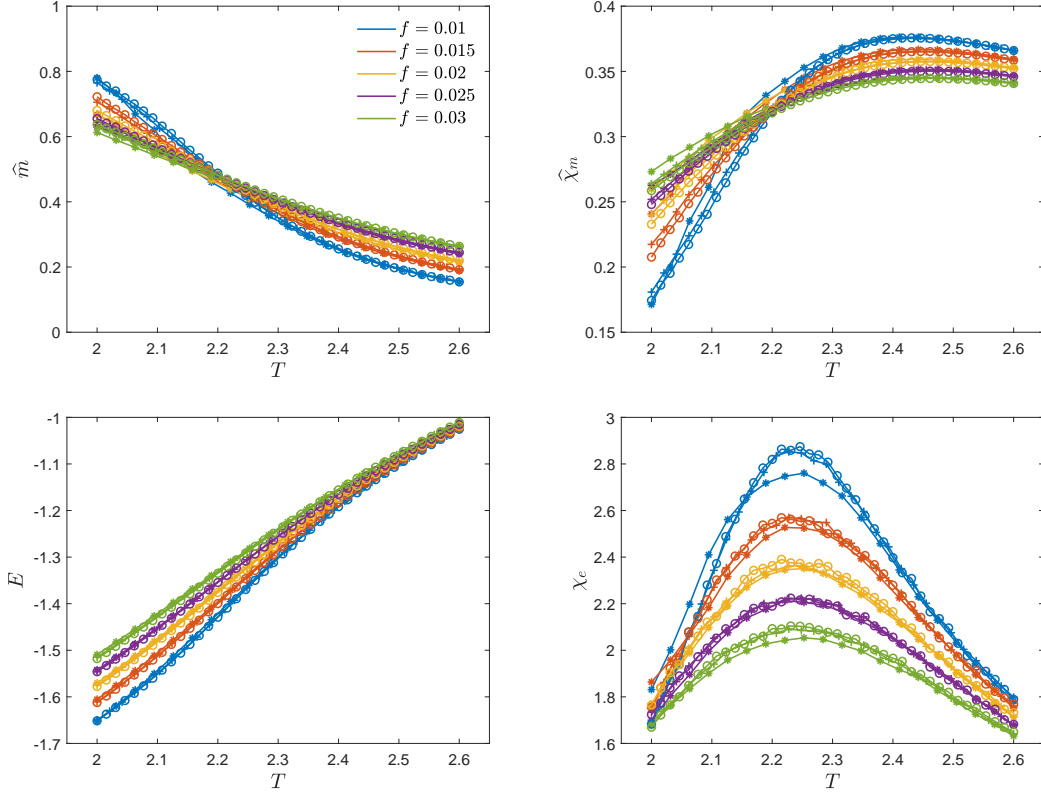


Figure 3.5: Temperature dependence of key thermodynamic quantities for various system sizes  $L$  and defect fractions  $f$ : (top-left) the proposed order parameter  $\hat{m}$ , (top-right) the generalized susceptibility  $\hat{\chi}_m$ , (bottom-left) the system's energy per spin  $E$ , and (bottom-right) the heat capacity  $\chi_E$ . Different markers refer to different system sizes:  $L = 100$  (\*);  $L = 200$  (+);  $L = 300$  (o). The order parameter  $\hat{m}$  transitions smoothly towards a non-zero value as the temperature decreases, signalling the emergence of the clustered phase, while the generalized susceptibility  $\hat{\chi}_m$  exhibits a broad peak associated with the phase transition temperature  $T_{c,m}$ . The heat capacity and energy curves show consistent behaviour, with  $T_{c,E}$  derived from the heat capacity peak. All quantities are averaged over ten realizations of defect configurations, and no finite-size effects are observed across the analysed range.

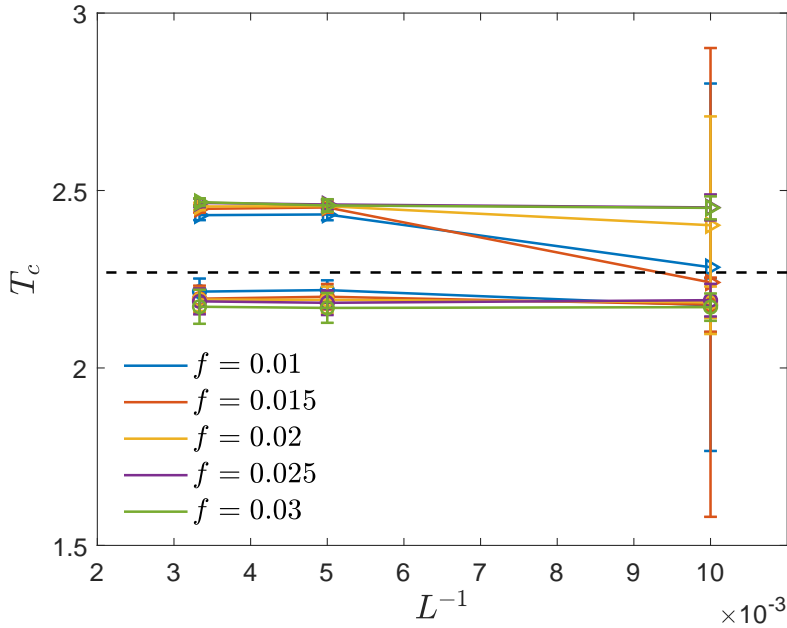


Figure 3.6: Critical temperature estimates as a function of the inverse system size  $L^{-1}$  for various defect fraction  $f$ . Different defect fractions are represented by different colours, as shown in the legend. The transition temperature  $T_{c,m}$  (triangles), derived from the peak of the generalized susceptibility  $\hat{\chi}_m$ , consistently exceeds the homogeneous critical temperature  $T_c$ , while  $T_{c,E}$  (circles), determined from the heat capacity peak, remains close to  $T_c$ .

The top-left panel of Fig. 3.5 shows the behaviour of the order parameter  $\hat{m}$ . As the temperature decreases,  $\hat{m}$  gradually transitions towards a non-zero value, indicating the emergence of the clustered phase. Notably, even at high temperatures,  $\hat{m}$  remains significantly different from zero, reflecting the effects of defects on the system's response. This behaviour differs markedly from that of homogeneous systems, where the order parameter exhibits a sharp transition, particularly for larger system sizes.

The generalized susceptibility  $\hat{\chi}_m$ , depicted in the top-right panel, displays a broad peak over the covered temperature range. The peak height diminishes as the defect fraction increases, suggesting a suppression of fluctuations in the presence of defects. In analogy with standard phase transition analysis, the temperature at which  $\hat{\chi}_M$  peaks is identified as the transition temperature  $T_{c,m}$ , corresponding to the point of maximum fluctuations and global rearrangement of the system. Averaging the peak positions over replicas yields a consistent estimate for  $T_{c,m}$ . Fig. 3.6 shows that these results are free from finite-size effects. The curves collapse without requiring rescaling, reinforcing the robustness of the transition characterization.

The bottom-left panel of Fig. 3.5 presents the energy per spin,  $E$ , while the bottom-

right panel shows the heat capacity,  $\chi_E$ . A notable observation is that the heat capacity peaks become less pronounced as the defect fraction increases. Additionally, the critical temperature derived from the heat capacity,  $T_{c,E}$ , identified as the peak position of  $\chi_E$ , is consistently lower than the critical temperature obtained from the proposed order parameter,  $T_{c,m}$ .

The absence of finite-size effects is evident in the energy and heat capacity curves for most cases, as no size-dependent variations are observed. However, an exception occurs for the system with  $L = 100$  and  $f = 0.01$ , where deviations in the susceptibility and heat capacity curves are observed compared to other configurations. This behaviour likely reflects a finite-size effect. For small system sizes and low defect fractions, a quasi-ferromagnetic phase can emerge, altering the expected cluster-paramagnetic phase transition dynamics.

Fig. 3.6 highlights distinct differences between the critical temperatures derived from the proposed order parameter ( $T_{c,m}$ ) and the heat capacity ( $T_{c,E}$ ). Specifically,  $T_{c,m}$  exceeds the critical temperature of the homogeneous system ( $T_c$ ), while  $T_{c,E}$  closely aligns with  $T_c$ , indicated by the black dashed line. This discrepancy persists across all defect fractions and system sizes.

Furthermore, the plot reveals that smaller systems and lower defect fractions exhibit lower values of  $T_{c,m}$  and significantly larger standard deviations. This behaviour arises due to the coexistence of paramagnetic-ferromagnetic and paramagnetic-clustered phase transitions in certain replicas. As discussed earlier, specific defect realizations in small systems may not energetically favour the formation of clusters. Instead, these replicas transition directly into the ferromagnetic phase, bypassing the clustered phase. This variability among replicas increases the standard deviation, particularly for smaller systems and low defect fractions.

The clustered state at low temperatures is characterized by long-range correlations and constrained spin dynamics—features not captured by the traditional order parameter (total magnetization). The gradual transition in the proposed order parameter,  $\hat{m}$ , and the broad peak in the generalized susceptibility,  $\hat{\chi}_m$ , indicate that the presence of defects broadens the transition and diminishes peak susceptibilities. This behaviour suggests that quenched disorder suppresses the sharp collective behaviour typically observed in homogeneous systems.

These findings highlight the utility of the proposed order parameter,  $\hat{m}$ , in identifying the transition to the clustered phase. By capturing the effects of defects on the phase transition,  $\hat{m}$  provides a more comprehensive view of the system's behaviour under disorder and offers valuable insights into the interplay between defects and phase transitions.

## Conclusion

To conclude this chapter, we summarize the main findings regarding the static properties of the two-dimensional Ising model with defects. Our analysis demonstrates that at sufficiently low temperatures, a clustered phase emerges, characterized by long-range

correlations and constrained spin dynamics. This phase is induced by the interplay between quenched disorder and thermal fluctuations, where defects introduce local defect-potentials that effectively bias the spin orientations. The clustered phase distinctly contrasts with the high-temperature paramagnetic phase, where spins freely fluctuate and no long-range order is observed.

In small system sizes and at low defect fractions, we have also observed a magnetized phase. However, our results indicate that this magnetized state is a quasi-phase that does not survive in the thermodynamic limit, as larger systems exhibit the expected transition from the clustered phase to the paramagnetic phase without evidence of spontaneous magnetization. This finding highlights the importance of system size in interpreting the phase behaviour of disordered magnetic systems.

The proposed order parameter,  $\hat{m}$ , has proven to be an effective tool for distinguishing the clustered and paramagnetic phases. Unlike traditional magnetization-based measures,  $\hat{m}$  captures the effects of local constraints imposed by defects, providing a robust means to characterize the static properties of the model. Additionally, the associated generalized susceptibility,  $\hat{\chi}_m$ , offers valuable insights into the broadening of the phase transition caused by defects and quenched disorder. The heat capacity,  $\chi_E$ , further supports these observations, with its critical temperature  $T_{c,E}$  aligning closely with the transition temperature of the homogeneous system,  $T_c$ . By contrast to the higher  $T_{c,m}$  derived from  $\hat{m}$ .

Our findings strengthen the analogy between the two-dimensional model with defects and the RFIM. Both systems exhibit frustration and symmetry breaking introduced by quenched disorder, leading to clustered configurations at low temperatures. However, the exact relationship between these models in terms of critical phenomena remains an open question. To explore this connection further, an extension of the analysis to three-dimensional systems with defects is warranted, possibly following the methodology used with success on the three-dimensional RFIM [44]. By studying the critical behaviour and deriving critical exponents, one could test whether the two models fall within the same universality class. Such an investigation would deepen our understanding of the broader implications of quenched disorder and the role of defects in phase transitions.



## Chapter 4

# Dynamic Properties

In the previous chapters, we explored the equilibrium conditions of homogeneous and heterogeneous Ising models. At equilibrium, a system settles into the global minimum state of the free energy and exhibits well-defined macroscopic properties, such as magnetisation, susceptibility, and correlation length.

Generally, the free energy landscape in phase space can display intricate structures. The global minima of this hypersurface are associated with equilibrium states, which a system naturally approaches as long as its dynamics satisfy the ergodic condition. However, the existence of local minima can influence the system's dynamics, as they may trap the system for prolonged times. These local minima are referred to as *metastable states*, and we can characterize them by a *metastable lifetime*, defined as the average time the system takes to escape from such states.

As a concrete example, let us consider the two-dimensional Ising model with the classical single-spin flip dynamics and periodic boundary conditions. Below the critical temperature, the equilibrium configuration corresponds to the magnetised state. However, when the system is initialized in a random configuration of spins and evolves under the Metropolis rule, long-lived intermediate configurations can emerge, specifically, *stripe configurations*, where spins of the same orientation form extended regions separated by sharp interfaces [71]. These configurations correspond to local minima of the free energy landscape. To escape such metastable states, the system must overcome an energy barrier, which involves the erosion and eventual collapse of the interfaces separating regions of opposite magnetisation. Since this process requires thermal activation, it occurs over extremely long timescales, rendering stripe configurations metastable for the system.

It is important to note that the choice of the update rule significantly influences the system's dynamic evolution and the prominence of metastable states. For instance, cluster algorithms, such as the Wolff algorithm, can drastically reduce the formation and persistence of stripe configurations. By enabling collective spin updates, these algorithms provide alternative pathways through the free energy landscape, allowing the system to bypass local minima and reducing the effective trapping in metastable states.

Interestingly, external perturbations can fundamentally alter the status of metastable and equilibrium states. Let us once again consider the 2D Ising model. Below the critical

temperature and in the absence of an external field, the system possesses two equivalent equilibrium states corresponding to spontaneous magnetisation. These states are global minima of the free energy and are symmetric with respect to spin inversion. However, when an external field is applied, the system's Hamiltonian acquires an additional term,  $-mh$ , where  $m$  is the magnetisation and  $h$  is the external field. This modification breaks the symmetry between the two minima: one of the states becomes the global minimum, while the other is downgraded to a local (metastable) minimum.

If, prior to applying the external field, the system resides in the now-unfavoured metastable state, the introduction of the field initiates a migration process towards the new equilibrium state. This migration, which occurs over relatively long timescales, is driven by the system's dynamics as it seeks to minimize its free energy. Understanding this transition process, particularly the mechanisms governing spin reversals and the dynamic pathways out of metastable states forms the central focus of this chapter.

The main original results presented and discussed in this chapter include the validation and extension of classical nucleation theory to account for the effects of defects in heterogeneous systems, the derivation of modified free energy expressions and critical cluster size dependencies incorporating defect characteristics, and the analysis of metastable lifetimes and spinodal transitions under varying defect densities. These contributions provide new insights into magnetization reversal processes and the role of structural heterogeneity in modifying dynamic properties.

## 4.1 Reversal process in homogeneous systems

Reversal processes in magnetic systems have been extensively investigated for over 50 years using computer simulations [72]–[74], theoretical studies [75], [76], and direct experiments on materials [77], [78]. These processes are observed in a variety of physical phenomena, including hysteresis loops and magnetic recording devices with bistable recording states. Moreover, the underlying theory extends naturally to describe other processes, such as vapour-liquid phase transitions and nucleation in solvent-solute mixtures [79], [80].

To illustrate the reversal process, consider a magnetized system initially aligned in a specific orientation (e.g., positive magnetization), in contact with a heat bath at a temperature below the Curie temperature. At thermodynamic equilibrium, the system preserves this magnetized state. Now, suppose an external magnetic field of opposite sign (negative) is suddenly applied. The system dynamics can be divided into three stages:

1. Initial relaxation ( $t_0$ ): following the quench, the system quickly adapts to the new external field, leading to a short relaxation time  $t_0$  during which the magnetization stabilizes at a metastable plateau  $m(t) = m_{MS}$ , corresponding to a local minimum in the free energy.
2. Metastable state ( $t_1$ ): the system remains trapped in the metastable state for an extended period  $t_1$ , during which small fluctuations of the order parameter are

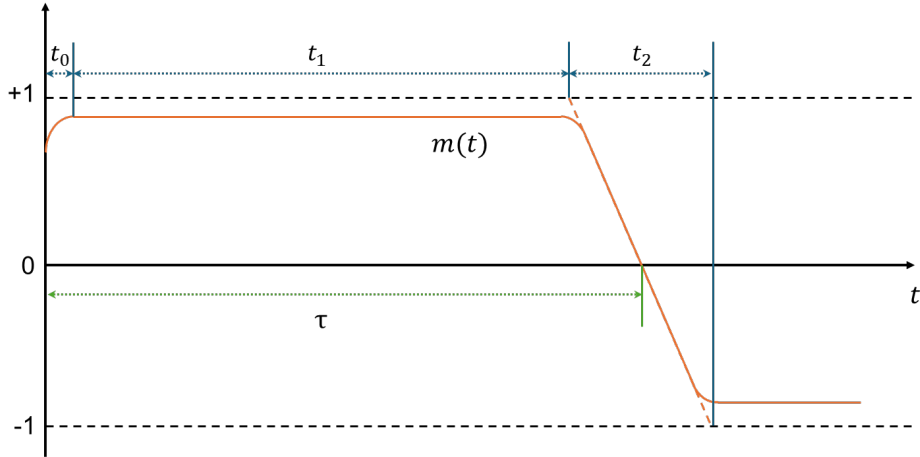


Figure 4.1: Schematic representation of the magnetization reversal process. The metastable lifetime  $\tau$  is defined as the time to cross  $m = 0$  after the field quench.  $t_0$ ,  $t_1$  and  $t_2$  represents the initial relaxation, the time spent in the metastable state and the time for the reversal process, respectively.

observed.

3. Reversal process ( $t_2$ ): eventually, the system transitions to the stable configuration with opposite magnetization, completing the reversal process. This transition is associated with a relaxation time  $t_2$ .

A schematic representation of the magnetization dynamics is provided in Fig. 4.1. The total metastable lifetime  $\tau$ , defined as the time between the field quench and the crossing of the  $m = 0$  line, depends on the external parameters, temperature  $T$ , and field strength  $h$ . This definition aligns with existing literature and facilitates quantitative analysis of the process.

At the microscopic level, the system reacts to the perturbation by forming regions of spins aligned with the external field (negative magnetization). These *droplets* expand over time until they fill the entire system, a phenomenon termed *nucleation*. The analogy with vapour-liquid phase transitions is evident: droplets represent regions of the stable phase emerging within the metastable phase.

The nucleation process can be analysed in terms of free energy. Forming a droplet involves two competing factors: (i) the energetic cost of creating a surface that separates regions of opposite magnetization, and (ii) the energetic gain of forming a stable-phase droplet. For small droplets, the surface energy dominates, leading to shrinkage and eventual disappearance of the droplet. By contrast, for sufficiently large droplets, the energetic gain outweighs the surface cost, resulting in droplet growth.

There exists a critical droplet size,  $\Gamma_c$ , with associated the highest free energy barrier. Droplets larger than  $\Gamma_c$  are more likely to grow, completing the reversal process, while

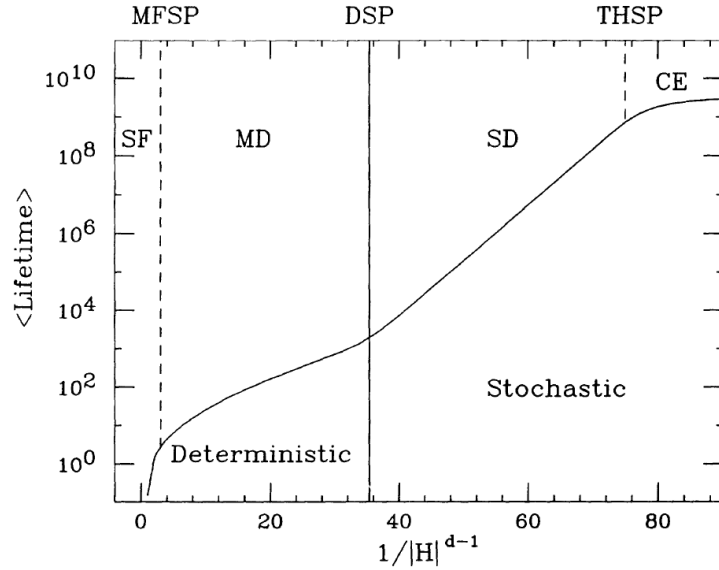


Figure 4.2: Schematic representation of the magnetization reversal regimes and critical fields as a function of the inverse of the external field. Source [73]

smaller droplets shrink. Thus, the critical cluster size  $\Gamma_c$  plays a key role in determining the dynamics of nucleation and magnetization reversal.

#### 4.1.1 Mechanisms of reversal

Magnetization reversal occurs through distinct mechanisms depending on the simulation conditions, specifically the external field strength  $h$ , temperature  $T$ , and system size  $L$  [73]. These mechanisms are categorized into four regimes, described below: the strong-field (SF) regime, the multi-droplet (MD) regime, the single-droplet (SD) regime, and the coalescence (CE) regime. Transitions between these regimes are marked by three critical fields. The *mean-field spinodal point*  $h_{\text{MFSP}}$  separates the SF and the MD regimes; the *dynamic spinodal point*  $h_{\text{DSP}}$  separates the MD and SD regimes; and the *thermodynamic spinodal point*  $h_{\text{THSP}}$  separates the SD and CE regimes.

It is important to note that the term *spinodal point* used here differs from the spinodal point in mean-field phase transition theory. A schematic summary of these regimes and transitions is shown in Fig. 4.2.

**Strong-Field (SF) regime.** In the SF regime ( $h > h_{\text{MFSP}}$ ), the metastable state ceases to exist as a local free energy minimum ( $t_0 \approx t_1 \approx 0$ ). The droplet picture is no longer valid, and magnetization reversal occurs through unstable, long-wavelength modes [76]. The metastable lifetime  $\tau$  reflects only the relaxation time  $t_2$ , which is typically short.

**Multi-Droplet (MD) regime.** For intermediate field strengths ( $h < h_{\text{MFSP}}$ ), the system enters the MD regime. Reversal proceeds via the simultaneous nucleation, growth, and coalescence of multiple droplets. The process is well-described by the Johnson-Mehl-Avrami-Kolmogorov theory [81]. Due to the averaging effect of multiple droplets, the magnetization dynamics  $m(t)$  appear smooth and deterministic, meaning that repeated measurements yield consistent results across different realizations.

**Single-Droplet (SD) regime.** As the field decreases further ( $h < h_{\text{DSP}}$ ), the nucleation process slows down due to a high free energy barrier and large critical droplet size. For small system sizes, the reversal process is driven by the formation and growth of a single critical droplet. The dynamics becomes stochastic (Poissonian), where the bottleneck is the first nucleation event ( $t_1 \gg t_2$ ). This scenario aligns with classical nucleation theory, which describes processes like phase separation in bi-phase mixtures through the first critical nucleation event.

The stochastic nature of the SD and MD regimes can be distinguished by analysing the ratio  $r = \sigma_\tau / \bar{\tau}$ , where  $\sigma_\tau$  and  $\bar{\tau}$  are the standard deviation and mean of the metastable lifetime, respectively. A value  $r > 0.5$  (typical of Poissonian processes) identifies the SD regime, while  $r < 0.5$  (typical of deterministic processes) indicates the MD regime [82].

**Coalescence (CE) regime.** In the absence of an external field or for sufficiently weak fields ( $h < h_{\text{THSP}}$ ), the system resides in the CE regime. Here, two stable states with opposite magnetization ( $\pm m_S$ ) coexist, and reversal occurs solely due to thermal fluctuations. The free energy difference between the metastable and stable states becomes negligible, leading to extremely long metastable lifetimes  $\tau$ . In the thermodynamic limit ( $L \rightarrow \infty$ ),  $\tau$  diverges, and no reversal is observed within practical simulation times [83].

In the following sections, we provide an overview of the main theoretical framework used to describe magnetisation reversal processes: classical nucleation theory (for SD reversals) and Johnson-Mehl-Avrami-Kolmogorov theory (for MD reversals).

#### 4.1.2 Classical nucleation theory

Classical Nucleation Theory (CNT) provides a robust framework for quantitatively describing the formation and growth of clusters during transitions from a metastable phase to a stable phase [79], [80]. CNT is particularly effective for predicting nucleation rates, defined as the number of clusters forming per unit area and time, though its assumptions require careful scrutiny [84]. For lattice-gas models, these assumptions are as follows:

- Droplet growth and shrinkage occur through sequential addition or removal of single spins. The merging or splitting of droplets is neglected. Since these processes are critical in the MD regime, CNT fully describes nucleation only in the SD regime. However, it can still capture the early stages of the MD process, including nucleation and initial droplet growth.

- Nucleation is treated as a single-step process with no intermediate metastable phases. This assumption may fail in more complex systems, such as crystal nucleation, where solute aggregation precedes crystallographic ordering [85].

The 2D Ising model satisfies these assumptions, making CNT a reliable candidate for describing nucleation processes in the SD regime. A brief overview of its theoretical framework is presented below.

CNT models nucleation as a temperature-driven stochastic process (Brownian motion) in cluster-size space. The free energy of the system,  $F_{\text{CNT}}(\lambda)$ , depends on the cluster size  $\lambda$ , assumed to be the reaction coordinate. It is expressed as:

$$F_{\text{CNT}}(\lambda) = 2\sigma(T)\sqrt{\pi\lambda} - 2h\lambda + \eta_L k_B T \log(\lambda) + A_3, \quad (4.1)$$

where  $\sigma(T)$  is the surface tension (assumed size-independent),  $h$  is the external field strength, and  $\eta_L$  is a correction factor accounting for surface roughening [86]. The first two terms have clear physical interpretations:  $2\pi\sigma(T)\sqrt{\lambda}$  represents the surface energy cost of creating a droplet interface, while  $-2h\lambda$  represents the bulk energy gain from droplet alignment with the external field. The logarithmic correction, derived by Langer, accounts for deviations from circular droplet shapes. For the homogeneous 2D Ising model,  $\eta_L = 5/4$ , confirmed numerically over a broad temperature range  $0.53T_c < T < 0.84T_c$  [87].

**Surface tension and anisotropy.** In the 2D Ising model, the surface tension  $\sigma(T)$  exhibits anisotropy due to the square lattice geometry, weakening with increasing temperature. Surface tension depends on the orientation of the droplet interface relative to the lattice axes. For parallel and diagonal directions, Onsager's exact solution [9] yields [88]:

$$\sigma_{\parallel}(T) = 2J + k_B T \ln \left( \tanh \left( \frac{J}{k_B T} \right) \right), \quad (4.2)$$

$$\sigma_{\text{diag}}(T) = \sqrt{2} k_B T \ln \left( \sinh \left( \frac{2J}{k_B T} \right) \right). \quad (4.3)$$

From these expressions, it is possible to define an effective surface tension  $\sigma_{\text{eff}}$  such as the surface free energy term for a droplet that satisfies the Wulff construction can be written in the form  $F_s = 2\sigma_{\text{eff}}(T)\sqrt{\pi\lambda}$  for all temperatures. This expression considers that the proper shape of a droplet is given by the Wulff construction (in particular, it is circular for  $T > 0.5T_c$  and becomes perfectly squared for  $T = 0$ ). The effective surface tension can be approximated with the following expression for  $T \geq 0.25T_c$  [89]

$$\sigma_{\text{eff}} \approx \frac{1}{2\sqrt{\chi(T)}} (\sigma_{\parallel}(T) + \sigma_{\text{diag}}(T)), \quad (4.4)$$

where  $\chi(T) = (1 - \sinh^{-4}(2J/k_B T))^{1/8}$  is the average concentration of positive spins from Onsager's solution. The temperature dependence of the surface tension components is shown in Fig. 4.3.

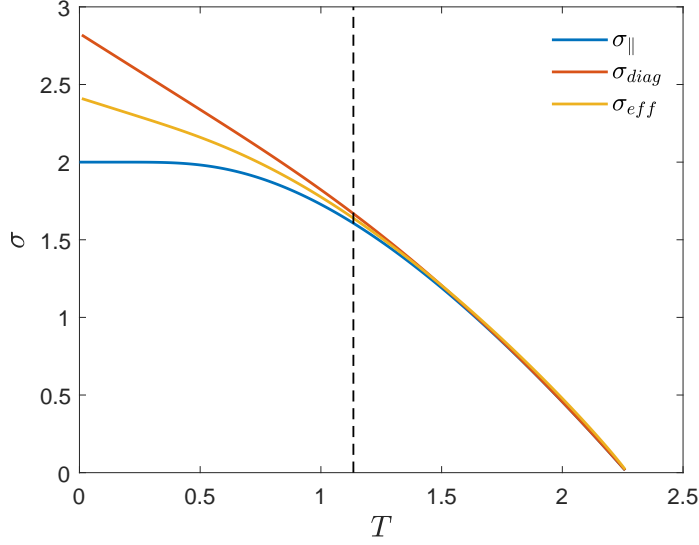


Figure 4.3: Temperature dependence of the surface tension components in the 2D Ising model (Eqs. 4.2-4.4). The dashed line indicates  $T = 0.5T_c$ , above which the droplet shape is assumed circular.

**Critical cluster and nucleation rate.** From Eq. (4.1), the critical cluster size  $\lambda_c$  is derived as:

$$\lambda_c = \left( \frac{2\sqrt{\pi}\sigma_{\text{eff}} + \sqrt{4\pi\sigma_{\text{eff}}^2 + 40hTk_B}}{8h} \right)^2. \quad (4.5)$$

The nucleation can be obtained thanks to Arrhenius's law [90], which describes the rate of occurrence for events with a free energy barrier  $\Delta F_c$  [90]:

$$I_{CNT} = D_c \Gamma \exp\left(-\frac{\Delta F_c}{k_B T}\right), \quad (4.6)$$

where  $D_c$  is the diffusion constant and  $\Gamma$  is the Zeldovich factor [91]. The diffusion constant, accounting for spin-flip rates at the droplet boundary, is:

$$D_c(T) = 2\beta_0(T)\sqrt{\pi\lambda_c}, \quad (4.7)$$

where  $\beta_0 \approx \exp[-\sigma_{\text{eff}}(T)/k_B T]$  is the average spin-flip rate at the boundary of the critical cluster.

The Zeldovich factor  $\Gamma$  measures the recrossing probability for the critical cluster and is defined as:

$$\Gamma = \left( \frac{\eta}{2\pi k_B T} \right)^{1/2}, \quad \eta = -\frac{\partial^2 F(\lambda)}{\partial \lambda^2} \Big|_{\lambda=\lambda_c}. \quad (4.8)$$

For systems with identical barrier heights, a steeper free energy landscape increases  $\Gamma$ , reducing the probability of critical cluster dissolution [92].

### 4.1.3 Validation of CNT with Ising model

The assumptions outlined above can be readily tested using numerical Monte Carlo simulations of the Ising model. With the advancement of specialised methods for investigating rare events, it is now feasible to directly compute the nucleation rate at fixed temperature and field strength and compare it to predictions from CNT. At low temperatures and weak field strengths, directly observing nucleation events within typical simulation times becomes challenging, as thermal fluctuations are ineffective in forming a critical cluster. To address this issue, the forward flux sampling technique was developed [93], [94].

**Forward flux sampling technique.** Forward Flux Sampling (FFS) is a simulation technique that decomposes the rare event process into a series of intermediate states (or interfaces) along a reaction coordinate. Starting from an initial state, the method incrementally propagates trajectories forward, calculating the flux of trajectories crossing each interface until the final state is reached. This staged approach ensures that computational resources are focused on the relevant regions of phase space, making FFS exceptionally well-suited for investigating rare but critical phenomena such as nucleation, chemical reactions, and protein folding.

The nucleation process of a droplet, from the metastable state to the complete reversal, can be decomposed into a series of stages. The trajectory of a droplet in the reaction coordinate space, from  $\lambda = 0$  to  $\lambda = N$ , is divided into smaller windows  $[\lambda_n, \lambda_{n+1})$  with fixed length  $\Delta\lambda$ . Let  $P(n)$  be the probability of observing a cluster transitioning from size  $\lambda = \lambda_n$  to  $\lambda = \lambda_{n+1}$  before shrinking back to the metastable phase. Then, the total nucleation probability is given by  $P_N = \prod_i P(i)$ . Since the nucleation rate accounts for the number of events per unit area and volume, the probability  $P_N$  is multiplied by the flux  $\phi_1$  (number of events per unit area and volume) that cross the initial barrier at  $\lambda_1$ . When calculating  $\phi_1$ , recrossing events of shrinking droplets must be excluded to avoid double counting. The nucleation rate can be expressed as:

$$I_{\text{FFS}} = \phi_1 P_N = \phi_1 \prod_i P(i). \quad (4.9)$$

In practice, it is sufficient to explore windows far enough into the reaction coordinate space where potential recrossing of the barrier has a negligible probability, such that  $P(i) \approx 1$ .

**Umbrella sampling technique.** To estimate the nucleation rate predicted by CNT, the free energy function  $F(\lambda)$  along the reaction coordinate must be obtained and analysed. This can be achieved using the Umbrella Sampling (US) technique [95]. In US, the configuration space is partitioned into multiple overlapping windows, each characterized by specific cluster sizes  $[\lambda_m, \lambda_{m+1}]$ , where the notation  $m$  distinguishes the windows from those used in FFS.

Unlike FFS, subsequent windows in US share an overlap  $\Delta\lambda$ , which is essential for reducing the statistical error in the free energy estimation. Within each window, a

cluster of size  $\lambda = \lambda_m$  is initialized, and the simulation is executed for a fixed number of iterations. Increasing the number of iterations reduces statistical error. During the simulation, any new state that exceeds the window boundaries is rejected, and the previous state is restored. At the end of the simulation, the relative free energy within each window is determined as:

$$f_m(\lambda) = -k_B T \ln[P_m(\lambda)], \quad (4.10)$$

where  $P_m(\lambda)$  is the sampling probability for a cluster of size  $\lambda$ , obtained as the ratio of the time spent by the system at cluster size  $\lambda$  to the total simulation time within the window.

The relative free energies  $f_m(\lambda)$  are shifted to ensure overlap between subsequent windows, and the total free energy function is anchored at  $F(\lambda = 1)$ , which corresponds to  $-k_B T \ln(\rho_{\text{MD}})$ , where  $\rho_{\text{MD}}$  is the monomer density (fraction of positive spins) in the metastable phase. The complete free energy function  $F(\lambda)$  is then given by:

$$F^{\text{US}}(\lambda) = -k_B T \ln(\rho_{\text{MD}}) - k_B T \ln \left[ \frac{P(\lambda)}{P(1)} \right], \quad (4.11)$$

where  $P(\lambda)$  is the total probability of sampling a cluster of size  $\lambda$ .

By reconstructing  $F(\lambda)$ , the free energy barrier and critical cluster size can be determined, enabling validation of CNT predictions for the nucleation rate in the Ising model. Also, we can readily calculate the Zeldovich factor in Eq. (4.6).

The diffusion coefficient can be estimated theoretically or derived by analysing the dynamics of a critical droplet. The two methods give comparable results within a factor of two of discrepancy [87]. For compliance with previous studies [87], [96], [97], we will present the diffusion coefficient directly from Monte Carlo simulations.  $D_c$  can be estimated considering the average trajectory for a droplet prepared in critical conditions. From the physical meaning of the diffusivity constant, it follows that

$$D_c = \frac{\langle [\lambda(t) - \lambda_c]^2 \rangle}{2t} \quad (4.12)$$

where  $t$  is the simulation time and  $\lambda(t)$  is the time evolution of the cluster size. We refer to the average over many simulations with  $\langle \dots \rangle$ .

**Validation of CNT at low temperatures.** The validation of CNT is carried out through a series of comprehensive tests, which include:

1. Verifying the agreement between the theoretical expression for the free energy function, Eq. (4.1), and the simulation results obtained using Eq. (4.11).
2. Testing the critical cluster size predicted by Eq. (4.5) using the US technique and showing its equivalence to alternative definitions.
3. Showing the equivalence between the two methods for deriving the diffusion coefficient, as given by Eq. (4.7) and Eq. (4.12).

4. Comparing the two nucleation rate expressions,  $I_{\text{CNT}}$  from Eq. (4.6) (derived via US) and  $I_{\text{FFS}}$  from Eq. (4.9).

Previous studies [87], [96] validated CNT primarily within a limited temperature range ( $T > 1$ ) providing satisfactory agreement between simulations and theoretical predictions. However, thanks to the exceptional efficiency of the  $N$ -Fold way algorithm in the low-temperature regime, we extend these validations to significantly lower temperatures, a regime previously unexplored. This advancement represents a novel contribution to the state of the art, as it enables the validation of CNT under conditions where nucleation processes are particularly challenging to observe.

The results presented here build upon and adapt original findings, also reported in [67]. Additionally, these validations serve to test the robustness and accuracy of the proposed algorithms and methodologies, particularly the novel cluster identification algorithm introduced in [67]. Beyond the present context, these tools and techniques hold significant potential for broader applications in the study of nucleation and related phenomena.

**Test 1: Validation of the free energy function.** The agreement between the theoretical free energy function and the results obtained from simulations using the US technique is demonstrated in Fig. 4.4. The left panel shows the free energy profiles for all analysed temperatures, where the simulation results (solid lines) are in excellent agreement with the theoretical expression in Eq. (4.1) (dashed lines). The theoretical curves completely overlap with the simulation data, even at the lowest temperatures considered, highlighting the robustness of the method.

The right panel of Fig. 4.4 presents the effective surface tension  $\sigma_{\text{eff}}$  extracted as a fitting parameter from the free energy curves (data points), alongside the theoretical prediction given by Eq. (4.4) (dashed line). The close agreement across the entire temperature range further validates the consistency between simulation and theory.

For these simulations, a lattice size of  $L = 100$  was used, with a slight modification of the US technique as proposed in [67]. Specifically, the window size  $\Delta\lambda$  was varied with temperature to optimize accuracy. At the highest temperature ( $T = 1.6$ ), a fixed window size of  $\Delta\lambda = 12$  was employed. As the temperature decreases,  $\Delta\lambda$  was systematically reduced to account for the steeper free energy landscape. This adaptive approach, combined with repeated measurements in regions of rapid free energy variation, effectively reduces statistical errors in the determination of the free energy function as given by Eq. (4.11).

**Test 2: Validation of the critical cluster size.** The critical cluster size  $\lambda_c$  can be determined from the free energy function using Eq. (4.5). Alternatively,  $\lambda_c$  can be defined as the cluster size at which the growth velocity of a droplet becomes zero. This alternative definition will be revisited in the following section. To test the consistency between the two approaches, we perform the following simulation.

Starting with a negatively magnetized cluster, we analyse cluster formation and growth after switching on an external field. Snapshots of the lattice are recorded at

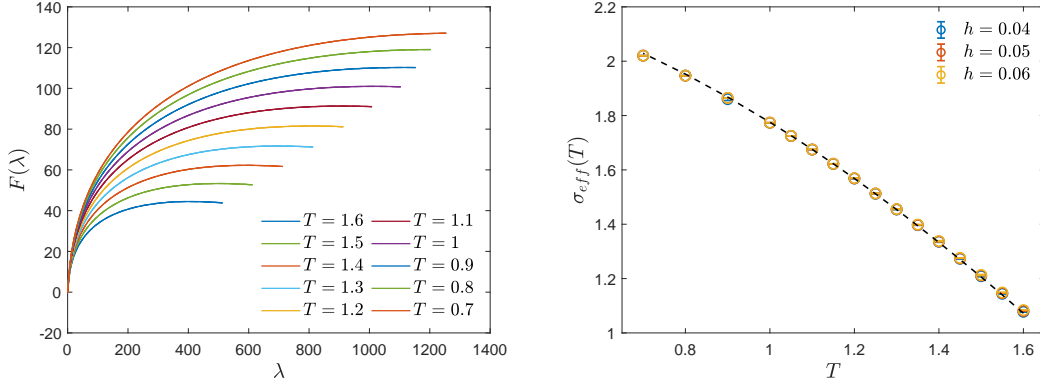


Figure 4.4: Validation of the free energy function and surface tension. Left panel: Comparison between the theoretical expression for the free energy function of the cluster size [Eq. (4.1)] and the simulation results obtained using the US technique for  $h = 0.05$ . Solid lines represent simulation data, while dashed lines correspond to the theoretical prediction. Right panel: The surface tension  $\sigma_{\text{eff}}$  (points) extracted from fitting the theoretical expression to the simulated free energy function, compared with the theoretical surface tension (dashed line). The agreement persists across the entire temperature range.

each time step, and cluster dynamics are tracked using a dedicated cluster identification algorithm. This algorithm assigns a unique label to each cluster and monitors changes in the cluster area at every spin flip. Further implementation details of the algorithm can be found in [67].

The algorithm carefully handles cluster merging and splitting events. When two or more clusters merge, the new cluster retains the label of the largest original cluster. In the case of equally sized clusters merging, the label is randomly assigned. Conversely, when a cluster splits into two or more, the largest fragment retains the original label, while the new fragments receive new labels. For equally sized splits, all clusters are assigned new labels. Although cluster merging and splitting introduces slight deviations in the measured growth velocity, their overall effect remains limited.

The growth velocities computed at different temperatures are shown in Fig. 4.5 (solid lines). A functional form inspired by Eq. (B.2),  $v(\lambda) = m\sqrt{\lambda} + q$ , is used to fit the data (dashed lines). This fit accurately captures the behaviour for intermediate cluster sizes. Deviations are observed at small cluster sizes due to thermal fluctuations, and at large cluster sizes due to cluster merging events. The critical cluster size  $\lambda_c$ , where the growth velocity crosses the  $x$ -axis, can be easily identified.

To reduce statistical uncertainty, a moving average with a window size of  $\Delta\lambda = 20$  was applied to the growth velocity data. The resulting estimates of  $\lambda_c$  from the growth velocity method are compared to those obtained from the US technique in Fig. 4.6. Although minor quantitative differences exist, both methods exhibit excellent agreement and show the same temperature dependence across all investigated field intensities. No-

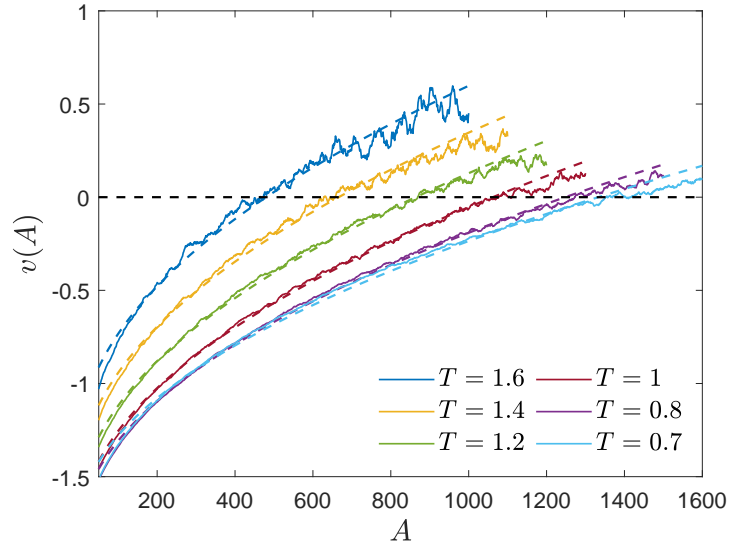


Figure 4.5: Growth velocity of a droplet as a function of its area for different temperatures. A lattice size of  $L = 100$  and an external field of  $h = 0.05$  were used. Solid lines represent simulation data, while dashed lines show the fit to the functional form  $m\sqrt{\lambda} + q$  from Eq. (B.2). The critical cluster size corresponds to the points where the velocity crosses the x-axis. Deviations due to thermal fluctuations (small sizes) and cluster merging (large sizes) are also observed.

tably, the  $\lambda_c$  values estimated using the US methodology are consistently slightly lower than those derived from the growth velocity method.

A further definition for the critical cluster size relies on the concept of the committor. The committor is a property of a configuration and it is defined as the probability that the given configuration will evolve to reach complete reversal. For a configuration with a critical cluster, the committor should be 0.5. We test now this definition and its agreement with previous estimations of the critical cluster size. In particular, for the previously analysed temperatures and field intensity, we prepare  $N_r = 200$  independent configurations in critical conditions (using the maximum in the free energy definition). For each of them, we let the configuration evolve to reach complete shrinkage of the droplets or complete reversal. We repeat the experiment  $N_p = 500$  times and compute the committor as the number of completed reversals divided by  $N_p$ .

The left panel of Fig. 4.7 shows the normalised committor histogram related to the  $N_r$  independent configurations for the case  $T = 1$  and  $h = 0.05$ . As expected, the probability distribution is centred at 0.5 and has a small standard deviation. The standard deviation gives a qualitative indication of the goodness of the assumption that the cluster size is a good reaction coordinate. The right panel of Fig. 4.7 shows the committor as a function of temperature for different field intensities. We can observe a slight deviation from the 0.5 expected value, even though it remains within the error bars of each data point. We

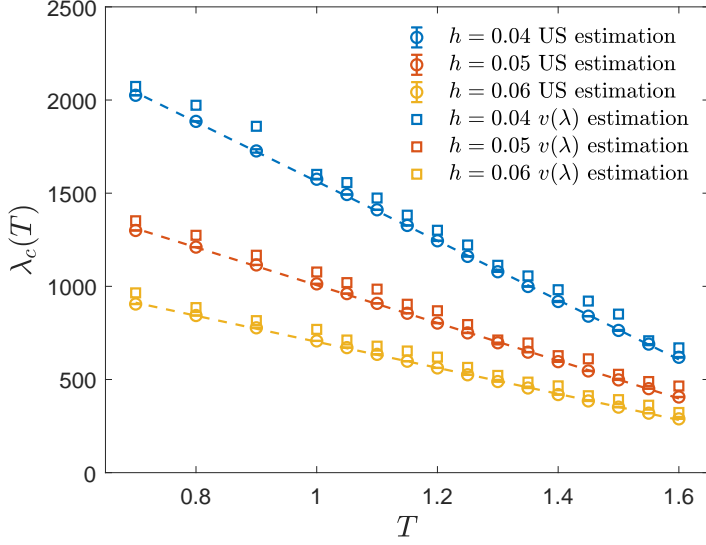


Figure 4.6: Critical cluster size  $\lambda_c$  as a function of temperature for different external field intensities. Circles represent the estimates from the free energy function [Eq. (4.5)], while squares denote the size at which the growth velocity  $v(\lambda)$  becomes zero. Dashed lines correspond to a linear interpolation of  $\lambda_c$  estimated via the US technique.

can say that  $\lambda_c$  is slightly underestimated if we consider the maximum in the free energy. The true value for the critical cluster size is larger, probably coherent with  $\lambda_c$  estimated from the cluster size growth velocity.

**Test 3: Theoretical expression for the diffusion coefficient.** To estimate the nucleation rate from CNT, we need to derive the diffusion coefficient  $D_c$  and the Zeldovich factor. The latter can be derived through direct application of Eq. (4.8) with the free energy given by CNT. For the former, we can use the theoretical expression Eq (4.7) for the attachment rate of particles at the boundary, or Eq (4.12) which measures directly from simulation the evolution of the droplet. The agreement between these two approaches is tested, extending the results presented by Ryu and Cay [87] to different field values and lower temperatures. The results are shown in Fig. 4.8.

The comparison between the theoretical expression (represented by dashed lines) and the simulation results (represented by points) reveals a statistically significant discrepancy. This observation aligns with the findings of Ryu and Cay [87], where the authors noted that an agreement within a factor of two was quite remarkable, given the strong approximation behind Eq. (4.7). Furthermore, for the purpose of estimating the nucleation rate, a discrepancy factor of two has minimal influence. Consequently, in the following analysis, we will rely on the direct estimation of the diffusion coefficient from simulations.

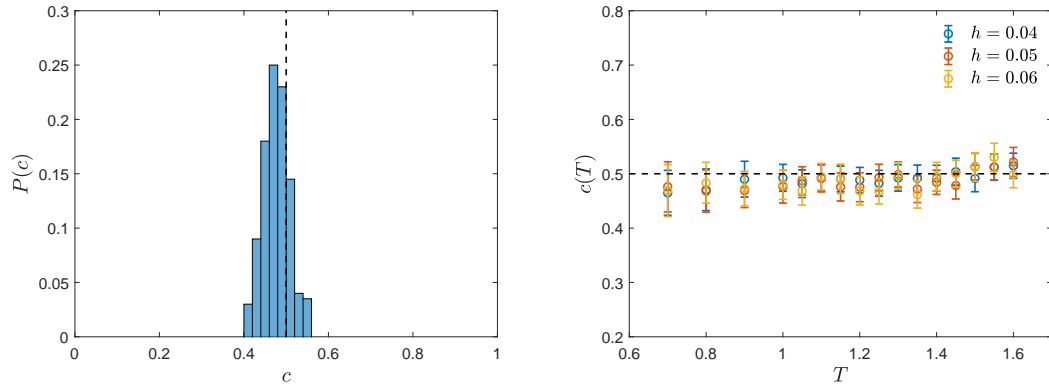


Figure 4.7: Left panel: committor probability distribution for configurations prepared in critical conditions for a system with  $L = 100$ ,  $h = 0.05$  and  $T = 1$ . Right panel: temperature dependence of the expectation value of the committor. The slight deviation from  $\langle c \rangle = 0.5$  can be inputted to a slight underestimation of  $\lambda_c$  if we follow take as a definition the maximum in the free energy function of the cluster size.

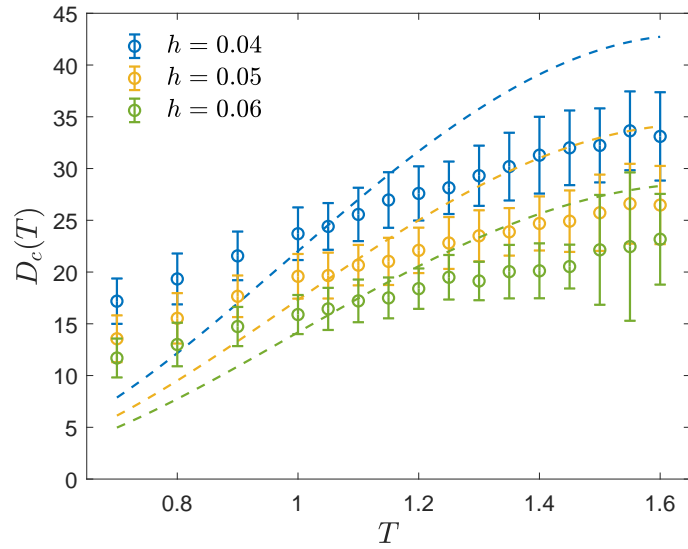


Figure 4.8: Diffusion coefficient estimation as a function of temperature for different choices of the external field. Dashed lines represent the theoretical estimation given by Eq. (4.7) whereas the points represent a direct estimation through Eq. (4.12).

**Test 4: Validation of the nucleation rate expression.** Next, we test the agreement between CNT and simulations in determining the nucleation rate. The upper panel of Fig. 4.9 shows the FFS calculations  $I(\lambda)$  at intermediate stages. For large cluster sizes,  $I(\lambda)$  reaches a plateau, indicating that the simulations have been extended sufficiently to ensure that all simulated trajectories have successfully reached the subsequent interface. The bottom panel of Fig. 4.9 displays the theoretical nucleation rate (represented by dashed lines) along with the simulation results obtained using the FFS technique (represented by dots). Remarkably, the agreement is excellent across all temperatures and field strengths considered, spanning more than 80 orders of magnitude. The validation of CNT at low temperatures is particularly notable, as it extends the analysis previously conducted by Ryu and Cay [87].

#### 4.1.4 Johnson-Mehl-Avrami-Kolmogorov theory

The Johnson-Mehl-Avrami-Kolmogorov (JMAK) was originally developed to describe the kinetics of phase transitions in materials, such as crystallization or the transformation of one solid phase into another [81], [98]–[100]. It is employed to describe real physical processes such as crystallisation kinetics in amorphous alloys [101], [102], amorphization and recrystallisation [103], [104], domain switching in ferroelectric [105] and ferromagnets [106] just to name a few.

Broadly speaking, JMAK theory models how the fraction of a transformed material evolves over time. We can write

$$X(t) = 1 - \exp(-Kt^n) \quad (4.13)$$

where  $K$  is the effective rate and  $n$  is the Avrami exponent. The exponent can vary depending on the nature of the process and the system dimensions. In general  $n = d + \gamma$ , where  $d$  accounts for the system dimensionality and  $\gamma = 0, 1$  depending on the condition. Following Kolmogorov classification, when the nucleation happens with uniform probability over all the lattice,  $\gamma = 1$  and the system is said  $\alpha$  model; when instead the nucleation proceeds from pre-existing nuclei (as in the case of heterogeneous nucleation),  $\gamma = 0$  and the system is called  $\beta$  model [107].

As mentioned above, it is built on the assumption that phase transitions occur through nucleation, subsequent growth and coalescence of transformed material and applies to the MD regime of reversal processes. In mathematical terms, the theory provides an expression for the transformed fraction  $X$  of volume in the stable phase as a function of time, incorporating parameters such as nucleation rate  $I$  and the cluster growth velocity  $v$

$$X(t) = 1 - \exp\left(-\frac{\Omega_d I v^d t^{d+1}}{d+1}\right) \quad (4.14)$$

Appendix B presents a simple derivation of the presented expression.

Avrami's law can be further generalized to account for time-dependent nucleation rates [108] and growth processes dependent on droplet size [109]. However, Avrami's law is only applicable under specific conditions. First, it is valid solely within the MD

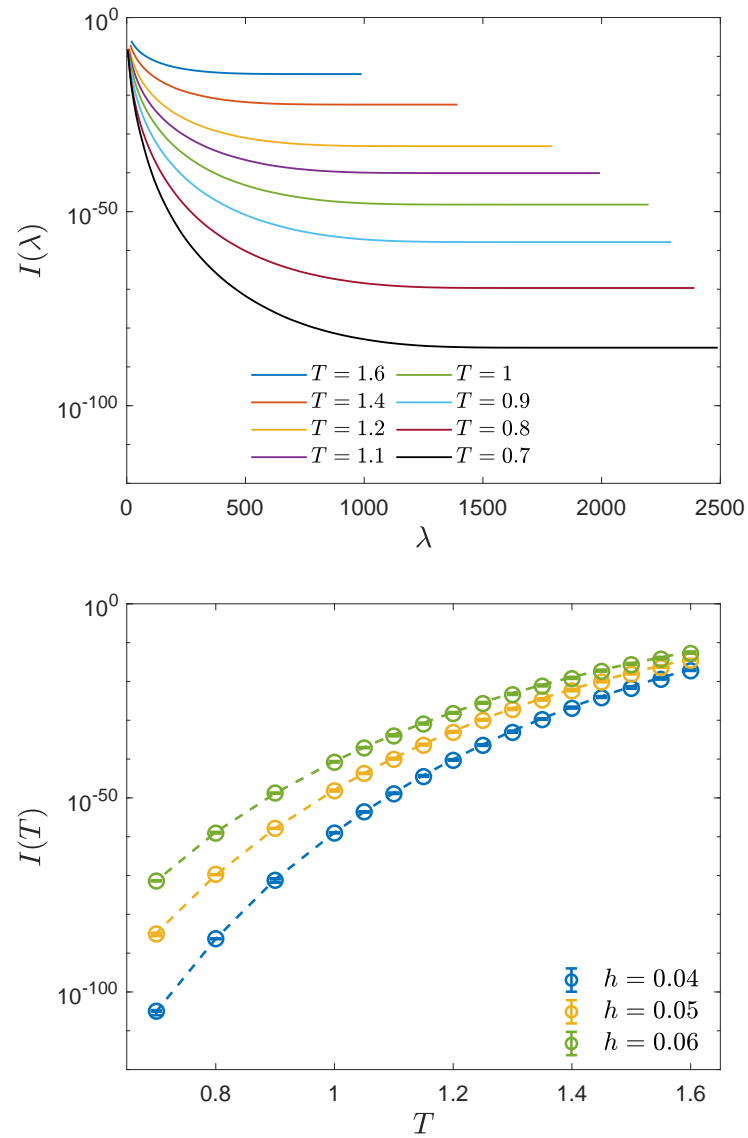


Figure 4.9: Top panel: FFS calculation for the nucleation rate to form a cluster of size  $\lambda$  at different temperatures for  $h = 0.05$ . Bottom panel: Nucleation rate estimation from simulations using the FFS technique for different temperatures and field strengths, for a system with  $L = 100$ . The dashed lines represent the theoretical CNT predictions. Excellent agreement is observed.

regime, where phase reversal occurs through the nucleation and simultaneous growth of multiple droplets. Second, since the nucleation process is treated in a coarse-grained manner, the theoretical predictions are reliable only at length scales significantly larger than the critical droplet radius  $R_c$ . Lastly, Avrami's law neglects droplet merging, which reduces interfacial tension. Consequently, deviations from this law are expected at both small and large time scales.

**Validation of Avrami's law** By following a key work by Ramos et al. [110], we can analyse the regime of validity of Avrami's expression. We follow a system's magnetisation  $m(t)$  during a simple reversal process. The system is prepared in equilibrium with a positive external field  $+h$ . At  $t = 0$ , the external field is reversed in sign and the magnetisation is recorded.

The magnetisation is linked to the fraction of converted material (in stable phase) through

$$m(t) \approx [m_{ms} - m_s]X(t) + m_s \quad (4.15)$$

where  $m_{ms}$  is the magnetisation in the metastable configuration and  $m_s$  is the magnetisation in the stable configuration. Moreover, the relaxation function  $\psi(t)$  of the reversal process follows

$$m(t) \approx [m(0) - m_s]\psi(t) + m_s \quad (4.16)$$

where  $m(0)$  is the magnetisation in the initial configuration. Therefore:

$$\psi(t) = \frac{m_{ms} - m_s}{m(0) - m_s} X(t) \quad (4.17)$$

We take  $m_s$  as the average value after the reversal. To validate Avrami's law, we perform a linear fit  $\log[\psi(t)] \sim \log(a) + bt^{d+1}$ , with  $d = 2$ . The coefficient  $a$  yields the value of the metastable magnetisation and  $b$  yields information regarding the out-of-equilibrium properties of the system. Specifically

$$a = \frac{m_{ms} - m_s}{m(0) - m_s} \quad (4.18)$$

and

$$b = \frac{\Omega_2 I v^2}{3} \quad (4.19)$$

The results of the analysis are presented in Fig. 4.10 for the specific case of  $h = 0.4$ . The comprehensive analysis encompasses temperatures in the range  $1.5 < T < 1.95$  and external fields in the range  $0.15 < h < 0.8$ . For each simulation, 200 reversal events are recorded, with magnetization values sampled at intervals of  $\Delta t = 0.1$ . The metastable lifetime  $\tau$  is determined at the crossing point where  $m = 0$ .

To ensure the system operates within the MD regime, the conditions  $h < h_{\text{MFSP}} = T/m_{\text{eq}}(T)$  and  $r = \sigma_\tau/\bar{\tau} < 0.5$  are imposed. Here,  $h_{\text{MFSP}}$  denotes the mean-field spinodal field,  $\sigma_\tau$  represents the standard deviation of the metastable lifetime, and  $\bar{\tau}$  is its mean. These criteria effectively exclude the SD and SF regimes. For all datasets, the goodness

of fit is assessed using the  $\chi^2$  statistic. A high  $p$ -value ( $p_\alpha > 0.05$ ) confirms the reliability of the linear fit and supports the consistency of the theoretical model with the simulation results.

To enhance clarity, each data series in Fig. 4.10 is vertically shifted by a constant value  $k$  along the  $y$ -axis. The fitting procedure is restricted to a specific temporal range to minimize the influence of droplet merging. Specifically, the fit is performed for time scales  $t < \tau$ , ensuring that the analysis captures the dynamics prior to significant droplet interactions. The figure also displays  $X(t)$  for  $t < 2\tau$ , allowing for a clear visualization of deviations from Avrami's law at extended time scales.

To exclude the initial transient phase, which accounts for droplet formation and the adaptation to the metastable state, the lower bound of the fitting interval,  $t_{\min}$ , is determined by optimizing the fitting parameters. This involves identifying the time point where the parameter  $a(t_{\min})$  reaches its minimum and the parameter  $b(t_{\min})$  reaches its maximum.

Across all investigated cases, excellent agreement is observed between the theoretical expression given by Eq. (4.14) and the simulation data. Deviations from the theoretical predictions become evident at longer times ( $t > \tau$ ), with these deviations becoming increasingly pronounced as the temperature decreases and the regime transitions from MD to SD dynamics.

#### 4.1.5 Metastable lifetime and spinodal line

The analysis of the metastable lifetime provides essential insights into the properties of the system. Empirically, the metastable lifetime is determined by recording the crossing of the  $m = 0$  threshold following external field quenching and subsequent magnetization reversal. Theoretical expressions for the metastable lifetime can be derived, depending on whether the system operates in the SD or MD regime.

In the SD regime, magnetization reversal is primarily driven by the nucleation of a critical droplet. The dominant timescale in this process is the formation of the critical droplet, as its subsequent growth occurs on a much shorter timescale. Consequently, the metastable lifetime is proportional to the inverse of the nucleation rate. Using Eq. (4.6), this yields:

$$\tau_{SD} \propto I^{-1} \propto \exp\left(\frac{\Delta F_c}{k_B T}\right). \quad (4.20)$$

In the MD regime, nucleation occurs rapidly, and the simultaneous growth of multiple droplets dominates the reversal process. The reversal time can be approximated by the average time  $t_0$  required for two droplets to coalesce. Let  $R_0$  denote the average separation between droplets. Two conditions are imposed:  $R_0 = v_0 t_0$ , where  $v_0$  is the radial velocity derived from Eq. (B.1), and  $I = (R_0^d t_0)^{-1}$ , following the definition of the nucleation rate. Solving these equations gives:

$$\tau_{MD} \approx t_0 = v_0^{-d/(d+1)} I^{-1/(d+1)} \propto R_c^{d/(d-1)} \exp\left(\frac{\Delta F_c}{(d+1)k_B T}\right). \quad (4.21)$$

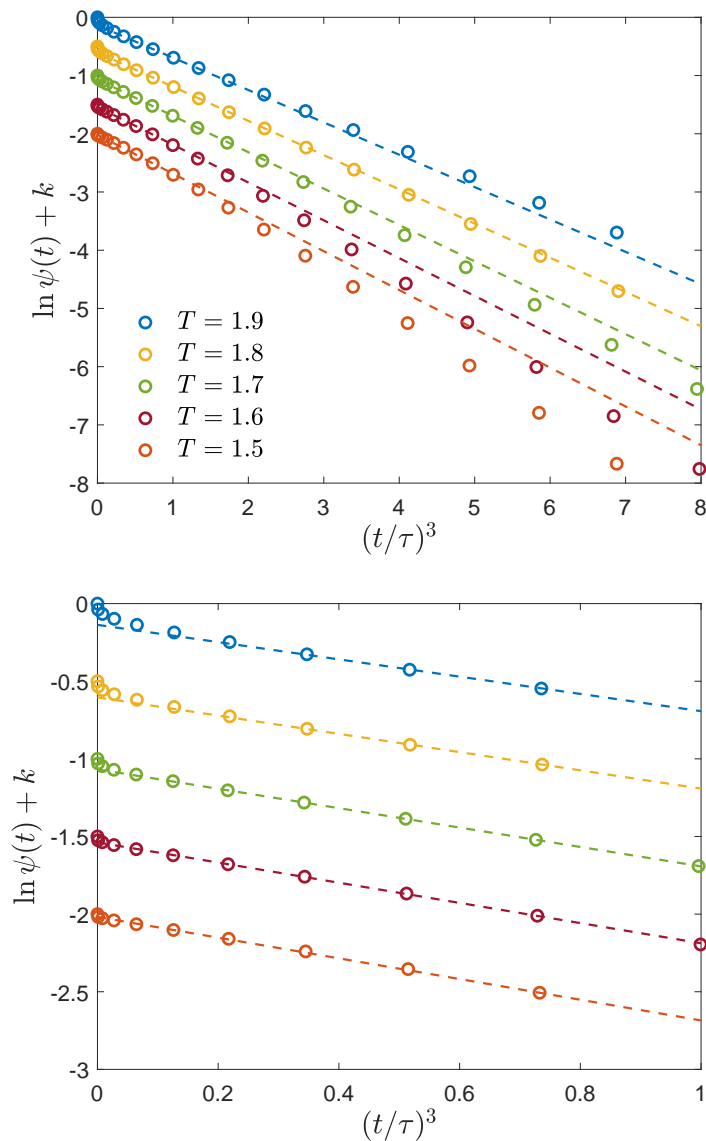


Figure 4.10: Relaxation of the Ising model described by the function  $\psi(t)$  as a function of scaled time  $t/\tau$ . Markers represent simulation data, while dashed lines correspond to the theoretical expression. Each data series is shifted vertically by a constant value  $k$  for clarity. The data correspond to different temperatures and the case  $h = 0.4$ . The theoretical fit is performed over the range  $t_{\min} < t < \tau$ , where  $t_{\min}$  is selected based on the optimization of fitting parameters. The top panel highlights the fitting range, while the bottom panel extends the time scale to  $2\tau$  to illustrate deviations from the fitted straight line.

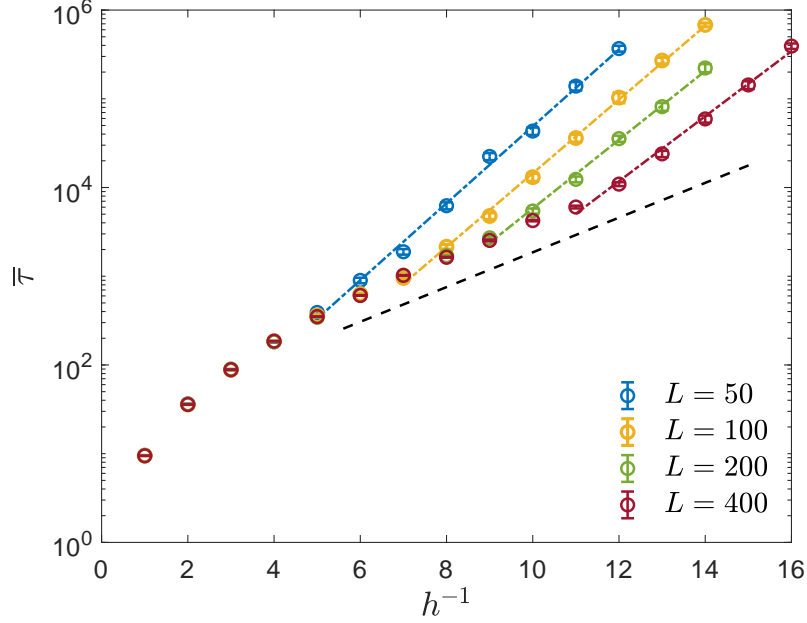


Figure 4.11: Metastable lifetime as a function of the inverse of the external field for a homogeneous system at different system sizes. The temperature is fixed at  $T = 1.7$ . The procedure follows Sides et al. [82].

The distinction between the SD and MD regimes is evident in simulations, particularly in the field dependence of the metastable lifetime. The dominant term in the free energy barrier,  $\Delta F_c$ , is inversely proportional to the external field  $h$ , neglecting weaker logarithmic corrections. Substituting Eq. (4.5) into Eq. (4.1) yields a linear dependence of  $\ln \bar{\tau}$  on  $h^{-1}$ . A change in the slope marks the transition from the MD to SD regime, as shown in Fig. 4.11. Here, the metastable lifetime is determined by the time at which the system's magnetization reverses sign under the influence of an external field.

The metastable lifetime serves as a discriminator between SD and MD regimes. The angular coefficient variation of the linear fit  $\ln \bar{\tau} \sim h^{-1}$  identifies the dynamic spinodal point ( $h_{\text{DSP}}$ ). Alternatively, a more robust method involves analyzing the ratio  $r = \sigma_\tau / \bar{\tau}$ . If  $r < 0.5$ , the system is in the MD regime; otherwise, the process is Poissonian, corresponding to the SD regime. The threshold value 0.5 follows the work of Sides et al. [82]. This method enables determining  $h_{\text{DSP}}$  for varying system sizes.

The transition between SD and MD regimes can also be induced by changing the system size  $L$ . The crossover occurs when  $L$  is proportional to the average droplet separation,  $R_0 = v_0 t_0 = v_0^{d+1} I^{-1/(d+1)}$ . In the limit  $h \rightarrow 0$ , neglecting the weak dependence of  $v_0$  on  $h$  through  $R_c$ , we obtain:

$$L \propto I^{-1/(d+1)} \propto \exp\left(-\frac{\Delta F_c}{(d+1)k_B T}\right). \quad (4.22)$$

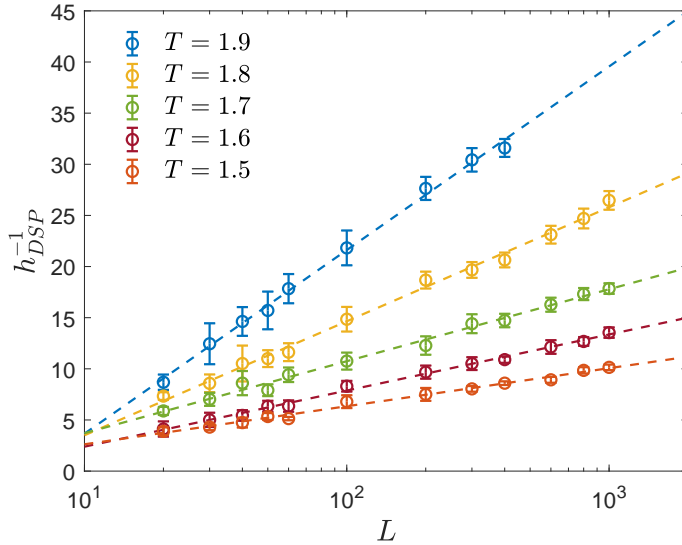


Figure 4.12: Dynamic spinodal line for a homogeneous system as a function of system size (logarithmic scale). The SD regime occurs above the line and the MD regime below it. Lowering the temperature expands the SD regime. A linear fit shows excellent agreement between simulation data and the theoretical prediction in Eq. (4.23). The analysis follows Sides et al. [82].

From Eqs. (4.1) and (4.5), generalized for any dimension  $d$ , the free energy barrier can be expressed as  $\Delta F_c = ah^{-(d-1)} + b \log(h)$ , where  $a$  and  $b$  are constants. Neglecting the weaker logarithmic dependence, we derive:

$$h_{\text{DSP}} \sim (\ln L)^{-1/(d-1)}. \quad (4.23)$$

This theoretical prediction is confirmed by an alternative approach based on expanding the free energy curve beyond the coexistence curve ( $h = 0$ ) and associating the imaginary part of the free energy with the nucleation rate [111].

Simulation results in two dimensions and the fit to Eq. (4.23) are shown in Fig. 4.12, for different temperatures. Simulations and theoretical predictions show good agreement, with the system size dependency aligning well with the derived expression for the dynamic spinodal point. Interestingly, the temperature influences the reversal regime. As the temperature is lowered, the SD region expands, thus, favouring a stochastic reversal process.

## 4.2 Reversal process in heterogeneous systems

Let's now consider the reversal process in a different environment. We turn our attention to heterogeneous systems, in particular to the model introduced in section 2.3.3

and whose thermodynamic properties have been analysed in Chapter 3. The model incorporates impurities/defects, modelled as fixed spins. In out-of-equilibrium processes, especially in magnetisation reversals, defects seed the nucleation and can significantly increase the temporal responsiveness of the system. We now characterise these effects and modify accordingly the theoretical expressions. The results presented here build upon and adapt original findings, also reported in [51].

### 4.2.1 CNT in the model with defects

As discussed in Chapter 3, the equilibrium configuration of the two-dimensional Ising model with defects exhibits clustering behaviour in the thermodynamic limit. When an external magnetic field is applied, the equilibrium configuration undergoes a transformation. In the thermodynamic limit, a non-zero external field ( $h \neq 0$ ) induces spontaneous magnetization, as the bulk term in the free energy,  $F_{\text{bulk}} = -hm$ , reduces the total free energy. This result is expected to hold even for finite system sizes  $L$ , although finite-size effects may significantly influence the stability of the magnetized configuration, particularly for small systems.

The presence of defects introduces substantial challenges to the magnetization reversal process. Specifically, three primary differences emerge when compared to the homogeneous case:

1. The metastable states induced by defects impede the reversal process. Defects encountered by the cluster during growth may cause pinning, rendering the free energy landscape more rugged, with multiple local minima.
2. The stable configuration of the system may correspond to either a magnetized state or a clustered state, depending on factors such as lattice size, external field strength, defect fraction, and temperature.
3. In addition to the external field acting as a driving force for the reversal process, the inherent randomness contributes to escape from the initial metastable state.

Regardless of whether the stable configuration is magnetized or clustered, the initial magnetised state of the system is metastable. Consequently, the framework of CNT can be adapted to describe the reversal process in heterogeneous systems. In the following, we generalize CNT and validate the free energy expression through simulations employing the US technique. Additionally, we test the nucleation rate formula using simulations based on the FFS method.

As outlined in Section 4.1.2, the generalization of CNT for the model with defects begins with the free energy balance required to form a droplet of area  $\lambda$ . In this model, random spins with fixed orientations induce modifications to both the surface and bulk terms of the free energy. Here,  $\lambda$  represents the total area of the droplet, including defects. The quantities  $n^+$  and  $n^-$  denote the number of positive and negative defects within the droplet, respectively.

Without loss of generality, let us consider the reversal process which produces droplets of negative spins. The surface term becomes

$$\Delta F_{\text{surf}} = 2\sigma_{\text{eff}}\sqrt{\pi\lambda} + 4\sigma_{\text{eff}}n^+ - 4\sigma_{\text{eff}}n^- \quad (4.24)$$

The first term is the same observed for homogeneous systems. The second term accounts for an extra perimeter surrounding positive defects after the droplet's nucleation. The third term is an energetic gain related to negative defects that share the orientation with the surroundings after the droplet's nucleation. The bulk term reads

$$\Delta F_{\text{bulk}} = -2h[\lambda - (n^+ + n^-)] \quad (4.25)$$

Here only the free spins are considered in the energy balance. We assume the Langer correction term is unaffected by the presence of defects, which proved to be correct for neutral defects (vacancies) [96]. Finally, the free energy balance for the formation of a droplet is

$$\Delta F_{\text{CNT}}(\lambda) = 2\sigma_{\text{eff}}\sqrt{\pi\lambda} + 4\sigma_{\text{eff}}(n^+ - n^-) - 2h[\lambda - (n^+ + n^-)] + \frac{5}{4}k_B T \log(\lambda) \quad (4.26)$$

Following [51], we now introduce two quantities:

1. The fraction of defects contained in a droplet  $\nu$ . Since the defect distribution is uniform, we expect  $\nu(f) \approx f$  for large droplets. Small droplets will have, instead,  $\nu(f) > f$  since they will nucleate with higher probability in areas with a strong unbalance of defects aligned with the external field.
2. The relative defect unbalance  $\mu = (n^- - n^+)/ (n^+ + n^-)$ . Also in this case we expect a different behaviour for large and small droplets. In particular,  $\mu \approx 1$  for small droplets, and  $\mu \approx 0$  for large droplets (balanced condition).

A discussion and a derivation of the optimal values of  $\nu$  and  $\mu$  is presented in Appendix C. With these definitions, Eq. (4.26) becomes:

$$\Delta F_{\text{CNT}}(\lambda) = 2\sigma_{\text{eff}}\sqrt{\pi\lambda} - 4\sigma_{\text{eff}}\lambda\mu\nu - 2h\lambda(1 - \nu) + \frac{5}{4}k_B T \log(\lambda) \quad (4.27)$$

Iterating the same procedure used for the homogeneous system, we obtain the expression of the critical cluster size

$$\lambda_c = \left( \frac{\sigma_{\text{eff}}\sqrt{\pi} + \sqrt{\sigma_{\text{eff}}^2\pi + 5k_B T[4\sigma_{\text{eff}}\mu\nu + 2h(1 - \nu)]}}{8\sigma_{\text{eff}}\mu\nu + 4h(1 - \nu)} \right)^2 \quad (4.28)$$

The free energy barrier can be rewritten as

$$\Delta F_{\text{CNT}}(\lambda_c) = \frac{5}{4}k_B T[\log(\lambda_c) - 2] + \sigma_{\text{eff}}\sqrt{\pi}\sqrt{\lambda_c} \quad (4.29)$$

We can now make an important observation. The critical radius does not diverge to infinity when the external field goes to zero, as it happens for the defect-free case. One can calculate the  $h = 0$  limit for the critical radius

$$\lambda_c^{h=0} = \left( \frac{\sqrt{\pi} + \sqrt{\pi + 20k_B T \nu \mu / \sigma_{\text{eff}}}}{8\mu\nu} \right)^2 \quad (4.30)$$

which depends on the relative defect unbalance  $\nu\mu$  inside the droplet and the surface tension  $\sigma_{\text{eff}}$ . Even without a field, the system will eventually develop a critical cluster through thermal fluctuations and spontaneously demagnetise. This is peculiar and in total agreement with the Imry-Ma argument [36] discussed previously in Section 2.3.2.

#### 4.2.2 Validation of CNT in the model with defects

We proceed with the analysis by testing the CNT free energy predictions for the model with defects. A system of size  $L = 100$  is considered, with defect fractions  $f = 0.01$ ,  $0.02$ , and  $0.03$  at various temperatures. The first case is particularly noteworthy: at low temperatures and in the absence of an external field, the equilibrium configuration corresponds to the magnetized state, as shown in Fig. 3.4. In this scenario, the driving force for the system to escape its initial metastable state is predominantly the external field. Conversely, at high temperatures, the magnetized configuration becomes metastable even in the absence of a field, and we anticipate that both the external field and randomness jointly contribute to the reversal process.

#### Free energy function

To account for randomness variability, we performed simulations considering multiple realisations of defect distributions. Specifically, 40 replicas were analysed, each with defects randomly positioned on the lattice. As initially anticipated, the free energy (determined via the US technique) becomes increasingly rugged as the temperature is lowered or the defect fraction is increased. However, by averaging over multiple replicas and tracking many droplets within the system, an overall smoothening of the free energy landscape is observed. Clear predictions of the surface tension and the free energy barrier can be derived.

The free energy expression given in Eq. (4.27) is tested by fitting the free energy estimation. the surface tension  $\sigma_{\text{eff}}$  is treated as a fitting parameter to identify deviations from the theoretical expression for the homogeneous system.  $\nu$  and  $\nu\mu$  are assumed independent from the cluster size as suggested in the analysis presented in Appendix C. The values used for these quantities are calculated according to the derivation in Appendix C and are reported in Tab. 4.1 for different defect fractions. The fits are displayed in Fig. 4.13. Panel a) depicts the free energy as a function of cluster size  $\lambda$  for  $f = 0.01$ . Solid lines correspond to simulation results using the US technique, while dashed lines represent fits based on the free energy expression. Panel b) illustrates the surface tension as a function of temperature for various defect fractions. For comparison,

	$f = 0.01$	$f = 0.02$	$f = 0.03$
$\nu$	0.015	0.026	0.036
$\nu\mu$	0.012	0.018	0.021

Table 4.1: Table showing the cluster parameters used for the critical cluster size derivation in Eq. 4.28.

the black dashed line represents the homogeneous surface tension predicted by Eq. (4.4). Notably, for higher defect fraction,  $\sigma_{\text{eff}}$  reaches a constant value at high temperatures. Panel c) shows the ratio between the free energy barrier at critical cluster size and the temperature. As the fraction of defects increases, the free energy barrier lowers. This is a clear indication that the presence of defects reduces the energetic cost associated with the reversal process.

The free energy fit demonstrates remarkable accuracy across all considered temperatures and defect fractions, confirming the versatility of the CNT framework in describing the escape from the initial metastable state. The rugged free energy landscape, expected at the level of individual replicas, is effectively mitigated by averaging over multiple realizations and droplets, thereby enabling smooth and reliable predictions. Examination of single-replica free energy landscapes reveals the presence of potential wells and pinning effects during the evolution path of a single cluster. As we will see, these effects will play a pivotal role in the analysis of Barkhausen noise in Chapter 6.

The effective surface tension,  $\sigma_{\text{eff}}$ , exhibits a marked dependence on the presence of defects. Across all temperatures and defect concentrations,  $\sigma_{\text{eff}}$  is consistently reduced compared to the defect-free system. This reduction arises from the effect of defects aligned with the external field. Indeed, the energetic cost associated with the cluster boundary lowers as these defects are incorporated into the growing droplet.

A clear dichotomy emerges between two defect types:

- Attracting defects: Defects aligned with the external field are readily incorporated into the growing droplet, aiding the reversal process.
- Pinning defects: Defects misaligned with the external field hinder droplet growth by roughening the free energy surface and inducing metastable states.

Among these, attracting defects play a dominant role, as evidenced by the pronounced reduction in surface tension with increasing defect fraction  $f$ . This behaviour aligns with the framework developed in Appendix C in which reversal occurs through the nucleation and growth of a single droplet within the most favourable environment, characterized by a high density of defects aligned with the external field. Such conditions not only enhance  $\Delta n$  but also promote a rapid evolution pathway due to the elevated concentration of attracting defects near the growing cluster.

While this qualitative explanation aligns with the observed trends, direct visualization of these effects remains elusive. Support for the role of pinning defects in the

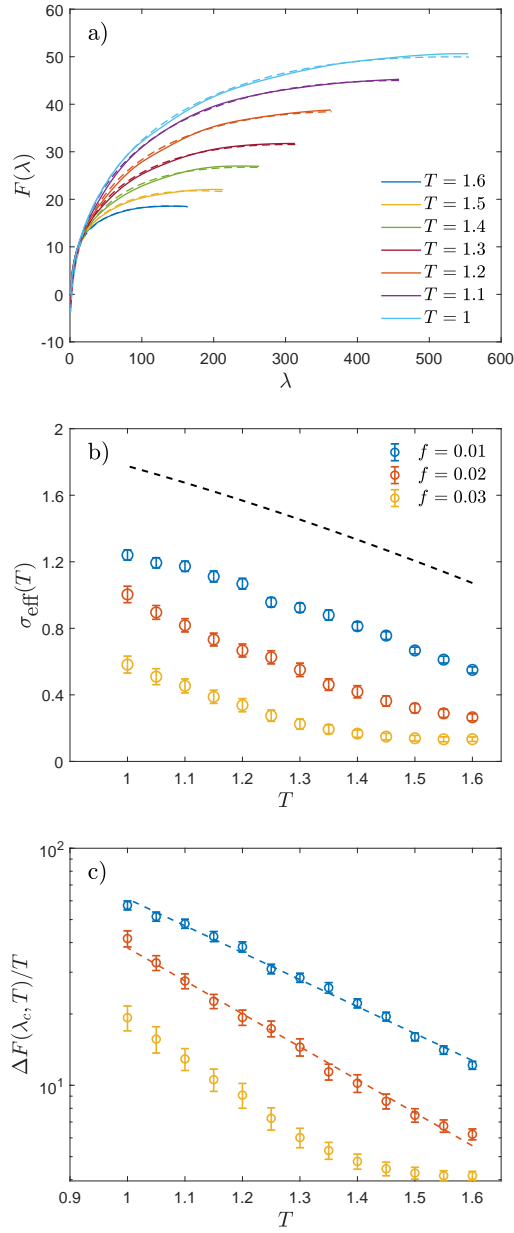


Figure 4.13: Panel a): Free energy as a function of cluster size  $\lambda$  for a system with defect fraction  $f = 0.01$ . Solid lines correspond to simulation results using the US technique, and dashed lines represent fits based on the theoretical free energy expression. Panel b): Surface tension as a function of temperature for defect fractions  $f = 0.01$ ,  $0.02$ , and  $0.03$ . The black dashed line indicates the homogeneous surface tension given by Eq. (4.4). Panel c): Free energy barrier as a function of temperature for different defect fractions. The dashed lines represent a linear interpolation for  $\log(\Delta F(\lambda_c)/T)$  as a function of  $T$ .

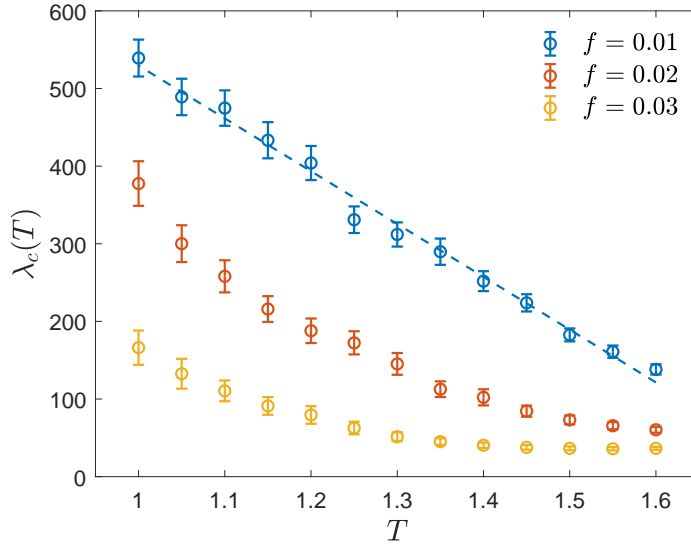


Figure 4.14: Critical cluster size as a function of temperature for different defect fractions obtained from the free energy fit. The dashed line represents a linear interpolation for the case  $f = 0.01$ . For higher defect fractions,  $\lambda_c(T)$  becomes constant at high temperatures.

reversal process will be further substantiated through the analysis of Barkhausen noise in Chapter 6.

From the fit of the free energy expression, an estimate for the critical cluster size,  $\lambda_c$ , can be obtained, as illustrated in Fig. 4.14. Notably, at high temperatures and higher defect fractions,  $\lambda_c(T)$  becomes constant. This behaviour indicates that temperature ceases to significantly influence the initiation of magnetization reversal. The presence of defects lowers the critical cluster size, making it small enough that even minor thermal fluctuations can trigger reversal events. In this case, the only relevant parameter is the defect fraction.

### Cluster growth velocity

To complement the analysis, we investigate the cluster growth velocity  $v(\lambda)$ , as described in Section 4.1.2. We fix  $f = 0.01$  and analyse  $N_r = 100$  distinct realizations of defects, each with a different spatial distribution. Starting from the magnetized state, we follow the evolution of the largest droplet under the influence of an external field  $h = 0.05$ , using the methodology established for the homogeneous case. This analysis is repeated for each replica, and the results are averaged to mitigate the effects of the disorder.

The average cluster growth velocity is presented in Fig. 4.15 for the system with  $f = 0.01$  at various temperatures. At high temperatures, the functional form  $v(\lambda) = m\sqrt{\lambda} + q$ , derived in Eq. (B.2), fits the data well, and a clear intersection with the  $\lambda$ -axis is observed, allowing for the determination of  $\lambda_c$ . However, as temperature decreases,

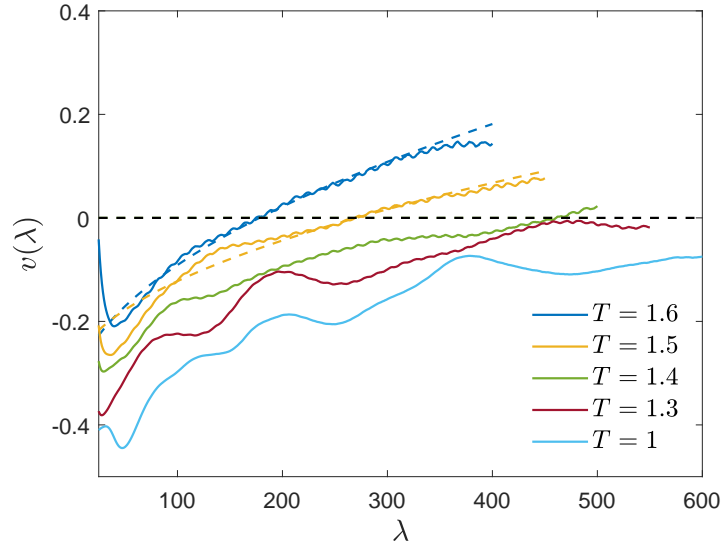


Figure 4.15: Growth velocity of a droplet as a function of its area  $\lambda$  for a system with defects ( $f = 0.01$ ) at different temperatures. A lattice of size  $L = 100$  and an external field  $h = 0.05$  were considered. Solid lines represent simulation data, while dashed lines correspond to fits of the functional form  $v(\lambda) = m\sqrt{\lambda} + q$ , as described in Eq. (B.2). The fit is accurate at high temperatures but deteriorates as temperature decreases. Where applicable, the crossing points with the  $\lambda$ -axis indicate the critical cluster sizes, compatible with the ones reported in Fig. 4.14.

$v(\lambda)$  becomes increasingly rugged, with the velocity often remaining negative and failing to intersect the  $\lambda$ -axis. Consequently, no critical cluster size can be determined from this method at low temperatures.

This behaviour aligns with the earlier analysis of the free energy landscape. The interplay between attracting and pinning defects profoundly influences cluster dynamics. As the droplet grows, it encounters a sequence of potential wells. Attractive defects accelerate growth ( $v(\lambda) > 0$ ), while pinning defects hinder expansion ( $v(\lambda) < 0$ ), resulting in multiple crossings of the  $\lambda$ -axis. This effect becomes more pronounced at lower temperatures, where potential wells in the free energy landscape are more effective at trapping the system during evolution.

The methodology proposed for estimating the critical cluster size by analyzing the cluster growth velocity is found to be effective under conditions of high external fields and elevated temperatures. For instance, in [51], the system was analysed at  $T = 1.8$  and  $h = 0.1$ , and the growth velocity for a system containing defects was observed to exhibit behaviour analogous to that of a homogeneous system. Under these conditions, the crossing point of  $v(\lambda)$  can be determined with high precision, enabling an accurate estimation of  $\lambda_c$ .

### Nucleation rate estimation

Finally, we assess the validity of the nucleation rate formula proposed by Classical Nucleation Theory (CNT) in the presence of defects. For clarity, we rewrite the expression:

$$I_{\text{CNT}} = D_c \Gamma \exp\left(-\frac{\Delta F_c}{k_B T}\right), \quad (4.31)$$

where  $D_c$  indirectly depends on the defect fraction  $f$  through the critical cluster size,  $\lambda_c$ . As previously discussed, defects reduce  $\lambda_c$ , thereby altering  $D_c$ . Additionally, a configuration-specific critical cluster size is often encountered, leading to a diffusion coefficient  $D_c$  that depends not only on  $f$  but also on the specific defect configuration. Determining  $D_c$  for each defect realization is computationally demanding.

To mitigate this challenge, we approximate  $D_c(f)$  by assuming  $D_c(f) \approx D_c(f=0)$ . This simplification significantly reduces computational costs while introducing only a minor deviation in the results. The nucleation rate is primarily governed by the exponential term  $\exp(-\Delta F_c/k_B T)$ , which varies over several orders of magnitude, whereas  $D_c$  typically fluctuates within a single order of magnitude. Hence, the approximation has a negligible effect on the final calculation.

The free energy barrier  $\Delta F_c$  is extracted from the free energy fit obtained via US calculations. Simultaneously, a direct estimation of the nucleation rate is performed using the FFS technique, considering  $N_r = 100$  realizations of defects.

An important methodological aspect requires attention. When calculating the total nucleation rate  $I_{\text{FFS}}$  using the FFS procedure, the transition probability  $P(n)$ , representing the likelihood of a cluster transitioning from size  $\lambda = \lambda_n$  to  $\lambda = \lambda_{n+1}$ , is averaged across all  $N_r$  replicas. This modifies Eq. (4.11) to:

$$I_{\text{FFS},1} = \overline{\phi_1 \prod_i P(i)}, \quad (4.32)$$

where  $\overline{\phantom{x}}$  denotes the average over defect realizations. Alternatively, one could compute  $I_{\text{FFS}}$  for each defect realization and then average the results over the defect configurations. We denote this second alternative definition with  $I_{\text{FFS},2}$ .

In Fig. 4.16, nucleation rates as a function of cluster size are shown for all  $N_r$  replicas (in grey), alongside  $I_{\text{FFS},1}$  (in blue) and  $I_{\text{FFS},2}$  (in orange). The second methodology,  $I_{\text{FFS},2}$ , fails to provide a representative value for a randomly sampled distribution. While mathematically valid, this approach has a significant practical limitation: only a subset of replicas contributes meaningfully to the average. Nucleation rates computed for individual replicas span several orders of magnitude, with the arithmetic average disproportionately weighted by the highest nucleation rates.

The top panel of Fig. 4.17 shows  $I_{\text{FFS},1}(\lambda)$  as a function of cluster size for different temperatures in the case of  $f = 0.01$ . Similar trends are observed for other defect fractions. The asymptotic value reached for large cluster sizes confirms the reliability of the FFS technique for nucleation rate measurements in the model with defects.

The bottom panel of Fig. 4.17 presents the nucleation rate as a function of temperature for various defect fractions at  $h = 0.05$ . Circles represent results from the FFS

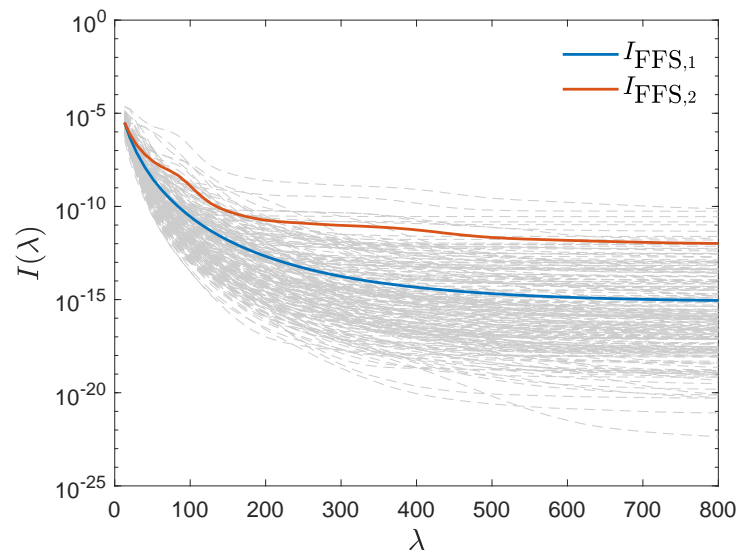


Figure 4.16: Nucleation rates as a function of cluster size  $\lambda$  for  $N_r = 100$  defect replicas. Grey lines represent individual replica calculations, showing a wide distribution across several orders of magnitude.  $I_{\text{FFS},1}$  (blue line) represents the nucleation rate obtained by averaging transition probabilities across replicas, while  $I_{\text{FFS},2}$  (orange line) corresponds to the nucleation rate derived from averaging individual replica results. The figure highlights the limitations of  $I_{\text{FFS},2}$  in accurately representing the ensemble behaviour.

technique, obtained by averaging over  $N_r = 100$  defect realizations, while dashed lines correspond to indirect estimates using Eq. (4.31) combined with free energy barriers from US calculations. The agreement between theoretical predictions and FFS results is particularly striking for  $f = 0.01$ , supporting the validity of CNT in describing the magnetization reversal process. This result emphasizes that the primary bottleneck for reversal is the nucleation of the initial critical droplet, as predicted by CNT. By accurately sampling the free energy barrier, CNT provides a reliable estimate of the nucleation rate.

At higher defect fractions ( $f = 0.02$  and  $f = 0.03$ ) and elevated temperatures, deviations between CNT predictions and FFS results can be observed. These discrepancies can be attributed to a transition from SD to MD reversal regimes, as defects facilitate simultaneous nucleation and coalescence of multiple droplets. In such cases, one of the main assumptions behind CNT (droplet growth and shrinkage through sequential addition or removal of single spins) is no longer satisfied and CNT cannot provide reliable estimations. Supporting this interpretation, the agreement between CNT and FFS results is recovered at lower temperatures, where the single-droplet regime dominates for all defect fractions.

### 4.2.3 JMAK theory in heterogeneous systems

We now consider the applicability of the JMAK theory to the Ising model with defects. For clarity, we first recall the JMAK equation, which describes the fraction of transformed material  $X(t)$  as a function of time  $t$ :

$$X(t) = 1 - \exp(-Kt^n) \quad (4.33)$$

Here,  $K$  is a rate constant, and  $n$  is the Avrami exponent that characterizes the nucleation and growth kinetics.

For the two-dimensional homogeneous Ising model, we have verified that the Avrami exponent is  $n = 3$ , as expected for all two-dimensional  $\alpha$  systems. By contrast, in heterogeneous systems ( $\beta$  systems), the Avrami exponent is theoretically expected to change to  $n = 2$  [107], owing to heterogeneity and fast nucleating droplets.

To evaluate the applicability of the Avrami expression to the Ising model with defects, we determine the best-fitting Avrami exponent by analysing the simulation data. We considered the same framework used for the homogeneous case presented in Section 4.1.4. The results are presented in Fig. 4.18 for the case of  $h = 0.4$ , for a system of size  $L = 100$  and defects fraction  $f = 0.02$ . Other fields and temperatures were analysed, obtaining similar results. The top panel considers the case  $n = 2$ , while the bottom panel examines  $n = 3$ . Surprisingly, the fit for  $n = 3$  provides a better linear relationship based on the  $\chi^2$  goodness-of-fit test. By comparing these results with the homogeneous case shown in Fig. 4.10, we observe that the data series exhibit striking similarities. We conclude that defects solely do not act as critical droplets initiating the reversal process.

At low temperatures and field amplitudes, the presence of defects primarily reduces the metastable lifetime and accelerates the reversal process compared to the homogeneous case. For example, the metastable lifetimes are  $\tau = (1.8 \pm 0.1) \times 10^3$  for the

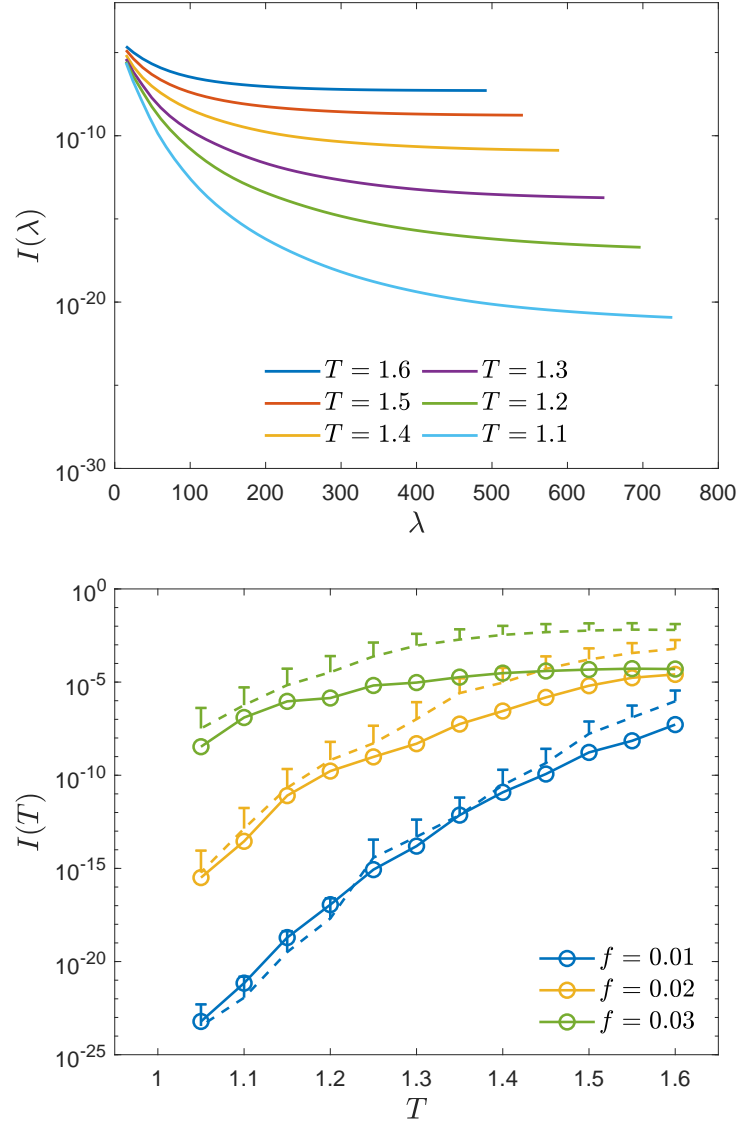


Figure 4.17: Top panel: Nucleation rates  $I_{\text{FFS},1}(\lambda)$  as a function of cluster size for different temperatures, with  $f = 0.01$ . Asymptotic values at large cluster sizes confirm measurement reliability. Bottom panel: Nucleation rates as a function of temperature for different defect fractions ( $f = 0.01$ ,  $f = 0.02$ , and  $f = 0.03$ ). Circles represent FFS results averaged over  $N_r = 100$  defect realizations, and dashed lines show theoretical estimates from Eq. (4.31).

homogeneous case and  $\tau = (2.0 \pm 0.1) \times 10^3$  for the model with defects at  $f = 0.02$  and  $h = 0.2$ . Within the MD regime, the primary effect of defects is to expedite the reversal process without altering its fundamental nature.

#### 4.2.4 Metastable lifetime and spinodal line modification

We proceed with the analysis and study the metastable lifetime for the model with defects. As for the homogeneous case, we consider Eqs. (4.20) and (4.21). Once again, we neglect the prefactor and focus solely on the exponential term  $\Delta F_c$ . Since  $\Delta F_c$  decreases monotonically with  $f$ , as shown in Fig. 4.13, higher defect fractions lead to shorter metastable lifetimes, irrespective of the reversal regime (MD or SD).

This effect is illustrated in Fig. 4.19, which shows the average metastable lifetime  $\bar{\tau}$  for various field intensities and defect fractions. As for the homogeneous case,  $\tau$  is defined as the time at which the sample magnetization changes sign under the influence of an external field. The average  $\bar{\tau}$  was obtained considering 200 reversal processes at temperature  $T = 1.8$ . Error bars are of the same size as the markers and are not shown for clarity.

When defects are introduced,  $\tau$  decreases by several orders of magnitude, particularly for weaker switching fields. Moreover, for  $f = 0.03$ ,  $\tau(h)$  appears to reach a plateau as  $h \rightarrow 0$ , supporting the argument that the ordered state remains metastable even without a field. The difference between the SD and MD regimes can still be observed, particularly for the  $f = 0.01$  case. For higher defect fractions, the difference becomes less noticeable, and smaller systems behave as larger ones.

We now consider the zero-field case, where the reversal occurs spontaneously. We can derive a relatively simple expression for the metastable lifetime in such conditions  $\tau_0$ , which highlights the main dependencies from the system's physical variables. For sufficiently large systems (within the MD regime), we consider Eqs. (4.21,4.29). The metastable lifetime can be expressed as:

$$\tau_0 \sim \exp \left( \frac{5k_B T (\log(\lambda_c^{h=0}) - 2) + 4\sigma_{\text{eff}} \sqrt{\pi} \sqrt{\lambda_c^{h=0}}}{12k_B T} \right) \quad (4.34)$$

By neglecting the weaker logarithmic dependence on the critical cluster size, we simplify Eq. (4.34) to:

$$\tau_0 \sim \exp \left( \frac{\sigma_{\text{eff}} \sqrt{\pi} \sqrt{\lambda_c^{h=0}}}{3k_B T} \right) = \exp \left[ \frac{\sigma_{\text{eff}} \pi}{24k_B T \mu \nu} \left( 1 + \sqrt{1 + \frac{20k_B T}{\sigma_{\text{eff}} \pi} \mu \nu} \right) \right] \quad (4.35)$$

Since  $\nu \mu$  is of the order of  $10^{-2}$  for the defect fractions considered ( $f < 0.1$ ), the term inside the square root is approximately unity. Thus, we further reduce the expression to:

$$\tau_0 \sim \exp \left( \frac{\sigma_{\text{eff}} \pi}{12k_B T \mu \nu} \right) \quad (4.36)$$

We now consider direct measurements from simulations. As in the homogeneous defect-free case, we define the metastable lifetime as the time at which the magnetization

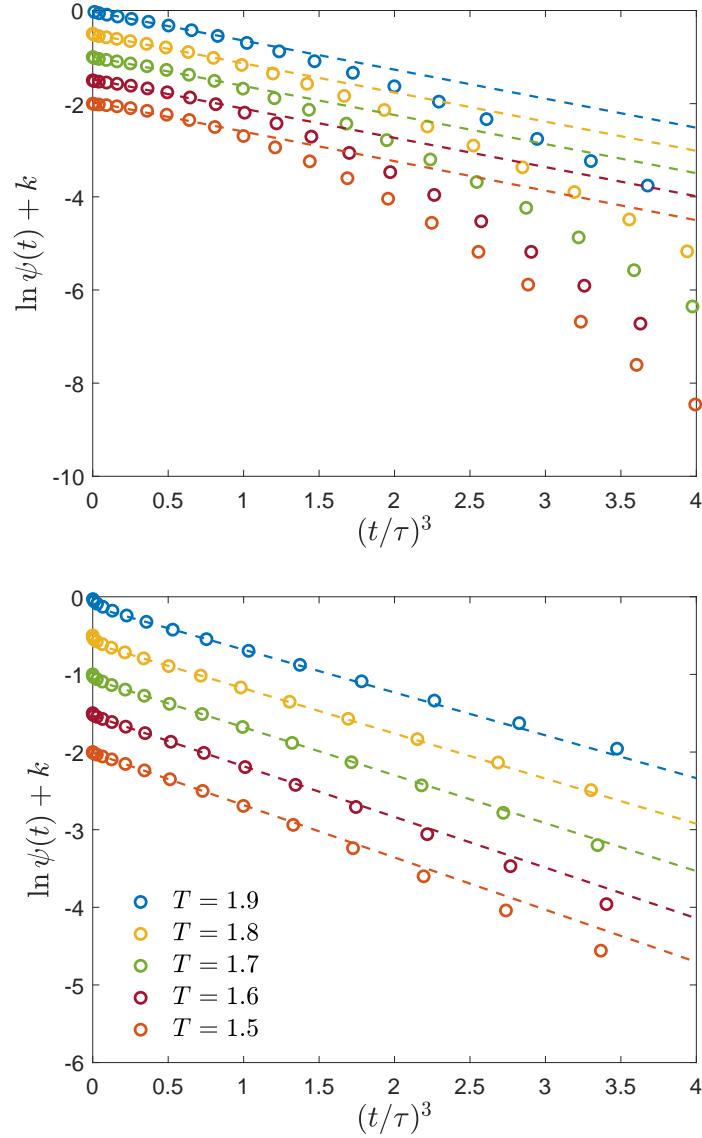


Figure 4.18: The logarithm of the relaxation of the Ising model with defects,  $\log \psi(t)$ , as a function of scaled time  $(t/\tau)^n$ . Markers represent simulation data, while dashed lines correspond to the theoretical expression in Eq. (4.33). For clarity, the data series are vertically shifted by a constant offset  $k$ . The results correspond to simulations conducted at various temperatures with  $h = 0.4$  and  $f = 0.02$ . The theoretical expression is fitted over the range  $t_{\min} < t < \tau$ , where  $t_{\min}$  minimizes the fitting parameter  $a$ , as explained for the homogeneous case. The top panel shows results considering the  $\beta$  systems ( $n = 2$ ), while the bottom panel displays results considering the  $\alpha$  system ( $n = 3$ ).

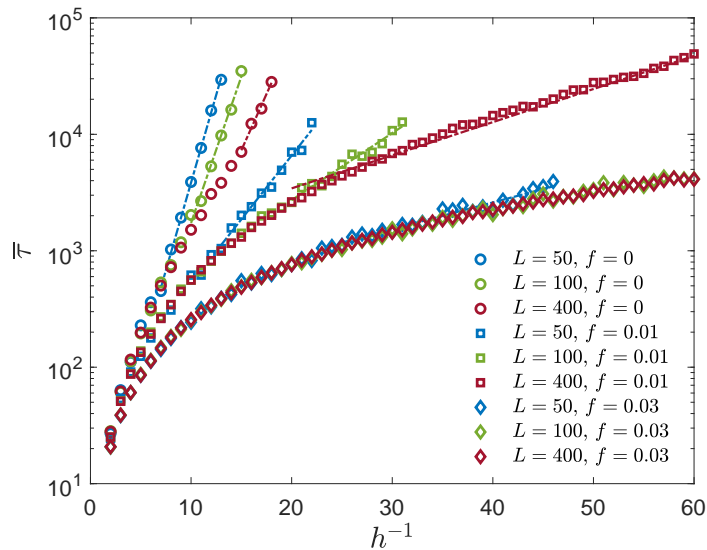


Figure 4.19: Metastable lifetime for the Ising model with defects as a function of the inverse of different switching field intensities. Different symbols represent distinct defect fractions, while colours indicate varying system sizes, as detailed in the legend.

crosses a threshold value midway through the reversal process. Specifically, starting from a positively magnetized initial configuration, the threshold is set to  $m_{\text{th}} = 0.5$ , which corresponds to the midpoint between the initial and stable clustered configurations.

The simulation results are shown in Fig. 4.20 for various defect fractions and temperatures. For a system with size  $L = 100$ ,  $N_r = 200$  repetitions of the reversal process are considered to obtain reliable estimations of the metastable lifetime without a field. The error bars are the same size as the markers and are not represented for clarity. Notably,  $\log \bar{\tau}_0 \sim f^\alpha$ , as represented by the dashed lines in the panel to the left. Interestingly, the power-law fit gives  $\alpha$  linear in temperature, ranging from 0.6 for high temperatures to  $\approx 1$  at low temperatures.

### Spinodal line

We now analyse the effect of defects on the spinodal line, which separates the SD and MD regimes of the magnetization reversal process. The introduction of defects is expected to significantly impact the macroscopic behaviour of the system by modifying the dominant reversal mechanisms.

The simulation results, shown in Fig. 4.21, demonstrate how the metastable lifetime distribution evolves with increasing defect fraction  $f$ . For a system of size  $L = 100$ , under an external field  $h = 0.05$  and temperature  $T = 1.8$ , the distribution for  $f = 0$  exhibits a Poissonian form characterized by a long right-hand tail, indicating SD regime. As  $f$  increases, the distribution shifts to a bell-shaped profile, which is a hallmark of the

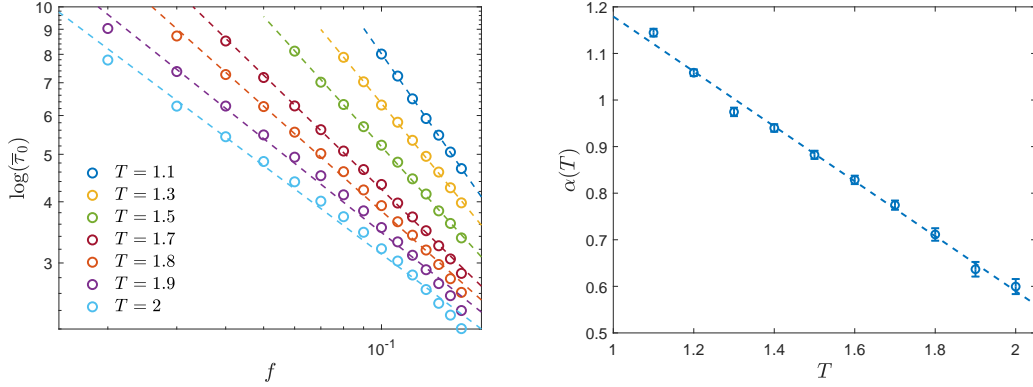


Figure 4.20: Left panel: Spontaneous demagnetization time (metastable lifetime) for the Ising model with defects in the absence of an external field, plotted as a function of the defect fraction  $f$  for different temperatures. The double logarithmic plot reveals a power-law behaviour,  $\log \bar{\tau}_0 \sim f^{-\alpha}$ . Dashed lines represent the best power-law fit. Right panel: Power-law exponent  $\alpha$  as a function of temperature.

multi-droplet regime.

This behaviour can be qualitatively explained by the emergence of additional nucleation sites as  $f$  increases. In the presence of defects, multiple nucleation events occur simultaneously, favouring the MD regime over the SD regime, where nucleation is spatially constrained. The transition to a bell-shaped distribution reflects the collective and spatially distributed nature of the reversal process in systems with a higher defect fraction.

Additionally, a substantial reduction in the expected metastable lifetime is observed with increasing  $f$ , consistent with the findings in Fig. 4.19. This result provides strong evidence for the alteration of the system's dynamics, confirming a transition from the SD to the MD regime as determined by the  $r = 0.5$  criterion.

We now focus on the case of zero magnetic field and analyse the nature of the transition in this regime. As in previous cases, we employ the criterion  $r = 0.5$  to distinguish between MD and SD types of transitions. The results are summarized in Fig. 4.22, which presents the mean metastable lifetime  $\bar{\tau}$  and the relative standard deviation  $r$  as functions of system size  $L$  and defect fraction  $f$ .

The left panel of Fig. 4.22 shows the behaviour of the mean metastable lifetime  $\bar{\tau}$  for various defect fractions  $f$ . It is evident that  $\bar{\tau}$  remains largely invariant with respect to changes in system size  $L$  for a fixed defect fraction. By contrast, the right panel depicts the variation of the relative standard deviation  $r(L)$ , highlighting the significant influence of system size. Here, the dynamic spinodal size  $L_{\text{ls}}(f)$  is determined as the system size at which  $r$  crosses the threshold of  $r = 0.5$ , with values obtained via linear interpolation in the vicinity of the crossing point.

A clear trend emerges: as the defect fraction  $f$  increases, the dynamic spinodal size  $L_{\text{ls}}$  decreases. This indicates that systems with lower defect fractions require larger sizes

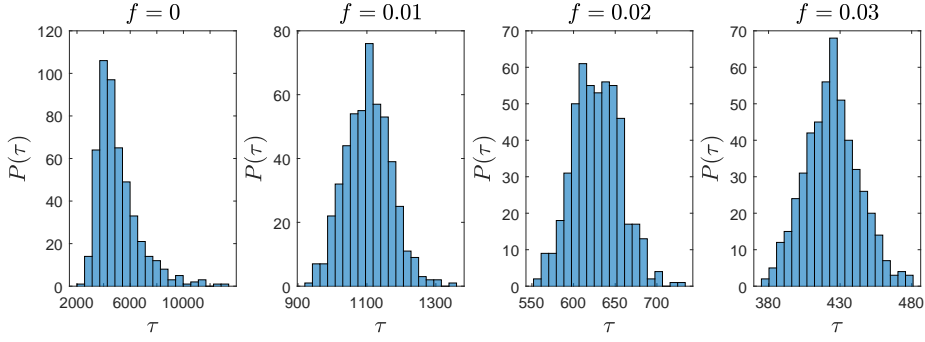


Figure 4.21: Lifetime probability distribution. From left to right,  $f$  increases from a homogeneous system to  $f = 0.03$ . The probability distribution changes from Poissonian in the first case to a Gaussian for the system with defects, indicating the modification of the reversal regime from SD to MD. Simulations for  $L = 100$ ,  $h = 0.05$  and  $T = 1.8$

to exhibit an MD-type transition. Consequently, determining  $L_{ls}$  for small  $f$  values becomes computationally prohibitive due to the extended simulation times required.

To estimate  $L_{ls}$ , we follow the approach developed in Section 4.1.5. Specifically, we consider the average distance between nucleating droplets,  $R_0$ , which is defined as:

$$R_0 = v_0^{d+1} I^{-1/(d+1)}, \quad (4.37)$$

where  $R_0$  sets the characteristic length scale separating the MD and SD regimes. When  $R_0 \gg L$ , only a single droplet is likely to form, initiating the reversal process. Conversely, when  $R_0 \ll L$ , multiple droplets can nucleate simultaneously, inducing the MD regime. Therefore, the dynamic spinodal size  $L_{ls}$  can be approximated as:

$$L_{ls} \approx R_0 \sim I^{-1/(d+1)} \propto \exp\left(\frac{\Delta F_c}{3k_B T}\right), \quad (4.38)$$

which has the same functional form as the zero-field metastable lifetime in Eq. (4.36).

The dependency  $L_{ls}(f)$  is assumed to follow a power law with a temperature-dependent exponent  $\alpha(T)$ . This assumption is confirmed by fitting the numerical results, as shown in Fig. 4.20. For higher defect fractions, the prefactor is determined via fitting, and this result is then extrapolated to estimate  $L_{ls}$  in the low-defect regime. For  $T = 1.8$ , we obtain  $L_{ls}(f = 0.02) = 5 \times 10^3$  and  $L_{ls}(f = 0.01) \approx 10^6$ .

Figure 4.23 summarizes the critical system size  $L_{ls}$  as a function of the defect fraction  $f$ . The results are well described by a logarithmic relation of the form  $\log(L_{ls}) \sim f^{-0.7}$ , consistent with the value of  $\alpha$  obtained for  $T = 1.8$ .

Figure 4.24 provides a comprehensive summary of our results on the spinodal line in the presence of both an external magnetic field  $h$  and quenched defects for the case  $T = 1.8$ . For various system sizes  $L$  and defect fractions  $f$ , we systematically varied the external field  $h$  and measured the relative standard deviation  $r$ . The critical spinodal field was identified as the value of  $h$  where  $r$  crosses the threshold 0.5.

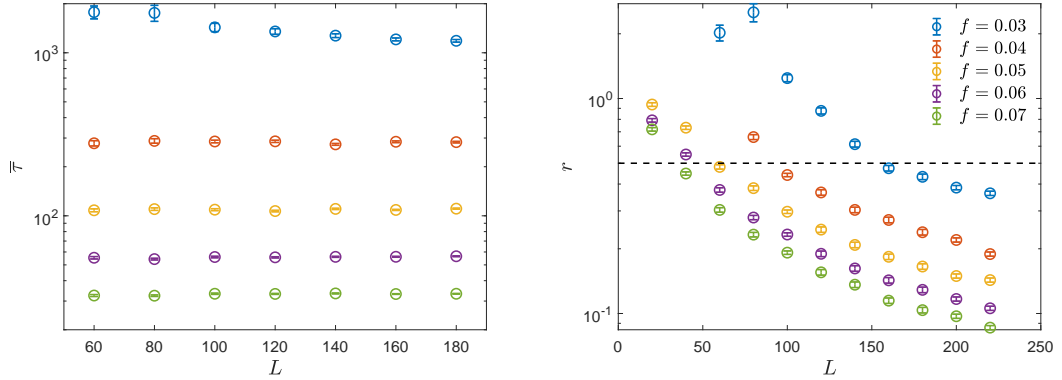


Figure 4.22: Left panel: Mean metastable lifetime  $\bar{\tau}$  as a function of system size  $L$  for different defect fractions  $f$ . The results demonstrate that  $\bar{\tau}$  remains constant for a fixed  $f$ . Right panel Relative standard deviation  $r(L)$  as a function of  $L$ , with the dynamic spinodal size  $L_{ls}$  identified as the point where  $r = 0.5$ . The reduction in  $L_{ls}$  with increasing  $f$  reflects the dependence of the transition type on defect concentration.

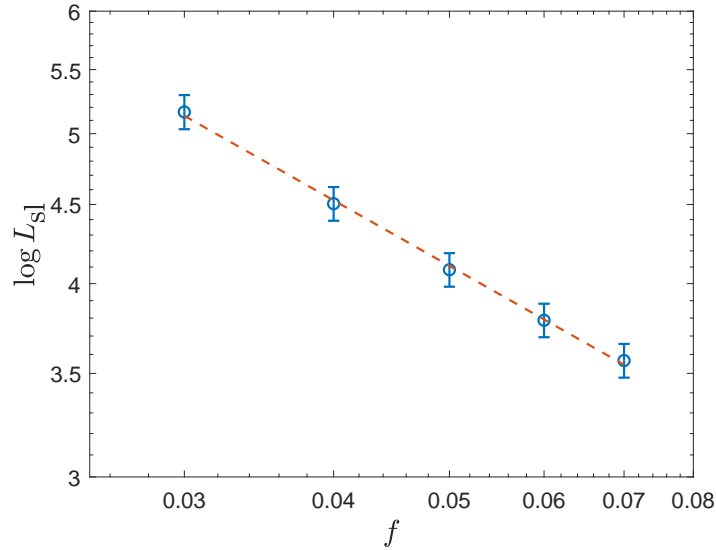


Figure 4.23: Critical system size  $L_{ls}$  associated with spontaneous demagnetization as a function of defect fraction  $f$ . Standard errors are estimated by repeating the measurements over multiple defect realizations. The dashed line corresponds to a fit of the form  $\log(L_{ls}) \sim f^{-0.7}$ , consistent with the value of  $\alpha$  for  $T = 1.8$  in Fig. 4.20.

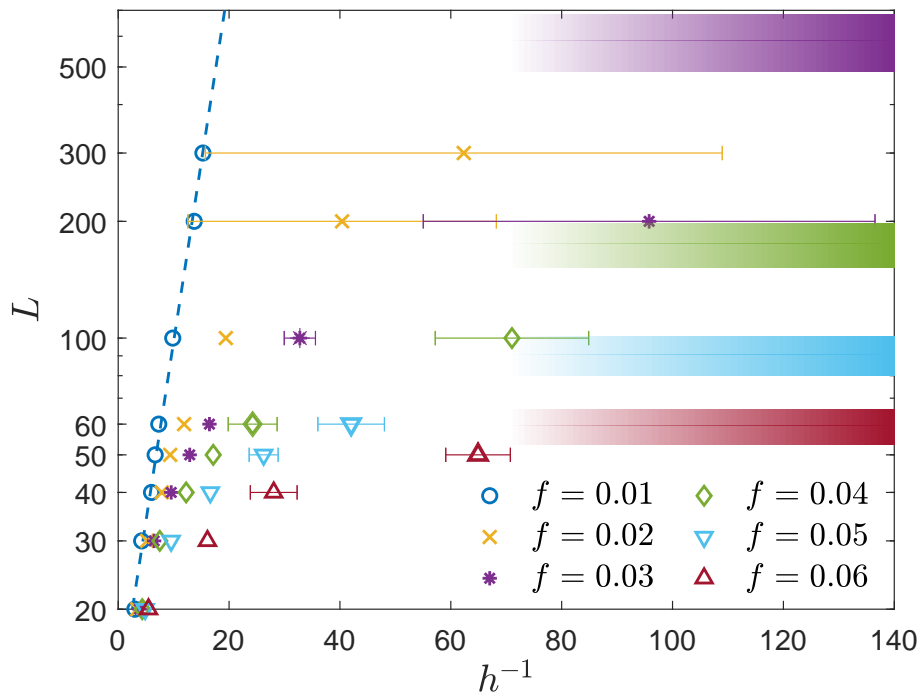


Figure 4.24: Phase diagram illustrating the position of the spinodal line as a function of the magnetic field  $h$  and system size  $L$  for different defect fractions  $f$ . Each colour corresponds to a specific defect fraction, as indicated in the inset. For each  $f$  and  $L$ , the critical spinodal field  $h$  is determined as the point where the relative standard deviation  $r$  of the metastable lifetime crosses 0.5. Horizontal error bars account for variations in critical  $h$  values across different realizations of the same defect fraction. For defect fractions  $f \geq 0.02$ , the limiting asymptote at zero field ( $h = 0$ ) is shown by the shaded regions on the right side of the figure, corresponding to the system size  $L_{ls}$  where the transition diagram. For  $f = 0.01$ ,  $L_{ls} \approx 10^6$ , which lies beyond the range of the displayed phase diagram.

To achieve a reliable estimate of the critical magnetic field, we created multiple system replicas with different defect configurations. The error bars in Fig. 4.24 represent the standard error of the critical  $h$  values from these replicas. Systems with higher defect densities required averaging over more replicas to account for sample variability. We specified an error bar threshold of 20% of the estimated spinodal point to ensure stability in the averages. For the highest defect density reported ( $f = 0.05$ ), up to 16,000 defect configurations were analysed. For larger systems ( $L \geq 200$ ), fewer replicas were used, specifically 200 for  $f = 0.01$  and 1,000 for  $f = 0.02$ , due to increased computational demands.

The shaded regions on the right side of Fig. 4.24 represent the behaviour of  $L_{ls}$  at zero field ( $h = 0$ ), as derived from previous results. The widths of these regions reflect the error bars associated with the determination of  $L_{ls}$ . Consistent with these findings, the spinodal curves exhibit a systematic dependence on both the defect fraction and the system size, reinforcing the relationship between the dynamic spinodal size  $L_{ls}$  and the defect-induced heterogeneities.

Insights from Figs. 4.24 confirm that the position of the spinodal line (i.e., the minimum system size required for deterministic behaviour) is strongly influenced by defect density. All data indicate that the spinodal line is linear with  $h^{-1}$  at high external field values (left side of the plot), coherent with what is found for the system with no defects where the linear trend also extends to intermediate and low  $h$  values. However, the presence of defects leads to a saturation point  $L_{sl}(f)$ , meaning that when  $L > L_{sl}(f)$ , the system behaves deterministically regardless of the external field strength.

The presence of quenched defects introduces significant modifications to both the metastable lifetime and the spinodal line, highlighting the interplay between disorder and system dynamics. In the case of the metastable lifetime, the inclusion of defects can alter the underlying nucleation process, by generally favouring the MD reversal process. This behaviour reflects how defects create additional nucleation sites that facilitate the reversal process, effectively lowering energy barriers and accelerating nucleation dynamics. The spinodal line shifts under the influence of defects. The critical spinodal field  $h$  decreases as the defect fraction increases. This reduction in  $h$  signifies that systems with higher defect concentrations transition to the MD regime at smaller system sizes, coherently with the findings related to the metastable lifetime analysis. At zero field, the metastable lifetime  $\tau_0$  strongly depends on  $L$  and  $f$ . As the defect concentration increases, the reversal process becomes progressively dominated by the MD regime, reducing the metastable lifetime by accelerating nucleation dynamics.

These findings collectively highlight that defects act as catalysts for phase transitions, promoting multi-droplet behaviour and reducing metastability, while also reshaping the spinodal line in a manner that depends sensitively on defect concentration and system size.

## Conclusion

This chapter has investigated the dynamic properties of homogeneous and heterogeneous systems, with a specific focus on the reversal processes in the two-dimensional Ising model. By employing advanced simulation techniques and extending classical theories, significant insights into the mechanisms underlying metastable states and their lifetimes have been gained.

In the homogeneous case, the analysis began with the Classical Nucleation Theory (CNT) as a framework to describe the formation and growth of clusters during magnetization reversal. Through rigorous validations using the Ising model, this study extended the applicability of CNT to regimes previously unexplored, notably at low temperatures where thermal fluctuations are minimal. The incorporation of simulation methodologies, such as the Forward Flux Sampling (FFS) and Umbrella Sampling (US) techniques, enabled precise calculations of critical parameters such as the nucleation rate, free energy barriers, and diffusion coefficients. These results confirmed the robustness of CNT in capturing the system dynamics exiting from metastable states while shedding light on the transition mechanisms in the single-droplet regime.

In heterogeneous systems, defects were shown to significantly alter the free energy landscape, creating pinning effects that both hindered and facilitated cluster growth depending on their alignment with the external field. We extended CNT to accommodate these structural heterogeneities, incorporating defect-driven terms into the free energy formulation. The resulting framework was validated through numerical simulations, revealing that defects reduce the energetic cost of reversal processes and lead to the spontaneous development of critical clusters, even in the absence of an external field. Such findings align with the Imry-Ma argument, highlighting the fundamental role of disorder in governing phase transitions.

An additional noteworthy effect of defects is their role in modifying the spinodal line that separates the multi-droplet (MD) regime from the single-droplet (SD) regime. Defects favour the MD regime, introducing a more deterministic behaviour in out-of-equilibrium dynamics. This deterministic influence, driven by defect-induced nucleation, contrasts with the stochastic nature typical of the SD regime and has significant implications for understanding the interplay between system size, disorder, and dynamical behaviour.

The implications of these findings are significant for physical systems where metastable states and phase transitions play a critical role. For instance, in magnetic recording technologies and materials science, understanding how defects influence nucleation rates and reversal times can guide the design of systems with improved stability and performance. Additionally, the methodologies developed herein are broadly applicable to other systems exhibiting metastability, such as crystallization processes, vapor-liquid transitions, and domain switching in ferroelectric materials.

In summary, this chapter has provided a detailed exploration of magnetization reversal processes, emphasizing the intricate balance between theoretical predictions and numerical validations. The extended frameworks and simulation techniques developed

here not only advance the current understanding of dynamic properties but also pave the way for future studies in both theoretical and applied physics of heterogeneous systems.

## Chapter 5

# Dynamic phase transition

In the previous chapter, we explored the mechanisms of magnetization reversal in homogeneous and heterogeneous systems under constant external fields. The focus was on understanding metastable states, nucleation dynamics, and the role of structural heterogeneities in altering the free energy landscape. Building on these results, this chapter shifts attention to another class of nonequilibrium phenomena: the dynamic phase transition (DPT), which emerges when the system is driven by a time-dependent, oscillatory external field. By introducing temporal periodicity, the interplay between competing timescales brings forth a dynamic analogue of equilibrium phase transitions.

The investigation of DPTs in heterogeneous systems, particularly those with structural defects, builds on the findings of Chapter 4. Defects, by modifying the local potential landscape, significantly influence the system dynamics. In the context of DPTs, we find that a random disposition of defects enhances the responsiveness of the system to external fields. On the other hand, by properly fine-tuning the configuration of defects it is possible to screen the system from the external field and therefore change the system's dynamic properties.

This chapter aims to provide a detailed understanding of DPT. The findings presented here are expected to have far-reaching implications, from the design of materials with tailored dynamic properties to the development of fast-switching magnetic devices. The transition from static to dynamic regimes represents a natural progression in the study of nonequilibrium systems, further bridging the gap between theory and application.

This chapter is structured as follows. Section 5.1.1 presents literature review on the DPT in homogeneous systems. For these systems, the transition is investigated by using key parameters such as the average magnetisation per cycle and the dynamic susceptibility. The similarities and differences between DPTs and equilibrium phase transitions are highlighted, with a focus on universality and critical phenomena.

Section 5.2 extends this analysis to heterogeneous systems. First, a literature review regarding the introduction of randomness via random bonds and random fields, and its effect on the DPT properties, is presented. Then, the effect of defects is analysed. The section contains original results also published in [53]. The effects of these hetero-

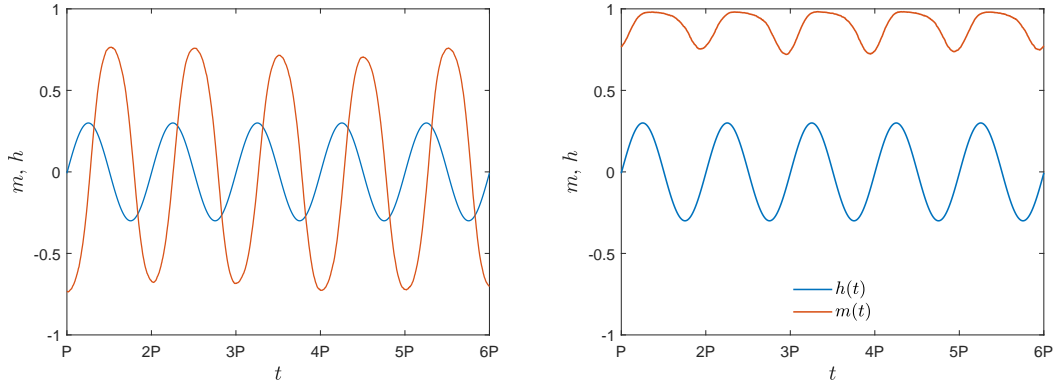


Figure 5.1: DPT for the Ising model. Solid lines represent the oscillating magnetic field (in blue) and the magnetization (in orange). The left panel depicts the magnetization in the dynamic disordered phase, which reverses every half-cycle. The right panel illustrates the dynamic ordered phase, where the magnetization is locked in a single equilibrium minimum, represented here by the positively magnetized configuration. For these simulations:  $L = 400$ ,  $h_0 = 0.3$ ,  $P = 258$ ,  $T = 1.9$  for the DDP, and  $T = 1.7$  for the DOP.

geneties on the dynamic critical temperature and susceptibility are explored, providing a comprehensive framework for understanding the DPT in real-world materials. Special attention is given to the interplay between local and global order parameters, as well as the role of quenched randomness in tuning the transition.

## 5.1 DPT in homogeneous systems

We consider an oscillating external field  $h = h_0 \sin(\omega t)$  as a prototype stimulus that consistently drives the system out of equilibrium. Below the Curie temperature, the system exhibits bistable behaviour, where magnetic spins align preferentially in either a positive or negative direction. The oscillating field alternately favours each direction during successive half-cycles. Under these conditions, two responses are possible. When the period of the external field is large compared to the system’s relaxation time, the magnetization follows the oscillations of the field, undergoing a complete reversal each half-cycle. In this regime, the system displays a dynamic paramagnetic phase, referred to as the Dynamic Disordered Phase (DDP). Conversely, when the field oscillates too rapidly, the system cannot respond quickly enough and becomes “locked” in one of the two magnetization states. In this regime, the system enters a dynamic ferromagnetic phase, called the Dynamic Ordered Phase (DOP). These two dynamic phases are schematically illustrated in Fig. 5.1.

The switch between these two phases is termed the dynamic phase transition [112], [113]. This transition arises from the competition between two key timescales: the period of the external magnetic field and the metastable lifetime (studied in the previous

chapter) defined as the time taken to return to equilibrium after a perturbation. When half of the field's period exceeds the metastable lifetime  $P/2 > \tau_{\text{MS}}$ , the system has sufficient time to adapt to the external stimulus, resulting in magnetization reversal during each half-cycle. Conversely, when the period decreases  $P/2 < \tau_{\text{MS}}$ , the magnetization reversal remains incomplete before the field changes direction again, causing the reversal to counteract itself, and the magnetization fails to switch.

In addition to the period of oscillation, two other critical parameters significantly influence the system's behaviour: the temperature and the amplitude of the external magnetic field. Together with the oscillation period, these parameters govern the dynamic phase in which the system resides as follows:

- **Temperature ( $T$ ):** Temperature plays a crucial role in controlling the thermal fluctuations within the system. These fluctuations directly affect the ability of the system to overcome energy barriers between magnetization states. Below a certain threshold, thermal agitation is so weak that spins are able to remain predominantly in an ordered state. However, as temperature increases, enhanced fluctuations can destabilize the magnetization, making it easier for the oscillating magnetic field to induce switching between states.
- **Field amplitude ( $h_0$ ):** The amplitude of the external field influences the strength of the driving force. For small amplitudes, the system may remain in the dynamically ordered phase, as the energy supplied is insufficient to induce periodic magnetization switching. As  $h_0$  increases, the system becomes more responsive to the field, facilitating transitions between the dynamically ordered and disordered phases. A bias field  $h_b$  can also be included  $h = h_0 \cos(\omega t) + h_b$ , producing peculiar effects. Its role will be analysed in the following.

The critical period  $P_c \approx \tau_{\text{MS}}$  embodies the effects of temperature and field amplitude, making it possible to control the transition between dynamic phases by varying any of these three parameters [114], [115].

### 5.1.1 Dynamic order parameter

In homogeneous systems, the DPT is characterized by the dynamic order parameter,  $Q$ , which is defined as the time-averaged magnetization over a full cycle of the oscillating external field [112], [116]:

$$Q = \frac{1}{P} \oint m(t) dt, \quad (5.1)$$

where  $P$  is the period of oscillation and  $m(t)$  is the instantaneous magnetization. For periods  $P > P_c$ , the system resides in the DDP. In this phase, the magnetization reverses completely during each half-cycle and the time-averaged magnetization  $Q$  is zero. By contrast, when  $P < P_c$ , the system enters the DOP. Here, the rapid oscillation of the field prevents the system from fully reversing its magnetization, resulting in a non-zero  $Q$ . Thus, the DPT represents a transition from  $Q = 0$  in the DDP to  $Q \neq 0$  in the DOP. This behaviour closely parallels that of equilibrium phase transitions, where the static

order parameter (magnetization) transitions between  $m = 0$  in the paramagnetic phase and  $m \neq 0$  in the ferromagnetic phase.

The nature of the DPT has been a subject of debate. Acharyya [115] observed that at high field amplitudes, the transition appears to be first-order, with a discontinuous jump in  $Q$ . However, Korniss *et al.* [114] demonstrated that these observations could be finite-size effects. Their study revealed that larger systems exhibit continuous transitions, suggesting that the DPT in infinite systems is second-order, as initially proposed by Tomé and de Oliveira using a mean-field approach [112].

Starting from Eq. (5.1), we can also define the dynamic susceptibility,  $\chi_Q$ , as an analogue to thermodynamic susceptibility [117]. The susceptibility reflects the system's response to an external conjugate field, which, in the context of the DPT, was initially unclear. Further analysis revealed that the conjugate field corresponds to a bias field superimposed on the oscillating magnetic field. Assuming the validity of the fluctuation-dissipation theorem, in the absence of a bias field the susceptibility can be expressed in terms of the variance of the order parameter:

$$\chi_Q = L^2 [\langle Q^2 \rangle - \langle |Q| \rangle^2], \quad (5.2)$$

where  $L$  is the linear size of the system, and the averages are taken over many cycles. The susceptibility peaks at the critical point, where fluctuations in the order parameter are maximal, providing a reliable criterion for locating the critical period  $P_c$ .

Analogous to equilibrium phase transitions, the Binder cumulant can be generalized to the dynamic case. The dynamic Binder cumulant is defined as:

$$U_Q = 1 - \frac{\langle Q^4 \rangle}{3\langle Q^2 \rangle^2}. \quad (5.3)$$

In the DOP,  $U_Q$  approaches  $2/3$ , whereas in the DDP,  $U_Q$  approaches 0. The Binder cumulant is a crucial tool for estimating the critical conditions using the ‘‘cumulant intersection method’’ [50]. In finite systems,  $U_Q$  displays a characteristic scaling behaviour, where plots of  $U_Q$  versus an external parameter (e.g., field amplitude, temperature, or period) for different system sizes intersect at a single critical point. This method is widely used for an accurate estimation of critical parameters in systems lacking analytical solutions.

The DPT shares striking qualitative and quantitative similarities with the thermodynamic phase transition (TPT). Monte Carlo simulations, especially on the two-dimensional kinetic Ising model, have been extensively utilized to investigate these parallels. Sides *et al.* [118] performed large-scale simulations and demonstrated that the DPT exhibits finite-size scaling behaviour, akin to equilibrium phase transitions. Through these simulations, the critical exponents  $\beta$ ,  $\gamma$ , and  $\nu$  were determined, confirming their consistency with those of the Ising universality class. This evidence firmly suggests that the DPT belongs to the same universality class as equilibrium second-order phase transitions [114], [118]. Mean-field numerical calculations further supported these findings [119], and subsequent studies extended this equivalence to three-dimensional Ising

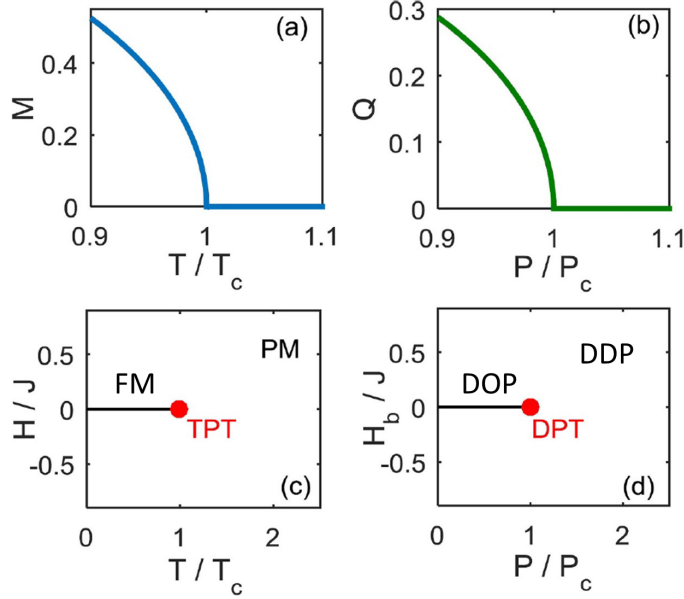


Figure 5.2: Comparison of phase diagrams between the DPT and the TPT. The top panels show the dynamic order parameter  $Q$  as a function of  $P/P_c$  for the DPT and magnetization  $M$  as a function of  $T/T_c$  for the TPT. The bottom panels present the  $(P, h_b)$  phase diagram for the DPT and the  $(T, h)$  phase diagram for the TPT. Red dots mark the critical points for both transitions. Source [123].

models [120] and triangular lattices [121]. These results collectively indicate that the kinetic Ising model retains the same universality class as its equilibrium counterpart.

However, the analogy between the DPT and TPT holds primarily near the critical point and in the absence of an external bias field superimposed on the oscillating magnetic field [122]. The introduction of a non-zero bias field  $h_b$  to the oscillating external field reveals intriguing features. For periods  $P > P_c$ , the dynamic order parameter  $Q$  varies continuously with  $h_b$ . Conversely, for  $P < P_c$ , a first-order transition in  $Q$  is observed when  $h_b$  changes sign. The  $(P, h_b)$  phase diagram for the DPT exhibits strong similarities to the  $(T, h)$  phase diagram for the TPT, as illustrated in Fig. 5.2.

This correspondence suggests that the bias field  $h_b$  acts as the conjugate field to the dynamic order parameter, analogous to the role of  $h$  in the TPT. Robb *et al.* [124] provided additional evidence for this analogy by investigating the scaling behaviour of the order parameter under critical conditions. They showed that the order parameter near criticality follows the scaling relation:

$$\langle Q \rangle (P = P_c, h_b \rightarrow 0) \propto h_b^{1/\delta_q}, \quad (5.4)$$

mirroring the equilibrium Ising model's relation:

$$\langle m \rangle (T = T_c, h \rightarrow 0) \propto h^{1/\delta_m}. \quad (5.5)$$

The critical exponents  $\delta_q$  and  $\delta_m$  were found to be consistent, further reinforcing the universality class correspondence between the DPT and TPT.

The derivative of the dynamic order parameter with respect to the bias field, known as the dynamic susceptibility  $\hat{\chi}_Q$ , exhibits behaviour analogous to its equilibrium counterpart. At critical conditions,  $\hat{\chi}_Q$  aligns with the susceptibility  $\chi_Q$  derived from the fluctuation-dissipation theorem in Eq. (5.2). This agreement underscores the validity of the fluctuation-dissipation theorem even in out-of-equilibrium conditions, while further solidifying the role of the bias field  $h_b$  as the conjugate field to the dynamic order parameter.

### 5.1.2 Hysteresis loop area

Dynamic hysteresis is another prominent feature of DPT. As the magnetization responds to the oscillating field, it exhibits a hysteresis loop, where the magnetization lags behind the external field. It is possible to define the hysteresis area over one cycle as

$$A = \frac{1}{P} \oint m(h)dh \quad (5.6)$$

This quantity is also important since it represents the dissipated energy by the system during an entire cycle of the external field. Moreover, it can be easily monitored in real experiments involving magnetic alloys or metals, which is of crucial importance to validate numerical results and the models considered.

Jung et al. [125] showed that the loop area follows a power law with respect to the field's driving frequency  $A \sim \omega^\beta$  with  $\beta = 2/3$  and tested the result through experiments on a bistable semiconductor laser. In numerical simulations, thanks to the work of Acharyya and Chakrabarti [126], [127], we can write

$$A \sim h_0^\alpha T^{-\beta} g\left(\frac{\omega}{h_0^\gamma T^\delta}\right) \quad (5.7)$$

where  $g(x) \sim x^\epsilon e^{-x^2/\sigma}$ . Here, the scaling exponents were determined from simulations on systems with different dimensions and for the case  $d = 2$ , we find  $\alpha = 1$ ,  $\beta = 0.75$ ,  $\gamma = 0.85$ ,  $\delta = 1.2$  and  $\epsilon = 0.36$ . A comparison with experiments performed on thin film (Fe/Au(001), Co/Cu(001) and Ni<sub>8</sub>OFe<sub>2</sub>O) provides a validation of the numerical simulation framework, even though quantitative discrepancies in the scaling exponents were found between different samples and the Monte Carlo simulations predictions [128]–[130].

The hysteresis curves are also the subject of study. They are usually categorised into three different classes, based on the shape of the function and the symmetric property [131]. Type 1 hysteretic loops are asymmetric curves and no coercivity is observed (crossing of the  $m = 0$  line each half cycle). The curve is observed for a system in the DOP. Type 2 hysteretic loops are again asymmetric but a coercive field is registered. The system displays such behaviour while switching from the DDP to the DOP. Finally, type 3 curves are symmetric curves centred in the origin of the plane  $(m, h)$ .

### 5.1.3 Experimental observations

It is crucial to have experimental support for the developed theoretical framework and also for results from numerical simulations. During the last 3 decades, numerous studies have been performed trying to discuss the emergence of DPT in real magnetic systems. Two are the main challenges to be overcome. First, a magnetic material with strong uniaxial anisotropy should be prepared. The uniaxial anisotropy in a system corresponds to a double-well potential in the Ginzburg-Landau framework, where the wells represent two stable magnetization states along the preferred axis. This anisotropy confines the system's dynamics to transitions between these wells, effectively reducing the accessible degrees of freedom and minimizing competing relaxation pathways. In contrast, isotropic systems lack a double-well structure and instead exhibit a flat or shallow potential landscape, allowing magnetization to fluctuate freely in multiple directions, which disrupts the coherent switching dynamics necessary to observe the DPT. Nowadays, numerous structures display this property, mainly ultra-thin layers. The second challenge regards time-resolved magnetisation measurements of ultra-thin structures. This was achieved thanks to the improvement of the Magneto-Optic-Kerr-Effect (MOKE) techniques for fast and precise measurements.

Along with the experiments cited in the previous section, investigating the loop area properties and suggesting the presence of DPT in such ultra-thin structures, other experiments proved the presence of DPT in real magnetic systems. Robb et al. [124] considered MOKE measurements over a  $\text{Co}(4\text{\AA})/\text{Pt}(7\text{\AA})_3$  multilayer. This material shows strong perpendicular anisotropy, resembling a suitable material for the observation of the DPT. The direct measurements of the average magnetisation per cycle  $\langle Q \rangle$  as a function of the magnetic field period  $P$  and the bias field  $h_b$  revealed peculiar properties traceable to what was observed in the two-dimensional Ising model in the mean-field theory framework. In particular,  $\langle Q(h_b) \rangle$  showed a sudden jump at  $h_b = 0$  in low period conditions. This is clearly shown in Fig. 5.3, where measurement of  $\langle Q \rangle$  were taken on Co films with (1010) crystallographic surface texture. Moreover, the variance of the order parameter  $\sigma^2(Q)$  showed a peak in the limit  $h_b \rightarrow 0$ , hinting at the presence of criticality and hence a DPT. Subsequently, Berger et al. [133] considered ultra-thin Co layers and characterised extensively the dynamic phase diagram through the Longitudinal Magneto-Optic Kerr Effect (L-MOKE) technique. It was found that  $Q(h_b)$  shows a first-order (discontinuous) transition for  $P < P_c$  and a second-order (continuous) transition for  $P > P_c$ . This finding supported the claim that the bias field acts as a conjugate field in the DPT and that the DPT is analogous to the TPT also through experiments. Anyway, the analogy holds only for small  $h_b$ , since anomalies not observed in the TPT were registered for strong bias fields.

## 5.2 DPT in random systems

Randomness is an intrinsic characteristic of real materials. Anomalies and imperfections in the fabrication process cannot be completely avoided. For this reason, numerical sim-

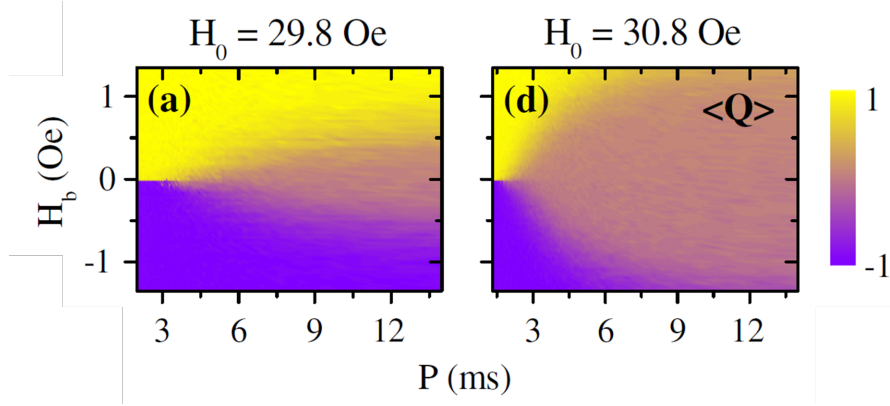


Figure 5.3: Experimental average magnetisation per cycle  $\langle Q \rangle$  as a function of the bias field  $h_b$  and oscillation period  $P$  for different choices of the field intensity  $h_0$ . Source [132].

ulations considering the dynamic behaviour of heterogeneous structures are of crucial importance to enhance our capabilities to properly design materials for real applications. We now examine the influence of quenched randomness on the dynamic response of a system subjected to an oscillating external field. As outlined in Chapter 4, heterogeneity introduced by quenched randomness creates conditions useful for the formation of droplets and amplifies the system's responsivity to external perturbations. Consequently, significant modifications to the properties of the DPT are expected in systems exhibiting quenched randomness. We expect the disordered phase to be generally favoured. To establish context, we begin with a concise overview of prior studies on the DPT in systems exhibiting quenched randomness. Following this, we turn our focus to the model incorporating defects, presenting the outcomes of the numerical analysis conducted. The primary effects of defects on the DPT are thoroughly examined, representing one of the central contributions of this thesis.

### 5.2.1 Random bond and random field Ising models

Vatansever and Fytas [121] have investigated the role of random bounds as a source of heterogeneity in the two-dimensional Ising model. They introduced heterogeneity through a bimodal distribution of the exchange interactions  $P(J_{xy}) = 1/2[\delta(J_{xy} - J_1) + \delta(J_{xy} - J_2)]$  with the constrain  $J_1 + J_2 = 1$  as to recover the homogeneous case for  $J_1 = J_2$ . By extensive numerical simulations, they analysed the system size scaling of the dynamic susceptibility peak  $\chi_Q \sim L^{\gamma/\nu}$ , the shift in the critical period  $P_{c,\text{hete}} = P_{c,\text{homo}} + bL^{-1/\nu}$  due to randomness and the specific heat  $\chi_E \sim \log(\log(L))$  and concluded that the RBIM displayed comparable critical exponents  $\nu$  and  $\gamma$  as found in the kinetic Ising model.

These findings were extended to the random bound Blümel-Capel model, an extension of the Ising model in which the spin variables  $\sigma$  can hold three values  $-1, 0, 1$  and a crystal-field coupling  $\Delta$  disfavour the  $\sigma = 0$  value.

They identified spatial symmetry breaking, where individual spins exhibit behaviour dependent on their local exchange interactions. To quantify this, they considered the local order parameter

$$Q_i = \frac{1}{P} \oint \langle s_i \rangle dt \quad (5.8)$$

This parameter captures the time-averaged magnetization for each spin over one cycle of the external field. Differences in  $Q_i$  revealed distinct spatial distributions of the local magnetization, particularly between the DDP and the DOP

By contrast to the RBIM, the RFIM introduces randomness through the external field rather than the exchange interactions. Specifically, most of the present studies in the literature [134], [135] consider the random field as an effect related to the oscillating field, for which  $h(t) = h_{0,i} \sin(\omega t)$  where  $h_{0,i}$  is a site-dependent random amplitude.

For example, Yukusel et al. [134] considered a trimodal field distribution  $P(h_{0,i}) = p\delta(h_{0,i}) + (1-p)/2[\delta(h_{0,i}-h_0) + \delta(h_{0,i}+h_0)]$ . Their analysis revealed significant deviations in the DPT phase diagram of the RFIM ( $J, h_0$ ) compared to its equilibrium counterpart. For weak field intensities  $h_0$  the transition between the dynamically disordered and ordered phases is second-order. As  $h_0$  increases, this transition becomes first-order, with coexistence observed between the two phases, suggesting the existence of a dynamical tricritical point. However, this remains a debated topic due to the lack of direct numerical verification.

Other studies have analysed the system response to oscillating fields considering quenched randomness in different conditions. In particular, the case of randomly switching external fields was the subject of intense studies through the mean-field approach [136]–[138], revealing the presence of order-disorder phase transition and tricritical points.

These studies approach quenched randomness in two distinct ways. In one case, randomness arises from site-dependent variations in the external field, as influenced by structural heterogeneity. In another, randomness is embedded in the spin-flip dynamics, where each spin's susceptibility to flipping is site-dependent, mimicking the effects of a local bias field superimposed on the uniform external field.

A different approach involves considering each magnetic moment of the structure coupled with the same external field (fixing the field amplitude independently from the lattice sites) but embedding the quenched randomness on the easiness with which each spin flips. This mimics the presence of an effective molecular field (bias local field) induced by a random heterogeneous structure that does not screen the external field. This picture can be represented by considering the same external field superimposed on a local, non-constant bias field which depends on the lattice site  $i$ . The effective local field now reads  $h_{\text{eff},i} = h_0 \sin(\omega t) + h_{b,i}$ . The Ising model with defects shares similarities with the RFIM in terms of quenched randomness. Here, we analyse the response to an oscillatory external field, aiming to understand how defects and quenched randomness influence the DPT.

### 5.2.2 The model with defects

We now present Monte Carlo simulations on the kinetic Ising model with defects. The results presented here build upon and adapt original findings, also reported in [53].

Averaging over quenched randomness presents significant challenges for numerical simulations, leading most studies to rely on mean-field or effective-field theories. As discussed in the previous chapter, equilibration times are notably longer in systems with quenched randomness compared to homogeneous systems, particularly at low temperatures. In this regime, the need for highly efficient algorithms becomes critical. The  $N$ -Fold way algorithm effectively addresses these challenges by dramatically improving computational efficiency and accelerating equilibration, especially in the low-temperature regime. This improvement is crucial for the current analysis, as quenched randomness lowers the temperature of the dynamic phase transition. Faster equilibration enables the simulation of multiple replicas within a shorter timeframe while maintaining the precision required for accurate parameter estimation.

The standard order parameter proves inadequate for capturing the effects of spatial symmetry breaking caused by defects. Instead, we focus on the local average magnetization per cycle  $Q_i$ , as introduced by Korniss et al. [114] and later employed by Vatansever and Fytas [121] as an insightful measure in the presence of random bonds. For heterogeneous systems, we define the order parameter:

$$\hat{Q} = \frac{1}{N} \sum_i |Q_i|, \quad (5.9)$$

where  $Q_i$  quantifies the individual behaviour of each spin  $i$  as in Eq. (5.8). This parameter identifies whether a spin is locked or follows the oscillating field and aggregates this information to indicate how many spins fail to follow the field oscillations.

The distinction between the standard average magnetization per cycle  $Q$  [Eq. (5.1)] and  $\hat{Q}$  emerges only when spatial symmetry is broken. For homogeneous systems,  $Q$  and  $\hat{Q}$  exhibit the same behaviour. However, in systems with defects, each spin behaves differently depending on its position and interactions with neighbouring spins. This phenomenon, observed in the RBIM [121], is particularly pronounced in the two-dimensional Ising model with defects. As seen in Section 3.1, under equilibrium conditions and a zero external field, the Ising model with defects forms magnetic clusters of coherently oriented spins. When a weak oscillating field is applied, these clusters are alternately favoured and disfavoured during each half-cycle of the field. Consequently, the clusters grow and shrink cyclically, but no net magnetization is observed, leaving  $Q \approx 0$  even at low temperatures.

Additionally, we generalize the quantities introduced in Section 5.1.1, adapting them for heterogeneous systems. The dynamic susceptibility reads:

$$\hat{\chi}_Q = \sum_i (\langle Q_i^2 \rangle - \langle |Q_i| \rangle^2), \quad (5.10)$$

where we assume the fluctuation-dissipation theorem applies to each individual site. We associate the dynamic critical temperature  $\Theta_c$  with a peak in the dynamic susceptibility.

We also consider the Binder cumulant:

$$\hat{U}_Q = 1 - \frac{\sum_i \langle Q_i^4 \rangle}{3N(\sum_i \langle Q_i^2 \rangle)^2}. \quad (5.11)$$

The cumulant provides additional insights into the phase transition by quantifying deviation from Gaussian-like fluctuations of the order parameter probability distribution. This is expected to happen for  $\hat{Q}$  at low temperatures.

The numerical results for the kinetic Ising model with defects at  $h_0 = 0.3$  are presented in Fig. 5.4. These simulations incorporate  $N_c = 5000$  oscillation periods, discarding the initial  $N_e = 100$  periods to ensure steady-state conditions. Averages were computed over  $N_r = 50$  independent realizations of the defect configurations. The fraction of defects  $f$  and system sizes  $L$  are indicated by distinct colours and symbols, as detailed in the caption of Fig. 5.4.

Panel (a) of Fig. 5.4 illustrates the temperature dependence of the dynamic order parameter  $\hat{Q}$ , defined in Eq. (5.9). The order parameter transitions from low values in the disordered phase at high temperatures to near unity in the ordered phase at low temperatures, signalling the DPT. Increasing the defect fraction  $f$  broadens the temperature range over which the transition occurs, reflecting the smoothening effect of defects. Notably,  $\hat{Q}$  exhibits negligible finite-size effects, as curves for different system sizes overlap, highlighting its robustness as an order parameter.

Panel (b) displays the dynamic susceptibility  $\hat{\chi}_Q$ , as defined in Eq. (5.10), normalized by the total number of spins. For each of the  $N_r$  replicas, the critical temperature is determined by locating the peak position of  $\hat{\chi}_Q$ . To achieve this, a fifth-order spline is used to fit the data, ensuring precise identification of the peak. The critical temperature  $\Theta_c$  associated with the DPT is then calculated as the average of the critical temperatures obtained from all replicas.

Panel (c) presents the Binder cumulant  $\hat{U}_Q$  [Eq. (5.11)], which provides additional insight into the transition. The modification of the binder cumulant definition, particularly the inversion of site summation and thermal averaging, modifies its finite-size scaling properties. Consequently, the curves collapse onto a universal behaviour, precluding the determination of  $\Theta_c$  from the usual crossing point of Binder cumulant curves. Nonetheless, the low-temperature asymptotic value of  $2/3$  is consistent with theoretical expectations, while  $U_Q$  decreases monotonically with increasing temperature.

The finite-size scaling of the critical temperature  $\Theta_c$  is analysed in Fig. 5.5. Here,  $\Theta_c(L)$  is plotted as a function of  $L^{-1}$ , and the linear fit confirms the scaling relation  $\Theta_{c,\infty} - \Theta_c(L) \sim L^{-1}$ . This result yields an estimate for the critical temperature in the thermodynamic limit,  $\Theta_{c,\infty}$ , and aligns with scaling behaviour observed in defect-free systems [114], suggesting a critical exponent  $\nu \approx 1$ .

The dependence of the thermodynamic critical temperature  $\Theta_{c,\infty}$  on  $f$  and  $h_0$  is represented in Fig. 5.6. Linear interpolations indicate that  $\Theta_{c,\infty}$  decreases linearly with both  $f$  and  $h_0$ . In the right panel, the static critical temperature for the defect-free Ising model [9] is marked with a red dot, which is consistent with the  $h_0 \rightarrow 0$  limit. For low defect fractions ( $f < 0.04$ ) and weak fields ( $h_0 < 0.7$ ), the critical temperature can be

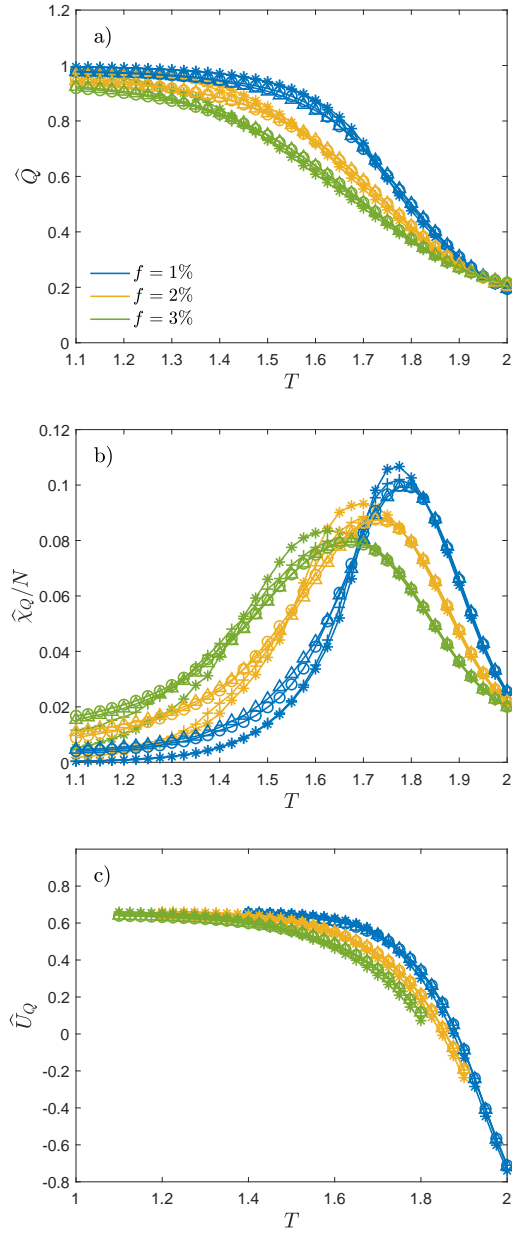


Figure 5.4: Dynamic behaviour of the two-dimensional kinetic Ising model with defects. Quantities are shown as functions of temperature. Colours represent defect fractions  $f = 0.01$  (blue),  $0.02$  (yellow),  $0.03$  (green), and symbols denote system sizes  $L = 60$  (\*),  $180$  (o),  $260$  ( $\Delta$ ). (a) Local order parameter  $\hat{Q}$  [Eq. (5.9)], (b) dynamic susceptibility  $\hat{\chi}_Q$  [Eq. (5.10)], and (c) Binder cumulant  $U_Q$  [Eq. (5.11)]. Error bars are omitted for clarity but are comparable to marker sizes.

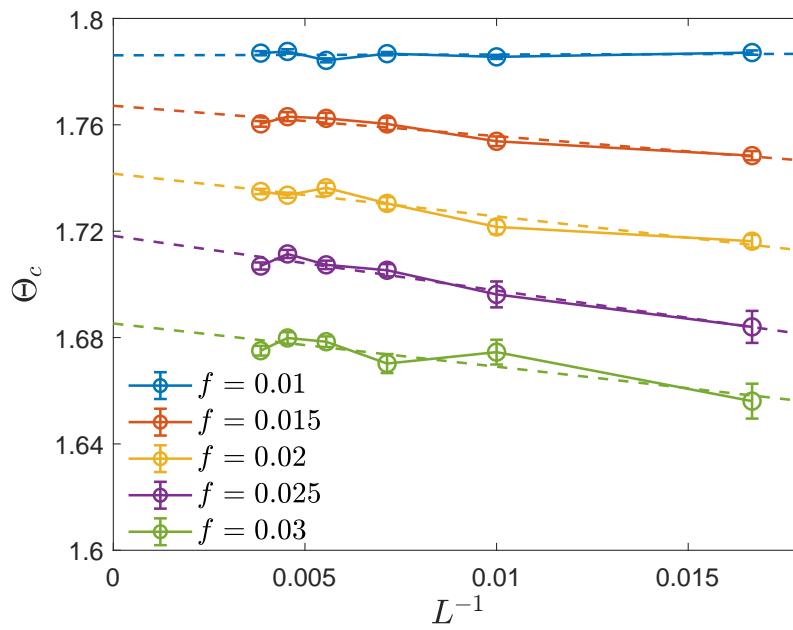


Figure 5.5: Finite-size scaling analysis of the critical temperature  $\Theta_c$  for various defect fractions and  $h_0 = 0.3$ . A linear fit suggests  $\Theta_c(L) \sim L^{-1}$ . Error bars represent variability across  $N_r = 50$  defect realizations.

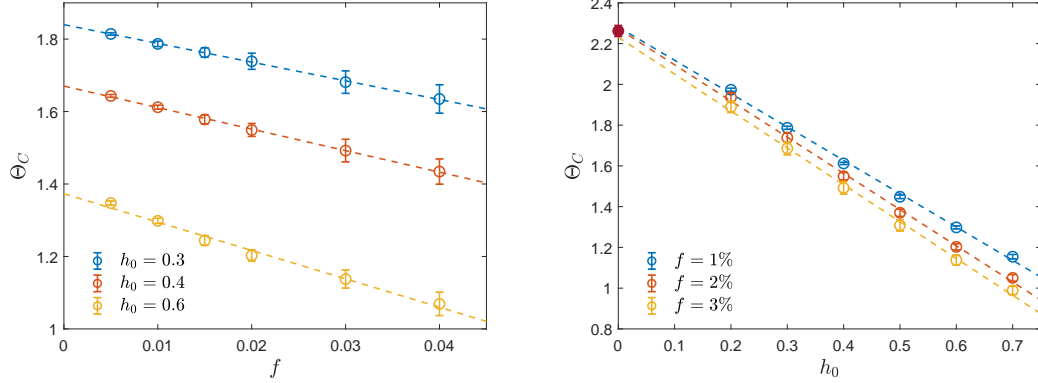


Figure 5.6: Critical temperature  $\Theta_{c,\infty}$  as a function of defect fraction  $f$  (left) and field amplitude  $h_0$  (right). Dashed lines indicate linear fits. The red point in the right panel marks the thermodynamic critical temperature for the defect-free model.

described by the empirical relation:

$$\Theta_{c,\infty} = T_c - h_0(a + bf), \quad (5.12)$$

where  $T_c$  is the static critical temperature, and  $a$  and  $b$  suitable constants.

These findings confirm that increasing heterogeneity through higher defect fractions reduces the critical temperature and favours the disordered phase. This behaviour aligns with intuitive expectations. The modified order parameter reduces computational demands, but its insensitivity to finite-size effects prevents the determination of critical exponents and universality classes through conventional scaling analyses.

### 5.2.3 Dynamic local properties of the model with defects

We continue our analysis by examining the local order parameter defined in Eq. (5.8). In our simulations, this quantity is computed and visualized in Fig. 5.7 for the specific case of  $f = 0.025$  and  $h_0 = 0.3$ . The upper panel illustrates the system behaviour at high temperatures, which resembles the homogeneous case under similar conditions. Most spins exhibit  $Q_i \approx 0$ , except in regions with a high concentration of positive or negative defects. Near the transition temperature, as shown in the middle panel, this effect becomes more pronounced. Wider regions are influenced by the surrounding defects, leading to the formation of distinct domains with positive and negative  $Q_i$  values.

At low temperatures, depicted in the lower panel, the system evolves into two prominent clusters with opposite  $Q_i$  values. Only a narrow boundary of “undecided” sites, where  $Q_i \approx 0$ , remains and oscillates under the influence of the external field. These maps bear resemblance to those presented by Vatansaver and Fytas [121] for the RBIM. However, in this model, the broken spatial symmetry in the low-temperature regime is more pronounced.

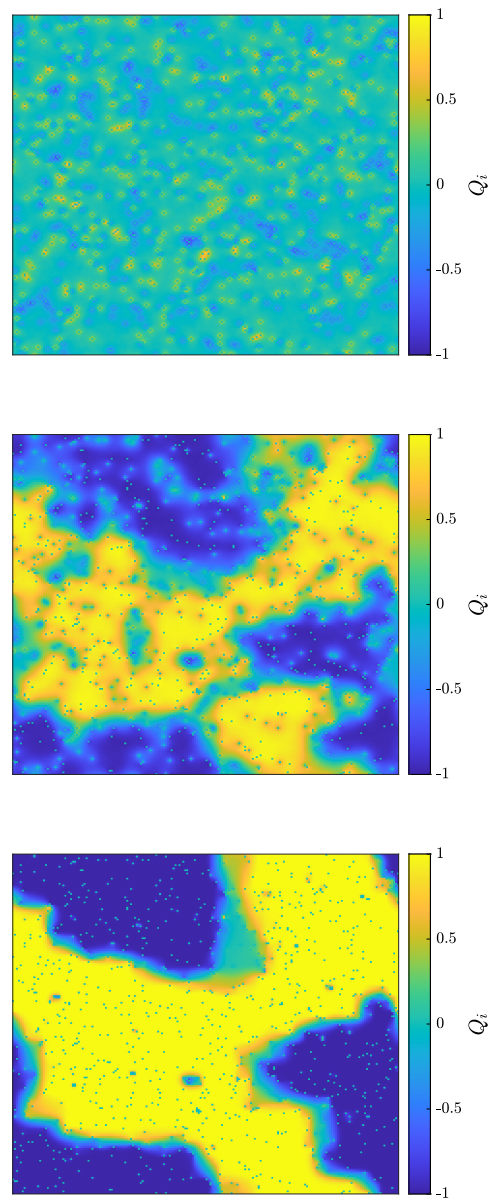


Figure 5.7: Local order parameter  $Q_i$  at different temperatures for  $f = 0.025$  and  $h_0 = 0.3$  and for a system of size  $L = 200$ . Upper panel: high-temperature regime  $T = 2.5$ ; middle panel: transition regime  $T = 1.6$ ; Lower panel: low-temperature regime  $T = 1$ .

In the RBIM, global ordering persists, and all spins align. By contrast, the presence of defects in our model results in clusters of non-oscillating spins with opposite orientations. This behaviour mirrors observations under static conditions, suggesting that the dynamic transition shares significant similarities with its static counterpart.

The concept of the “influence of neighbouring sites” was introduced and formalised in Section 2.3.3 through the definition of the local potential,  $\phi_i$ , which depends on the distribution of defects. We now examine whether  $\phi_i$  is correlated with the local dynamic properties of the system.

Figure 5.8 illustrates the correlation between the local order parameter  $Q_i$  and the local average magnetization per cycle for a system of size  $L = 260$ , with  $h_0 = 0.3$  and various defect fractions. The top panel quantifies the relation between  $\phi$  and  $Q$ . It has been generated using  $N_r = 30$  replicas simulated under critical conditions ( $T = \Theta_c$ ). To quantify the correlation, we computed the Spearman correlation coefficient, which exceeds 0.9 for all cases. This indicates a strong positive correlation between the local potential  $\phi_i$  and the local average magnetization per cycle. Furthermore, all curves collapse onto a single trend regardless of the defect fraction,  $f$ . This suggests that the relationship  $Q(\phi)$  is independent of  $f$ , demonstrating that  $\phi_i$  effectively captures the influence of defects in pinning the free sites. The bottom panel shows the relationship  $\phi_i(Q_i)$  at different temperatures for a system with  $f = 0.02$ . The correlation remains strong for  $T \geq \Theta_c$  but weakens as the temperature decreases below the critical point.

#### 5.2.4 Tuning the DPT with randomness

The presence of defects alters the dynamic properties of the system. In particular, systems with the same number of defects can show completely different behaviour depending on the presence or absence of regions with a high unbalance of defects (high potential regions). It is therefore essential to investigate the link between the dynamic properties (such as the critical temperature and the height of the susceptibility peak) and the distribution of defects.

First of all, we need to define a quantitative parameter describing the overall defect distribution. To this aim, we consider  $\phi_{\text{def}}$  as defined by Eq. (2.39). As investigated in Appendix A,  $\phi_{\text{def}}$  follows a Gaussian distribution for random configurations with standard deviation and expected value following the relationship  $\sigma_{\phi}, \overline{\phi_{\text{def}}} \sim f^{-0.3} L^{-1}$ .

To be able to explore a larger range of values for  $\phi_{\text{def}}$ , we devise a numerical algorithm that produces a configuration with desired value  $\phi_{\text{def}} = \hat{\phi}_{\text{def}}$ . Starting from a random configuration, the algorithm displaces the defects to minimize the measure  $(\phi_{\text{def}} - \hat{\phi}_{\text{def}})^2$  with a simulated annealing procedure. Configurations with different  $\phi_{\text{def}}$  are represented in Fig. 5.9.

For low  $\phi_{\text{def}}$ , defects dispose forming dipoles of opposite defects value. In this way, positive and negative defects balance out their relative influence in the surrounding area and the local potential remains limited over all the space. High  $\phi_{\text{def}}$  induce the separation of positive from negative defects and, consequently, the formation of two distinct areas with high potential values (in absolute value), as indicated by the colour in the bottom right panel. Therefore,  $\phi_{\text{def}}$  captures the strength of the defect effect, differentiating

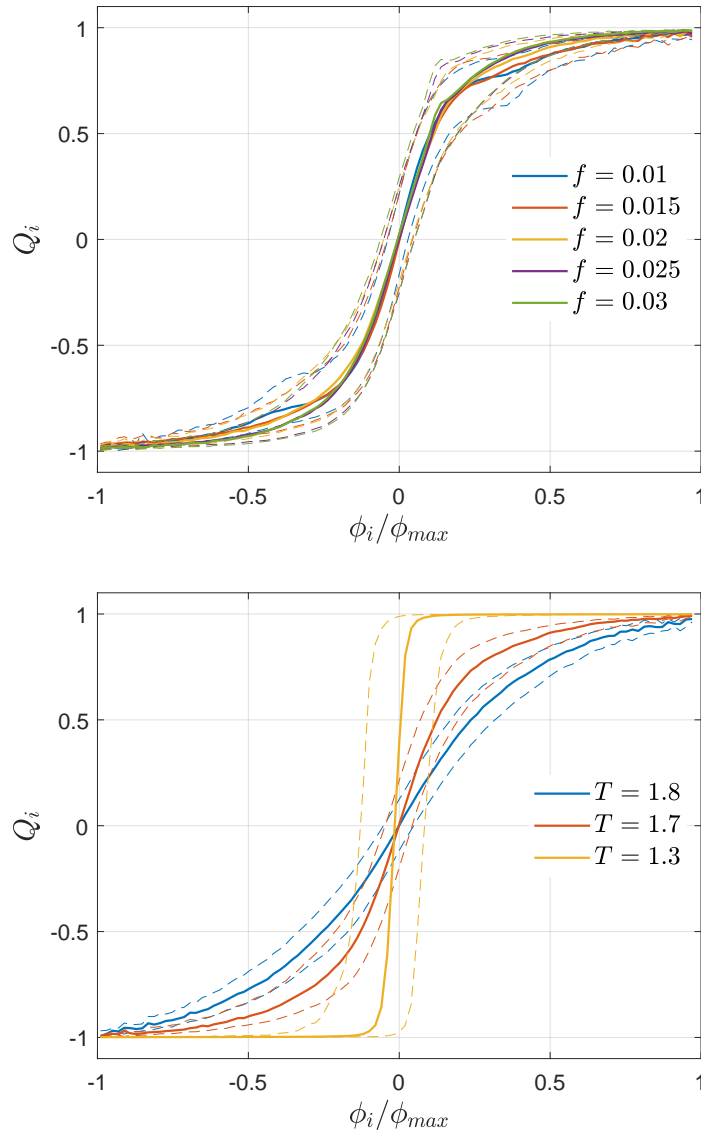


Figure 5.8: Correlation between the local potential  $\phi_i$  and the local average magnetisation per cycle  $Q_i$  for different fractions of defects at the critical temperature in the top panel, and for  $f = 0.02$  and different temperatures in the bottom panel. The solid lines report the median value of the potential for sites with local average magnetisation per cycle  $Q_i$ . The dashed lines indicate the first and third quartiles.

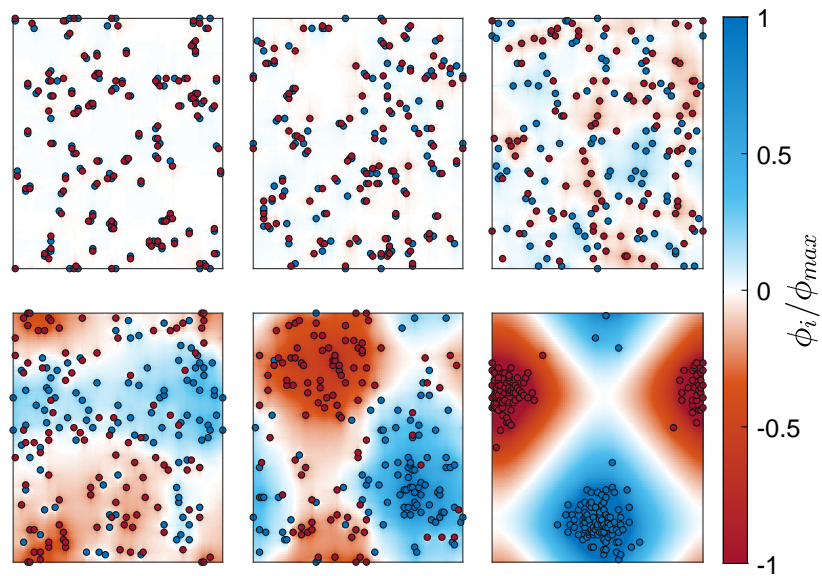


Figure 5.9: Defects configuration with increasing potential index value  $\phi_{\text{def}}$ . Top row, from left to right:  $\phi_{\text{def}} = 0.049$ ,  $0.065$  and  $0.13$ ; bottom row, from left to right:  $\phi_{\text{def}} = 0.26$ ,  $0.52$  and  $0.98$ . Each configuration shows the local potential distribution. The colour bar indicates the intensity of the potential. Blue (red) circles represent positive (negative) defects.

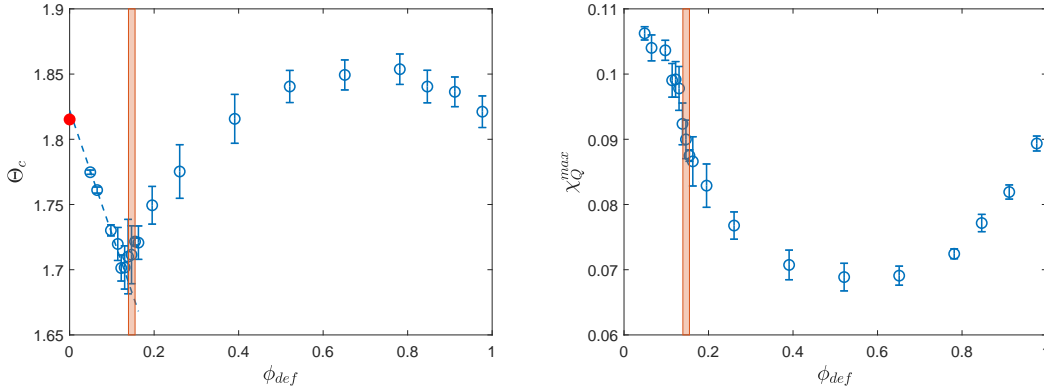


Figure 5.10: Dynamical properties for the system with defects as a function of the configuration potential index. The orange rectangle indicates the range of  $\phi_{def}$  values related to random configurations (one standard deviation of difference from the average  $\phi_{def}$  of random configurations). Left panel: critical temperature. Right panel: dynamic susceptibility peak.

configurations in which free spins are more constrained by the defect position from the ones resembling homogeneous structures. For this reason,  $\phi_{def}$  is a good candidate to be highly correlated with dynamical properties.

To verify the correlation between the potential index and the system's dynamical properties we investigate the dynamic response of  $N_r = 200$  defect configurations covering the range  $\phi_{def} \in [0, 1]$ . Each configuration is simulated for  $N_c = 5000$  period of oscillation, over a temperature range encompassing the dynamic critical temperature. For these simulations,  $h_0 = 0.3$ ,  $f = 0.02$  and  $L = 100$  were selected. We assume the findings to hold also for systems at the thermodynamic limit. For this reason, the critical temperature and the susceptibility peak were approximated with  $\Theta_c(L = 100)$  and  $\chi_Q^{max}(L = 100)$  respectively.

Fig. 5.10 summarises our results. The left panel represents the critical temperature as a function of the potential index. The orange rectangle indicates the range of values within a standard deviation  $\sigma_\phi$  from the average  $\overline{\phi_{def}}$ , locating the position of random configurations on the x-axes. Interestingly, the lowest critical temperature is registered for quasi-random configurations. We deduce the most effective strategy to favour the DDP is to distribute defects randomly.

The linear interpolation for  $\phi_{def} \rightarrow 0$  coincides with the critical temperature for the homogeneous system indicated by the red dot. This supports the thesis that in low potential index configuration, positive and negative defects are distributed compensating each other. From random configuration, as the potential index increases, the critical temperature increases as well, until reaching a point of maximum. Within this region, areas with strong local potential emerge. Free spins in such areas have a preferential direction of orientation and, as a result, become less affected by the oscillating field. The DOP becomes favoured.

This trend reverses for  $\phi_{\text{def}} > 0.8$ . To generate configurations with such strong potential, the defects cluster within small regions. The riff, representing spins at  $\phi_i \approx 0$ , which locates an equal distance between positive and negative defects widens and more spins act like in the homogeneous condition. Consequently, systems with the lowest and highest potentials, resembling, respectively, a super-multipole of shielded defects and two opposing super-clusters, exhibit a dynamic critical temperature comparable to that of a system without defects.

The right panel of Fig. 5.10 presents the dynamic susceptibility peak  $\chi_Q^{\text{max}}$  as a function of the potential index. Once again, the orange rectangle indicates the region occupied by random configurations. The limit for  $\phi_{\text{def}} \rightarrow 0$ , which coincides with the homogeneous (defect-free) system has the highest value. We can conclude that defects decrease the susceptibility peak, independently from the actual disposition of defects, and cause a smoothening of the transition.

We repeat the same analysis but for a different measure of the defect's effect on the system. The Delaunay triangulation [90], [139] is employed to analyse the spatial configuration of defects within the system under periodic boundary conditions. For each triangle in this triangulation, the area  $A_i$  is computed alongside the sum  $e_i \in \{-3, -1, +1, +3\}$  of the values of the defects located at its vertices. The normalized areal index  $\mathcal{A}$  is defined as:

$$\mathcal{A} = \frac{\sum_{\text{triangles}} |e_i| A_i}{\sum_{\text{triangles}} A_i}. \quad (5.13)$$

This index quantifies the geometric influence of the defect distribution, varying within the range  $[+1, +3]$ . Higher values correspond to larger Delaunay triangles whose vertices contain defects of the same sign, reflecting significant clustering effects.

For the same  $N_r = 200$  configurations used in the potential analysis, we derive the normalised area index  $\mathcal{A}$  and correlate the measure with the dynamical properties. Fig. 5.11 shows the Delaunay construction of the configurations shown in Fig. 5.9. Red (blue) triangles represent regions with three positive (negative) defects at the vertexes, whereas orange (light blue) triangles represent regions with two positive (negative) and one negative (positive) defects at the vertexes. Interestingly, configurations with minimum and maximum potential indexes do not correspond to configurations with minimum and maximum areal indexes. For example, the bottom right panel has the same normalised area index as the top right panel. The top middle panel has the minimum  $\mathcal{A}$  and the bottom middle has the maximum  $\mathcal{A}$ .

The correlation between the normalised area index and the dynamic properties is summarised in Fig. 5.12. The right panel demonstrates a near-linear decline in the magnetic susceptibility peak as  $\mathcal{A}$  increases. This trend highlights that the normalised configuration index and specifically the quantity and size of triangles serve as a reliable measure of the sharpness of the DPT.

Additionally, the lack of a reduction in  $\Theta_c$  for high area-index values indicates that this metric effectively distinguishes between two scenarios: one where clustered defects strongly impact nearby regions while leaving a significant portion unaffected (as in the bottom right panel of Fig. 5.9), and another where defects are more evenly distributed,

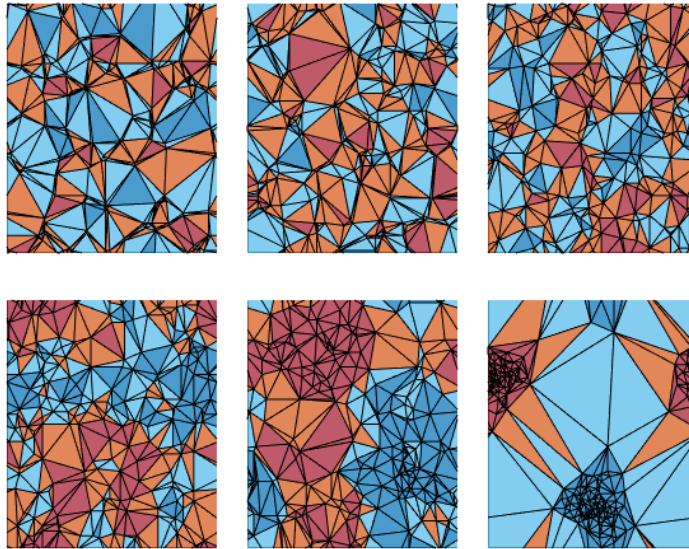


Figure 5.11: Delaunay construction for the configuration of defects shown in Fig. 5.9. The configuration index for the configurations is  $\mathcal{A} = 1.42, 1.38,$  and  $1.46$  for the top row;  $\mathcal{A} = 1.76, 2.17,$  and  $1.46$  for the bottom row. Red (blue) triangles represent regions with three positive (negative) defects at the vertexes, whereas orange (light blue) triangles represent regions with two positive (negative) and one negative (positive) defects at the vertexes.

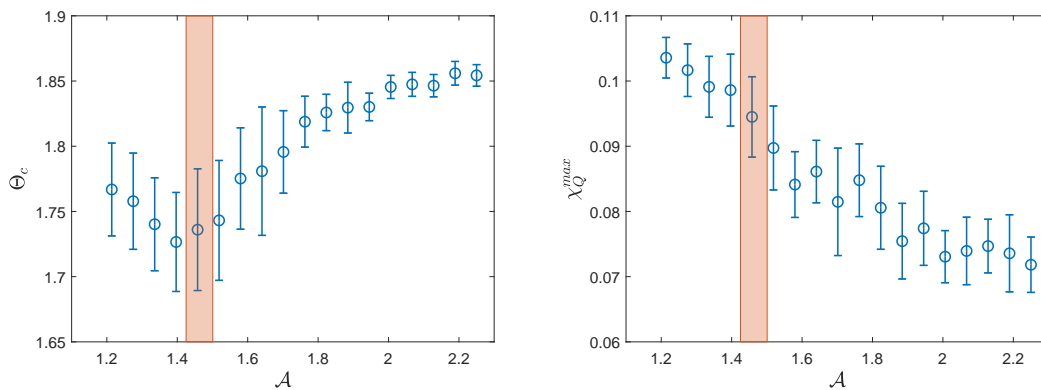


Figure 5.12: Dynamical properties for the system with defects as a function of the normalised area index. The orange rectangle indicates the range of  $\mathcal{A}$  values related to random configurations (one standard deviation of difference from the average  $\mathcal{A}$  of random configurations). Left panel: critical temperature. Right panel: dynamic susceptibility peak.

exerting control over roughly half the system (as in the bottom middle panel). The former configuration belongs to the high potential index region, whereas it is correctly recognised as having similar properties to random configurations when we consider the normalised area index.

## Conclusion

In this chapter, we investigated the Dynamic Phase Transition (DPT) in heterogeneous systems, with a specific focus on the effect of quenched randomness and defect distributions. Our findings highlighted several important phenomena that deepen the understanding of DPT and provide pathways for practical applications in real magnetic systems.

Firstly, we observed that quenched randomness universally favours the dynamically disordered phase by lowering the critical temperature  $\Theta_c$  and smoothing the transition. This is consistent with previous findings for the RBIM, affirming the robustness of this behaviour across different heterogeneous systems.

Secondly, our analysis of the model with defects revealed that the spatial arrangement of defects has a significant impact on the dynamic properties of the system. Using the potential index  $\phi_{\text{def}}$ , we showed that defect configurations with higher potential indices lead to higher  $\Theta_c$ . This is reasonable since strongly clustered defects (which are associated to high  $\phi_{\text{def}}$ ) create localized regions insensitive to the oscillating field. Conversely, random configurations minimize  $\Theta_c$ , promoting the dynamic disordered phase. This suggests that  $\phi_{\text{def}}$  serves as a reliable metric for tuning the critical behaviour of the system.

Furthermore, our results revealed the critical role of defect distribution geometry, quantified through the normalized area index  $\mathcal{A}$ . While both  $\phi_{\text{def}}$  and  $\mathcal{A}$  provide similar insights,  $\mathcal{A}$  proved particularly effective in distinguishing configurations where defects are clustered versus more evenly distributed. The correlation between these indices and dynamic properties underscores their potential utility in predictive modelling and material optimization.

From an application perspective, these findings open new avenues for designing materials with tailored dynamic responses. By rearranging defect distributions, it is possible to fine-tune the critical temperature and enhance or suppress the disordered phase. For example, fast-switching magnetic devices could benefit from configurations optimized for higher  $\Theta_c$ , ensuring stable operation under rapid external oscillations. The proposed defect displacement algorithm offers a systematic approach to achieving desired dynamic properties, making it a practical tool for engineers and material scientists.

In conclusion, the insights gained in this chapter not only contribute to the theoretical understanding of DPT in heterogeneous systems but also offer a framework for leveraging these phenomena in real-world applications. Future research could expand on these findings by exploring three-dimensional systems, other forms of randomness, or experimental validation using advanced fabrication and measurement techniques.

## Chapter 6

# Avalanches in random magnetic systems

In the previous chapters, we explored the dynamical properties of the Ising model with defects, focusing on key phenomena such as magnetization reversal and dynamic phase transitions. This analysis provided critical insights into how systems evolve under the influence of external fields, highlighting both equilibrium and out-of-equilibrium behaviour.

Building on these foundational studies, this chapter explores the progression of the magnetisation reversal, with a focus on the bursty dynamics characterized by the emergence of avalanches. By integrating the findings from the previous chapters, we analyse how local interactions give rise to global avalanche phenomena, especially under the influence of quenched randomness.

This chapter is organized as follows: we begin by reviewing the theoretical foundations of avalanche dynamics in complex systems. Next, we present original numerical simulation results, also published in [52], focusing on Barkhausen noise statistics and highlighting how quenched randomness and external perturbations shape avalanche characteristics. We then analyse interevent time (IET) statistics in complex systems, with particular attention to the impact of defects and imperfections. Our original findings, also partially published in [54], reveal that IETs for the considered process (single spin reversal under an oscillating external field) follow an exponential distribution in homogeneous systems but shift to power-law distributions when defects are introduced in both high- and low-temperature regimes.

### 6.1 Avalanches and crackling noise

Many natural and artificial systems exhibit a remarkable similarity in their response to external perturbations. Instead of releasing energy in a smooth and continuous manner, these systems often do so in discrete bursts of varying magnitude. This phenomenon is vividly observed in earthquakes, where the energy released during a single event can span several orders of magnitude, from minor tremors involving grains of dirt to catastrophic

events shifting entire continental plates [140], [141]. These bursts of activity generate signals commonly referred to as *crackling noise* [142]. Crackling noise is now recognized as a hallmark of systems poised near criticality, where long-range correlations and power-law scaling dominate their dynamics.

The term “crackling noise” was first popularized in condensed matter physics to describe the sporadic energy release observed in slowly driven systems, such as Barkhausen noise in ferromagnets [143] or acoustic emissions during material fracture [144], [145]. This concept has since expanded to include a broad spectrum of phenomena, providing a unifying framework for understanding systems where local interactions lead to emergent collective behaviour. The discrete energy bursts, referred to as *avalanches*, consist of multiple interconnected events. During an avalanche, the system reorganizes, rapidly releasing energy accumulated over time.

Avalanches and crackling noise offer a powerful lens through which to study far-from-equilibrium phenomena and non-linear dynamics, with implications spanning various fields. In Geophysics, they provide insights into earthquake dynamics [140]; in Material Science, they give information on fracture mechanisms [146]; in Neuroscience, they describe the behaviour of neuronal avalanches [147]; and in Finance, they help model market crashes. Despite their ubiquity, understanding how microscopic mechanisms, heterogeneity, and driving conditions shape macroscopic avalanche statistics and system responses remains a significant challenge.

A central theoretical tool for analysing avalanches and crackling noise is the renormalisation group (RG) theory [148]. RG theory studies how a system’s properties evolve under coarse graining, a process that reduces the system’s degrees of freedom by mapping it onto a simpler version of itself at a different scale. Iterative coarse-graining produces a flow in the space of possible system configurations, leading to fixed points where the system’s properties remain invariant under further scaling transformations. At these fixed points, systems exhibit *self-similarity*, meaning their behaviour appears unchanged across different length scales. This concept underpins universality: systems that flow toward the same fixed point share identical large-scale behaviour, even if their small-scale properties differ.

Self-similarity also explains the emergence of power-law distributions in systems exhibiting crackling noise. Physical quantities such as avalanche size or duration follow probability distributions of the form  $P(x) \sim x^{-\alpha}$ , where  $\alpha$  is a scaling exponent [142]. This power-law scaling implies that smaller avalanches occur far more frequently than larger ones, but no single characteristic scale dominates the dynamics. Instead, avalanches of all sizes contribute to the system’s behaviour, creating a fractal-like structure in time and space, as suggested by RG theory.

But how do real systems achieve the scale invariance observed in crackling noise? This phenomenon is closely tied to criticality. Systems at or near a critical state exhibit long-range correlations and collective interactions, giving rise to emergent behaviour that is self-similar across scales. Remarkably, criticality is not as rare in natural systems as one might expect. Many systems are capable of sustaining critical conditions autonomously through a process called self-organized criticality, where feedback mechanisms naturally

drive the system toward a critical state without fine-tuning [149], [150].

### 6.1.1 Power law analysis

Power laws are a key hallmark of avalanches, offering a mathematical framework to describe the distribution of event sizes, durations, or inter-event times in systems exhibiting critical dynamics. These laws manifest as straight lines on a log-log plot, with a slope corresponding to the scaling exponent, providing a clear diagnostic signature. Recognizing power laws involves analysing data for scale invariance, where no characteristic size dominates, and ensuring that deviations from the expected behaviour are not artefacts of finite-size effects or noise. By identifying these patterns, we can uncover avalanche-like dynamics in diverse systems.

Binning data is a common practice when analysing power laws, as it helps visualising the probability distribution of event sizes or other quantities [151]. Logarithmic binning is particularly well-suited for power-law distributions because it preserves the scale invariance and ensures adequate sampling in the sparsely populated tail regions. In logarithmic binning, the bin edges are defined as powers of a base  $b > 1$ , such that the edges of the ( $i$ )-th bin are:

$$\text{Bin edges: } [b^{i-1}, b^i), \quad (6.1)$$

where  $i = 1, 2, 3, \dots$ , and  $b$  is chosen to suit the data range and desired resolution. The counts in each bin,  $N_i$ , are calculated as the number of data points falling within these bounds. To convert the bin counts into a probability density that accounts for the varying bin widths, the normalized bin height  $p_i$  is computed as:

$$p_i = \frac{N_i}{N \cdot (b^i - b^{i-1})}, \quad (6.2)$$

where  $N$  is the total number of data points, and  $b^i - b^{i-1}$  is the width of the  $i$ -th bin. This normalization ensures that the area under the histogram approximates the probability distribution.

Logarithmic binning helps reveal the scaling region in power-law data, typically appearing as a straight line on a log-log plot. Another suitable approach uses the cumulative distribution function (CDF), which avoids binning entirely and is defined as:

$$P(X \leq x) = \frac{\text{Number of events with } X \leq x}{N}. \quad (6.3)$$

One of the most reliable approaches to analysing power laws and deriving the critical exponent is presented by the Maximum Likelihood Estimation (MLE), which we now briefly present. For extensive treatment of the topic, we refer to [152]. MLE maximizes the likelihood function, which is the probability of observing the given dataset under a specific model. The idea is to find the parameter values (especially the scaling exponent  $\alpha$  for a power-law distribution) that make the observed data most probable. This is

based on the principle that the best estimate of the parameters is the one that makes the data most likely. MLE is applicable to both continuous and discrete data, with differences in the treatment of the probability distribution. For continuous data, the probability density function of a power-law distribution is defined as:

$$p(x) = \frac{\alpha - 1}{x_{\min}} \left( \frac{x}{x_{\min}} \right)^{-\alpha}, \quad x \geq x_{\min}, \quad (6.4)$$

where  $x_{\min}$  is the lower bound above which the power-law behaviour holds, and  $\alpha > 1$  is the scaling exponent. Given  $n$  observed data points  $x_1, x_2, \dots, x_n$  such that  $x_i \geq x_{\min}$ , the log-likelihood function is:

$$\ln L(\alpha) = n \ln(\alpha - 1) - n \ln x_{\min} - \alpha \sum_{i=1}^n \ln \frac{x_i}{x_{\min}}. \quad (6.5)$$

To estimate  $\alpha$ , the log-likelihood function is maximized, yielding the solution:

$$\hat{\alpha} = 1 + n \left[ \sum_{i=1}^n \ln \frac{x_i}{x_{\min}} \right]^{-1}. \quad (6.6)$$

More often real data do not follow continuous probability distributions. For example, this happens for word frequencies in text, the number of letters or e-mails exchanged, network degree (number of connections in a network per node) distribution, and avalanches in sand piles. For this reason, a different analysis should be considered. For discrete data, the probability mass function of a power-law distribution is:

$$P(x) = \frac{x^{-\alpha}}{\zeta(\alpha, x_{\min})}, \quad x \geq x_{\min}, \quad (6.7)$$

where  $\zeta(\alpha, x_{\min}) = \sum_{k=x_{\min}}^{\infty} k^{-\alpha}$  is the Hurwitz zeta function, which normalizes the distribution. The log-likelihood function now reads:

$$\ln L(\alpha) = -n \ln \zeta(\alpha, x_{\min}) - \alpha \sum_{i=1}^n \ln x_i. \quad (6.8)$$

The scaling exponent  $\alpha$  is estimated by numerically maximizing  $\ln L(\alpha)$ , as there is no closed-form solution in the discrete case. An approximated expression  $\hat{\alpha}$  can be derived considering the discrete distribution as a continuous one in which data are rounded to the near integer value. This gives:

$$\hat{\alpha} \approx 1 + n \left[ \sum_{i=1}^n \ln \frac{x_i}{x_{\min} - \frac{1}{2}} \right]^{-1}. \quad (6.9)$$

This estimation is particularly helpful when high accuracy is not required. In particular, it provides accurate results within 1% of error for suitable  $x_{\min}$  [152].

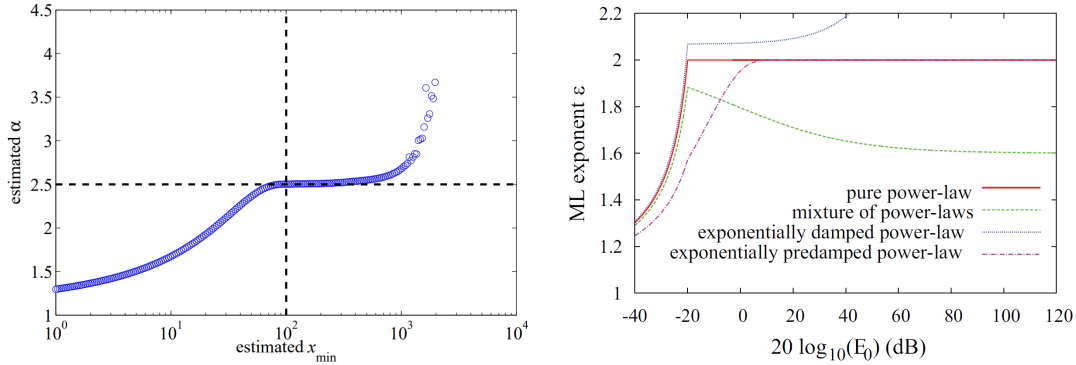


Figure 6.1: Left panel: power law exponent estimated through the MLE as a function of the lower bound for synthetic data following  $P(x) \sim x^{-2.5}$  for  $x > 10^2$ . Source [152]. Right panel: behaviour of the power law exponent estimated through the MLE as a function of the lower bound for different probability distributions. Source [153].

A key aspect of applying MLE in both cases is determining  $x_{\min}$ , which defines the range of the data that conforms to a power-law distribution. A simple procedure can be iterated to obtain a reliable estimation for  $x_{\min}$ . It consists of iterating the critical exponent estimation as a function of the lower bound  $\hat{\alpha}(x_{\min})$ . The reliable value of  $x_{\min}$  is typically identified as the point where the exponent stabilizes, reflecting the region where the data exhibits clear power-law behaviour and is no longer influenced by background noise or finite-size effects. This is shown in Fig. 6.1, where the  $\hat{\alpha}$  is represented as a function of the lower bound  $x_{\min}$ , for a synthetic distribution generated from a power law distribution with  $\alpha = 2.5$  and  $x_{\min} = 10^2$ .

The curve exhibits a plateau starting from  $x_{\min} = 10^2$ , indicating a stabilisation of the estimation not subjected to slight changes in  $x_{\min}$ . This method is straightforward and relatively simple to apply. However, it is subjective and sensitive to fluctuations. For this reason, a quantitative method is desirable. This is achieved by considering a quantitative comparison between the reliability of the fit made at different  $x_{\min}$  by using Kolmogorov-Smirnov (KS) distance [154]. The KS distance [155] is a statistical measure of the goodness of fit between the empirical Cumulative Distribution Function (CDF) of the data and the CDF of the power-law model. If we indicate with  $S(x)$  the CDF for the empirical data, and with  $P(x)$  the theoretical CDF given by  $\hat{\alpha}(x_{\min})$ , then the KS distance is defined as:

$$D(x_{\min}) = \max_{x \geq x_{\min}} |S(x) - P(x)| \quad (6.10)$$

Then, the best estimation for  $x_{\min}$  is given by the choice that minimises the KS distance, and therefore the difference between the fitted distribution and the theoretical one.

Power laws can often be challenging to recognize, as their apparent presence in data may sometimes be misleading. A meticulous analysis involving statistical tests and model comparison is crucial to verify whether the observed distribution truly follows a power law or is better represented by other fat-tailed distributions, such as log-normal or

stretched exponential forms. This process includes assessing goodness-of-fit, evaluating scaling ranges, and accounting for finite-size effects or data truncation. Without careful scrutiny, the risk of mischaracterising the underlying dynamics increases, leading to incorrect interpretations of the processes driving the observed phenomena.

Many methodologies were devised to test the presence of a power law. A qualitative indication of the presence of a power law can be obtained by considering the power law exponent as a function of the lower bound  $\hat{\alpha}(x_{\min})$ , as introduced above [153]. The left panel of Fig. 6.1 shows the main differences between the power-law and other types of distributions. As  $x_{\min}$  is changed, and different parts of the distribution are used for the fit, the characteristics of the empirical probability distributions emerge. The true power law can be recognised as a straight line. Deviations from this behaviour can be indications of exponential dampening or a mixture of power laws.

A quantitative estimation of the agreement between empirical data and the proposed theoretical distribution is given by the Goodness-Of-Fit (GOF) Test [152]. The GOF test utilizes the KS distance to assess the agreement between the empirical data and the fitted power-law model. If the empirical KS statistic ( $KS_e$ ) falls below a predefined threshold, the fit is considered optimal, and the estimated power-law exponent is deemed acceptable. However, determining this threshold is not straightforward, as several factors influence the result, such as the number of measurements used in the fit and the estimated power-law exponent. To address this challenge, ( $KS_e$ ) is compared to the KS distance ( $KS_s$ ) between synthetic data generated using the estimated parameters ( $\hat{\alpha}, \hat{x}_{\min}$ ) from the fitted power-law model. Importantly, the parameters ( $\hat{\alpha}, \hat{x}_{\min}$ ) are not used as estimates for the synthetic data but are instead independently fitted. By repeating this comparison  $N$  times with different independent synthetic datasets, we can assess the reliability of the empirical fit. A  $p$ -value is then calculated as the fraction of times  $KS_e < KS_s$  holds true. If  $p > 0.1$ , the power-law distribution is considered a valid model for the empirical data.

Importantly, the  $p$ -value is strongly subjected to the number of measurements participating in the fit. This is represented in Fig. 6.2, where the  $p$ -value for the GOF test from different distributions is represented as a function of the number of measurements  $n$ . As  $n$  increases, the  $p$ -value for empirical data following non-power law distributions (log-normal and dampened exponential) drops rapidly at 0, indicating, as expected, rejection of the power law hypothesis for these cases.

## 6.2 Barkhausen noise statistics

*Barkhausen Noise* (BN) is one of the most iconic out-of-equilibrium processes in magnetic systems, characterized by avalanches and crackling noise. When a magnetic system in the ferromagnetic phase is subjected to a slowly varying external field that induces magnetization reversal, the magnetization evolves through abrupt, discrete jumps of varying magnitude. First discovered by Heinrich Barkhausen in 1919 [143], [156], BN provided the first indirect evidence for the existence of magnetic domains and domain walls in ferromagnetic materials. The phenomenon arises from the collective motion of

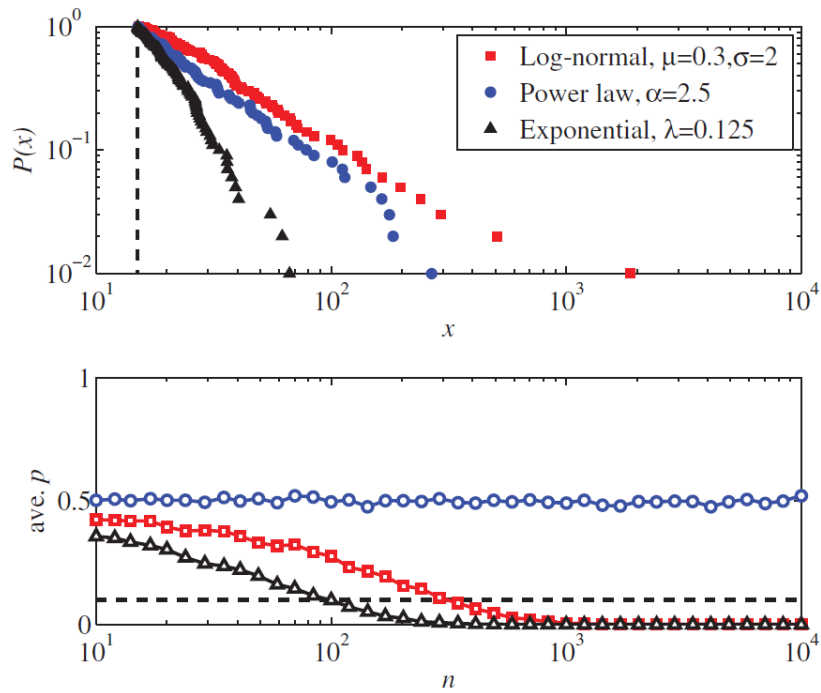


Figure 6.2: Top panel: probability distribution derived from synthetic data generated following fat-tailed distributions. Bottom panel: performances on the GOF test for the identification of the power law. The  $p$ -value is shown as a function of the number of measurements. It quickly drops to zero for the log-normal and exponential distributions and remains at 0.5 for the pure power law distribution. Source [152]

domain walls as they overcome energy barriers imposed by material imperfections [157].

Experimentally, these magnetization jumps, denoted  $\Delta M$ , follow a power-law distribution:

$$P(\Delta M) \sim (\Delta M)^{-\tau}, \quad (6.11)$$

where the exponent  $\tau$  depends on the specific material. Here, the notation  $\tau$  is adopted for consistency with the standard literature on BN.

Studying BN avalanches offers valuable insights into the universal properties of out-of-equilibrium systems, such as scaling laws and critical exponents. These features establish analogies between BN and other phenomena exhibiting crackling noise, including earthquakes and plastic deformation. Moreover, understanding BN has significant practical implications for magnetic device design, as it affects material performance, signal fidelity, and overall reliability. The statistical analysis of BN allows identifying and controlling the factors that govern avalanches and paves the way for the development of materials with tailored magnetic responses.

Numerical simulations have proven instrumental in advancing our understanding of BN. Since BN is largely attributed to material imperfections, quenched randomness models have been extensively studied. In particular, the RFIM at zero temperature has been analysed in three, four, five, and six dimensions [158], demonstrating strong agreement between experimental findings and theoretical predictions. Comparisons of critical exponents suggest that experimentally observed systems belong to the same universality class as these models.

Despite significant progress, the role of temperature in BN remains relatively poorly explored in both experimental and theoretical studies. Early investigations within the framework of self-organized criticality [159], [160] highlighted the pronounced influence of temperature on BN. Experimental studies by Puppin and Zani [161] revealed that the critical exponent  $\tau$  for BN in thin Fe films varies with temperature, decreasing from room temperature to 10 K. This temperature dependence has been corroborated by Monte Carlo simulations of the RBIM [52] and RFIM [162], both of which reproduce the trend observed experimentally.

### 6.2.1 Temperature behaviour of the Barkhausen noise statistic

To investigate the interplay between temperature and randomness in the emergence of power laws and avalanches associated with BN, we analysed a two-dimensional Ising model with defects at non-zero temperatures. Building on the approach presented in [52], we here modify and align the performed analysis with the theoretical framework outlined in the previous section.

Monte Carlo simulations were conducted in the low-temperature regime, below the critical temperature. To ensure computational efficiency, particularly in the presence of defects, we employed the  $N$ -Fold way algorithm. The simulations examined defect fractions  $f = 0.01, 0.02, \text{ and } 0.03$ , over a range of temperatures:  $T = 0.6, 0.7, 0.8, 0.9, 1.0, 1.1, 1.2, \text{ and } 1.3$ . The system was driven by an oscillating magnetic field with an

amplitude of  $h = 1$  and a period of  $P = 10^6$ , chosen to ensure that the system completes magnetization reversal during each half-cycle, characteristic of the DDP.

The presence of defects markedly altered the magnetization dynamics compared to a homogeneous system, where reversal typically occurs in a single large jump. Defects introduced metastable states along the evolution path, temporarily trapping the system and significantly slowing the reversal process, especially under slow field variation. In such scenarios, the system exhibited quasi-equilibrium behaviour.

Ten distinct defect configurations for each selected temperature and defect fraction were considered and simulated for ten hysteresis cycles. Magnetization was recorded at specific times  $t_n = t_0 + n\Delta t_{\text{meas}}$ , where  $\Delta t_{\text{meas}}$  represents the measurement interval. Magnetization jumps were calculated as the differences between consecutive measurements. To address potential artefacts arising from the finite measurement interval, consecutive jumps of the same sign were aggregated, preventing large intrinsic jumps from being artificially decomposed into multiple smaller ones. This procedure ensured that the results accurately reflected the intrinsic behaviour of the system rather than artefacts.

**Role of sampling time frequency** The sampling interval  $\Delta t_{\text{meas}}$  is a critical parameter influencing the analysis of BN statistics. Figure 6.3 illustrates its effect for a system with  $L = 200$  at a temperature  $T = 1.3$  during a single hysteresis cycle. Panel (a) shows the probability distribution of magnetization jumps for various  $\Delta t_{\text{meas}}$  values in the case of  $f = 0.02$ .

In oversampling conditions (green downward triangles), large jumps are artificially split into smaller ones due to random fluctuations in the quasi-equilibrium regime. This results in an exponential cut-off, with no jumps larger than  $\Delta M > 0.01$  observed. As  $\Delta t_{\text{meas}}$  increases, the statistics begin to encompass a broader range of magnetization jumps, revealing a clear power-law behaviour from  $\Delta M > 0.01$  (a threshold slightly exceeding the amplitude of thermal fluctuations) up to a maximum observable cluster size of approximately  $\Delta M \approx 2$ . Within this range, the power-law exponent is consistent with experimental observations  $\tau \approx 1.7$ . However, further increases in  $\Delta t_{\text{meas}}$  lead to the frequent observation of larger clusters, disrupting the power-law behaviour.

The validity of the power-law hypothesis was tested using the GOF test described earlier. Panel (c) shows the  $p$ -value of the test as a function of  $\Delta t_{\text{meas}}$ . The power-law behaviour is most evident for intermediate  $\Delta t_{\text{meas}}$  values, where the magnetization jump statistics cover a broad range of jump sizes. The  $p$ -value peaks in this range, confirming the power-law hypothesis ( $p$ -value  $> 0.1$ ).

Panel (b) presents the variation of the estimated power-law exponent  $\tau$  with  $\Delta t_{\text{meas}}$  for different defect fractions. For  $\Delta t_{\text{meas}}$  values within the power-law regime,  $\tau(\Delta t_{\text{meas}})$  reaches a plateau, particularly for  $f = 0.01$  and  $f = 0.03$ . In both undersampling and oversampling conditions, the estimated  $\tau$  is too low or too high, respectively, aligning with qualitative expectations from earlier analyses. Notably, the defect fraction  $f$  strongly influences this behaviour, as shown in panel (c). Systems with higher defect fractions exhibit power-law behaviour across a broader range of  $\Delta t_{\text{meas}}$  values, reflecting the impact of randomness on the dynamics.

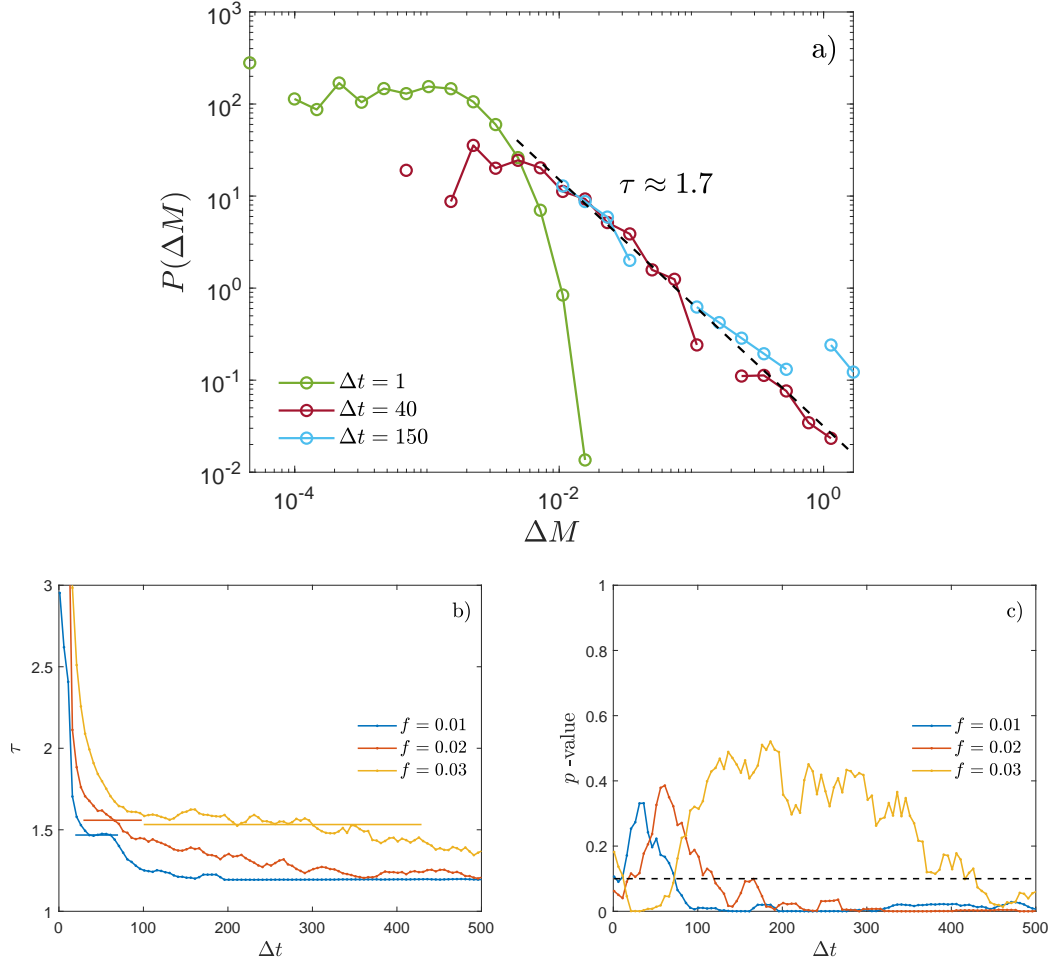


Figure 6.3: Effect of the sampling time  $\Delta t_{\text{meas}}$  on BN statistics. Panel (a): Probability distribution of magnetization jumps for three sampling conditions. Green downward triangles: oversampling condition; red squares: well-sampled condition; light blue upward triangles: undersampling condition. Solid lines guide the eye, and the black dashed line represents the best-fit power law for  $\Delta M > 0.01$  in the well-sampled condition. Panel (b): Estimated power-law exponent  $\tau$  as a function of  $\Delta t_{\text{meas}}$  for three defect fractions. Solid lines indicate the range of  $\Delta t_{\text{meas}}$  values where power-law behaviour is observed. Panel (c):  $p$ -value of the GOF test for the power-law hypothesis versus  $\Delta t_{\text{meas}}$ . The dashed line indicates the threshold for power-law acceptance ( $p$ -value  $> 0.1$ ).

**The role of temperature and defect fraction** We now analyse the separate effects of temperature and defect fraction on the avalanche probability distribution. The sampling interval is fixed at  $\Delta t_{\text{meas}} = 5$ , simulating an experimental scenario where the measurement time is predetermined.

Panel (a) of Fig. 6.4 illustrates the impact of temperature for a system with size  $L = 200$  and defect fraction  $f = 0.02$ . At  $T = 0.9$ , a pure power-law behaviour  $P(\Delta M) \sim \Delta M^{-\tau_c}$  is observed, with a critical exponent  $\tau_c \approx 1.7$ . For temperatures above the critical value ( $T > T_c$ ), the power law exhibits an exponential cut-off, similar to the behaviour observed under large  $\Delta t_{\text{meas}}$ . Conversely, for  $T < T_c$ , the distribution deviates from the pure power law, as it includes several additional large jumps.

This temperature dependence can be understood in terms of metastable states. As discussed in Section 3.1, the equilibrium configuration of the 2D model with defects in a zero-field environment contains clusters and numerous energetic local minima, corresponding to metastable states. At higher temperatures, thermal fluctuations dominate, fragmenting transitions between metastable states into smaller jumps. By contrast, at lower temperatures, the system tends to move more rapidly into stable energy minima, bypassing metastable states along the magnetization reversal path. A fine-tuning of temperature is therefore necessary to observe a pure power-law distribution.

Panel (b) of Fig. 6.4 examines the effect of the defect fraction  $f$  at a fixed temperature of  $T = 0.9$ . Subcritical behaviour is observed for  $f < 0.02$ , where the power-law behaviour is disrupted by large jumps, while supercritical behaviour emerges for  $f > 0.02$ , where an exponential cut-off dominates. The number of metastable states, directly controlled by the defect fraction, modifies the critical temperature  $T_c$  at which a pure power law is observed.

Finally, panel (c) of Fig. 6.4 presents the avalanche distributions for various defect fractions under critical conditions, where  $T = T_c(f)$ . Interestingly, these distributions share the same critical exponent,  $\tau_c \approx 1.7$ , consistent with experimentally observed values in magnetic materials at low temperatures [161]. Notably, panel (c) also suggests that  $\tau_c$  is independent of temperature within the critical regime.

This latter observation, however, contrasts with previous numerical studies of the RBIM and experimental observations [161], [162], which report a temperature dependence of  $\tau_c$ . The discrepancy between the model with defects and the RBIM may arise because the two models belong to different universality classes, leading to distinct critical exponent behaviour. Additionally, differences between the numerical results and experimental data may stem from variations in magnetization sampling methods. In experiments, magnetization jumps are typically identified as differences between consecutive metastable states, which are determined directly from the hysteresis cycle by identifying regions where magnetization remains constant over many consecutive measurements.

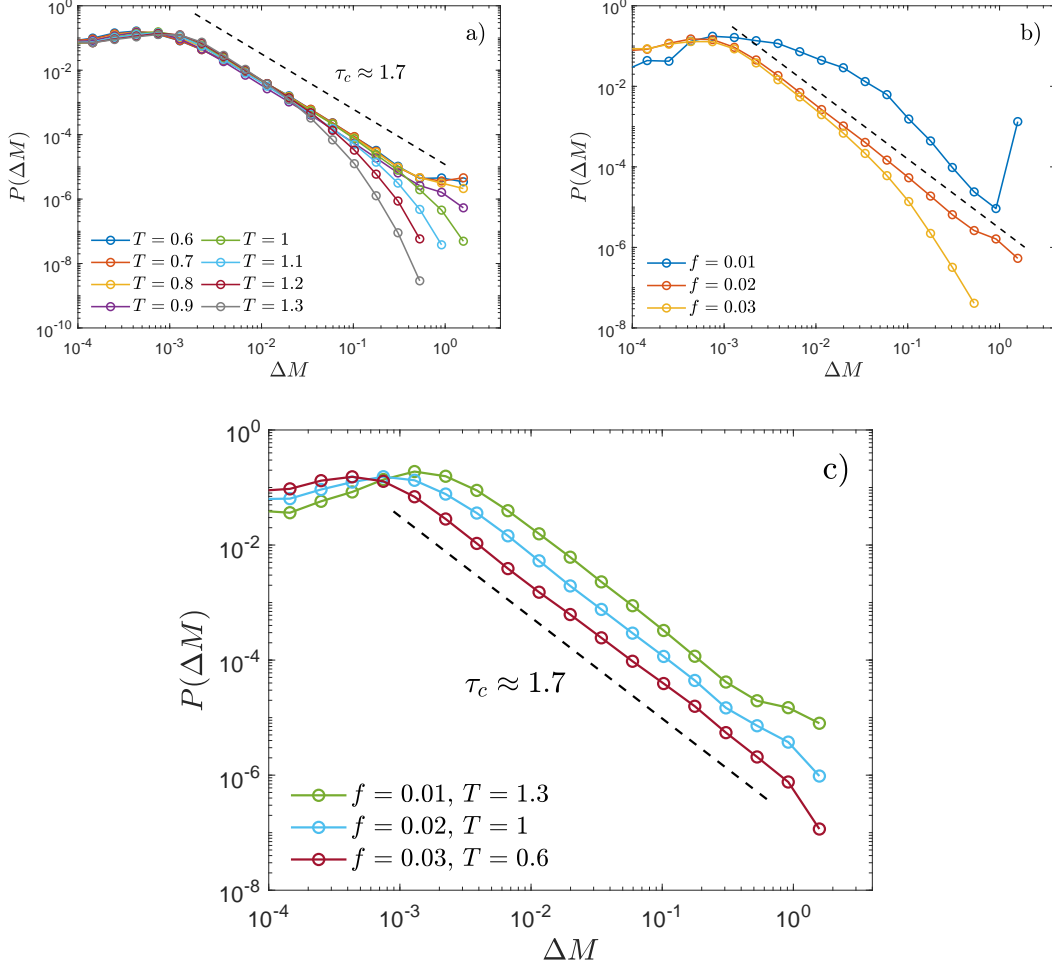


Figure 6.4: Effect of temperature (panel a) and defect fraction (panel b) on the avalanche probability distribution. The power law exhibits an exponential cut-off in supercritical conditions ( $T > T_c$  or  $f > f_c$ ) and is enriched by large jumps in subcritical conditions ( $T < T_c$  or  $f < f_c$ ). Under critical conditions, a pure power law with  $\tau_c \approx 1.7$  emerges for  $\Delta M > 10^{-4}$ , as indicated by the black dashed lines. Panel (a): defect fraction fixed at  $f = 0.02$ . Panel (b): temperature fixed at  $T = 0.9$ . Panel (c): power-law distributions under critical conditions for different defect fractions, with temperatures adjusted to maximize the  $p$ -value of the GOF test for  $\Delta M > 5 \times 10^{-3}$ . All cases share the same critical exponent  $\tau_c \approx 1.7$ .

### 6.3 IET statistics in complex systems

Building on the understanding of BN and the role of quenched randomness in generating power laws, we shift our focus to the temporal aspect of event distributions. Specifically, we investigate the distribution of inter-event times (IETs), the waiting times between successive events, emphasizing the emergence of power-law distributions as heterogeneity is introduced. While power laws in avalanche sizes arise from spatial correlations that intensify at criticality, power-law IET distributions are a manifestation of a broad spectrum of relaxation times. This behaviour underscores the intrinsic complexity of the system, where disorder and, more broadly, heterogeneity strongly influence temporal correlations.

IETs often follow an exponential distribution, indicative of memoryless, Poissonian processes with a characteristic waiting time. This behaviour represents a scenario where each element of the system operates independently, unaffected by the timing of prior events. Queueing theory provides a useful analogy: in a simple queue where tasks or individuals arrive independently and at random intervals, the inter-arrival times are exponentially distributed [163]. However, in complex systems, such as email correspondence or the exchange of letters [164]–[166], elements no longer act independently. Instead, individuals make informed decisions about when to respond, influenced by prior interactions and contextual factors. These dependencies between events lead to IET distributions that are heavy-tailed, often taking the form of power laws. Such patterns, where the probability of long waiting times decays more slowly than exponentially, reveal strong temporal correlations. Similarly, earthquakes exhibit heavy-tailed frequency distributions of events [140], further demonstrating how complexity and interdependence shape temporal statistics.

Our analysis highlights the pivotal role of quenched randomness in driving this transition. We observe that homogeneous systems without defects typically exhibit uniform relaxation dynamics characterized by a single timescale. By contrast, disorder fragments the energy landscape into numerous metastable states, each with its own relaxation dynamics. This multiplicity of timescales results in a broad, heavy-tailed distribution of waiting times. The emergence of power-law IETs reflects the system's capacity to produce complex, scale-invariant temporal structures due to randomness.

To investigate IET distributions, we consider the Ising model as a representative prototype for homogeneous systems. An oscillating magnetic field,  $h(t) = h_0 \sin(\omega t)$ , is superimposed on the system, driving it out of equilibrium. The macroscopic behaviour of the system has been already studied in Chapter 5. The primary events of interest are spin-flip reversals, which can occur in response to the external field during each half-cycle. Each spin in the system is tracked independently, resulting in a maximum of  $N$  spin-flip reversals per half-cycle.

To distinguish genuine spin reversals from random fluctuations, the time evolution of each spin  $s_i(t)$  is monitored and averaged over a half-cycle:

$$s_i(n) = \langle \sigma_i(t) \rangle_n = \frac{1}{P} \int_{t_i}^{t_f} \sigma_i(t) dt, \quad (6.12)$$

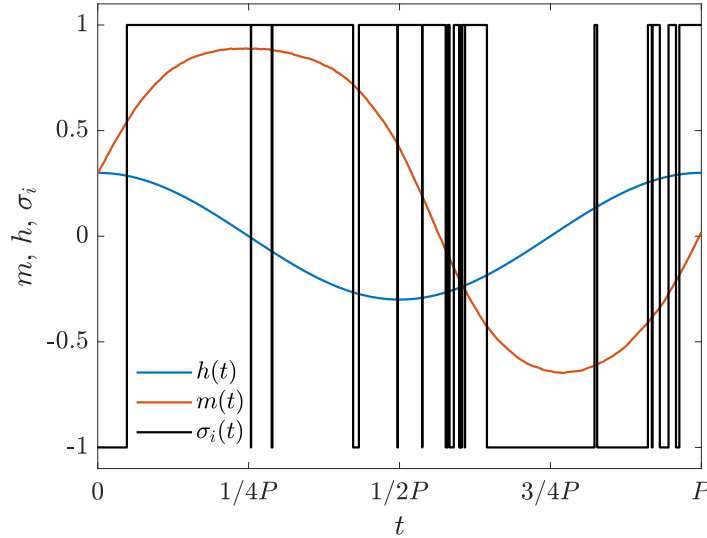


Figure 6.5: Time evolution of a homogeneous system in the presence of an oscillating magnetic field. The magnetization (orange) and external field (blue) are shown, along with the direction of an individual spin (black), which undergoes a reversal event after a half-cycle.

where  $t_i = nP/2 + t_0$  and  $t_f = (n + 1)P/2 + t_0$ , with  $t_0 < P/2$  as the initial time. The choice of  $t_0$  has minimal influence on the results so that we set  $t_0 = 0$ . Consequently, averages are computed over successive  $P/2$  intervals. Figure 6.5 illustrates the tracked physical quantities.

In Figure 6.5, the orange and blue lines represent the magnetization and external field, respectively. The simulation, performed for a system of size  $L = 400$ , with  $h_0 = 0.3$ ,  $P = 258$ , and critical temperature  $T = 1.8$ , demonstrates a periodic, deterministic magnetization behaviour characteristic of the MD regime. The black line depicts the time evolution of an individual spin, highlighting stochastic thermal fluctuations that occasionally cause spin flips, even when the external field is at its maximum (at  $P/4$  and  $3P/4$ ). In this example, a reversal event occurs after one half-cycle.

The IET is defined as the number of half-cycles between two consecutive spin-flip reversals at the same site. This metric effectively captures the dynamic behaviour of the system: short IETs are expected to be found in the DDP, where most spins flip during each half-cycle, while longer IETs emerge in the DOP, characterized by infrequent spin reversals driven by the external field.

The IET probability distribution is obtained by monitoring the system's time evolution over many cycles, aggregating statistics across all lattice sites. The homogeneous, defect-free system serves as a baseline for comparison against heterogeneous systems with defects, which will be discussed in Section 6.3.3. These two cases exhibit distinct features and significant differences in their dynamic behaviour.

### 6.3.1 Poissonian IET statistics in homogeneous systems

We begin by examining the homogeneous case using Monte Carlo simulations implemented with the  $N$ -Fold way algorithm and Glauber dynamics. Figure 6.6 illustrates the reversal IET probability distribution,  $P_{\text{rev}}(n)$ , at various temperatures spanning the dynamic critical temperature,  $\Theta_c$ . This analysis allows us to explore the conditions in both the DDP and the DOP. For all considered temperatures and field amplitudes, the data closely follow an exponential distribution:

$$P_{\text{rev}}(n) \sim e^{-\lambda n}. \quad (6.13)$$

To estimate the average IET,  $\langle n \rangle(T)$ , we use MLE, yielding  $\langle n \rangle(T) = \lambda^{-1}$ . Panel (b) of Figure 6.6 shows  $\langle n \rangle$  as a function of the rescaled temperature,  $T - \Theta_c$ , for different field amplitudes  $h_0$ .

Interestingly, in both the DOP and DDP, the data exhibit an exponential relationship:  $\lambda^{-1} \sim \exp(-kT)$ , where  $k$  is a constant. In the DOP,  $k$  is independent of the field amplitude  $h_0$ , whereas in the DDP, it displays only a weak dependence on  $h_0$ . It is worth noting that  $\lambda < 1$  in the DDP, despite the lower bound of  $\langle n \rangle$  being 1 due to discretization. A value of  $\lambda^{-1} < 1$  simply indicates a low probability of observing IETs greater than 1. Remarkably, the critical temperature  $\Theta_c$  can be identified as the point where  $\lambda^{-1}$  crosses the threshold value of 1. At lower temperatures ( $T < \Theta_c$ ), the average IET increases ( $\langle n \rangle > 1$ ), while at higher temperatures ( $T > \Theta_c$ ), there is a low probability of registering IETs greater than 1 ( $\lambda^{-1} < 1$ ).

### 6.3.2 Two-states Markov process for homogeneous systems

We now introduce a simplified theoretical framework aimed at explaining the simulation results. The key assumption is that the reversal event of each spin can be treated as an independent and identically distributed random variable. Moreover, the reversal probability does not depend on the outcome of previous events.

The behaviour of the  $i$ -th spin can be represented by a two-state Markov chain, as illustrated in Figure 6.7. Here,  $h$  denotes the average direction of the external field over a half-cycle. At each half-cycle, the  $i$ -th spin can exist in one of two states. When the average direction  $s_i$  over the half-cycle aligns with the external field, the system is in state A. Conversely, when  $s_i$  opposes the field, the system is in state B. The transition probabilities between these states are denoted by  $\alpha$  and  $\beta$ . Specifically:

- $\alpha$ : the probability of transitioning from state A to state B after a half-cycle. Since the field direction reverses each half-cycle,  $\alpha$  corresponds to the probability that a single spin does not follow the external field. Thus,  $1 - \alpha$  represents the reversal probability  $p_{\text{rev}}(i)$  for a spin in state A.
- $\beta$ : the probability of transitioning from state B to state A, i.e., the likelihood that a spin not following the field in the current half-cycle will align with it in the next. Similarly,  $1 - \beta$  represents the reversal probability for a spin in state B.

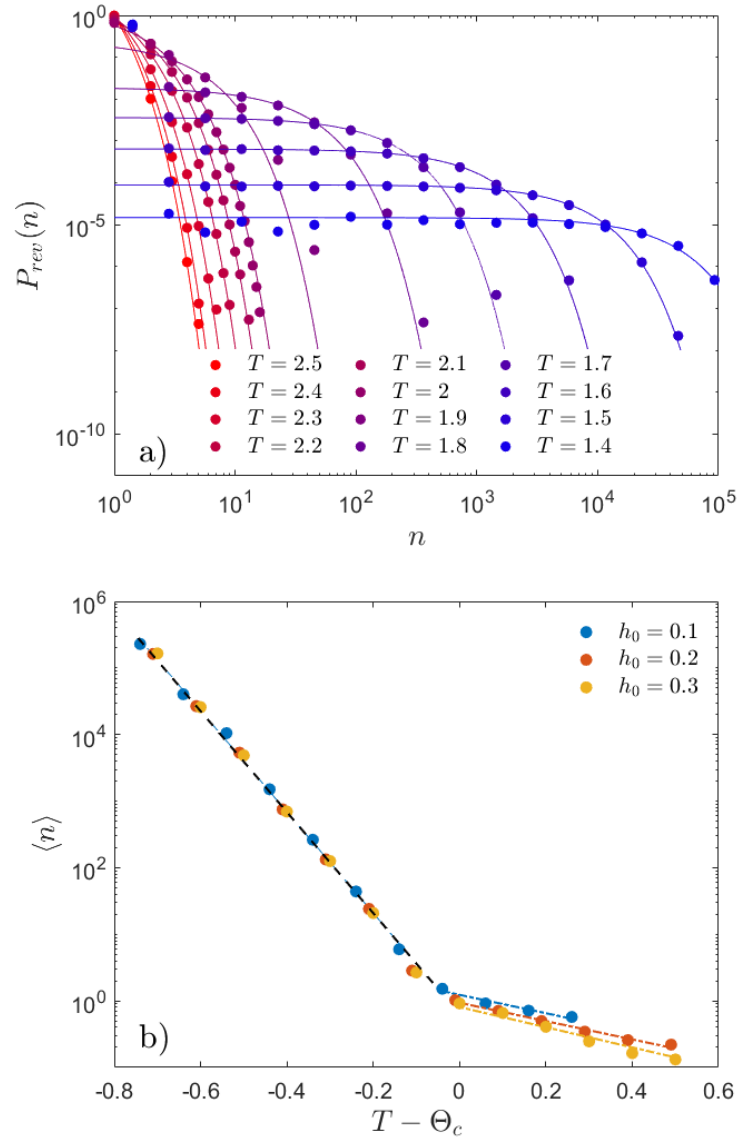


Figure 6.6: IET analysis for the homogeneous (defect-free) Ising model. Panel (a) shows the IET probability distribution at different temperatures, encompassing the DOP and DDP (here located at  $T = 1.8$ ). Markers represent data points from simulations, and solid lines show the best exponential fits. Panel (b) shows the average IETs as a function of the rescaled temperature  $T - \Theta_c(h_0)$  for different field amplitudes in a semi-logarithmic plot. Two linear fits, represented by dashed lines, are shown for the high- and low-temperature cases.

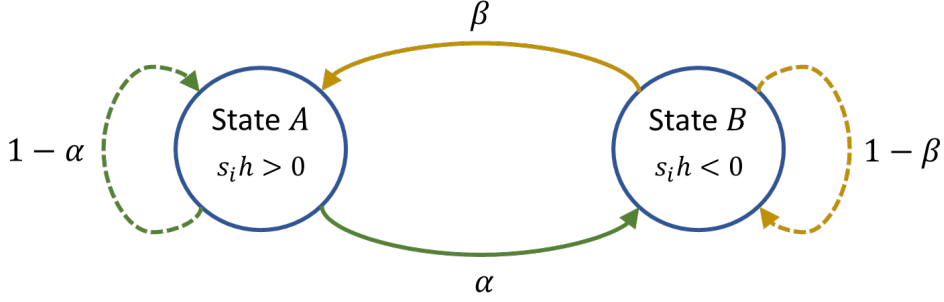


Figure 6.7: Two-state Markov chain representing the state of the  $i$ -th spin each half cycle.  $\alpha$  and  $\beta$  represent the transition rates of the Markov chain.

Starting from this Markov chain, we derive the probability distribution for the IETs. Specifically, the reversal probability after  $2n + 1$  half-cycles is given by:

$$P_{\text{rev}}(2n + 1) = s_A \alpha^n \beta^n (1 - \alpha) + s_B \alpha^n \beta^n (1 - \beta), \quad (6.14)$$

where the first term refers to the probability of observing a reversal event after  $2n + 1$  half-cycles starting from state A, and the second term corresponds to a reversal event starting from state B. Here,  $s_A$  and  $s_B$  denote the equilibrium probabilities of finding a spin in state A or B, respectively.

Using basic manipulations, Eq. (6.14) can be rewritten as:

$$P_{\text{rev}}(2n + 1) = \alpha^n \beta^n [s_A(1 - \alpha) + s_B(1 - \beta)]. \quad (6.15)$$

From Markov chain theory, the equilibrium probabilities  $s_A$  and  $s_B$  can be expressed as functions of the transition rates:

$$s_A = \frac{\alpha}{\alpha + \beta}, \quad s_B = \frac{\beta}{\alpha + \beta}. \quad (6.16)$$

Substituting these expressions into the equation above yields the probability distribution for a reversal event after  $n$  half-cycles:

$$P_{\text{rev}}(2n + 1) = (\alpha\beta)^n \left( 1 - \frac{\alpha^2 + \beta^2}{\alpha + \beta} \right). \quad (6.17)$$

This probability distribution is exponential, consistent with the initial assumption of Markovianity for the reversal events. Furthermore, the average IET  $\langle n \rangle$  can be expressed in terms of the transition probabilities as:

$$\langle n \rangle = -\frac{1}{\log(\alpha\beta)}. \quad (6.18)$$

To validate the proposed approach, we rely on Monte Carlo simulations. Transition rates  $\alpha$  and  $\beta$  are computed at various temperatures  $T$  and field amplitudes  $h_0$ , and the results for  $\langle n \rangle$  are compared with the analytical expression in Eq. (6.18).

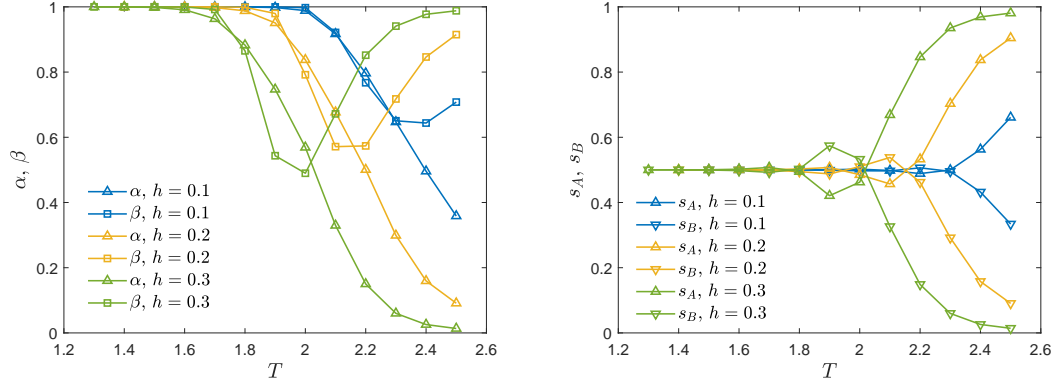


Figure 6.8: Transition rates and equilibrium probability of states for the Markov process represented in Fig. 6.7 as a function of temperature and for different choices of the external field. Left panel: transition rates  $\alpha$  and  $\beta$  computed considering direct calculation from simulations. Right panel: equilibrium probability of states  $s_A$  and  $s_B$ . Markers show direct computation from simulations; solid lines the computation from the transition rates through Eqs.(6.16).

The left panel of Fig. 6.8 illustrates the transition rates  $\alpha$  and  $\beta$  as functions of  $T$ , calculated for different values of  $h_0$ . Error bars, which are smaller than the markers, are omitted for clarity. The temperature dependence aligns with expectations. At high temperatures ( $T > \Theta_c$ ), each spin is expected to undergo a reversal event each half-cycle, compatible with  $\alpha \approx 0$ , especially for higher field intensity. Deviations observed near  $T \approx \Theta_c$  are attributed to the emergence of long-range correlations. By lowering the temperature,  $\alpha$  is expected to increase, signalling a more difficult reversal event for spins in state A.

By contrast, the behaviour of  $\beta$  is less intuitive.  $\beta$  is expected to stay close to 1 at all temperatures, indicating the low probability of observing a reversal event where the spin maintains an average direction opposite to the external field over both consecutive half-cycles. This is compatible with the data in Fig. 6.8 for both high and low temperatures. For intermediate temperatures, where  $T \approx \Theta_c$  deviations are observed. We can give an intuitive explanation for this behaviour.

Let's assume the average direction of each spin in the time interval  $\Delta t \ll P/2$ ,  $\langle \sigma(t) \rangle$ , is well represented by the magnetisation  $m(t)$ . Then, the crossing of  $m(t)$  of the zero value determines when all the spins have changed the average direction. Let's consider the case where the system is negatively magnetised and,  $h(t)$  becomes positive. If  $m(t) > 0$  happens at time  $t < P/4$  (early flip), the average direction of each spin over the half cycle is in the direction of the field, thus positive. If  $t > P/4$  (late flip), then the average direction over the half cycle is negative and no reversal has happened. Anyway, for both of these cases, each spin is oriented in the positive direction at the end of the period of oscillation. To remain in state B, a spin should undergo a late flip followed

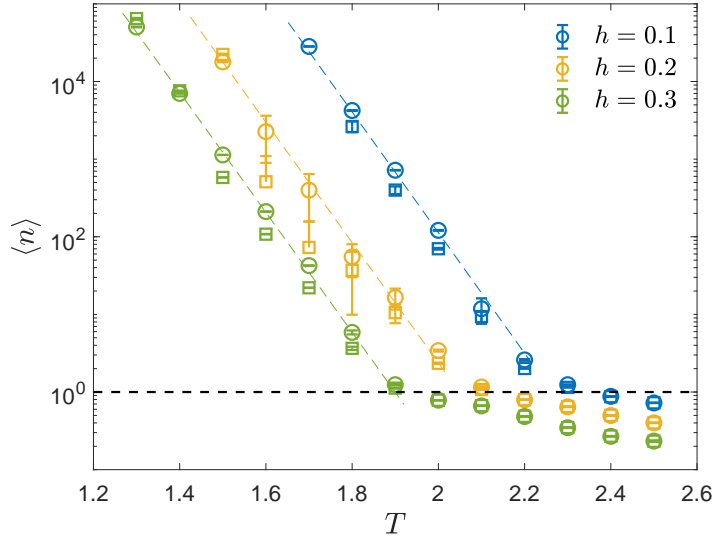


Figure 6.9: Average IET as a function of temperature for different external field amplitudes. Squares represent analytical predictions using Eq. (6.18); circles show direct calculations from simulations. Dashed lines indicate linear fits to guide the eye.

by not a reversal event (late flip or no flip at all). In this way, the behaviour of the spin is like it has undergone a reversal event maintaining in both consecutive half-cycles an average direction opposite to the external field. For  $T \approx \Theta_c$ , the magnetisation lags behind the external field. If the lag is larger than  $P/2$ , each spin undergoes a late flip at each half-cycle. This means that each spin remains always in state B, thus inducing  $\beta = 1$ . The initial assumption  $m(t) = \langle \sigma(t) \rangle$  is rather simplistic but entails the main reason why  $\beta$  differs from 1 at the critical temperature.

The right panel of Fig. 6.8 compares the equilibrium probabilities  $s_A$  and  $s_B$  obtained directly from simulations with those derived from Eqs. (6.16). Markers represent simulation results, while solid lines show the theoretical values. The agreement between the two confirms the validity of the framework. At high temperatures,  $s_A$  dominates as spins align with the external field, while at low temperatures, the field's influence diminishes, leading to  $s_A = s_B = 0.5$ .

Finally, Fig. 6.9 shows the consistency between the simulated average IET (circle markers) and the analytical prediction from Eq. (6.18) (square markers). The good agreement across temperatures and field amplitudes validates the two-state Markov chain as a reliable model for describing IET behaviour in homogeneous systems. This framework will serve as a basis for analysing the heterogeneous system behaviour.

### 6.3.3 Fat-tailed IET statistics in disordered systems

We now examine the model with defects, focusing on the system's response to an oscillating field at temperatures spanning the DPT. Simulations were performed for a minimum of  $10^3$  and a maximum of  $10^6$  cycles, depending on the temperature. Panel (a) of Fig. 6.10 presents the IET probability distributions for three different temperatures (super-critical, critical, and sub-critical conditions) with  $f = 0.025$ , system size  $L = 200$ , and external field amplitude  $h_0 = 0.3$ . A key finding is the emergence of distinct discrete power laws in both the super- and sub-critical cases, described by  $P_{\text{rev}}(n) \sim n^{-\alpha}$ .

Numerical confirmation of these power laws was achieved using the GOF test described earlier, albeit with a relaxed criterion. Specifically, we required the KS distance for empirical data to be at most five times larger than that of synthetic data. This relaxation is justified as follows: as shown in Fig. 6.2, the  $p$ -value is sensitive to the number of measurements  $n$ , with larger  $n$  leading to stricter test outcomes. Minor deviations due to exponential cutoffs or slight inaccuracies in estimating the lower bound  $x_{\text{min}}$  can cause the test to reject a valid power-law hypothesis. For the cases analysed, the number of reversal events ranged from  $n \sim 10^8$  to  $10^{10}$  in the high- and low-temperature regimes, respectively. Finite-size effects and limited defect realizations may also contribute to deviations. The relaxed criterion accommodates these factors.

Using maximum likelihood estimation (MLE) for discrete distributions, two distinct exponents were identified:  $\alpha_{\text{low}} \approx 2$  in the low-temperature regime and  $\alpha_{\text{high}} \approx 3$  in the high-temperature regime. Simulations for varying defect fractions yielded similar values, as shown in the inset of panel (a). Near the dynamic critical temperature, the IET distribution deviates from power-law behaviour.

Panel (b) of Fig. 6.10 displays the avalanche size probability distribution  $P_{\text{aval}}(S)$ . Here, an avalanche size  $S$  represents the number of connected spins undergoing reversal in the same half-cycle. At critical conditions ( $T \approx 1.6$ ),  $P_{\text{aval}}(S)$  exhibits a power-law distribution spanning four orders of magnitude, indicating collective dynamics. Interestingly, the temperature dependence contrasts with the behaviour of BN statistics analysed in Section 6.2. At high temperatures (blue upward triangles), large reversal clusters dominate, whereas at low temperatures (yellow downward triangles), an exponential cut-off is observed. At critical conditions, a power law with exponent  $\beta_c \approx 1.42 \pm 0.2$  is identified. This result was confirmed across different defect fractions, ensuring the temperature corresponding to the dynamic critical temperature  $\Theta_c(f)$ . Notably,  $\beta_c$  is independent of  $f$  within statistical uncertainty, as depicted in the inset of panel (b).

**The role of the potential** As already said, the effect of defects is to break the spatial symmetry. Once again, we consider the defect-potential defined in Eq. (2.38) which tracks the influence of defects on the free spins in the lattice. The defect-potential was already used as a useful tool to predict the local static and dynamic properties of the system (Section 3.1 and Section 5.2). We now extend the investigation to the current problem, searching for properties that correlate with it. This could enhance our understanding of the system's behaviour, increasing its predictability.

To this aim, we concentrate on local events for each site and we record the local IET

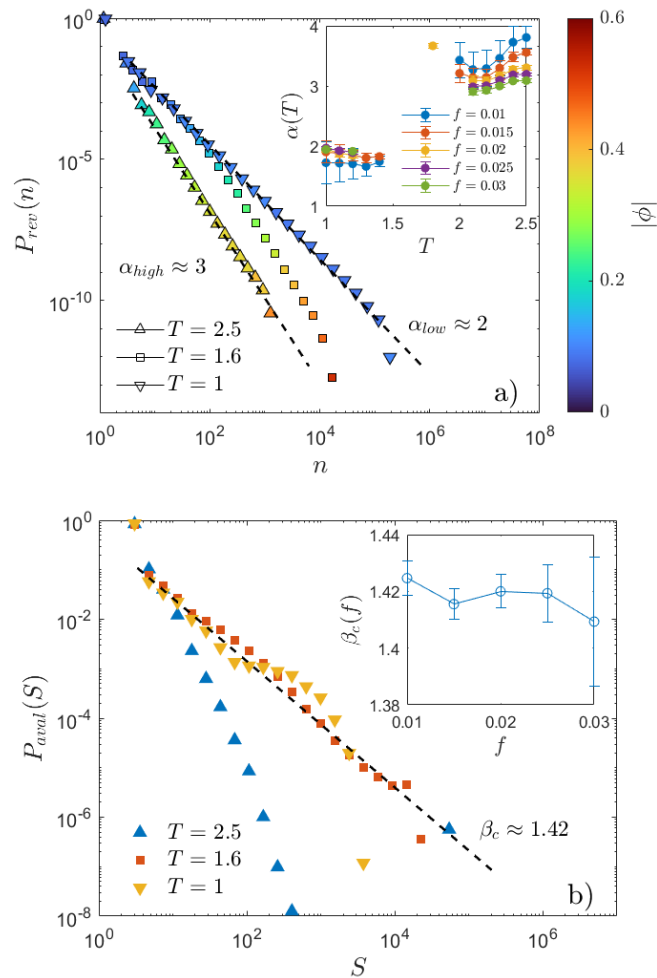


Figure 6.10: Probability distribution of panel a) the IET, and b) reversal cluster size. Simulations performed with  $P = 258$ ,  $h_0 = 0.3$ ,  $f = 0.025$  and  $L = 200$ . The different markers indicate different temperatures:  $T = 1$  (downward triangles);  $T = 1.6$  (squares);  $T = 2.5$  (upward triangles). The markers represent the logarithmic binning of the data, whereas the dashed line is the best power law fit, when applicable. Panel a): the high- and low-temperature cases show a power law behaviour with different exponents ( $\alpha_{low}$  and  $\alpha_{high}$ ). The inset shows the power law exponent as a function of temperature for different defect fractions, for the data series that give  $p$ -value of the GOF test larger than 0.1. Panel b): only the distributions in critical conditions gave a power law behaviour. At low temperatures, an exponential dampening is observed; at high temperatures, large avalanche sizes are recorded which destroys the power law behaviour. The inset shows the critical exponent for different defect fractions.

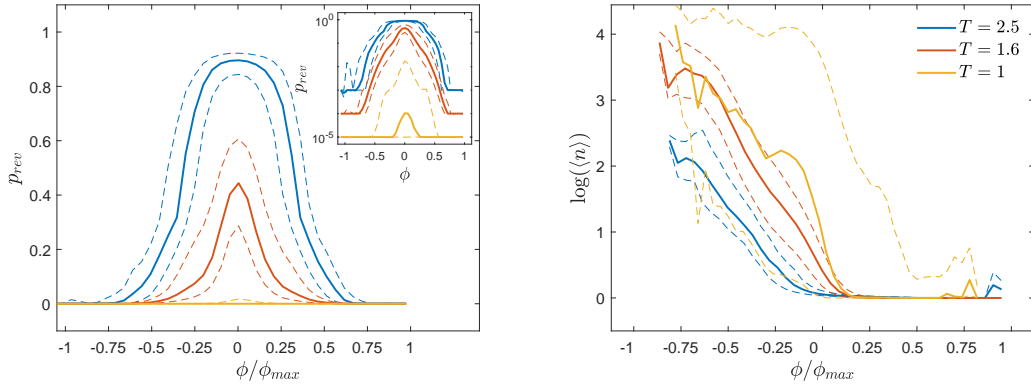


Figure 6.11: Correlation between the local potential  $\phi(i)$  and the local reversal probability  $p_{rev}$ , panel a), and the local average reversal time  $\langle n \rangle$ , panel b) for different temperatures. The solid lines represent the median whereas the dashed lines the first and third quartiles. Panel a): the inset shows the same curves in the main panel but on a semi-logarithmic scale. Simulation parameters:  $L = 200$ ,  $P = 258$ ,  $h_0 = 0.03$ ,  $P = 258$  and  $f = 0.025$ .

probability distribution. As an indicator of the local property, we derive the probability of observing a reversal event at site  $i$  in a specific half-cycle,  $p_{rev}$ . We then correlate this quantity with the local potential. Panel a) of Fig. 6.11 shows the influence of the local potential  $\phi$  (scaled by the maximum potential  $\phi_{max}$ ) over the local reversal probability  $p_{rev}$  at different temperatures and for a system with  $L = 200$ ,  $h_0 = 0.3$ ,  $P = 258$  and  $f = 0.025$ .

The solid lines represent the median whereas the dashed lines the first and third quartiles.  $p_{rev}(\phi)$  resembles a symmetric bell-shaped function. The quartiles suggest that most spins follow the displayed behaviour and, consequently, that the local potential is a well-posed quantity describing the dynamic properties of the system. For the high and critical temperature case, the local potential captures well the location of sites where the reversal is rather frequent (location of the riffs separating the regions with strong potential). Sites with a higher probability of undergoing a reversal are characterised by  $\phi \approx 0$ , whereas spins with stronger potential show a preferential direction of orientation, with  $p_{rev}$  decreasing rapidly to zero as the potential intensifies. This behaviour is also observed for the low-temperature case, as depicted in the inset showing  $p_{rev}(\phi)$  on a semi-logarithmic plot. The peak of the curve gives interesting information. In the high-temperature case,  $p_{rev}(0) \approx 1$ , suggesting almost all spins with  $\phi \approx 0$  undergo a reversal event each half-cycle (similar to the homogeneous case). At the critical temperature,  $p_{rev}(0) \approx 0.5$ .

To complement the previous analysis, we consider the local average IET for each site, distinguishing between switching events in the positive ( $-s_i(n) \rightarrow s_i(n+1)$ ) and negative ( $s_i(n) \rightarrow -s_i(n+1)$ ) directions. Panel b) of Fig. 6.11 illustrates the relationship between the local potential  $\phi$  and the average IET  $\langle n \rangle$  for switches from negative to positive. For

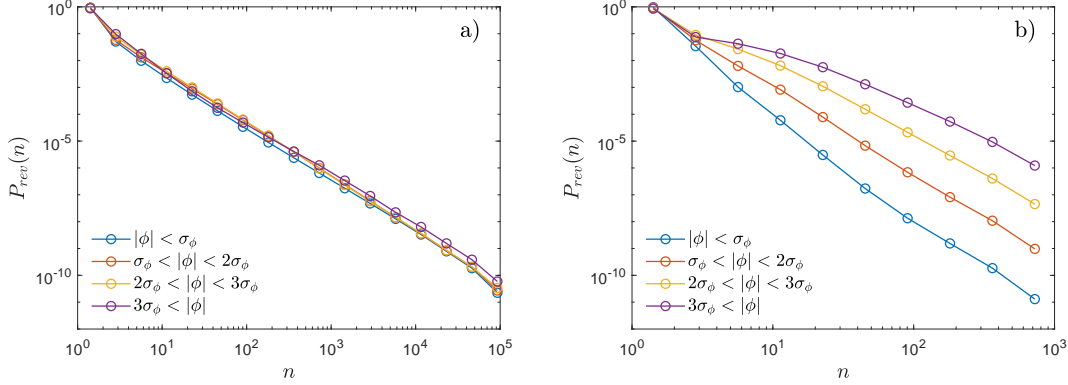


Figure 6.12: IET probability distributions for sites grouped by potential intensity. Panel (a): low-temperature regime. Panel (b): high-temperature regime.

sites with positive potential,  $\langle n \rangle$  remains null, indicating a strong propensity to align with the external field in the direction favoured by the potential. Conversely,  $\langle n \rangle$  increases significantly for  $\phi < 0$  as the temperature decreases. A specular plot is observed for switches in the opposite direction, with  $\langle n \rangle(\phi)$  mirrored across the  $\phi$  axis.

We now investigate the IET probability distribution  $P_{\text{rev}}(n)$  across sites grouped by their local potential. To achieve this, the lattice is divided into four zones based on the standard deviation  $\sigma_\phi$  of the potential distribution  $P(\phi)$ : low ( $|\phi| < \sigma_\phi$ ), medium ( $\sigma_\phi < |\phi| < 2\sigma_\phi$ ), strong ( $2\sigma_\phi < |\phi| < 3\sigma_\phi$ ), and very strong ( $|\phi| > 3\sigma_\phi$ ) potentials. For each group, we compute  $P_{\text{rev},\phi}(n)$  in the low- and high-temperature regimes, shown in panels (a) and (b) of Fig. 6.12, respectively.

In the low-temperature regime,  $P_{\text{rev},\phi}(n)$  exhibits a power-law behaviour with exponent  $\alpha = \alpha_{\text{low}}$ , independently from the potential intensity. This indicates a collective phenomenon, where mobility constraints affect all sites equally. By contrast, in the high-temperature regime,  $P_{\text{rev},\phi}(n)$  does not follow a power law as the GOF test gave  $p$ -value lower than 0.1 for all considered potential intensities. Instead, the overall power-law distribution emerges from the superposition of non-power-law distributions from different site classes, as depicted in Fig. 6.10.

Finally, the colour coding in Fig. 6.10 provides additional insights. Each bin is coloured according to the average absolute potential  $\bar{\phi}$  of the contributing measurements. In the low-temperature regime, a single colour dominates, reflecting the uniform contribution of all sites to  $P_{\text{rev}}(n)$ . In the high-temperature regime, a colour gradient appears. In particular, sites with low potential value have a lower probability of producing larger IETs. Larger IETs are associated with sites with stronger potential value.

#### 6.3.4 Four-states Markov process for heterogeneous systems

Building on the homogeneous system approach, we extend the Markov chain framework to model the system's behaviour in the presence of defects. A critical feature introduced

by defects is the spatial symmetry breaking observed at low temperatures. Indeed, as discussed in Sec. 5.2, spins in the system exhibit a preferential orientation determined by the local potential. To accurately capture the dynamics in the low-temperature regime, we include the local potential as a central element of the Markov chain framework. This incorporation is achieved through the following two modifications:

1. Expansion of the state space: We introduce an additional state variable to represent whether the considered spin aligns with its equilibrium direction. This quantity is defined as the product  $s\phi$ , where  $s$  denotes the spin orientation and  $\phi$  represents the local potential.
2. Potential-dependent transition rates: Transition rates between states are explicitly modelled as functions of the local potential. This refinement leads to a family of four-state Markov chains, where each chain corresponds to a specific value of the local potential.

These enhancements enable a detailed representation of the system's dynamics in the presence of defects, particularly at low temperatures, where the effects of local potentials are most pronounced.

A representative four-state Markov chain is illustrated in Fig. 6.13. Each state is defined by a different pair of values ( $|s\phi|, |sh|$ ). Specifically:

- State  $A_2$ : The average spin direction is aligned with both the external field and the local potential.
- State  $B_2$ : The average spin direction is aligned with the local potential but not the external field.
- State  $A_1$ : The average spin direction is aligned with the external field but not the local potential.
- State  $B_1$ : The average spin direction is misaligned with both the external field and the local potential.

In other words, the label A (or B) denotes states that are aligned (or misaligned) with the external field. Similarly, the index 1 (or 2) represents states that are misaligned (or aligned) with the local potential.

In Fig. 6.13, arrows indicate potential transitions. Where not depicted, a direct transition cannot occur. For instance, after one half-cycle, transitions from  $A_1$  to  $B_2$  or  $A_2$  to  $B_1$  are forbidden because, after one half-period,  $h$  changes sign while the local potential remains quenched. Consequently, regardless of whether the spin undergoes a reversal event, exactly one of the two products,  $s_i h$  or  $s_i \phi_i$ , changes its sign. Transitions in which both products change signs are forbidden, as are self-transitions where neither product changes the sign. This framework provides a clear visualization of reversal events, which occur when a spin transitions across the horizontal dashed line separating states  $A_1$  and  $B_1$  from  $A_2$  and  $B_2$ .

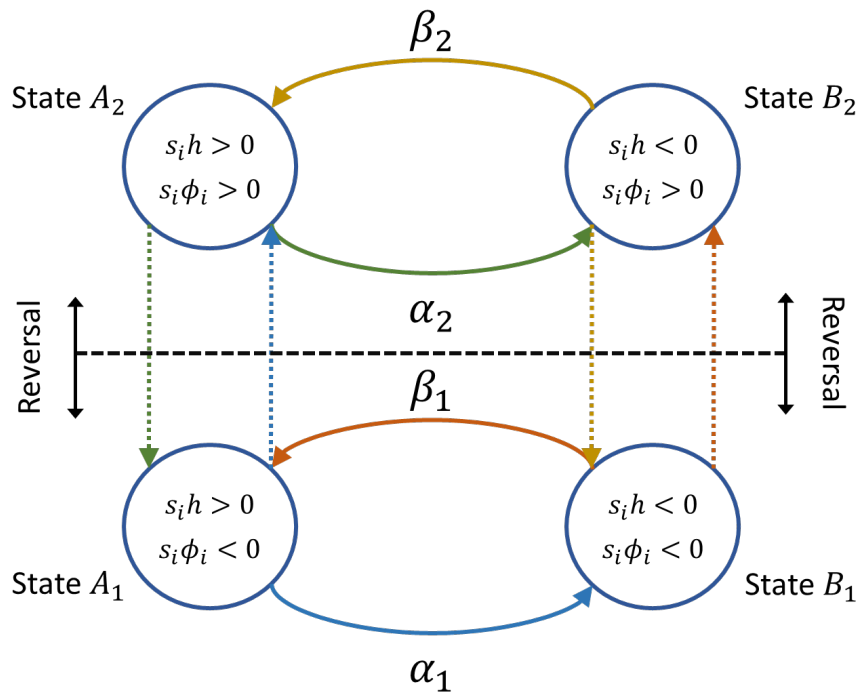


Figure 6.13: Schematic representation of the four-state Markov chain, illustrating transitions between states based on  $(|s\phi|, |sh|)$ . The dashed horizontal line indicates the boundary for reversal events.

Importantly, the proposed Markov chain exhibits a periodicity of 2. A spin cannot return to its initial state in a single transition; instead, it must pass through one of its two neighbouring states first. This periodicity necessitates careful consideration when studying the steady-state condition. A key consequence of this periodicity is that after initialization, the number of spins in states  $A_1$  and  $B_2$  at step  $t$  equals the number of spins in states  $A_2$  and  $B_1$  at step  $t + 1$ .

Regardless of the initial condition, on average, half of the spins in the lattice occupy states  $A_1$  and  $B_2$ , while the remaining half occupy states  $A_2$  and  $B_1$ . This balance arises from the symmetry in the distribution of the local potential, as discussed in Appendix A. Consequently, at every half-cycle, we can assume the number of spins in states  $A_2$  and  $B_1$ ,  $N_{A,2} + N_{B,1}$ , remains  $N/2$ , and the same holds for the sum  $N_{A,1} + N_{B,2}$ .

To compute the equilibrium state probabilities, we impose the invariance condition for the periodic Markov chain with a period of 2. As illustrated in Fig. 6.13, the transition matrix  $M$  is given by

$$M = \begin{pmatrix} 0 & \beta_2 & 1 - \alpha_1 & 0 \\ \alpha_2 & 0 & 0 & 1 - \beta_1 \\ 1 - \alpha_2 & 0 & 0 & \beta_1 \\ 0 & 1 - \beta_2 & \alpha_1 & 0 \end{pmatrix}. \quad (6.19)$$

For simplicity, we do not explicitly include the dependency on the potential  $\phi$ , though the transition rates and the transition matrix are functions of  $\phi$ .

The equilibrium probabilities of being in states  $A_1$ ,  $B_1$ ,  $A_2$ , and  $B_2$  are denoted by the column vector  $\mathbf{S} = (p_{A1}, p_{B1}, p_{A2}, p_{B2})$ . The equilibrium condition is expressed as:

$$\mathbf{S} = M^2 \mathbf{S} \quad (6.20)$$

By solving this system and applying the conditions  $p_{A1} + p_{B2} = p_{A2} + p_{B1} = 0.5$ , we obtain the equilibrium probabilities:

$$\begin{aligned} p_{A1} &= \frac{1}{2} \frac{\alpha_2 \beta_2 - \beta_1 - \beta_2 + \beta_1 \beta_2}{\alpha_1 \alpha_2 + \alpha_1 \beta_1 + \alpha_2 \beta_2 + \beta_1 \beta_2 - \beta_1 - \beta_2 - \alpha_1 - \alpha_2} \\ p_{B1} &= \frac{1}{2} \frac{\alpha_2 \beta_2 - \alpha_1 - \alpha_2 + \alpha_1 \alpha_2}{\alpha_1 \alpha_2 + \alpha_1 \beta_1 + \alpha_2 \beta_2 + \beta_1 \beta_2 - \beta_1 - \beta_2 - \alpha_1 - \alpha_2} \\ p_{A2} &= \frac{1}{2} \frac{\beta_1 \beta_2 - \beta_1 - \beta_2 + \alpha_1 \beta_1}{\alpha_1 \alpha_2 + \alpha_1 \beta_1 + \alpha_2 \beta_2 + \beta_1 \beta_2 - \beta_1 - \beta_2 - \alpha_1 - \alpha_2} \\ p_{B2} &= \frac{1}{2} \frac{\alpha_1 \beta_1 - \alpha_1 - \alpha_2 + \alpha_1 \alpha_2}{\alpha_1 \alpha_2 + \alpha_1 \beta_1 + \alpha_2 \beta_2 + \beta_1 \beta_2 - \beta_1 - \beta_2 - \alpha_1 - \alpha_2} \end{aligned} \quad (6.21)$$

To check the Markovian character of the reversal process, we conducted numerical simulations to compute the transition rates  $(\alpha_1, \alpha_2, \beta_1, \beta_2)$  using the  $N$ -Fold way algorithm with Glauber dynamics. The system size was fixed at  $L = 200$ , and the defect fraction and external field strength were set to  $f = 0.04$  and  $h = 0.3$ , respectively. Simulations were performed across various temperatures to assess the model's accuracy. The four transition rates are presented in Fig. 6.14, highlighting their dependence on

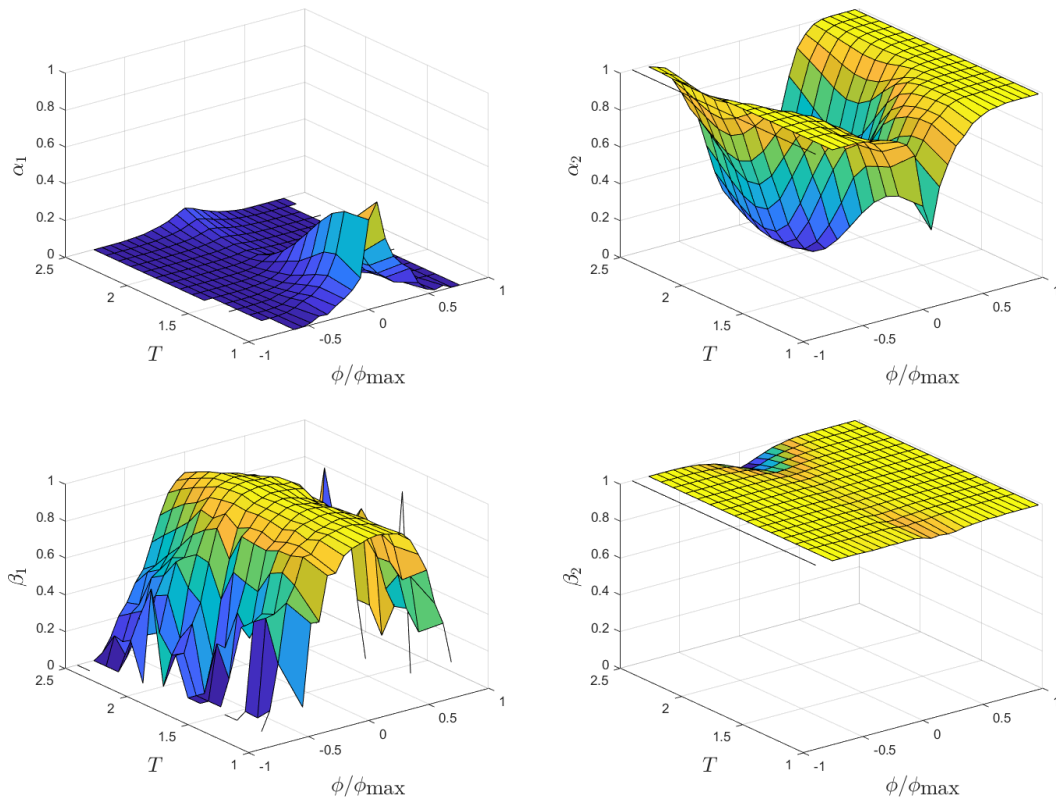


Figure 6.14: Transition rates for the four-states Markov chain model as a function of temperature and local potential.  $\alpha_1$  (top left),  $\alpha_2$  (top right),  $\beta_1$  (bottom left),  $\beta_2$  (bottom right). Simulation parameters:  $L = 200$ ,  $f = 0.04$ ,  $h_0 = 0.3$ .

temperature and local potential. To ensure reliable estimates, transition rates at a fixed temperature were averaged over all sites with the same local potential. As expected,  $\alpha_1 \approx 0$  especially at high temperatures. Indeed, starting from state  $A_1$ , the probability of ending up in the unfavoured state  $B_1$  (spin anti-aligned with field and local potential) is small compared to that of going to the favourite state  $A_2$  (spin aligned with both field and local potential). Deviations at small temperatures and local field intensity are reasonable, as each spin is also influenced by the behaviour of the neighbouring spins, potentially making state  $B_1$  more favourable. Similarly, this argument qualitatively applies also to  $1 - \beta_2$ .  $\alpha_2$  shows the probability to jump in state  $B_2$  instead of  $A_1$ , starting from state  $A_2$ . Qualitatively, it represents the probability of following the local potential instead of the external field. Reasonably, we observe  $\alpha_2 \approx 1$  for strong field amplitudes, reaching 0 for  $\phi \approx 0$  where the driving field becomes more effective. The same reasoning applies to  $1 - \beta_1$ .

Notably,  $\alpha_1 + \beta_2 = 1$  and  $\alpha_2 + \beta_1 = 1$  hold at high temperatures. Considering these expressions in Eq. (6.21), we observe  $p_{A,1} + p_{B,2} = 0.5$  and  $p_{A,2} + p_{B,1} = 0.5$ . With suitable rearrangement, we can see that the four-state Markov process can be reduced to a two-state Markov process, identical to that of the Homogeneous case analysed in Sec. 6.3.2. This indicates that the external field dominates the dynamics in this regime, overshadowing the influence of the local potential.

Next, we derived equilibrium state probabilities and reversal probabilities using Eq. (6.21) and compared these results with direct estimations obtained by tracking individual spin behaviour.

The equilibrium state probabilities  $\mathbf{S}$  for the four Markov chain states  $A_1$ ,  $B_1$ ,  $A_2$ , and  $B_2$  were analysed as functions of the local potential at three temperatures: high temperature ( $T = 2.5$ ), transition temperature ( $T = 1.7$ ), and low temperature ( $T = 1.0$ ). Fig. 6.15 illustrates these probabilities, where solid lines represent direct measurements from spin time evolution, and dotted lines correspond to theoretical predictions based on Eq. (6.21).

Regardless of temperature, spins with strong local potentials preferentially occupy states  $A_2$  and  $B_2$ , characterized by a positive product  $s\phi$ . This tendency becomes more pronounced as the temperature decreases. At high and intermediate temperatures, theoretical predictions align closely with direct measurements, and the equilibrium state probabilities are symmetric under potential sign reversal. In contrast, at low temperatures, the theoretical predictions deviate from direct measurements. Moreover, the latter shows deviate significantly from  $p_{A1} \approx p_{B1} \approx 0$  and  $p_{A2} \approx p_{B2} \approx 0.5$  for large enough  $|\phi|$ . As expected, the relations  $p_{A1} + p_{B2} = p_{A2} + p_{B1} = 0.5$  hold for both direct estimations and theoretical predictions based on transition rates.

The findings indicate that the reversal process can be well described by a four-state Markov chain at high and critical temperatures, but fails to be Markovian at low temperatures. The fundamental assumption of the Markovian model is that spin reversal is influenced solely by the local potential and the external field. However, at low temperatures, collective dynamics emerge, and the reversal of a single spin is no longer an isolated process. Instead, it is strongly influenced by the simultaneous reversal of

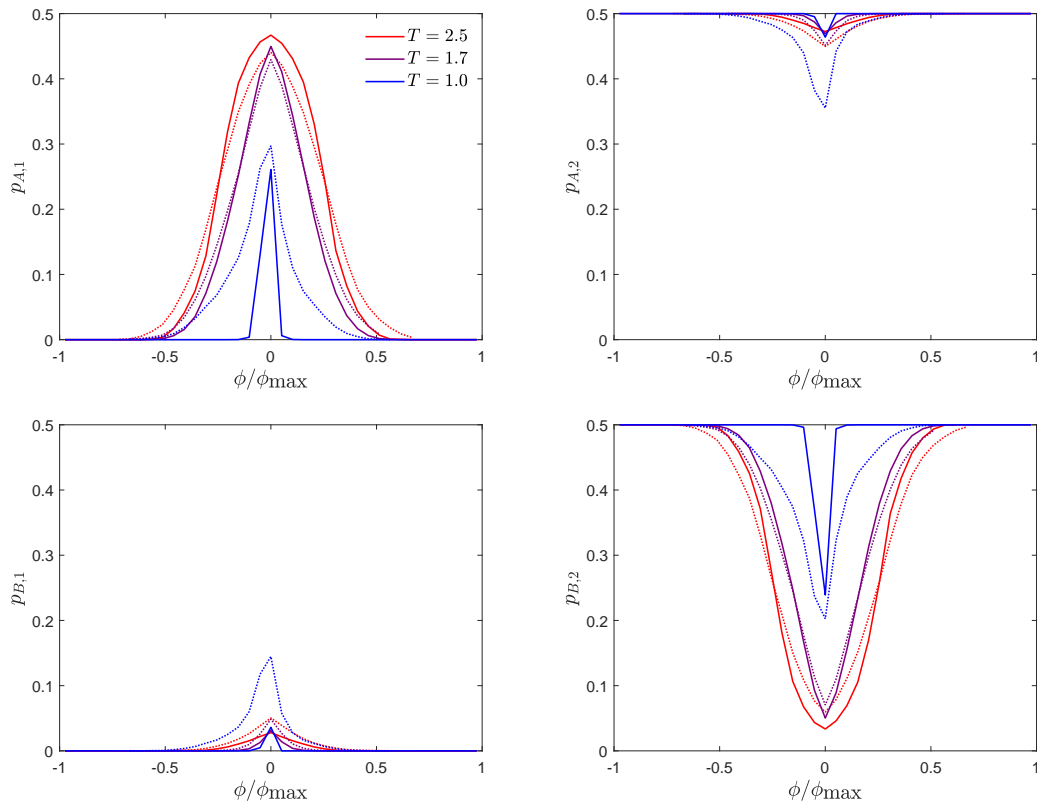


Figure 6.15: Equilibrium probabilities for states  $A_1$  (top left),  $B_1$  (top right),  $A_2$  (bottom left), and  $B_2$  (bottom right) as functions of the local potential. Results are shown for three temperatures: high temperature ( $T = 2.5$ ), transition temperature ( $T = 1.7$ ), and low temperature ( $T = 1.0$ ). Solid lines depict direct computations, while dotted lines indicate theoretical estimates. Simulation parameters:  $L = 200$ ,  $f = 0.04$ ,  $h_0 = 0.3$ .

nearby spins.

These results align with observations from the cluster size analysis of reversal events (see panel b of Fig. 6.10). At high temperatures, the correlation length is short, leading to the formation of small spin clusters. In this regime, individual spins behave independently, and the local potential becomes a dominant factor influencing spin behaviour. However, as the temperature decreases, larger spin clusters emerge, and reversal events encompass entire clusters rather than isolated spins. In this scenario, the local potential's influence diminishes, and the interactions among neighbouring spins undergoing reversals become the primary determinant of spin dynamics. This highlights the increasing importance of spin-spin interactions at low temperatures, overshadowing the role of defects and local potential in driving reversal events.

## Conclusion

In this chapter, we have explored the phenomenon of avalanches in out-of-equilibrium processes, focusing on their statistical characterization and the critical dynamics underpinning their formation. By integrating insights from Barkhausen noise and reversal interevent time statistics, we examined the interplay between temperature, quenched randomness, and metastable states, which are crucial in shaping the macroscopic properties of these systems.

By employing Monte Carlo simulations, we demonstrated that achieving a pure power-law distribution in magnetization jumps requires precise tuning of temperature and defect fraction. At critical conditions, characterized by an optimal balance of thermal fluctuations and disorder, the system exhibited a critical exponent  $\alpha_c \approx 1.7$ , aligning closely with experimental observations in low-temperature magnetic materials. Deviations from criticality, however, introduced exponential cut-offs or large jumps that disrupted the power-law behaviour, underlining the sensitivity of these dynamics to system parameters.

We observed differences between the Ising model with defects and other models, such as the RBIM. This suggests that these systems may belong to distinct universality classes. This distinction highlights the importance of considering microscopic details when modelling avalanches and their associated critical phenomena.

The analysis of reversal IET statistics revealed significant distinctions between homogeneous and heterogeneous systems under the influence of an oscillating external field. In homogeneous systems, IETs between local reversal events follows an exponential distribution, consistent with memoryless Poissonian processes. A two-state Markov chain model with transition rates dependent on temperature and external field amplitude was proposed and it was found to describe accurately the emergence of exponential IET distributions in different conditions. At the dynamic critical temperature, the average IET indicated the transition between the dynamic ordered and disordered phases, emphasizing the role of thermal fluctuations and field intensity in driving spin reversals.

By contrast, heterogeneous systems with defects exhibits complex, scale-invariant IET distributions characterized by discrete power-law behaviour in both subcritical and

supercritical regimes. The interplay between quenched randomness and local energy barriers fragments the relaxation dynamics, introducing a broad spectrum of timescales. The emergence of power laws, with distinct exponents in low- and high-temperature regimes, highlights the critical influence of defects on temporal correlations. This intricate behaviour underscores the importance of randomness and heterogeneity in shaping out-of-equilibrium dynamics, offering insights into universal relaxation processes in disordered systems



## Chapter 7

# Conclusion

This thesis has provided a comprehensive investigation into the static and dynamic properties of the Ising model with defects, introducing significant advancements in understanding the effects of disorder in complex systems. The primary focus was to develop and analyse a novel variant of the Ising model, wherein defects were incorporated as fixed spins. This model captures the interplay between localized heterogeneity and global properties, with strong evidence supporting its relevance to real-world systems and its classification within the same universality class as the Random Field Ising Model (RFIM). Notably, the model with defects is computationally advantageous, as highly efficient algorithms such as the  $N$ -Fold way and multi-spin coding can be easily adapted for this case. In this sense, the model with defects is not just a special case of the RFIM but a compelling alternative for simulating the behaviour of the RFIM with more efficient dynamics. By simplifying the computational cost while retaining critical disorder-induced phenomena, the model presents a robust platform for exploring metastable states, avalanche dynamics, and other emergent behaviour.

The thesis explored the potential of the model with defects to simulate real physical systems. Applications such as understanding crackling noise in ferromagnets, bistability in switching devices, and precipitation in heterogeneous media demonstrate its versatility. In socio-economic and biological contexts, the fixed spins effectively model agents resistant to external influences, akin to opinion dynamics in social networks or static heterogeneities in protein folding landscapes. These contributions establish the model as a pivotal tool for studying the interplay between quenched randomness and emergent phenomena across diverse fields.

**Quasi-phases and equilibrium configuration** In Chapter 3, the equilibrium configurations and quasi-phases of the Ising model with defects were analysed. The results revealed the presence of a pseudo-ferromagnetic phase contingent on defect density and system temperature. By leveraging overlap distributions and cluster analysis, the quasi-phases were characterized, showcasing how defects act as pinning centres, stabilizing localized domains. The equilibrium configurations highlighted the significant impact of defect distribution on macroscopic observables, offering critical insights into how local-

ized disorder governs global system behaviour. These findings are visually represented in Fig. 3.1, which illustrates the domain structures for different temperatures.

**Metastable lifetimes and spinodal line modification** Chapter 4 delved into the mechanism of reversal processes in homogeneous and heterogeneous systems, focusing on the classical Nucleation Theory (CNT) framework. First, we modified CNT to account for the inclusion of defects. We analysed the free energy function of the cluster size and the nucleation rate for the Ising model with defects. We found a lowering of the free energy barrier and an increase of the nucleation rate by several orders of magnitude compared with the defect-free case. When the field is the driving force of the reversal, theoretical expressions and simulation results show good agreement, as presented in Fig. 4.17. This represents a novel and interesting result, showcasing the wide regime of applicability of CNT despite the numerous assumptions behind it.

We also analysed the effect of defects on the metastable lifetime and the spinodal line. The metastable lifetime, defined as the time a system remains in a metastable state before transitioning to a stable configuration, was found to be significantly influenced by the defect density. In particular, the system with defects exhibits a reduction of the metastable lifetime, reflecting enhanced reactivity to external stimulus variation when defects are added. The spinodal line, which marks the boundary separating the multi-droplet and single-droplet regimes of reversal, was observed to shift due to the presence of defects, favouring the multi-droplet reversal regime.

These findings elucidate how disorder modifies nucleation dynamics, demonstrating the significant role of defect-induced energy barriers in shaping the behaviour of metastable systems. Such insights enhance our understanding of metastability and the predictive power of models incorporating quenched randomness.

**The effect of defect on the dynamic phase transition** The Dynamic Phase Transition (DPT) of the Ising model with defects was explored in Chapter 5. A novel order parameter was introduced to analyse the ability of individual spins to follow an oscillating external field in the two-dimensional system. The analysis revealed that a random distribution of defects generally promotes the dynamic disordered phase, leading to a significant reduction in the dynamic critical temperature. This finding provides valuable insight into how defect-induced randomness affects the phase dynamics under external modulation.

Moreover, defects offer novel opportunities for tuning system properties. By arranging defects in specific configurations, it is possible to design systems that exhibit desired dynamic behaviour, such as controlled hysteresis and tailored phase characteristics. For example, Fig. 5.10 demonstrates the correlation between the potential index, which quantifies the defect distribution, and the dynamic critical temperature, illustrating the potential for defect engineering to modulate phase transitions effectively.

These results open promising avenues for material design and engineering applications, where specific defect patterns can be strategically employed to optimize dynamic

performance, bridging the gap between theoretical predictions and practical implementations.

### **Barkhausen noise and Interevent time statistics in heterogeneous systems**

Chapter 6 focused on out-of-equilibrium dynamics, particularly the Barkhausen noise statistics and interevent time distributions.

For the Ising model with defects, the Barkhausen noise statistics exhibited robust power-law behaviour. Under critical conditions, the critical exponent of the power-law distributions aligned well with low-temperature experimental measurements. However, differences were observed in the temperature dependence of the critical exponent compared to real experiments and the random bond Ising model, highlighting the unique features introduced by defects in this model.

The analysis of single spin reversal events highlighted key differences between homogeneous and heterogeneous systems. In homogeneous systems, the interevent times (IET) followed an exponential distribution, indicative of uncorrelated dynamics. In contrast, the presence of defects in the heterogeneous model gave rise to fat-tailed IET probability distributions, reflecting collective behaviour. These distributions adhered to a power-law form across both high- and low-temperature regimes, albeit with distinct critical exponents. To complement the simulation results, a Markov chain model was developed, offering a theoretical framework to explain the simulation results in both system types.

These findings emphasize the potential of the Ising model with defects to simulate heterogeneous systems effectively, offering a robust statistical framework for interpreting real-world crackling phenomena and their dependence on underlying disorders.

**Future directions** The research presented in this thesis opens several promising avenues for future exploration. Extending the model to three-dimensional lattices and incorporating more complex interaction schemes could provide deeper insights into disorder-induced phenomena in higher-dimensional systems. Investigating time-dependent disorders or dynamic defects could further elucidate nonequilibrium processes and their implications for metastability and phase transitions. Additionally, integrating machine-learning techniques into the analysis could enhance the efficiency of parameter space exploration and pattern recognition in defect configurations.

The potential applications of the Ising model with defects extend far beyond the scenarios discussed herein. From designing robust materials to modelling collective dynamics in biological and socio-economic systems, the insights gained from this thesis lay a strong foundation for interdisciplinary research. Future studies could focus on experimental validations and collaborative approaches to refine the theoretical framework and expand its applicability, ensuring that this model continues to contribute meaningfully to the understanding of complex systems.



## Appendix A

# Investigation of the defect-potential

We present the analysis of the defect-potential distribution and the defect-potential index and their dependency on the cluster size  $L$  and defect fraction  $f$ . Figure A.1 illustrates the probability distribution of the relative defect-potential  $\phi/\phi_{\max}$  across the lattice sites. The distribution is well-approximated by a Student's  $t$ -distribution. Insets in the figure depict the degrees of freedom  $\nu$  of the distribution and the standard deviation  $\sigma$  obtained from Gaussian fits. Notably,  $\nu$  increases as a power law,  $\nu \sim L^\alpha$ , where  $\alpha$  is independent of the defect fraction, suggesting that  $P(\phi)$  converges to a Gaussian distribution in the thermodynamic limit. Additionally, the ratio  $\sigma/\phi_{\max}$  remains approximately constant over the range of lattice sizes considered.

Figure A.2 presents the statistics of  $\phi_{\text{def}}$  for configurations with randomly distributed defects. Both the potential index  $\phi_{\text{def}}$  and its standard deviation  $\sigma_\phi$  exhibit power-law scaling with system size, following  $\sim L^{-\alpha}$ , where  $\alpha = 1$  is independent of the defect fraction. The data points collapse well when plotted as functions of  $\phi_{\text{def}}f^{0.3}$  and  $\sigma_\phi f^{0.3}$ , respectively as shown in the inset of the two panels.

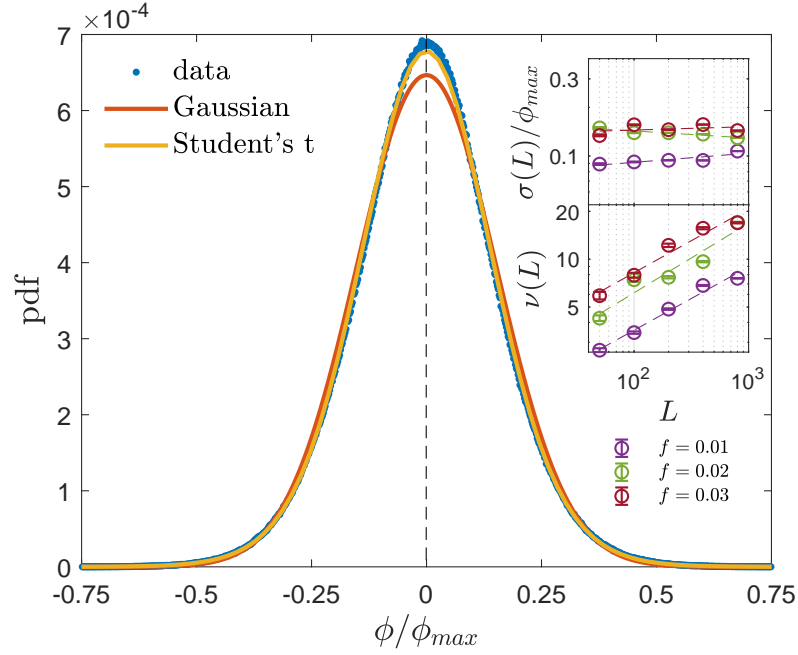


Figure A.1: Defect potential distribution for a lattice of size  $L = 800$  with a defect fraction  $f = 0.03$ . The distribution is well-approximated by a Student's  $t$ -distribution, as shown by the fitting curves. Insets illustrate the dependence of the degrees of freedom  $\nu$  and the standard deviation  $\sigma$  on system size and defect fraction.

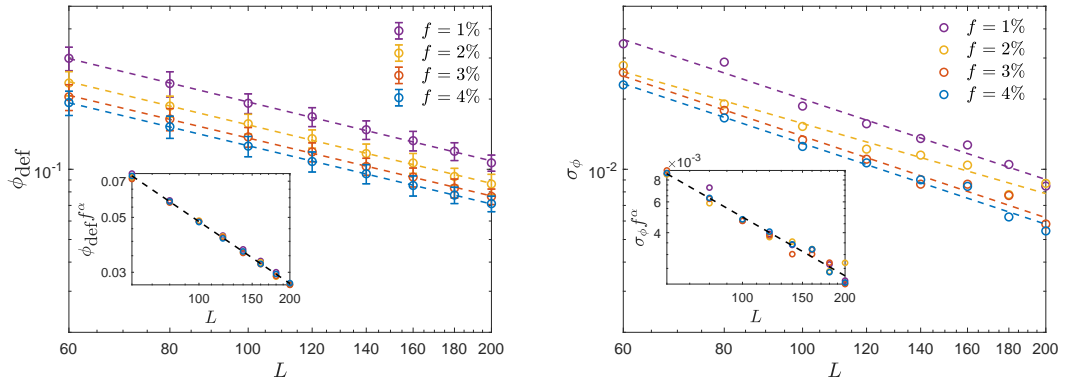


Figure A.2: Statistics of the defect potential index  $\phi_{\text{def}}$  (left) and its standard deviation  $\sigma_{\phi}$  (right) for a random defect distribution. Both quantities show power-law dependence on system size. The insets of both panels show the data collapse of  $f^{0.3}\phi_{\text{def}}$  and  $f^{0.3}\sigma_{\phi}$ , respectively.

## Appendix B

# Avrami's law derivation

We now present a derivation of Avrami's law presented in Sec.4.1.4. The starting point considers the following assumptions:

- The system resides in a metastable state under steady-state conditions when brought out of equilibrium. In this regime, physical variables remain constant over time until the reversal process is complete. Notably, the transition from the initial configuration to the metastable phase is disregarded.
- The growth velocity of a supercritical droplet is proportional to its surface area. Consequently, smaller droplets shrink rapidly, while larger clusters grow more slowly.

The second assumption follows from the Allen-Cahn approximation [76], [167], which states that, in big enough clusters, the growth velocity  $v$  of a droplet of stable phase is linear with the curvature of the droplet itself. For a circular droplet, since the curvature is proportional to the inverse of the radius  $R^{-1}$  it follows that  $v(R) = a/R + b$ . In specific, it can be derived the following expression for the radial velocity of growth in any dimension  $d$ :

$$v(R) = (d - 1)\Gamma(R_c^{-1} - R^{-1}) \quad (\text{B.1})$$

with  $\Gamma$  a factor which considers the details of the dynamics and  $R_c$  the critical radius of the droplet. This expression entails that  $v(R) = 0$  is 0 for a critical droplet. This is reasonable since subcritical droplets tend to shrink and supercritical droplets tend to grow. For large droplets ( $R \gg R_c$ ), one obtains that  $v(R) = (d - 1)\Gamma R_c^{-1} = v_0$  and constant in time. Since the volume  $V$  is related to the droplet's radius through  $V = \Omega_d R^d$  and  $dV = d\Omega_d R^{d-1} dR$  one can rearrange the Eq. (B.1) and write

$$\frac{dV}{dt} = d(d - 1)\Gamma \left( \frac{\Omega_d^{1/d}}{R_c} V^{1-1/d} - \Omega_d^{2/d} V^{1-2/d} \right) \quad (\text{B.2})$$

In two dimensions, the growth velocity expression becomes

$$\frac{dV}{dt} = 2\pi\Gamma \left( \frac{1}{\sqrt{\pi}R_c} \sqrt{\lambda} - 1 \right) = 2\pi\Gamma\lambda_c \left( \sqrt{\lambda} - \sqrt{\lambda_c} \right) \quad (\text{B.3})$$

where we recall that  $\lambda$  indicates the cluster's area. We see that  $V(\lambda)$  is null when the droplet is in critical conditions. A direct test of Eq. (B.3) is shown in Fig. 4.5 for a system with size  $L = 100$  and field  $h = 0.05$  at different temperatures. By considering large enough droplets, we can neglect the second term in Eq. (B.2) and write

$$dV \approx d\Omega_d^{1/d} v_0 V^{1-1/d} dt \quad (\text{B.4})$$

This equation states that the volume variation is proportional to the surface area, coherent with the second assumption.

To derive Eq. (4.14), we begin with an equation describing the variation of  $X$  within a unit time interval. The differential quantity  $dX$  is proportional to the fraction of the untransformed volume, multiplied by the transformation rate arising from nucleation or growth of droplets:

$$dX = (1 - X)I(t')V(t, t') dt', \quad (\text{B.5})$$

where  $I(t')$  represents the nucleation rate at time  $t'$ , and  $V(t, t')$  is the area at time  $t$  of a droplet nucleated at time  $t'$ .

The first assumption implies that  $I(t') = I$ , a constant nucleation rate independent of time. The second assumption, grounded in Eq. (B.4), implies that  $V(t, t') = \Omega_d v_0^d (t - t')^d$ , where  $\Omega_d$  is a geometrical factor,  $v_0$  is the characteristic velocity, and  $d$  is the spatial dimensionality of the system. Imposing the initial condition  $X(t = 0) = 0$  (no initial stable phase material), we integrate the equation to obtain:

$$\ln(1 - X(t)) = -\frac{I\Omega_d v_0^d t^{d+1}}{d+1}. \quad (\text{B.6})$$

From this, Eq. (4.14) follows.

## Appendix C

# Optimal defect unbalance

In principle, multiple locations are available for the nucleation of a droplet of area  $\lambda$ . It is reasonable to assume that the nucleation will happen in the “optimal position” corresponding to the region with a higher concentration of defects aligned with the external field (in this case, negative). Indeed, it should be easier for the system to nucleate droplets within regions with higher concentrations of seeding sites. Let’s then estimate  $(\nu_{opt}, \mu_{opt})$  corresponding to the values of  $\nu$  and  $\mu$  for a droplet in such an “optimal position”.

Let’s consider a system with size  $L$  with a fraction of defects equal to  $f$ . We change the perspective and deal with the total number of defects in a droplet  $n_T = \nu\lambda = n^+ + n^-$  and the defects unbalance  $\Delta n = n_T\mu = n^- - n^+$ . Assuming  $\lambda \ll L^2f$ , each site has a probability  $f/2$  to host either a positive or negative defect. We can write the probability of finding exactly  $n^+$  and  $n^-$  within a cluster of size  $\lambda$  (including the defects) as:

$$P_1(\lambda, f, n^+, n^-) = \frac{\lambda!}{n^+!n^-!(\lambda - n^+ - n^-)!} \left(\frac{f}{2}\right)^{n^++n^-} (1-f)^{\lambda-n^+-n^-} \quad (\text{C.1})$$

Let’s write the probability of observing a cluster with  $n_T$  defects

$$P_2(\lambda, f, n_T) = \sum_{i=0}^{n_T} P_1(\lambda, f, n_T - i, i) \quad (\text{C.2})$$

Also, we write the probability of observing a cluster with defect unbalance  $\Delta n$

$$P_3(\lambda, f, \Delta n) = \begin{cases} \sum_{i=0}^{(\lambda-\Delta n)/2} P_1(\lambda, f, i, i + \Delta n) & \text{if } \Delta n \geq 0 \\ \sum_{i=0}^{(\lambda+\Delta n)/2} P_1(\lambda, f, i - \Delta n, i) & \text{if } \Delta n < 0 \end{cases} \quad (\text{C.3})$$

Given these quantities, we can derive the optimal value of the defect unbalance  $\Delta n_{opt}$  and the corresponding total number of defects  $n_{T_{opt}}$ .

Among  $K$  independent nucleation sites ( $K \approx L^2/\lambda$ ), we search for the optimal one with the highest defect unbalance. We first write the probability of finding an imbalance smaller than  $\Delta n$ .

$$P_4(\lambda, f, \Delta n) = \sum_{i=-\lambda}^{\Delta n-1} P_3(\lambda, f, i) \quad (\text{C.4})$$

Then, the probability distribution for the optimal  $\Delta n$  is given by

$$P_5(\lambda, f, K, \Delta n_{opt}) = P_4(\lambda, f, \Delta n_{opt} + 1)^K - P_4(\lambda, f, \Delta n_{opt})^K \quad (\text{C.5})$$

where the first term refers to the probability of having  $\Delta n < \Delta n_{opt} + 1$  for each independent region, whereas the second term cancels the chances of having all the independent regions with  $\Delta n < \Delta n_{opt}$ . Then

$$\mathbb{E}[\Delta n_{opt}] = \sum_{\Delta n=-\lambda}^{\lambda} \Delta n P_5(\lambda, f, K, \Delta n_{opt}) \quad (\text{C.6})$$

Finally, by employing Bayes' rule we can express the probability distribution for the total number of defects  $n_{T_{opt}}$  for an optimal configuration

$$\begin{aligned} P_6(\lambda, f, n_T | \Delta n_{opt}) &= \frac{P(\Delta n | n_T) P_2(\lambda, f, n_T)}{P_3(\lambda, f, \Delta n)} \\ &= \frac{1}{2^{n_T}} \binom{n_T}{(n_T + \Delta n)/2} \frac{P_2(\lambda, f, n_T)}{P_3(\lambda, f, \Delta n)} \end{aligned} \quad (\text{C.7})$$

Thus

$$\mathbb{E}[n_{T_{opt}}] = \sum_{n_T=\Delta n}^{\lambda} n_T P_6(\lambda, f, n_T | \Delta n_{opt}) \quad (\text{C.8})$$

The results for variable defect fraction and fixed cluster size ( $\lambda = 0.50$ ) are shown in the top panel of Fig. C.1. Interestingly, a double logarithmic plot reveals a reasonable power law behaviour  $\Delta n_{opt} \sim f^{0.5}$  for the whole range of interest. The inset shows the ratio  $\Delta n/n_T$  for the optimal configuration. For small fractions of defects, it is fairly safe to assume  $\Delta n/n_T \approx 1$ , even though deviations from 1 can be observed as the cluster size increases. The middle and bottom panels show the dependency of the two quantities on the cluster size for different defect fractions. An asymptotic behaviour is observed for both of them when divided by the cluster size.

From Eq. (C.6) and Eq. (C.7) we can derive  $\nu_{opt} = n_{T_{opt}}/\lambda$  and  $\mu_{opt} = \Delta n_{T_{opt}}/n_{opt}$  to be used in Eq. (4.27). For large  $\lambda$ , in agreement with the middle and bottom panels of Fig. C.1, we can assume  $\nu\mu$  and  $\nu$  independent from  $\lambda$  and only dependent on  $f$ . In particular, we assume this to be valid for the whole range of cluster sizes characterising the development of a droplet and therefore in the free energy expression Eq. (4.27).

Let's now investigate the dependency from the defect fractions. By performing a linear fit over  $f$  for small defect fractions, we find  $\nu = f$  with good agreement. Then, we test a power-law behaviour

$$\mu\nu \sim f^\alpha \quad (\text{C.9})$$

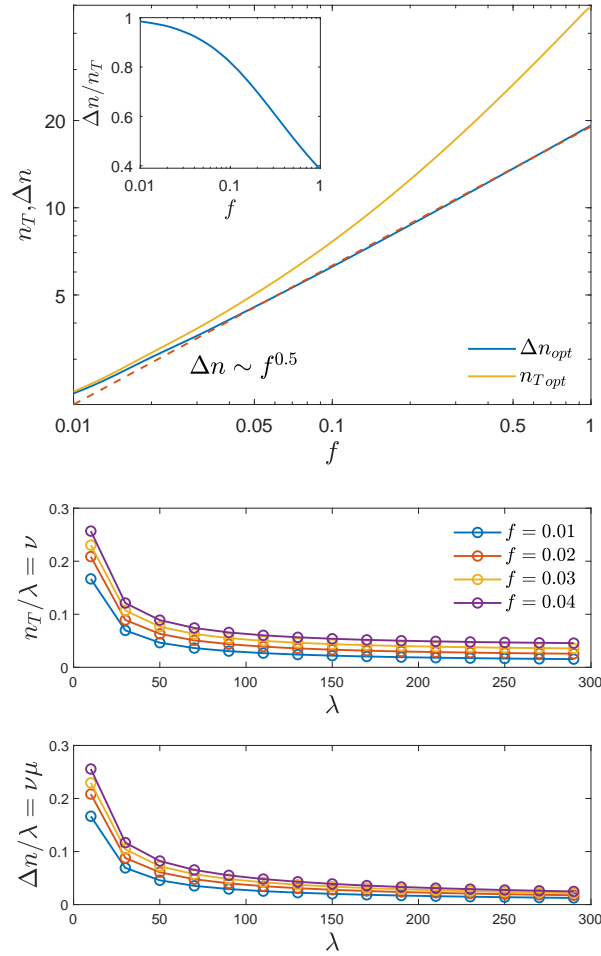


Figure C.1: Cluster properties for variable cluster size  $\lambda$  and defect fractions  $f$ . Top panel: total number of defects  $n_T$  [Eq. (C.8)] and defects unbalance  $\Delta n$  [Eq. (C.6)] for a cluster of size  $\lambda = 50$  likely to be the first nucleating droplet (optimal cluster) as a function of the fraction of defects.  $\Delta n$  follows a power law behaviour with good approximation:  $\Delta n(f) \sim f^{0.5}$ . The inset shows the ratio  $\Delta n/n_T$ , which remains  $\approx 1$  for small fractions of defects ( $f < 0.1$ ). This indicates that almost all defects in an optimal cluster have the same sign. Middle and bottom panels: fraction of defects  $n_T/\lambda = \mu$  and defect unbalance  $\Delta n/\lambda = \nu\mu$  in a droplet as a function of the cluster size. Different fractions of defects are analysed as indicated in the legend. Both quantities saturate as  $\lambda$  is increased. As expected,  $\nu(f) \sim f$  is compatible with the numerical data in the large  $\lambda$  limit. System size used for numerical computation:  $L = 100$ .

as suggested in the top panel of Fig. C.1. We find that  $\alpha \approx 0.5$  works well, even for large clusters.

These approximations are expected to hold primarily in the low-temperature regime, where thermal fluctuations are reduced, and the system's behaviour becomes more sensitive to defect distribution. At high temperatures, cluster formation is easier regardless of defect distribution. As a result, the high-temperature imbalance parameter  $\mu$  is expected to approach unity. Consequently,  $\mu\nu \sim f^\alpha$  with  $\alpha = 0.5$  in the low-temperature regime, increasing to  $\alpha = 1$  in the high-temperature regime.

# Bibliography

- [1] P. Lenz, B. Zagrovic, J. Shapiro, and V. S. Pande, “Folding probabilities: A novel approach to folding transitions and the two-dimensional Ising-model,” *J. Chem. Phys.*, vol. 120, no. 14, pp. 6769–6778, 2004.
- [2] J. A. Hertz, *Introduction to the theory of neural computation*. Crc Press, 2018.
- [3] M. Mobilia, “Nonlinear q-voter model with inflexible zealots,” *Phys. Rev. E*, vol. 92, no. 1, p. 012 803, 2015.
- [4] P. Ehrenfest, “*Phasenumwandlungen im üblichen und erweiterten Sinn, klassifiziert nach dem entsprechenden Singularitäten des thermodynamischen Potentials* (Phase transformations in the usual and extended sense, classified according to the corresponding singularities of the thermodynamic potential),” *Proc. Akad. Wet. Amsterdam*, vol. 36, pp. 153–157, 1933.
- [5] G. Jaeger, “The Ehrenfest Classification of Phase Transitions: Introduction and Evolution,” *Archive for History of Exact Sciences*, vol. 53, no. 51, p. 81, 1998.
- [6] F. Amir and Z. Yuwen, *Fundamentals of Multiphase Heat Transfer and Flow*. Springer Cham, 2020.
- [7] I. Ernst, “Beitrag zur theorie des ferromagnetismus,” *Z. Phys.*, vol. 31, no. 1, pp. 253–258, 1925.
- [8] R. Peierls, “On Ising’s model of ferromagnetism,” in *Mathematical Proceedings of the Cambridge Philosophical Society*, Cambridge University Press, vol. 32, 1936, pp. 477–481.
- [9] L. Onsager, “Crystal Statistics. I. A Two-Dimensional Model with an Order-Disorder Transition,” *Phys. Rev.*, vol. 65, pp. 117–149, 3-4 1944.
- [10] D. S. Fisher, G. M. Grinstein, and A. Khurana, “[theory of random magnets],” *Phys. Today*, vol. 41, no. 12, pp. 56–67, 1988.
- [11] J. Restrepo and J. Greneche, “Magnetic properties and critical behavior of random  $\alpha$ -Fe Mn Al alloys: An Ising Monte Carlo study,” *Phys. Rev. B*, vol. 71, no. 6, p. 064 406, 2005.
- [12] H. Salehinejad and S. Valaee, “Ising-dropout: A regularization method for training and compression of deep neural networks,” in *ICASSP 2019-2019 IEEE International Conference on Acoustics, Speech and Signal Processing (ICASSP)*, IEEE, 2019, pp. 3602–3606.

- [13] K. Binder and A. P. Young, “Spin glasses: Experimental facts, theoretical concepts, and open questions,” *Rev. Mod. Phys.*, vol. 58, no. 4, p. 801, 1986.
- [14] A. B. Harris, “Effect of random defects on the critical behaviour of Ising models,” *J. Phys. C: Solid State Phys.*, vol. 7, no. 9, p. 1671, 1974.
- [15] M. Aizenman and J. Wehr, “Rounding of first-order phase transitions in systems with quenched disorder,” *Phys. Rev. Lett.*, vol. 62, pp. 2503–2506, 21 1989.
- [16] S. F. Edwards and P. W. Anderson, “Theory of spin glasses,” *J. Phys. Condens. Matter*, vol. 5, no. 5, p. 965, 1975.
- [17] H. Nishimori, *Statistical physics of spin glasses and information processing: an introduction*. Clarendon Press, 2001.
- [18] E. Vincent, “Ageing, rejuvenation and memory: The example of spin-glasses,” in *Ageing and the glass transition*, Springer, 2007, pp. 7–60.
- [19] K. Jonason, E. Vincent, J. Hammann, J. P. Bouchaud, and P. Nordblad, “Memory and Chaos Effects in Spin Glasses,” *Phys. Rev. Lett.*, vol. 81, pp. 3243–3246, 15 1998.
- [20] J. A. Mydosh, *Spin glasses: an experimental introduction*. CRC Press, 1993.
- [21] L. Fernandez, E. Marinari, V. Martin-Mayor, G. Parisi, and J. Ruiz-Lorenzo, “Universal critical behavior of the two-dimensional Ising spin glass,” *Phys. Rev. B*, vol. 94, no. 2, p. 024402, 2016.
- [22] H. Ballesteros, A. Cruz, L. Fernandez, *et al.*, “Critical behavior of the three-dimensional Ising spin glass,” *Phys. Rev. B*, vol. 62, no. 21, p. 14237, 2000.
- [23] D. Sherrington and S. Kirkpatrick, “Solvable model of a spin-glass,” *Phys. Rev. Lett.*, vol. 35, no. 26, p. 1792, 1975.
- [24] D. Panchenko, *The Sherrington-Kirkpatrick model*. Springer Science & Business Media, 2013.
- [25] G. Parisi, “A sequence of approximated solutions to the SK model for spin glasses,” *J. Phys. A-Math.*, vol. 13, no. 4, p. L115, 1980.
- [26] F. Guerra and F. L. Toninelli, “The thermodynamic limit in mean field spin glass models,” *Commun. Math. Phys.*, vol. 230, pp. 71–79, 2002.
- [27] F. Guerra, “Broken replica symmetry bounds in the mean field spin glass model,” *Commun. Math. Phys.*, vol. 233, pp. 1–12, 2003.
- [28] M. Talagrand, “The Parisi formula,” *Ann. Math.*, pp. 221–263, 2006.
- [29] T. Nattermann, “Theory of the random field Ising model,” in *Spin glasses and random fields*, World Scientific, 1998, pp. 277–298.
- [30] N. G. Fytas, V. Martín-Mayor, M. Picco, and N. Sourlas, “Review of recent developments in the random-field Ising model,” *J. Stat. Phys.*, vol. 172, pp. 665–672, 2018.

- [31] S. Fishman and A. Aharony, “Random field effects in disordered anisotropic antiferromagnets,” *J. Phys. C: Solid State Phys.*, vol. 12, no. 18, p. L729, 1979.
- [32] D. Belanger, “Random-field experiments in dilute antiferromagnets,” *Ph. Trans.*, vol. 11, no. 1-4, pp. 53–89, 1988.
- [33] S. Dierker and P. Wiltzius, “Random-field transition of a binary liquid in a porous medium,” *Phys. Rev. Lett.*, vol. 58, no. 18, p. 1865, 1987.
- [34] W. Fenzl and J. Peisl, “Hydrogen in metallic alloys as an example of a lattice gas with random field and random bonds,” *Phys. Rev. Lett.*, vol. 54, no. 19, p. 2064, 1985.
- [35] A. Berretti, “Some properties of random Ising models,” *J. Stat. Phys.*, vol. 38, pp. 483–496, 1985.
- [36] Y. Imry and S.-k. Ma, “Random-field instability of the ordered state of continuous symmetry,” *Phys. Rev. Lett.*, vol. 35, no. 21, p. 1399, 1975.
- [37] K. Binder, “Random-field induced interface widths in Ising systems,” *Z. Phys. B*, vol. 50, no. 4, pp. 343–352, 1983.
- [38] S. Chatterjee, “Absence of replica symmetry breaking in the random field Ising model,” *Commun. Math. Phys.*, vol. 337, no. 1, pp. 93–102, 2015.
- [39] F. Krzakala, F. Ricci-Tersenghi, and L. Zdeborová, “Elusive spin-glass phase in the random field Ising model,” *Phys. Rev. Lett.*, vol. 104, no. 20, p. 207 208, 2010.
- [40] F. Krzakala, F. Ricci-Tersenghi, D. Sherrington, and L. Zdeborová, “No spin glass phase in the ferromagnetic random-field random-temperature scalar Ginzburg–Landau model,” *J. Phys. A.*, vol. 44, no. 4, p. 042 003, 2011.
- [41] A. Aharony, Y. Imry, and S.-k. Ma, “Lowering of Dimensionality in Phase Transitions with Random Fields,” *Phys. Rev. Lett.*, vol. 37, pp. 1364–1367, 20 1976.
- [42] A. Young, “On the lowering of dimensionality in phase transitions with random fields,” *J. Phys. C: Solid State Phys.*, vol. 10, no. 9, p. L257, 1977.
- [43] G. Parisi and N. Sourlas, “Random magnetic fields, supersymmetry, and negative dimensions,” *Phys. Rev. Lett.*, vol. 43, no. 11, p. 744, 1979.
- [44] N. G. Fytas and V. Martín-Mayor, “Universality in the three-dimensional random-field Ising model,” *Phys. Rev. Lett.*, vol. 110, no. 22, p. 227 201, 2013.
- [45] N. G. Fytas and V. Martín-Mayor, “Efficient numerical methods for the random-field Ising model: Finite-size scaling, reweighting extrapolation, and computation of response functions,” *Phys. Rev. E*, vol. 93, no. 6, p. 063 308, 2016.
- [46] N. G. Fytas, V. Martín-Mayor, M. Picco, and N. Sourlas, “Phase transitions in disordered systems: the example of the random-field Ising model in four dimensions,” *Phys. Rev. Lett.*, vol. 116, no. 22, p. 227 201, 2016.
- [47] N. G. Fytas, V. Martin-Mayor, M. Picco, and N. Sourlas, “Specific-heat exponent and modified hyperscaling in the 4D random-field Ising model,” *J. Stat. Mech.: Theory Exp.*, vol. 2017, no. 3, p. 033 302, 2017.

- [48] N. G. Fytas, V. Martín-Mayor, M. Picco, and N. Surlas, “Restoration of dimensional reduction in the random-field Ising model at five dimensions,” *Phys. Rev. E*, vol. 95, no. 4, p. 042 117, 2017.
- [49] R. Brout, “Statistical mechanical theory of a random ferromagnetic system,” *Phys. Rev.*, vol. 115, no. 4, p. 824, 1959.
- [50] K. Binder, *Monte Carlo Simulation in Statistical Physics*, 1992.
- [51] F. Etti, T. J. Sluckin, and P. Biscari, “The effect of defects on magnetic droplet nucleation,” *Physica A*, vol. 611, p. 128 426, 2023.
- [52] F. Etti, F. Perani, S. Turzi, and P. Biscari, “Finite-temperature avalanches in 2D disordered Ising models,” *J. Stat. Phys.*, vol. 190, no. 4, p. 89, 2023.
- [53] F. Etti, T. Coupé, T. J. Sluckin, E. Puppini, and P. Biscari, “Dynamic Phase Transition in 2D Ising Systems: Effect of Anisotropy and Defects,” *Entropy*, vol. 26, no. 2, p. 120, 2024.
- [54] F. Etti, T. J. Sluckin, and P. Biscari, “Inter-Event Time Power Laws in Heterogeneous Systems,” *arXiv preprint arXiv:2411.10608*, 2024.
- [55] P. Timonin, “Spin ice in a field: Quasi-phases and pseudo-transitions,” *J. Exp. Theor. Phys.*, vol. 113, pp. 251–265, 2011.
- [56] M. E. Newman and G. T. Barkema, *Monte Carlo methods in statistical physics*. Clarendon Press, 1999.
- [57] D. Landau and K. Binder, *A guide to Monte Carlo simulations in statistical physics*. Cambridge university press, 2021.
- [58] N. Metropolis, A. W. Rosenbluth, M. N. Rosenbluth, A. H. Teller, and E. Teller, “Equation of state calculations by fast computing machines,” *J. Chem. Phys.*, vol. 21, no. 6, pp. 1087–1092, 1953.
- [59] A. B. Bortz, M. H. Kalos, and J. L. Lebowitz, “A new algorithm for Monte Carlo simulation of Ising spin systems,” *J. Comput. Phys.*, vol. 17, no. 1, pp. 10–18, 1975.
- [60] S. Kirkpatrick, C. D. Gelatt Jr, and M. P. Vecchi, “Optimization by simulated annealing,” *Science*, vol. 220, no. 4598, pp. 671–680, 1983.
- [61] E. Marinari and G. Parisi, “Simulated tempering: a new Monte Carlo scheme,” *EPL*, vol. 19, no. 6, p. 451, 1992.
- [62] W. Kerler and P. Rehberg, “Simulated-tempering procedure for spin-glass simulations,” *Phys. Rev. E*, vol. 50, no. 5, p. 4220, 1994.
- [63] K. Hukushima and K. Nemoto, “Exchange Monte Carlo method and application to spin glass simulations,” *J. Phys. Soc. Jpn.*, vol. 65, no. 6, pp. 1604–1608, 1996.
- [64] R. J. Glauber, “Time-dependent statistics of the Ising model,” *J. Math. Phys.*, vol. 4, no. 2, pp. 294–307, 1963.

- [65] J. Bertoin, F. Martinelli, Y. Peres, and P. Bernard, *Ecole d'été de Probabilités de Saint-Flour. 27, lectures on probability theory and statistics: Ecole d'été de probabilités de saint-flour XXVII - 1997*. Springer, 1999.
- [66] M. Suzuki and R. Kubo, "Dynamics of the Ising model near the critical point. I," *J. Phys. Soc. Jpn.*, vol. 24, no. 1, pp. 51–60, 1968.
- [67] F. Etti, D. Mandal, and D. Quigley, "Low temperature nucleation rate calculations using the N-Fold way," *arXiv preprint arXiv:2412.19278*, 2024.
- [68] J. Plascak, L. E. Zamora, and G. P. Alcazar, "Ising model for disordered ferromagnetic Fe- Al alloys," *Phys. Rev. B*, vol. 61, no. 5, p. 3188, 2000.
- [69] S. Sinha and P. K. Mandal, "Dynamical properties of random-field ising model," *Phys. Rev. E*, vol. 87, no. 2, p. 022 121, 2013.
- [70] F. Guerra, "About the overlap distribution in mean field spin glass models," *Int. J. Mod. Phys. B*, vol. 10, no. 13n14, pp. 1675–1684, 1996.
- [71] T. Blanchard and M. Picco, "Frozen into stripes: Fate of the critical Ising model after a quench," *Phys. Rev. E*, vol. 88, no. 3, p. 032 131, 2013.
- [72] E. Stoll and T. Schneider, "Computer simulation of critical properties and metastable states in a finite square Ising system," *Phys. Rev. A*, vol. 6, no. 1, p. 429, 1972.
- [73] P. A. Rikvold, H. Tomita, S. Miyashita, and S. W. Sides, "Metastable lifetimes in a kinetic Ising model: dependence on field and system size," *Phys. Rev. E*, vol. 49, no. 6, p. 5080, 1994.
- [74] D. W. Heermann, A. Coniglio, W. Klein, and D. Stauffer, "Nucleation and metastability in three-dimensional Ising models," *J. Stat. Phys.*, vol. 36, pp. 447–470, 1984.
- [75] M. E. Fisher, "The theory of condensation and the critical point," *Phys. Phys. Fiz.*, vol. 3, no. 5, p. 255, 1967.
- [76] J. D. Gunton and M. Droz, *Introduction to the theory of metastable and unstable states*. Springer, 1983.
- [77] J. Ferré, V. Repain, J.-P. Jamet, *et al.*, "Magnetisation reversal dynamics in an ultrathin magnetic film and the creep phenomenon," *Phys. Status Solidi A*, vol. 201, no. 7, pp. 1386–1391, 2004.
- [78] T. Ostler, J. Barker, R. Evans, *et al.*, "Ultrafast heating as a sufficient stimulus for magnetization reversal in a ferrimagnet," *Nat. Commun.*, vol. 3, no. 1, p. 666, 2012.
- [79] K. Dima, *Nucleation: Basic Theory with Applications*. Oxford:Butterworth Heine-  
mann, 2000.
- [80] S. Karthika, T. Radhakrishnan, and P. Kalaichelvi, "A review of classical and nonclassical nucleation theories," *Cryst. Growth Des.*, vol. 16, no. 11, pp. 6663–6681, 2016.

- [81] M. Fanfoni and M. Tomellini, “The Johnson-Mehl-Avrami-Kolmogorov model: A brief review,” *Nuovo Cimento Soc. Ital. Fis. D*, vol. 20, no. 7, pp. 1171–1182, 1998.
- [82] S. W. Sides, P. A. Rikvold, and M. A. Novotny, “Stochastic hysteresis and resonance in a kinetic Ising system,” *Phys. Rev. E*, vol. 57, pp. 6512–6533, 6 1998.
- [83] H. Tomita and S. Miyashita, “Statistical properties of the relaxation processes of metastable states in the kinetic Ising model,” *Phys. Rev. B*, vol. 46, pp. 8886–8893, 14 1992.
- [84] K. E. Blow, D. Quigley, and G. C. Sosso, “The seven deadly sins: When computing crystal nucleation rates, the devil is in the details,” *J. Chem. Phys.*, vol. 155, no. 4, p. 040901, 2021.
- [85] P. G. Vekilov, “The two-step mechanism of nucleation of crystals in solution,” *Nanoscale*, vol. 2, no. 11, pp. 2346–2357, 2010.
- [86] J. S. Langer, “Theory of Nucleation Rates,” *Phys. Rev. Lett.*, vol. 21, pp. 973–976, 14 1968.
- [87] S. Ryu and W. Cai, “Numerical tests of nucleation theories for the Ising models,” *Phys. Rev. E*, vol. 82, p. 011603, 1 2010.
- [88] M. E. Fisher and A. E. Ferdinand, “Interfacial, Boundary, and Size Effects at Critical Points,” *Phys. Rev. Lett.*, vol. 19, pp. 169–172, 4 1967.
- [89] V. A. Shneidman, K. A. Jackson, and K. M. Beatty, “On the applicability of the classical nucleation theory in an Ising system,” *J. Chem. Phys.*, vol. 111, no. 15, pp. 6932–6941, 1999.
- [90] R. Becker and W. Döring, “Kinetische Behandlung der Keimbildung in übersättigten Dämpfen,” *Ann. Phys.*, vol. 416, no. 8, pp. 719–752, 1935.
- [91] B. Zeldovich J, *Acta Physicochim. URSS*, 1943.
- [92] A. C. Pan and D. Chandler, “Dynamics of Nucleation in the Ising Model,” *J. Phys. Chem. B*, vol. 108, no. 51, pp. 19681–19686, 2004.
- [93] R. J. Allen, D. Frenkel, and P. R. ten Wolde, “Simulating rare events in equilibrium or nonequilibrium stochastic systems,” *J. Chem. Phys.*, vol. 124, no. 2, p. 024102, 2006.
- [94] R. J. Allen, C. Valeriani, and P. R. ten Wolde, “Forward flux sampling for rare event simulations,” *J. Condens. Matter Phys.*, vol. 21, no. 46, p. 463102, 2009.
- [95] G. M. Torrie and J. P. Valleau, “Nonphysical sampling distributions in Monte Carlo free-energy estimation: Umbrella sampling,” *J. Comput. Phys.*, vol. 23, no. 2, pp. 187–199, 1977.
- [96] D. Mandal and D. Quigley, “Nucleation rate in the two dimensional Ising model in the presence of random impurities,” *Soft Matter*, vol. 17, pp. 8642–8650, 38 2021.

- [97] D. Mandal and D. Quigley, "Mapping the influence of impurity interaction energy on nucleation in a lattice-gas model of solute precipitation," *Soft Matter*, vol. 20, no. 36, pp. 7174–7184, 2024.
- [98] A. Kolmogorov, "K statisticheskoy teorii kristallizatsii metallov [On the statistical theory of crystallization of metals]," *Izv. Akad. Nauk SSSR, Ser. Mat.*, pp. 355–359, 1937.
- [99] M. Avrami, "Kinetics of Phase Change. I General Theory," *J. Chem. Phys.*, vol. 7, no. 12, pp. 1103–1112, 1939.
- [100] W. A. Johnson, "Reaction kinetics in process of nucleation and growth," *Trans. Am. Inst. Min. Metall. Eng.*, vol. 135, pp. 416–458, 1939.
- [101] G. Ghosh, M. Chandrasekaran, and L. Delaey, "Isothermal crystallization kinetics of Ni<sub>24</sub>Zr<sub>76</sub> and Ni<sub>24</sub>(Zr X)<sub>76</sub> amorphous alloys," *Acta Mater.*, vol. 39, no. 5, pp. 925–936, 1991.
- [102] Z.-Z. Yuan, X.-D. Chen, B.-X. Wang, and Z.-J. Chen, "Crystallization kinetics of melt-spun Co<sub>43</sub>Fe<sub>20</sub>Ta<sub>5.5</sub>B<sub>31.5</sub> amorphous alloy," *J. Alloys Compd.*, vol. 399, no. 1, pp. 166–172, 2005.
- [103] G.-Z. Quan, J. Pan, and Z.-h. Zhang, "Phase transformation and recrystallization kinetics in space–time domain during isothermal compressions for Ti–6Al–4V analyzed by multi-field and multi-scale coupling FEM," *Mater. Des.*, vol. 94, pp. 523–535, 2016.
- [104] J. S. Blázquez, A. F. Manchón-Gordón, J. J. Ipus, C. F. Conde, and A. Conde, "On the use of JMAK theory to describe mechanical amorphization: A comparison between experiments, numerical solutions and simulations," *Metals*, vol. 8, no. 6, 2018.
- [105] Y.-H. Shin, I. Grinberg, I.-W. Chen, and A. M. Rappe, "Nucleation and growth mechanism of ferroelectric domain-wall motion," *Nature*, vol. 449, no. 7164, pp. 881–884, 2007.
- [106] S.-B. Choe and S.-C. Shin, "Magnetization reversal in Co/Pd multilayers with varying Co sublayer thickness," *J. Appl. Phys.*, vol. 81, no. 8, pp. 5743–5745, 1997.
- [107] K. G. F. Janssens, D. Raabe, E. Kozeschnik, M. A. Miodownik, and B. Nestler, *Computational materials engineering: an introduction to microstructure evolution*. Academic Press, 2010.
- [108] M. C. Weinberg, D. P. Birnie, and V. A. Shneidman, "Crystallization kinetics and the JMAK equation," *J. Non-Cryst. Solids*, vol. 219, pp. 89–99, 1997, Glass Crystallization.
- [109] V. A. Shneidman, K. A. Jackson, and K. M. Beatty, "Nucleation and growth of a stable phase in an Ising-type system," *Phys. Rev. B*, vol. 59, pp. 3579–3589, 5 1999.

- [110] R. A. Ramos, P. A. Rikvold, and M. A. Novotny, “Test of the Kolmogorov-Johnson-Mehl-Avrami picture of metastable decay in a model with microscopic dynamics,” *Phys. Rev. B*, vol. 59, pp. 9053–9069, 14 1999.
- [111] J. Langer, “Theory of the condensation point,” *Ann. Phys.*, vol. 41, no. 1, pp. 108–157, 1967.
- [112] T. Tomé and M. J. de Oliveira, “Dynamic phase transition in the kinetic Ising model under a time-dependent oscillating field,” *Phys. Rev. A*, vol. 41, pp. 4251–4254, 8 1990.
- [113] Y. Yüksel and E. Vatansever, “Dynamic phase transition in classical Ising models,” *J. Phys. D: Appl. Phys.*, vol. 55, no. 7, p. 073 002, 2021.
- [114] G. Korniss, C. J. White, P. A. Rikvold, and M. A. Novotny, “Dynamic phase transition, universality, and finite-size scaling in the two-dimensional kinetic Ising model in an oscillating field,” *Phys. Rev. E*, vol. 63, p. 016 120, 1 2000.
- [115] M. Acharyya, “Nonequilibrium phase transition in the kinetic Ising model: Existence of a tricritical point and stochastic resonance,” *Phys. Rev. E*, vol. 59, pp. 218–221, 1 1999.
- [116] B. K. Chakrabarti and M. Acharyya, “Dynamic transitions and hysteresis,” *Rev. Mod. Phys.*, vol. 71, no. 3, p. 847, 1999.
- [117] S. Sides, P. A. Rikvold, and M. Novotny, “Kinetic Ising model in an oscillating field: Avrami theory for the hysteretic response and finite-size scaling for the dynamic phase transition,” *Phys. Rev. E*, vol. 59, no. 3, p. 2710, 1999.
- [118] S. Sides, P. Rikvold, and M. Novotny, “Kinetic Ising model in an oscillating field: Finite-size scaling at the dynamic phase transition,” *Phys. Rev. Lett.*, vol. 81, no. 4, p. 834, 1998.
- [119] O. Idigoras, P. Vavassori, and A. Berger, “Mean field theory of dynamic phase transitions in ferromagnets,” *Phys. B: Condens. Matter*, vol. 407, no. 9, pp. 1377–1380, 2012.
- [120] H. Park and M. Pleimling, “Dynamic phase transition in the three-dimensional kinetic Ising model in an oscillating field,” *Phys. Rev. E*, vol. 87, p. 032 145, 3 2013.
- [121] E. Vatansever and N. G. Fytas, “Dynamic phase transitions in the presence of quenched randomness,” *Phys. Rev. E*, vol. 97, no. 6, p. 062 146, 2018.
- [122] G. M. Buendía and P. A. Rikvold, “Fluctuations in a model ferromagnetic film driven by a slowly oscillating field with a constant bias,” *Phys. Rev. B*, vol. 96, no. 13, p. 134 306, 2017.
- [123] P. Riego, P. Vavassori, and A. Berger, “Towards an understanding of dynamic phase transitions,” *Physica B*, vol. 549, pp. 13–23, 2018.
- [124] D. Robb, P. Rikvold, A. Berger, and M. Novotny, “Conjugate field and fluctuation-dissipation relation for the dynamic phase transition in the two-dimensional kinetic Ising model,” *Phys. Rev. E*, vol. 76, no. 2, p. 021 124, 2007.

- [125] P. Jung, G. Gray, R. Roy, and P. Mandel, “Scaling law for dynamical hysteresis,” *Phys. Rev. Lett.*, vol. 65, pp. 1873–1876, 15 1990.
- [126] M. Acharyya and B. K. Chakrabarti, “Monte carlo study of hysteretic response and relaxation in ising models,” *Physica A*, vol. 192, no. 3, pp. 471–485, 1993.
- [127] M. Acharyya, “Comparison of mean-field and Monte Carlo approaches to dynamic hysteresis in Ising ferromagnets,” *Physica A*, vol. 253, no. 1-4, pp. 199–204, 1998.
- [128] Y.-L. He and G.-C. Wang, “Observation of dynamic scaling of magnetic hysteresis in ultrathin ferromagnetic Fe/Au(001) films,” *Phys. Rev. Lett.*, vol. 70, pp. 2336–2339, 15 1993.
- [129] Q. Jiang, H.-N. Yang, and G.-C. Wang, “Scaling and dynamics of low-frequency hysteresis loops in ultrathin Co films on a Cu (001) surface,” *Phys. Rev. B*, vol. 52, no. 20, p. 14 911, 1995.
- [130] B.-C. Choi, W. Lee, A. Samad, and J. Bland, “Dynamics of magnetization reversal in thin polycrystalline Ni 80 Fe 20 films,” *Phys. Rev. B*, vol. 60, no. 17, p. 11 906, 1999.
- [131] A. Punya, R. Yimnirun, P. Laoratanakul, and Y. Laosiritaworn, “Frequency dependence of the Ising–hysteresis phase–diagram: Mean field analysis,” *Physica B*, vol. 405, no. 16, pp. 3482–3488, 2010.
- [132] P. Riego, P. Vavassori, and A. Berger, “Metamagnetic anomalies near dynamic phase transitions,” *Phys. Rev. Lett.*, vol. 118, no. 11, p. 117 202, 2017.
- [133] A. Berger, O. Idigoras, and P. Vavassori, “Transient behavior of the dynamically ordered phase in uniaxial cobalt films,” *Phys. Rev. Lett.*, vol. 111, no. 19, p. 190 602, 2013.
- [134] Y. Yüksel, E. Vatansever, Ü. Akıncı, and H. Polat, “Nonequilibrium phase transitions and stationary-state solutions of a three-dimensional random-field Ising model under a time-dependent periodic external field,” *Phys. Rev. E*, vol. 85, no. 5, p. 051 123, 2012.
- [135] E. Costabile and J. R. de Sousa, “Phase transitions in a three-dimensional kinetic spin-1/2 Ising model with random field: effective-field-theory study,” *Phys. Rev. E*, vol. 85, no. 1, p. 011 121, 2012.
- [136] J. Hausmann and P. Ruján, “Stationary properties of a randomly driven Ising ferromagnet,” *Phys. Rev. Lett.*, vol. 79, no. 18, p. 3339, 1997.
- [137] M. Acharyya, “Nonequilibrium phase transition in the kinetic Ising model: Dynamical symmetry breaking by randomly varying magnetic field,” *Phys. Rev. E*, vol. 58, no. 1, p. 174, 1998.
- [138] N. Crokidakis, “Nonequilibrium phase transitions and tricriticality in a three-dimensional lattice system with random-field competing kinetics,” *Phys. Rev. E*, vol. 81, no. 4, p. 041 138, 2010.

- [139] A. M. Becker and R. M. Ziff, “Nouvelles applications des paramètres continus à la théorie des formes quadratiques,” *J. fur Reine Angew. Math.*, vol. 133, pp. 97–178, 1907.
- [140] B. Gutenberg, *Seismicity of the earth and associated phenomena*. Read Books Ltd, 2013.
- [141] F. Meng, L. N. Y. Wong, and H. Zhou, “Power law relations in earthquakes from microscopic to macroscopic scales,” *Sci. Rep.*, vol. 9, no. 1, p. 10705, 2019.
- [142] J. P. Sethna, K. A. Dahmen, and C. R. Myers, “Crackling noise,” *Nature*, vol. 410, no. 6825, pp. 242–250, 2001.
- [143] H. Barkhausen, “Zwei mit Hilfe der neuen Verstärker entdeckte Erscheinungen,” *Phys. Z.*, vol. 20, no. 17, pp. 401–403, 1919.
- [144] F. Wittel, F. Kun, H. Herrmann, and B. Kröplin, “Fragmentation of shells,” *Phys. Rev. Lett.*, vol. 93, no. 3, p. 035504, 2004.
- [145] J. Rosti, X. Illa, J. Koivisto, and M. J. Alava, “Crackling noise and its dynamics in fracture of disordered media,” *J. Phys. D: Appl. Phys.*, vol. 42, no. 21, p. 214013, 2009.
- [146] M. J. Alava, P. K. Nukala, and S. Zapperi, “Statistical models of fracture,” *Adv. Phys.*, vol. 55, no. 3-4, pp. 349–476, 2006.
- [147] L. De Arcangelis, C. Perrone-Capano, and H. J. Herrmann, “Self-organized criticality model for brain plasticity,” *Phys. Rev. Lett.*, vol. 96, no. 2, p. 028107, 2006.
- [148] J. J. Binney, N. J. Dowrick, A. J. Fisher, and M. E. Newman, *The theory of critical phenomena: an introduction to the renormalization group*. Oxford University Press, 1992.
- [149] P. Bak, C. Tang, and K. Wiesenfeld, “Self-organized criticality: An explanation of the  $1/f$  noise,” *Phys. Rev. Lett.*, vol. 59, no. 4, p. 381, 1987.
- [150] P. Bak, C. Tang, and K. Wiesenfeld, “Self-organized criticality,” *Phys. Rev. A*, vol. 38, no. 1, p. 364, 1988.
- [151] M. E. Newman, “Power laws, Pareto distributions and Zipf’s law,” *Contemp. Phys.*, vol. 46, no. 5, pp. 323–351, 2005.
- [152] A. Clauset, C. R. Shalizi, and M. E. Newman, “Power-law distributions in empirical data,” *SIAM rev.*, vol. 51, no. 4, pp. 661–703, 2009.
- [153] E. K. Salje, A. Planes, and E. Vives, “Analysis of crackling noise using the maximum-likelihood method: Power-law mixing and exponential damping,” *Phys. Rev. E*, vol. 96, no. 4, p. 042122, 2017.
- [154] A. Clauset, M. Young, and K. S. Gleditsch, “On the frequency of severe terrorist events,” *J. Confl. Resolut.*, vol. 51, no. 1, pp. 58–87, 2007.
- [155] W. H. Press, W. T. Vetterling, S. A. Teukolsky, and B. P. Flannery, *Numerical recipes in C++ the art of scientific computing*. Cambridge university press, 2001.

- [156] D. Spasojević, S. Bukvić, S. Milošević, and H. E. Stanley, “Barkhausen noise: Elementary signals, power laws, and scaling relations,” *Phys. Rev. E*, vol. 54, no. 3, p. 2531, 1996.
- [157] S. Zapperi, *Crackling Noise: Statistical Physics of Avalanche Phenomena*. Oxford University Press, 2022.
- [158] O. Perković, K. Dahmen, and J. P. Sethna, “Avalanches, Barkhausen noise, and plain old criticality,” *Phys. Rev. Lett.*, vol. 75, no. 24, p. 4528, 1995.
- [159] M. Vergeles, “Self-organization at nonzero temperatures,” *Phys. Rev. Lett.*, vol. 75, no. 10, p. 1969, 1995.
- [160] G. Caldarelli, “Mean field theory for ordinary and hot sandpiles,” *Physica A*, vol. 252, no. 3-4, pp. 295–307, 1998.
- [161] E. Puppini and M. Zani, “Magnetic hysteresis and Barkhausen noise in thin Fe films at 10 K,” *J. Condens. Matter Phys.*, vol. 16, no. 8, p. 1183, 2004.
- [162] M. Metra, L. Zorrilla, M. Zani, E. Puppini, and P. Biscari, “Temperature-dependent criticality in random 2D Ising models,” *Eur. Phys. J. Plus*, vol. 136, no. 9, pp. 1–14, 2021.
- [163] L. Kleinrock, *Queuing Systems, Volume I: Theory*, 1975.
- [164] J. G. Oliveira and A.-L. Barabási, “Darwin and Einstein correspondence patterns,” *Nature*, vol. 437, no. 7063, pp. 1251–1251, 2005.
- [165] A. Vázquez, J. G. Oliveira, Z. Dezsö, K.-I. Goh, I. Kondor, and A.-L. Barabási, “Modeling bursts and heavy tails in human dynamics,” *Phys. Rev. E*, vol. 73, no. 3, p. 036 127, 2006.
- [166] A.-L. Barabasi, “The origin of bursts and heavy tails in human dynamics,” *Nature*, vol. 435, no. 7039, pp. 207–211, 2005.
- [167] S. M. Allen and J. W. Cahn, “A microscopic theory for antiphase boundary motion and its application to antiphase domain coarsening,” *Acta Mater.*, vol. 27, no. 6, pp. 1085–1095, 1979.